Microwave Rotation-Tunnelling Spectroscopic and Theoretical Studies on Weakly Bound Molecular Complexes: Intermolecular Bonding across the Periodic Table

A Thesis

Submitted for the Degree of

Doctor of Philosophy

in the Faculty of Science

by

Arijit Das

भारतीय विज्ञान संस्थान

Department of Inorganic and Physical Chemistry

INDIAN INSTITUTE OF SCIENCE

Bangalore- 560012, India

July 2021

This page intentionally left blank.

Dedicated to my Family

This page intentionally left blank.

DECLARATION

———————■———————

I hereby declare that the work presented in this Thesis titled "**Microwave Rotation-Tunnelling Spectroscopic and Theoretical Studies on Weakly Bound Molecular Complexes: Intermolecular Bonding across the Periodic Table**" has been carried out by me at the Department of Inorganic and Physical Chemistry, Indian Institute of Science, Bangalore, India, under the supervision of Professor E. Arunan.

Arijit Das

July 2021   Arijit Das

This page intentionally left blank.

C E R T I F I C A T E

———————■———————

I hereby certify that the work presented in this Thesis entitled "**Microwave Rotation-Tunnelling Spectroscopic and Theoretical Studies on Weakly Bound Molecular Complexes: Intermolecular Bonding across the Periodic Table**" has been carried out by Mr Arijit Das at the Department of Inorganic and Physical Chemistry, Indian Institute of Science, Bangalore, India, under my supervision.

July 2021

Professor E. Arunan

(Research Supervisor)

This page intentionally left blank.

ACKNOWLDGEMENTS

———————■———————

I'd like to express my sincere thanks to Dr Richard Henchman, Dr Nick Lockyer, Prof. Klaus Müller-Dethlefs, and Prof. Arunan for letting me present a poster at the *Manchester International Symposium 2019.*

I thank Dr Chris Medcraft for all his help regarding the experiment. Without his initial clues, this Thesis would have been impossible.

I would like to thank Dr Eva Gougoula for teaching every detail in handling the chirped-pulse Fourier transform microwave spectrometer. I want to express my gratitude to her for her assistance in writing section 2.3 of the Thesis. She is a fantastic colleague to work with. I also thank her for her kind friendship. I also thank Dr John C. Mullaney for his kind friendship in Newcastle.

I would like to thank Dr Eva Gougoula for teaching every detail in handling the chirped-pulse Fourier transform microwave spectrometer. I'd want to express my gratitude to her for her assistance in writing section 2.3 of the Thesis.. I thank her for help in writing section 2.3 of the Thesis. She is a fantastic colleague to work with. I also thank her for her kind friendship. I also thank Dr John C. Mullaney for his kind friendship in Newcastle.

I thank all the members of the Chemical Dynamics Group. It was a pleasure to be a part of this group. I have learnt a lot from the wonderful talks during the group meetings. Special thanks to Prof. E. Arunan, Prof. P.K. Das for their enthusiastic involvement and valuable inputs during the talks.

I thank the present (Prof. E. Arunan) and past chairs (Prof. S. Umapathy and Prof. P. K. Das) of our department for their constant support and the entire infrastructure provided for research.

I thank the integrated PhD convenors Prof. A. J. Bhattacharya and Prof. N. Jayaraman for their help during the first two years of my stay here as an Integrated PhD student.

I sincerely thank all the course instructors for their endless passion and patience.

I gratefully acknowledge financial support from IISc for the fellowship. I am thankful to GARP IISc for providing funds for me to present our research findings at the International Symposium on Molecular Spectroscopy in Illinois. I am also grateful to

I would like to thank all the members of the '2016' Al(l)chemists' club. It was fun working with them for arranging different programs for the department. I'll cherish those memories for a long time.

I would like to thank all my Int PhD batchmates Allen, Atul, Biswajit, Deep, Kishan, Lalit, Nitin, Rajab, Rajeev, Ratul, Ravindra, Sahil, Somarupa. We had lots of fun time in coursework, assignments, and birthdays.

I would like to thank my college friends, Subrata, Sourav, Soumyadip, and school friend Subhankar, Ranjan, for their friendship.

I would like to thank all the members of the IISc Athletics team. I thank Ramaraj and coach sir for their encouraging words.

I want to extend my sincere thanks to my wonderful friend Miss Enakshmi Goswami. I have not even managed to come to IISc without her help, support, and affection. Thank you for tolerating my all-non-senses!

Finally, I would like to thank my family. I cannot express how grateful I am to my parents, Mr Benoy Kumar Das and Ms Hasi Das, for their unwavering support and understanding during my academic journey. They have never doubted my decisions and are always supportive irrespective of outcomes. I also want to express my heartfelt gratitude to my elder brother (Mr Arindam Das) and Boudi (Ms Keya Das) for their steadfast support and assistance. My eldest brother and Boudi made great sacrifices that cannot be conveyed in words. I'd want to thank my late grandparents, on whom I often reflect when it comes to life principles.

Please accept my apologies if I have missed any names.

Arijit Das

This page intentionally left blank.

Contents

This page intentionally left blank.

P R E F A C E

Intermolecular interactions play a very significant role in the structure and properties of molecules of life such as water, proteins and DNA. Microwave spectroscopy offers precise structural information on the near-equilibrium geometry of small dimers and trimers in isolation. Computational studies such as the Atoms in Molecules (AIM) analysis, non-covalent interactions (NCI) index and natural bond orbital (NBO) analysis are used to supplement rotational spectroscopic investigations.

Chapter 1 of this Thesis gives a summary of intermolecular interactions. This Chapter also discusses the theoretical aspects of rotational spectroscopy.

The rotational spectra of the weakly complexes were obtained using the Balle-Flygare Fourier transform microwave spectrometer (Bangalore, India) (BF-FTMW) and the chirped-pulse Fourier transform microwave spectrometer (Newcastle, UK) (*CP-FTMW*). Chapter 2 provides a brief overview of both spectrometers. This Chapter also provides a summary of theoretical techniques such as AIM, NCI, and NBO analysis.

Chapter 3 of the Thesis discusses the rotational spectra and structure of $(H_2S)_2$. The K_a = 1 transitions of H_2S dimer and several isotopologues were observed in a pulsed nozzle Fourier transform microwave spectrometer. These transitions give unequivocal proof that, at ultra-low temperatures, hydrogen sulphide (H_2S) forms hydrogen-bonded dimers in the same way as water does, despite the fact that ice and solid H_2S seem substantially different in bulk. Also, using the AIM theory, we have shown that H_2S dimer satisfies all the criteria proposed by Koch and Popelier to be hydrogen-bonded.

The rotational spectra, structure, and dynamics of the $(H_2S)_2(H_2O)$ complex are discussed in Chapter 4. The weakly bound complex between two hydrogen sulphide molecules and one water molecule, $(H_2S)_2(H_2O)$, was identified from its

rotational spectrum observed at conditions of supersonic expansion. The spectra of parent species were obtained using a chirped-pulse Fourier transform microwave spectrometer (Newcastle, UK) (*CP-FTMW*). The isotopologues were identified with Balle-Flygare Fourier transform microwave spectrometer (Bangalore, India) (*BF-FTMW*). Analysis of experimental results reveals that the three monomers are bound in a triangular arrangement through *S-H⋯S*, *O-H⋯S* and *S-H⋯O* hydrogen bonds. This geometry contains numerous characteristics that indicate the cooperative nature of the intermolecular interaction. The rotational spectrum shows a doubling of the lines caused by the internal rotation of the H_2O moiety about its C_2 axis. The break with axial molecular symmetry and the simplified internal dynamics allowed us to investigate $(H_2S)_2(H_2O)$ at a level of structural detail that has not yet been possible for $(H_2O)_3$ and $(H_2S)_3$ with rotational spectroscopy due to their zero-dipole moment.

Rotational spectroscopy could provide valuable information about the potential energy hypersurface of the weakly bound complexes. In this regard, we have measured the donor-acceptor interchange tunnelling splitting in the ground vibrational state of $Ar(H_2O)_2$ in Chapter 4. In the previous investigations, the donor-acceptor tunnelling splitting in fully deuterated species $Ar(D_2O)_2$ was measured to be 106 MHz. However, it could not be measured for the $Ar(H_2O)_2$, as the splitting was expected to be several GHz. With the help of a four-fold periodic potential, we have accurately predicted the fingerprints of donor-acceptor interchange tunnelling transitions and measured the splitting in $Ar(H_2O)_2$.

In Chapter 6, we have looked beyond hydrogen bonding and explore other intermolecular bonding across the Periodic Table. The slopes of the binding energy versus electron density at the bond critical point were derived for each main group element. Our results show that intermolecular bonding can be classified into two types: intermolecular bonding (IMB) with a covalent molecule (IMB-C) and intermolecular bonding (IMB) with an ionic molecule (IMB-I). The IMB-C includes hydrogen, halogen, chalcogen, pnictogen, tetrel (excluding carbon bonds), and boron bond (but not triel bond). IMB-I contains lithium, sodium, beryllium, magnesium bonds and triel bonds. The binding energy versus electron density plot of the IMI-C class generally has a low slope, whereas the IMB-I type has a high slope. Carbon bonds are distinct from

the other members of the group. Carbon is a hesitant partner in tetrel bonds due to the absence of lower energy d-orbitals. The electron density between the two atoms is extremely low, and the binding energy grows fast with electron density, resulting in a high slope value for the carbon bond. The slopes for Li, Na, Be, Mg, Ca-bonds were found out to be comparable, whereas the slope for the hydrogen bond remains standout. Several similarities eventually lead us to propose a common name, '*Alkalene bond*,' for the intermolecular bonding in alkali and alkaline earth metals.

Chapter 7 concludes with a summary and outlook.

The energy, wavefunction, and probability density for a one-dimensional periodic potential are given in Appendix 1. Our results suggest that the wavefunctions just above the barrier are still confined to some extent. Since these periodic potentials represent large amplitude motion in weakly bound complexes along the vibrational coordinate, the localisation of the wavefunction above the barrier height suggests the probability of a hydrogen bond above the barrier.

This page intentionally left blank.

List of Tables

Appendix Tables

Table A.7. Matrix Elements for the even levels (only 10*10 matrix is shown, for calculation we have taken a 50*50 matrix).

Table A.8. Matrix Elements for the odd levels (only 10*10 matrix is shown, for calculation we have taken a 50*50 matrix)

Table A.9. Eigenvector for the even block (cos block) with $V_2=100$ cm^{-1} and B=1.0 cm^{-1}.

Table A.10. Eigenvectors for the even block (sin block) with $V_2=100$ cm^{-1} and B=1.0 cm^{-1}.

Table A.11. First five wavefunctions for even (cos) energy levels.

Table A.12. First five wavefunctions for odd (sin) energy levels.

Table A.13. Probability density for even energy (cos) levels. Potential well defined at 80% of energy.

Table A.14. Probability density for odd energy (sin) levels. Potential well defined at 80% of energy.

List of Figures

Figure 4.2. A portion of the spectrum for $(H_2S)_2(H_2O)$ is displayed. The spectrum was recorded in the argon carrier gas. A magnified version of the 3_{03}-2_{02} and 3_{13}-2_{02} spectra are shown in the bottom panel, which clearly indicates two states.

Figure 4.3. Parent and isotopologues observed in this study for $(H_2S)_2(H_2O)$ complex. The chirped-pulse Fourier transform microwave spectrometer (CP-FTMW) was used to get the spectra of the parent species. The Balle-Flygare Fourier transform microwave spectrometer (BF-FTMW) was used to obtain its isotopologues.

Figure 4.4. Labelling of the atoms used in Kraitchman's analysis. The approximate locations of the principal axes are shown in the figure. The c principal axis is perpendicular to the plane of the paper.

Figure 4.5: Structural parameters for $(H_2S)_2(H_2O)$ complex. The values in black are derived from the fitting of the r_0 structure to the experimentally derived moments of inertia of all the isotopologues. The grey values are from substitution analysis (r_s structure).

Figure 4.6. Heavy atom distances (in Å) in $HSH\cdots OH_2$, $HOH\cdots SH_2$, $HSH\cdots SH_2$ and $(H_2S)_2(H_2O)$. The distances between heavy atoms decrease in the $(H_2S)_2H_2O$ complex, indicating hydrogen bonding cooperation. Values are in Å.

Figure 4.7. Barrier for C_2 rotation of water in the $(H_2S)_2(H_2O)$ complex calculated at B3LYP/aug-cc-pVDZ level.

Figure 4.8. Atoms in Molecules (AIM) topological analysis of $HSH\cdots SH_2$, $HOH\cdots SH_2$, $HSH\cdots OH_2$ and $(H_2S)_2(H_2O)$. The black dots show the bond critical points (BCP). The blue and red values represent electron density at the bond critical point computed using the B3LYP and MP2 methods.

Figure 4.9. Non-covalent interactions (NCI) index plot for $HSH\bullet\bullet\bullet OH_2$, $HOH\bullet\bullet\bullet SH_2$, $HSH\bullet\bullet\bullet SH_2$ and $(H_2S)_2(H_2O)$.

Figure 5.1. Energy level diagram for $(H_2O)_2$. The numbers represent the spin statistical weights of each of the six $(H_2O)_2$ and $(D_2O)_2$ states.

Figure 5.2. Structures and principal axes of $(H_2O)_2$ and $Ar(H_2O)_2$ complexes. In these two systems, the a-axis and b-axis are swapped.

Figure 5.3. Energy level diagram for $Ar(H_2O)_2$ complex. The solid blue line represents rigid-rotor-like a-dipole transitions. Green solid lines denote the b-dipole Kp' even transitions. The green dotted line indicates the b-dipole Kp' odd transitions.

Figure 5.4. Stick diagram showing A_1, B_1, and E_1 states of $(H_2O)_2$, $Ar(H_2O)_2$, and their fully deuterated counterparts.

1000-2000 (in cyan) and above 2000 (in blue) are classified as high, intermediate, and low slope, respectively. The correlation coefficient (CC) or R^2 of the fit for each element are also indicated.

Figure 6.7. Electron density variation for a typical covalent (N_2), ionic (NaF) and van der Waals (Ne_2) molecule. Similar differences could be seen in boron ($F_3B\cdots OH_2$), sodium ($FNa\cdots OH_2$) and carbon ($FH_3C\cdots OH_2$) bonds.

Figure 6.8. The ratio of the potential ($|V(r)|$) and kinetic ($G(r)$) energy densities of the electrons at BCP for the different intermolecular bonds formed by main group elements of the Periodic Table. The $|V(r)|/\ G(r)$ ratio has been used for the characterisation of bonding in three regions, namely closed-shell (<1.00) (in blue), intermediate (1.00-2.00) (in cyan), and shared-shell (>2.00) (in green) interaction.

Figure 6.9. The ratio of the first ($|\lambda_1|$) and third (λ_3) eigenvalues of the Hessian matrix at BCP for the different intermolecular bonds formed by the main group elements of the Periodic Table. The ($|\lambda_1|)/\lambda_3$ ratio has been used for the characterisation of bonding in three regions, namely closed-shell (<0.25) (in blue), intermediate (0.25-1.00) (in cyan), and shared shell interaction (>1.00) (in green).

Appendix Figures

Figure A.1. Representative periodic potential showing the effect of zero-point motion on the equilibrium structure of a hydrogen-bonded complex. On the left: The criterion proposed by Goswami et.al. On the right: Slightly modified criterion proposed from current probability density analysis.

Figure A.2 Three-fold potential and energy levels (Only the first few energy levels are shown in the diagram). The energy values are given in Table A.3. Reproduced results from reference 14, figure 2.

Figure A.3. Wavefunctions (even and odd block) for a three-fold potential. Reproduced results from reference 14, figure 2.

Figure A.4. Splitting due to donor-acceptor interchange tunnelling in ($H_2O)_2$ and ($D_2O)_2$. Values are in cm^{-1}.

Figure A.5. Potential well defined at 80% of the energy of a two-fold potential. Region 2 and Region 2 ′ have been described as the "inside the well". Region 1, Region 1′, Region 3 have been defined as the "outside the well".

Figure A.6. Potential well defined at 80% of the energy of a three-fold potential. Region 2, Region 2′, and Region 2″ have been described as the "inside the well." Region 1, Region 1′, Region 3, and Region 3′ have been defined as the "outside the well."

Figure A.7. Probability density for odd energy levels for V_2=100 cm^{-1} and $\mathbf{B}$=1.0 cm^{-1}. The yellow line denotes the energy level below 100 cm$^{-1,}$ and the blue line indicates the energy level above 100 cm^{-1}. The top panel shows the probability density "inside the well" and the bottom one "outside the well". The black line denotes the delocalisation value.

Figure A.8. Probability density for even energy levels for V_2=100 cm^{-1} and $\mathbf{B}$=1.0 cm^{-1}. The yellow line denotes the energy level below 100 cm^{-1}, and the blue line indicates the energy level above 100 cm^{-1}. The top panel shows the probability density "inside the well" and the bottom one "outside the well". The black line denotes the delocalisation value.

Figure A.9. Probability density for all energy levels for V_2=100 cm^{-1} and $\mathbf{B}$=1.0 cm^{-1}. The yellow line denotes the energy level below 100 cm$^{-1,}$ and the blue line indicates the energy level above 100 cm^{-1}. The top panel shows the probability density "inside the well" and the bottom one "outside the well". The black line denotes the delocalisation value.

Figure A.10. Probability density for all energy levels for V_2=100 cm^{-1} and $\mathbf{B}$=1.0 cm^{-1}. The yellow line denotes the energy level below 100 cm^{-1}, and the blue line indicates the energy level above 100 cm^{-1}. The top panel shows the probability density "inside the well" and the bottom one "outside the well". The black line denotes the delocalisation value. The integrating region is kept at 80% of total energy. This diagram is similar to Figure A.9 and provided once again for completeness.

Figure A.11. Probability density for all energy levels for V_2=100 cm^{-1} and $\mathbf{B}$=1.0 cm^{-1}. The yellow line denotes the energy level below 100 cm^{-1}, and the blue line indicates the energy level above 100 cm^{-1}. The top panel shows the probability density "inside the well" and the bottom one "outside the well". The black line denotes the delocalisation value.

Figure A.12. Probability density for all energy levels for V_2=100 cm^{-1} and $\mathbf{B}$=1.0 cm^{-1}. The yellow line denotes the energy level below 100 cm$^{-1,}$ and the blue line indicates the energy level above 100 cm^{-1}. The top panel shows the probability density '"inside the well" and the bottom one "outside the well". The black line denotes the delocalisation value.

Figure A.13. Probability density for all energy levels for V_2=100 cm^{-1} and $\mathbf{B}$=1.0 cm^{-1}. The yellow line denotes the energy level below 100 cm$^{-1,}$ and the blue line indicates the energy level above 100 cm^{-1}. The top panel shows the probability density "inside the well" and the bottom one "outside the well". The black line denotes the delocalisation value.

Figure A.14. Probability density for odd energy levels for $V_2=10$ cm^{-1} and **B**$=1.0$ cm^{-1}. The yellow line denotes the energy level below 10 cm^{-1}, and the blue line denotes the energy level above 10 cm^{-1}. The top panel shows the probability density "inside the well" and the bottom one "outside the well". The black line denotes the delocalisation value.

Figure A.15. Probability density for even energy levels for $V_2=10$ cm^{-1} and **B**$=1.0$ cm^{-1}. The yellow line denotes the energy level below 10 cm^{-1}, and the blue line denotes the energy level above 10 cm^{-1}. The top panel shows the probability density "inside the well" and the bottom one "outside the well". The black line denotes the delocalisation value.

Figure A.16. Probability density for all energy levels for $V_2=10$ cm^{-1} and **B**$=1.0$ cm^{-1}. The yellow line denotes the energy level below 10 cm^{-1}, and the blue line indicates the energy level above 10 cm^{-1}. The top panel shows the probability density "inside the well" and the bottom one "outside the well". The black line denotes the delocalisation value.

Figure A.17. Probability density for odd energy levels for $V_2=1000$ cm^{-1} and **B**$=1.0$ cm^{-1}. The yellow line denotes the energy level below 1000 cm-1, and the blue line denotes the energy level above 1000 cm^{-1}. The top panel shows the probability density "inside the well" and the bottom one "outside the well". The black line denotes the delocalisation value.

Figure A.18. Probability density for even energy levels for $V_2=10$ cm^{-1} and **B**$=1.0$ cm^{-1}. The yellow line denotes the energy level below 1000 cm^{-1}, and the blue line denotes the energy level above 1000 cm^{-1}. The top panel shows the probability density "inside the well" and the bottom one "outside the well". The black line denotes the delocalisation value.

Figure A.19. Probability density for all energy levels for $V_2=1000$ cm^{-1} and **B**$=1.0$ cm^{-1}. The yellow line denotes the energy level below 1000 cm^{-1}, and the blue line indicates the energy level above 1000 cm^{-1}. The top panel shows the probability "inside the well" and the bottom one "outside the well". The black line indicates the delocalisation value.

Figure A.20. Probability density for all energy levels for $V_2=100$ cm^{-1} and **B**$=10.0$ cm^{-1}. The yellow line denotes the energy level below 100 cm^{-1}, and the blue line indicates the energy level above 100 cm^{-1}. The top panel shows the probability density "inside the well" and the bottom one "outside the well". The black line denotes the delocalisation value.

Figure A.21. Probability density for all energy levels for $V_3=100$ cm^{-1} and **B**$=1.0$ cm^{-1}. The yellow line denotes the energy level below 100 cm^{-1}, and the blue line denotes the energy level above 100 cm^{-1}. The top panel shows the probability density "inside the well" and the bottom one "outside the well". The black line denotes the delocalisation value.

This page intentionally left blank.

List of Symbols

A, B, C	Rotational constants
B	Internal rotational constant
$D_J, D_{JK}, D_K, d_1, d_2$	Distortion constants
I_a, I_b, I_c	Moments of inertia about their cyclic permutations over the *a*-, *b*- and *c*-inertial axis
P_a, P_b, P_c	Planar moments about their respective cyclic permutations over the *a*-, *b*- and *c*-inertial axis
μ_a, μ_b, μ_c	Dipole moment component along the *a*, *b,* and *c* principal axes.
J	Total angular momentum
K	Projection of the total angular momentum on the *body-fixed axis*
K_a	Projection of J onto the a-rotational axis of the molecule
K_c	Projection of J onto the c-rotational axis of the molecule
M	Projection of the total angular momentum on the *space-fixed axis*
κ	Ray's asymmetry parameter
$\Delta E, \Delta E_{BSSE}, \Delta E_{BSSE+ZPE}$	Binding energy, Basis set superposition error corrected binding energy, Basis set superposition error and zero-point corrected binding energy
r_e, r_s, r_o, r_m	Equilibrium, substitution, ground state (effective) and mass dependent structure.
D	Dissociation energy
ρ	Electron density
$\nabla^2 \rho$	Laplacian of electron density

$\lambda_1, \lambda_2, \lambda_3$	Eigenvalues of the Hessian Matrix of electron density
V, G	Potential and kinetic energy density
s	Reduced density gradient

This page intentionally left blank.

Properties of Nuclides

(Properties of nuclides of relevance reproduced from the NIST database)

Element Symbol	Atomic Number	Atomic Mass	Isotopic Abundance	Nuclear Spin
H	1	1.00782503223(9)	99.985(70)	½
		2.01410177812(12)	0.0115(70)	1
		3.016 0492779(24)	0	½
O	8	15.994914 61957(17)	99.757(16)	0
		16.99913175650(69)	0.038(1)	5/2
		17.99915961286(76)	0.205(14)	0
S	16	31.972 071 1744(14)	94.99(26)	0
		32.971 458 9098(15)	0.75(2)	3/2
		33.967 867 004(47)	4.25(24)	0
		35.967 080 71(20)	0.0001(1)	0
Ar	18	35.967 545 105(28)	0.3336(21)	0
		37.962 732 11(21)	0.0629(7)	0
		39.962 383 1237(24)	99.6035(25)	0

Link: (Atomic Weights and Isotopic Compositions with Relative Atomic Masses | NIST)

This page intentionally left blank.

CHAPTER 1

Introduction

This page intentionally left blank.

Chapter 1: Introduction

1.1 Intermolecular Interactions

Intermolecular interactions play a decisive role in every form of matter, e.g., solid, liquid, and gas. Though intermolecular interactions appear to be well understood in a broad sense, at a deeper molecular level, it is still evolving. As Wolfgang Pauli stated, "The best that most of us can hope to achieve in science is simply to misunderstand at a deeper molecular level." For instance, Pauling pointed out a 1920 paper from Latimer and Rodebush[1] as "the discovery of the hydrogen bond." After its discovery, it took almost 90 years to define the hydrogen bond[2,3] comprehensively. The importance of intermolecular bonding has been articulated extensively in various books, reviews, and reports across the diverse field of physics, chemistry, and biology in the last few decades. The realisation of intermolecular interaction was most likely influenced by the Clausius-Clapeyron equation, which indicates the molar heat of vaporisation as a function of the substrate and its intermolecular forces. The higher molar heat of vaporisation means stronger intermolecular forces.

$$\frac{d \ln P}{dT} = \frac{\Delta H_{vap}}{RT^2}$$

The van der Waals equation of state corrects two real gas properties: the excluded volume of gas particles (b) and attractive forces (a) between gas molecules.

$$(P + \frac{a}{n^2 V^2})(V - nb) = nRT$$

The van der Waals coefficients are well tabulated in the literature. The a-coefficients of water vapour (H_2O) and hydrogen sulphide (H_2S) gas are 5.536 and 4.490 L^2bar/mol^2, respectively[4]. The higher the value of a the stronger the attraction between molecules. The difference in a value resulted in a wide disparity between H_2S and H_2O; H_2O is a liquid at room temperature, whereas H_2S remains a gas. The boiling point of

hydrogen sulphide is -60°C and whereas water boils at 100°C. The high boiling point of water indicates the stronger intermolecular forces between water moieties. These interactions enormously influence the physical properties both at the bulk and molecular level. The physical forces involved with these interactions could be decisive in understanding the intermolecular interactions. The intermolecular interaction energy could be partitioned into electrostatics, induction, exchange, and dispersion. In a true sense, the individual contributions are not measurable in the experiment; we could only measure the total interaction energy. However, this partition is helpful to understand the nature and origin of the intermolecular interactions. The proportions of electrostatics, induction, exchange, and dispersion in particular intermolecular interactions led to a conflation of the van der Waals interaction and the hydrogen bond. Technically, there is no difference in physical forces between hydrogen bonding and van der Waals interactions. Hydrogen bonding should be considered as a class of van-der Waals interaction[5]. A recent IUPAC technical report[3] points out that no single physical/chemical force can be attributed to hydrogen bonding. Hydrogen bonding could have more contribution from electrostatics or dispersion, depending on the nature of the donor and acceptor. The weak interactions are not limited to hydrogen bonds. Several weak interactions have been identified/defined in recent times. Aerogen bonding[6,7] (renamed as noble gas bond[8]), halogen bonding[9,10,11,12], chalcogen bonding[13,14,15], pnictogen bonding[16,17,18,19,20], tetrel bonding[21,22,23,24], and triel[25] bonding are all examples of comparable intermolecular bonds. Lithium bonding[26,27], beryllium bonding[28,29,30,31], and magnesium bonding[32,33,34] have all been proposed for the alkali and alkaline earth groups. We propose the name "alkalene bond" to include all intermolecular interactions formed by the alkali and alkaline earth metals in this Thesis.

1.2 Rotational Spectroscopy

Chemists are used to investigating molecules bound together by chemical bonds with dissociation energy in the tens of thousands of cm^{-1}. Intermolecular bonds are roughly 10^{2}-10^{3} times weaker than typical chemical bonds (in a narrower sense). At room temperature, bonds with dissociation energies comparable to or weaker than the thermal

energy (kT) would not be stable. The development of vacuum technology and molecular beams enabled the temperature of molecular species reduced to just a few Kelvin, where weakly bound gas complexes can remain associated. In this Thesis, we probe these interactions in molecular beams using microwave spectroscopy. In spectroscopy, we get different information about these interactions depending on the frequency of light and technique. Microwave spectroscopy allows for the exact determination of geometrical properties like bond lengths, angles, and dihedrals of the weakly bound complexes in the gas phase. It is critical to understand that microwave spectroscopy does not draw a link, i.e., a bond, between the two atoms; instead, it can only tell us how far apart they are. After acquiring the experimental geometry, we seek assistance from several theoretical techniques such as Atoms in Molecules (AIM)[35], non-covalent interactions (NCI) index[36], and natural bond orbital analysis (NBO)[37] to examine the precise nature of these interactions. Each of these theories has its own set of benefits and drawbacks, and we use all of them with the hope of understanding these interactions thoroughly. The different quantum chemical calculations used in this Thesis will be reviewed in Chapter 2.

This Chapter is concerned with explaining the theoretical basis of rotational spectroscopy. These particulars are mentioned briefly because they are covered in detail in a handful of excellent monographs[38,39,40,41]. Rotational transitions are fitted to a Hamiltonian, allowing the determination of spectroscopic constants. All the molecules presented in this Thesis are asymmetric tops.

1.2.1 The Moment of Inertia Tensor

The principal axis system resolves rotational motion along three mutually perpendicular body fixed axes. The diagonalisation of the moments of inertia tensor yields the direction of the primary axes and the moment of inertia (I) along each of them.

The moment of inertia tensor is a second-order tensor given by the matrix:

$$I = \begin{bmatrix} \sum_i m_i(y_i^2 + z_i^2) & -\sum_i m_i x_i y_i & -\sum_i m_i x_i z_i \\ -\sum_i m_i y_i x_i & \sum_i m_i(x_i^2 + z_i^2) & -\sum_i m_i y_i z_i \\ -\sum_i m_i z_i x_i & -\sum_i m_i z_i y_i & \sum_i m_i(x_i^2 + y_i^2) \end{bmatrix}$$

Here the position of the ith particle x_i, y_i, z_i are given in the body-fixed axis system (x, y, z), with the origin being the centre-of-mass. The moments of the inertia matrix can be diagonalised (I') by an orthogonal transformation matrix X that transforms the moments of inertia matrix (I). The matrix X represents a rotation of the coordinate system, which can be written as follows:

$$X^{-1}IX = I'$$

The matrix X has columns that are the normalised eigenvectors of I. The I' matrix is a diagonal matrix whose elements are the eigenvalues of I. This new coordinate system is called the principal axis system (a, b, c), and I' has the form:

$$I' = \begin{pmatrix} I_a & 0 & 0 \\ 0 & I_b & 0 \\ 0 & 0 & I_c \end{pmatrix}$$

Where $I_a = \sum_i m_i(b_i^2 + c_i^2), I_b = \sum_i m_i(a_i^2 + c_i^2), I_c = \sum_i m_i(a_i^2 + b_i^2)$ and by convention $I_a \leq I_b \leq I_c$

Molecules can be classified based on the values of the three moments of inertia (see Table 1.1). The classes are as follows:

Table 1.1. Classification of molecules based on their principal moments of inertia.

Class	Moments of inertia	Examples
Spherical Tops	$I_a=I_b=I_c$	CH_4, SF_6
Linear Rotors	$I_a=0$, $I_b=I_c$	CO, HCN
Symmetric Tops	*Prolate:* $I_a<I_b=I_c$	CH_3Cl,
	Oblate: $I_a=I_b<I_c$	NH_3, BF_3
Asymmetric Tops	$I_a<I_b<I_c$	H_2O, CH_2Cl_2

 Any molecule's geometry may be reduced to three rotational constants, *A, B*, and *C*, which are inversely proportional to the moments of inertia about the three principal axes, *a, b*, and *c*. The *abc* axis system is often oriented so that the *A* rotational constant has the greatest magnitude, and the *C* rotational constant has the smallest.

1.2.2   Geometrical Shapes of the Molecules

1.2.2.1 Spherical Tops

As spherical tops have equal moments of inertia along each axis, $I_a=I_b=I_c$, and have no dipole moment, it is unusual to probe them using microwave spectroscopy. However, in a few special cases, such as CH_4 rotational spectra has been observed, as centrifugal distortion can induce a dipole moment for higher *J* values[42]. The rotational energy expression for a spherical top is the same as that for a diatomic.

1.2.2.2 Linear Rotors

For a rigid rotor in a field-free space, the rotational Hamiltonian can be written as,

$$H\psi = \frac{P^2}{2I}\psi$$
$$= \frac{J(J+1)\hbar^2\psi}{2I}$$
$$= BJ(J+1)\psi$$

And the corresponding energy levels are given by $E_J= BJ(J+1)$

The *J* levels may be split by an applied electric/magnetic field, known as Stark/Zeeman splitting. A quantum number *M* or M_J represents the projection of J onto the lab frame axis; the *2J+1* levels are degenerate, and their degeneracy is lifted by an electric or magnetic field.

1.2.2.3 Symmetric Tops

For a symmetric top, any two of the principal moments of inertia are equal. This is due to the system's symmetry. For the prolate top, *'a'* is the symmetry axis, whereas for the oblate top, *'c'* is the symmetry axis.

There are three quantum numbers (*J,K,M*) used in rotational spectroscopy. Two axis systems are commonly utilised to understand the rotation of a molecule. The first one is *a laboratory or space-fixed system* denoted by (**X, Y, Z**), and the second one is the *body-fixed or molecular coordinate* system denoted as (*x,y,z*). The body-fixed coordinate system could be easily identified with principal axes *(a,b,c)* system with the help of different representations (will be discussed in section 1.2.5). The three Euler angles describe the orientation of the molecular system relative to the space-fixed system. The rigid rotor Hamiltonian is given by:

$$H = \frac{P_a^2}{2I_A} + \frac{P_b^2}{2I_B} + \frac{P_c^2}{2I_C}$$

It is known that the square of the total angular momentum operator P^2 commutes with the rigid rotor Hamiltonian and the following eigenvalue equation is fulfilled.

$$P^2\psi \mid JKM >= \hbar^2 J(J+1)\psi \mid JKM > \qquad J = 0,1,2,3....$$

The operator for the projection of the total angular momentum on the *body-fixed axis* P_z commutes with the rigid rotor Hamiltonian. The following eigenvalue equation is fulfilled.

$$P_z\psi \mid JKM >= \hbar K\psi \mid JKM > \qquad K = -J \ to + J$$

The operator for the projection of the total angular momentum on the *space-fixed axis* P_Z commutes with the rigid rotor Hamiltonian. The following eigenvalue equation is fulfilled. This quantum number is only relevant in the presence of external (electric or magnetic) fields.

$$P_Z\psi \mid JKM >= \hbar M\psi \mid JKM > \qquad M = -J \ to + J$$

The rigid rotor Hamiltonian is expressed as:

$$H = [\frac{P_a^2}{2I_A} + \frac{P_b^2}{2I_B} + \frac{P_c^2}{2I_C}] |JKM\rangle$$

$$= [\frac{P_a^2}{2I_A} + \frac{1}{2I_B}(P_b^2 + P_c^2)] |JKM\rangle \ (For \ a \ prolate \ top)$$

$$Since \ P^2 = P_a^2 + P_b^2 + P_c^2$$

$$P_b^2 + P_c^2 = P^2 - P_a^2$$

$$= [\frac{P^2}{2I_B} + (\frac{1}{2I_A} - \frac{1}{2I_B})P_a^2] |JKM\rangle$$

$$= [\frac{h^2}{2I_B}J(J+1) + (\frac{h^2}{2I_A} - \frac{h^2}{2I_B})K^2] |JKM\rangle$$

$$E_{JK} = BJ(J+1) + (A-B)K_a^2 \ (For \ a \ prolate \ top)$$

Similarly, for an oblate top, it can be shown that,

$$E_{JK} = BJ(J+1) + (C - B)K_c^2 \ (For \ an \ oblate \ top)$$

1.2.2.4 Asymmetric Tops

For an asymmetric top, the moments of inertia along the three-principal axis are not equal. The rigid asymmetric rotor Hamiltonian is given by:

$$\hat{H} = \frac{P_a^2}{2I_A} + \frac{P_b^2}{2I_B} + \frac{P_c^2}{2I_C}$$

For an asymmetric rotor, K no longer commutes with the Hamiltonian. The above equation with ($I_A \neq I_B \neq I_C$) has no general solutions and must be solved numerically. However, for some specific values of J, analytical solutions are available for a rigid rotor[41,43]. The asymmetric top Hamiltonian can be solved using a symmetric top basis set.

$$\hbar^2 H = AP_a^2 + BP_a^2 + CP_a^2$$

$$where \ A = \frac{\hbar^2}{2I_A}, B = \frac{\hbar^2}{2I_B}, C = \frac{\hbar^2}{2I_C} \ ,$$

$$\hbar^2 \hat{H} = (\frac{A+B}{2})(P_a^2 + P_b^2) + CP_c^2 + (\frac{A-B}{2})(P_a^2 - P_b^2)$$

$$= (\frac{A+B}{2})P^2 + (C - \frac{A+B}{2})P_c^2 + (\frac{A-B}{4})[(P^+)^2 + (P^-)^2].$$

The following symmetric top matrix elements are,

$$\left\langle JK \left| P^2 \right| JK \right\rangle = \hbar^2 J(J+1),$$

$$\left\langle JK \left| P_c^2 \right| JK \right\rangle = \hbar^2 K^2,$$

$$\left\langle JK+2 \left| (P^-)^2 \right| JK \right\rangle = \hbar^2[(J-K)(J+K+1)(J-K-1)(J+K+2)]^{1/2}$$

$$\left\langle JK-2 \left| (P^+)^2 \right| JK \right\rangle = \hbar^2[(J+K)(J-K+1)(J+K-1)(J-K+2)]^{1/2}$$

With the symmetric top basis functions, the asymmetric top Hamiltonian has matrix elements with $\Delta K=0$ and $\Delta K= \pm 2$

The basis set for $J=1$ has three members $|1,1\rangle$, $|1,0\rangle$, $|1,-1\rangle$, and the Hamiltonian is the 3×3 matrix:

$$H_{11} = \left\langle 1,1 | H | 1,1 \right\rangle = (\frac{A+B}{2})\left\langle 1,1 | P^2 | 1,1 \right\rangle + (C - \frac{A+B}{2})\left\langle 1,1 | P_c^2 | 1,1 \right\rangle + (\frac{A-B}{4})[\left\langle 1,1 | (P^+)^2 + (P^-)^2 | 1,1 \right\rangle]$$

$$= A + B + (C - \frac{A+B}{2}) + 0$$

$$= C + \frac{A+B}{2}$$

$$H_{12} = 0 + 0 + 0 = 0$$

$$H_{13} = 0 + 0 + \frac{A-B}{4}[\left\langle 1,1 | (P^+)^2 | 1,-1 \right\rangle] + \frac{A-B}{4}[\left\langle 1,1 | (P^-)^2 | 1,-1 \right\rangle]$$

$$= 0 + 0 + \frac{A-B}{4}[(1-(-1)(1-1+1)(1-(-1)-1)(1-1+2)]^{1/2}$$

$$= 0 + 0 + \frac{A-B}{4}[2 \times 1 \times 1 \times 2]^{1/2}$$

$$= \frac{A-B}{2}$$

Exchanging the second and third rows and columns, we obtain:

$$
\begin{pmatrix}
C+\dfrac{A+B}{2} & 0 & \dfrac{A-B}{2} \\
0 & A+B & 0 \\
\dfrac{A-B}{2} & 0 & C+\dfrac{A+B}{2}
\end{pmatrix}
\rightarrow
\begin{pmatrix}
C+\dfrac{A+B}{2} & \dfrac{A-B}{2} & 0 \\
\dfrac{A-B}{2} & C+\dfrac{A+B}{2} & 0 \\
0 & 0 & A+B
\end{pmatrix}
$$

And then solving the secular equation

$$
\begin{vmatrix}
C+\dfrac{A+B}{2}-\lambda & \dfrac{A-B}{2} \\
\dfrac{A-B}{2} & C+\dfrac{A+B}{2}-\lambda
\end{vmatrix}
= 0
$$

$$
\lambda = C + A
$$
$$
or, \lambda = C + B
$$

For $J=1$, The three solutions are $A+B$, $A+C$, and $B+C$. The labelling of the energy levels is carried out by considering the correlation diagram connecting prolate and oblate tops (see Figure 1.1). The higher K_a values have higher energies for a prolate top, while for an oblate top, the higher K_c levels have lower energies. For, asymmetric tops the levels are labelled as $J_{K_a K_c}$ (the King-Hainer-Cross notation[44], also previously known as K_{-1} and K_{+1}), where J is a good quantum number, but K_a and K_c are just the labelling for the asymmetric top. Only in the prolate or oblate top limits the K_a and K_c become good quantum numbers. The degree of asymmetry can be quantified by an asymmetry parameter, κ *(kappa)*, which varies from -1 (prolate top) to +1 (oblate top). The asymmetry parameter, also known as *Ray's asymmetry parameter*[45], has the following definition:

$$
\kappa = \frac{2B - A - C}{A - C}
$$

The notation $J_{K_a K_c}$ allows the three energy levels associated with $J=1$ to be labelled

$$
E\,(1_{01}) = A+B,
$$

$$E\ (1_{11}) = A+C$$

$$\text{and } E\ (1_{01}) = B+C$$

The explicit energy level expressions (*J=0,1 and 2*) have been published for a rigid asymmetric rotor. For other *J* values, the functional dependence of each energy level must be determined each time when fitting spectral transitions.
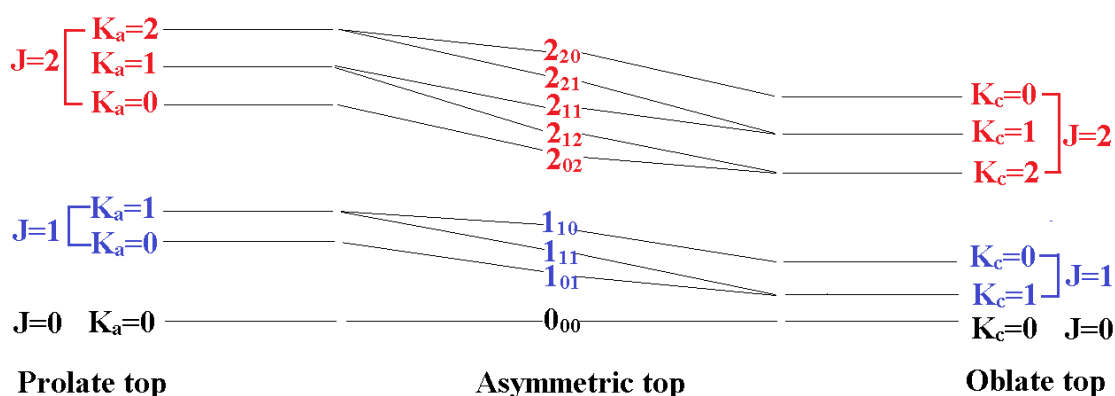
Figure 1.1. Prolate-oblate correlation diagram useful for labelling asymmetric top levels. [J=0 (Black), J=1 (Blue) and J=2 (Red) energy levels are shown].

1.2.3   **Selection Rules**

For a linear molecule, the allowed transitions are:

$$\Delta J = \pm 1$$

For a symmetric top, the selection rules are:

$$\Delta J = 0,\ \pm 1,\ \Delta K = 0$$

For an asymmetric top, the allowed transitions are:

$$\Delta J = 0,\ \pm 1$$

In general, an arbitrary asymmetric top molecule has three dipole moment components, μ_a, μ_b and μ_c along the principal axes. Each non-zero component allows specific transitions. In terms of ΔK_a and ΔK_c, the selection rules are provided in Table 1.2.

Table 1.2. Selection rules for ΔK_a and ΔK_c.

Dipole Component	$\Delta K_a = 0$	$\Delta K_c = 0$
$\mu_a \neq 0$	$0, \pm2, \dots$	$\pm1, \pm3, \dots$
$\mu_b \neq 0$	$\pm1, \pm3, \dots$	$\pm1, \pm3, \dots$
$\mu_c \neq 0$	$\pm1, \pm3, \dots$	$0, \pm2, \dots$

1.2.4   Centrifugal Distortion Constants

In a diatomic, as the molecule rotates, the bond will lengthen up, and the moments of inertia will increase. As the bond can lengthen in only one direction, only the primary distortion term D is required in the semi-rigid rotor approximation:

$$E(J) = BJ(J+1) - DJ^2(J+1)^2$$

The constant D is called centrifugal distortion constant; there are higher-order distortion constants that lead to energy level expression:

$$E(J) = BJ(J+1) - D[J(J+1)]^2 + H[J(J+1)]^3 + L[J(J+1)]^4 + M[J(J+1)]^5 + \dots$$

The equilibrium vibrational frequency (ω_e) is related to distortion constant and rotational constant by Kratzer relationship:

$$D = \frac{4B_e^3}{\omega_e^2}$$

For a prolate symmetric top, three distortion terms (D_J, D_{JK}, D_K) are required to get the energy level for semi-rigid rotor Hamiltonian,

$$E_{JK} = BJ(J+1) + (A-B)K^2 - D_J J^2(J+1)^2 - D_{JK} J(J+1)K^2 - D_K K^4$$

The transition frequencies are then given by,

$$\upsilon_{J+1,K \leftarrow J,K} = 2B(J+1) - 4D_J(J+1)^3 - 2D_{JK}(J+1)K^2$$

1-13

The centrifugal distortion constants and spectra for an asymmetric top molecule are substantially complex. A detailed mathematical treatment could be found in Chapter VIII of Gordy and Cook[41].

The first order energy expression is given by

$$E = E_r + E_d$$

Here E_r is the energy of a rigid rotor. E_d can be defined using five distortion constants $(\Delta_J, \Delta_{JK}, \Delta_K, \delta_J, \delta_K)$.

$$E_d = -\Delta_J J^2(J+1)^2 - \Delta_{JK} J(J+1)\langle P_z^2 \rangle - \Delta_K \langle P_z^4 \rangle - 2\delta_J J(J+1)\langle P_x^2 - P_y^2 \rangle -$$
$$\delta_K \langle P_z^2(P_x^2 - P_y^2) + (P_x^2 - P_y^2)P_z^2 \rangle$$

It is essential to mention that Watson developed two different reductions for asymmetric top molecules, namely A and S-reduction[46]. The A reduction (i, e., asymmetric reduction) is straightforward but will begin to become inaccurate for nearly symmetric asymmetric top molecules, and S-reduction should be used for these cases. In this Thesis, S-reduction has been used for fitting the rotational spectrum of $(H_2S)_2$, which is a nearly prolate asymmetric top molecule with $\kappa = -0.99$. The A-reduction has been used for $Ar(H_2O)_2$ with $\kappa = -0.69$. The relationship between the distortion coefficients of A and S reduction can be found in Table 8.16 of the book *Microwave Molecular Spectra* by Gordy and Cook[41].

1.2.5 Representation

There are six different possible combinations in which the (x, y, z) body fixed axes system can be identified with the (a, b, c) principal axis of inertia (see Table 1.3).

Table 1.3. Identification of (x, y, z) body fixed axes with principal axes (a, b, c).

	I^r	II^r	III^r	I^l	II^l	III^l
x	b	c	a	c	a	b
y	c	a	b	b	c	a
z	a	b	c	a	b	c

The I^r and III^l type representations are sufficient to handle most asymmetric tops. Both identifications, of course, give the same energy levels; however, each identification has a particular advantage for specific ranges of κ. For a nearly prolate top (κ close to -1), I^r representation is more suitable whereas, for a nearly oblate top III^l representation is more convenient to use.

1.2.6   Tunnelling- Rotational Transitions

Large amplitude motions often complicate microwave spectra of weakly bound complexes. These motions are manifested as splitting in the spectral transitions. These tunnelling effects contain important information about the vibrational potential energy surface, but these transitions are difficult to predict, and assignments of these spectral lines are often non-trivial. A handful of fully assigned and well-understood dynamics of weakly bound complexes can be found in the literature.

The molecular point group is not a symmetry group of the complete Hamiltonian, but it is a symmetry group of the vibronic Hamiltonian. Molecular symmetry (MS) (chemically feasible operations of complete nuclear permutation inversion group) handles the rovibronic and spin states of these weakly bound complexes. The book '*Molecular Symmetry and Spectroscopy*' by Bunker and Jensen[47] cover the molecular symmetry group in great detail.

1.3   **Spectral Prediction and Fitting**

In the Balle-Flygare Fourier transform microwave spectrometer (*BF-FTMW*), the bandwidth associated with individual measurements was generally limited to around 1 MHz. Therefore, a good guess about the molecular structure is required to search for the rotational transitions. From *ab-initio* calculations, rotational constants, centrifugal distortion constants, and dipole moments are obtained along the three principal axes. These are used to predict the rotational transitions of the molecules in the operating range of the spectrometer (i.e., 2-26 GHz). A Fortran program (executable file can be downloaded from Kisiel's website, PROSPE[48]) called *ASROT* is used to predict the rotational transitions. The observed rotational transitions are fitted to suitable Hamiltonian using the *ASFIT* program to obtain experimentally determined rotational

constants and centrifugal distortions. Other than *ASROT* and *ASFIT*, Herb Pickett's powerful and versatile *SPCAT/SPFIT*[49] program have been used in this Thesis to predict and fit rotational transitions. The executable files for *SPCAT/SPFIT* can be downloaded from the JPL website[50]. Novick[51] has provided suitable documentation to use *SPCAT/SPFIT*. The tunnelling spectra have been fitted using the *ASYM82* program[52].

In a chirped-pulse Fourier transform microwave spectrometer (*CP-FTMW*), modern digital electronics dramatically improves the bandwidth of the measurement. Western's[53] *PGOPHER* program is used to visualize, predict and fit microwave transitions. *PGOPHER* comes with the user-friendly graphical interface[54], which is also suitable for fitting nuclear quadrupole coupling constants and spin-rotation coupling terms.

Table 1.4. A typical fit for the b-dipole (E₁ state) Ar(H₂O)₂ transitions[55] with various fitting programs.

	ASFIT[48]	*SPFIT*[49]	*PGOPHER*[54]	*ASYM82*[52]
A/MHz	6253.0064(52)	6253.006(5)	6253.0064(52)	6253.0064(52)
B/MHZ	2428.5109(19)	2428.511(2)	2428.5109(19)	2428.5109(19)
C/MHz	1739.0734(18)	1739.073(2)	1739.0734(18)	1739.0734(18)
Δ_J */kHZ*	26.742(42)	26.74(4)	26.742(42)	26.742(42)
Δ_{JK}/*kHZ*	151.57(19)	151.6(2)	151.57(19)	151.57(19)
Δ_K/*kHZ*	-120.9(11)	-121.(1)	-120.9(11)	-120.9(11)
δ_J//*kHZ*	7.610(11)	7.61(1)	7.610(11)	7.610(11)
δ_K */kHZ*	135.23(39)	135.2(4)	135.23(39)	135.23(39)
RMS/internal		8.05	8.05(Residue Window)	8.05
RMS/external	10.39		10.39(Log Window)	10.4

There are two kinds of error (internal, external) reported by various fitting programs, as shown in Table 1.4. The internal error or *a priori* errors are based on the fit and the value assigned for the measurement errors. The external error or *parameter error* could be obtained easily by scaling the internal errors as following:

$$External\ error\ (rms) = Internal\ error * \sqrt{\frac{n}{n-m}}$$

Where n is the number of transitions and m is the number of independently fit parameters. The program SPFIT[49] reports internal or a *priori* RMS error in the fit and this needs to be multiplied with the proper factor to get the *posteriori* error. Also, this could be done automatically by the program PIFORM on Kisiel's website[48]. The ASFIT program directly reports the *posteriori* error. The PGOPHER[54] and ASYM82[52] both report the *priori* and *posteriori* errors in the program.

1.4 Experimental Rotational Constants to Structure

Given a full enough data set, rotational spectroscopy allows for very accurate structure determination in the gas phase. Spectral measurement and assignment are required for the naturally abundant isotopologue(s), followed by measurement and assignment of the spectra of isotopically substituted equivalent. From the rotational constants, moments of inertia could be determined, which helps in structure determination. A few different methods of determining molecular geometries have been developed. A detailed description could be found in the excellent article by Kisiel[56]. A very brief description relevant to the Thesis has been given:

1.4.1 Equilibrium Structure (r_e)

Chemists across the field mostly use the equilibrium structure of a molecule. Spectroscopists in most of the cases failed to obtain a reliable correction to the equilibrium. Rotational spectra usually lead to vibrationally averaged rotational constant mainly at the ground vibrational state, which differs significantly from its equilibrium ones. The rotational constant of a linear molecule is dependent on the vibrational state as follows,

$$B_v = B_e - \alpha_e(v + \frac{1}{2}) + ...$$

Here α_e and v are vibrational coefficients and vibrational quantum numbers. Determination of equilibrium geometries would require rotational transitions from many vibrational states for both parent and isotopic species. For diatomic molecules, equilibrium geometries could be determined as rotational transitions could be obtained for many vibrational states. For symmetric and asymmetric top molecules, most often, this is more difficult.

1.4.2 Substitution Structure (r_s)

The substitution method for determining structure is preferred when a limited number of isotopic species is available. Kraitchman's equations[57] could be used to find the position of the substituted atom from the centre of mass. For a non-planar asymmetric top molecule, the coordinate of the substituted atom is given as follows:

$$|a| = \left[\frac{\Delta P_a}{\mu}(1 + \frac{\Delta P_b}{I_a - I_b})(1 + \frac{\Delta P_c}{I_a - I_c}) \right]^{\frac{1}{2}}$$

$$|b| = \left[\frac{\Delta P_b}{\mu}(1 + \frac{\Delta P_c}{I_b - I_c})(1 + \frac{\Delta P_x}{I_b - I_a}) \right]^{\frac{1}{2}}$$

$$|c| = \left[\frac{\Delta P_c}{\mu}(1 + \frac{\Delta P_a}{I_c - I_a})(1 + \frac{\Delta P_b}{I_c - I_b}) \right]^{\frac{1}{2}}$$

where,

$$\Delta P_a = (\frac{1}{2})(-\Delta I_a + \Delta I_b + \Delta I_c)$$

$$\Delta P_b = (\frac{1}{2})(-\Delta I_b + \Delta I_c + \Delta I_a)$$

$$\Delta P_c = (\frac{1}{2})(-\Delta I_c + \Delta I_a + \Delta I_b)$$

Here ΔI_a ($I_a{'}$-I_a) and so on are the changes in the principal moments of inertia due to isotopic substitution. The P_a, P_b, and P_c are planar moments of inertia. In the Thesis, the *KRA* program from Kisiel's website[48] has been used for Kraitchman's equation. The program uses the above-mentioned equation to calculate the coordinates of the

substituted atom. The obtained Cartesian's are converted to internals using *EVAL* program[48].

1.4.3   Ground State or Effective structure (r_0)

The usual structural analysis is based on determining the ground state structure. For a simple diatom, the ground state bond length r_0 can be readily found using:

$$r_0 = \left(\frac{\hbar}{8\pi^2 \mu B_0} \right)^{\frac{1}{2}}$$

Here B_0 is the ground state rotational constant. For Symmetric and asymmetric top molecules, the *STRFIT* program has been routinely used. The *STRFIT*[56] fit uses a least-square fitting method to directly fit moments of inertia rather than rotational constants to get the geometrical parameters. A large number of isotopologues are often needed to get a reasonably well-defined parameter.

1.4.4   Mass Dependent Structure (r_m)

As the equilibrium geometries are challenging to determine primarily for symmetric and asymmetric top, Watson[58] derived *the r_m* method to obtain equilibrium quality geometries. Two coefficients, c_α and d_α, are used to incorporate vibrational-rotational interaction to the inertial expression:

$$I_0^\alpha = I_m^\alpha + c_\alpha (I_m^\alpha)^{\frac{1}{2}} + d_\alpha \left(\frac{m_1 m_2 ... m_N}{M} \right)^{\frac{1}{2N-2}}$$

Here I_m^α is a rigid moment of inertia calculated directly from the fitted structural internals, α represents three inertial axes (*a, b, c*), M is the total mass of the molecule, N is the total number of atoms, and m_i is the mass of a constituent atom. If only c_α are used in the fit, that leads to r_m^1 structure, and with both c_α and d_α leads to r_m^2 structure.

1.5 **Thesis Overview**

Rotational spectroscopy and several theoretical approaches were used to investigate intermolecular interactions in weakly bound complexes in this Thesis. ***Chapter 2*** describes the experimental techniques associated with rotational spectroscopy. Also, Chapter 2 describes theoretical methods, Atoms and Molecules (AIM), non-covalent interactions (NCI) index plots and natural bond orbital (NBO) analysis. Rotational spectra and dynamics of $(H_2S)_2$ have been reported in ***Chapter 3***. This chapter confirms the hydrogen bond in the dimer and its similarity with its oxygenated analogue, i.e., $(H_2O)_2$. ***Chapter 4*** reports microwave spectra of $(H_2S)_2H_2O$; this Chapter provides an understanding of H_2O and H_2S interactions. ***Chapter 5*** reports donor-acceptor interchange tunnelling splitting spectra of $Ar(H_2O)_2$ probed using rotational spectroscopy. ***Chapter 6*** provides a comprehensive description of intermolecular interaction across the periodic table using state-of-the-art *ab-initio* methods. A closer look at group 2 metals leads us to "alkalene bond," a common name proposed for intermolecular bonding in alkali and alkaline earth elements. ***Chapter 7*** provides summary, conclusion, and outlook. *Appendix 1* presents the wavefunction, energy, and probability density calculations for a one-dimensional periodic potential model.

1.6   **References**

1.   Latimer, W. M. & Rodebush, W. H. Polarity and ionization from the standpoint of the Lewis theory of valence. *J. Am. Chem. Soc.* **42**, 1419–1433 (1920).

2.   Arunan, E. *et al.* Definition of the hydrogen bond (IUPAC Recommendations 2011). *Pure Appl. Chem.* **83**, 1637–1641 (2011).

3.   Arunan, E. *et al.* Defining the hydrogen bond: An account (IUPAC Technical Report). *Pure Appl. Chem.* **83**, 1619–1636 (2011).

4.   Weast, R. C. *Handbook of chemistry and physics 53rd edition*. (Chemical Rubber Pub., 1972).

5.   Arunan, E. & Mani, D. Dynamics of the chemical bond: inter- and intra-molecular hydrogen bond. *Faraday Discuss.* **177**, 51–64 (2015).

6.   Bauzá, A. & Frontera, A. Aerogen Bonding Interaction: A New Supramolecular

Force? *Angew. Chemie Int. Ed.* **54**, 7340–7343 (2015).

7.   Bauzá, A. & Frontera, A. π-Hole aerogen bonding interactions. *Phys. Chem. Chem. Phys.* **17**, 24748–24753 (2015).

8.   Bauzá, A., Alkorta, I., Elguero, J., Mooibroek, T. J. & Frontera, A. Spodium Bonds: Noncovalent Interactions Involving Group 12 Elements. *Angew. Chemie Int. Ed.* (2020).

9.   Legon, A. C. The halogen bond: an interim perspective. *Phys. Chem. Chem. Phys.* **12**, 7736–7747 (2010).

10.   Metrangolo, P. & Resnati, G. Halogen Bonding: A Paradigm in Supramolecular Chemistry. *Chem. – A Eur. J.* **7**, 2511–2519 (2001).

11.   Alkorta, I., Blanco, F., Solimannejad, M. & Elguero, J. Competition of Hydrogen Bonds and Halogen Bonds in Complexes of Hypohalous Acids with Nitrogenated Bases. *J. Phys. Chem. A* **112**, 10856–10863 (2008).

12.   Clark, T., Hennemann, M., Murray, J. S. & Politzer, P. Halogen bonding: the σ-hole. *J. Mol. Model.* **13**, 291–296 (2007).

13.   Wang, W., Ji, B. & Zhang, Y. Chalcogen Bond: A Sister Noncovalent Bond to Halogen Bond. *J. Phys. Chem. A* **113**, 8132–8135 (2009).

14.   Manna, D. & Mugesh, G. Regioselective Deiodination of Thyroxine by Iodothyronine Deiodinase Mimics: An Unusual Mechanistic Pathway Involving Cooperative Chalcogen and Halogen Bonding. *J. Am. Chem. Soc.* **134**, 4269–4279 (2012).

15.   Bleiholder, C., Werz, D. B., Köppel, H. & Gleiter, R. Theoretical Investigations on Chalcogen−Chalcogen Interactions: What Makes These Nonbonded Interactions Bonding? *J. Am. Chem. Soc.* **128**, 2666–2674 (2006).

16.   Scheiner, S. A new noncovalent force: Comparison of P···N interaction with hydrogen and halogen bonds. *J. Chem. Phys.* **134**, 94315 (2011).

17.   Del Bene, J. E., Alkorta, I., Sanchez-Sanz, G. & Elguero, J. Structures, Energies,

References

Bonding, and NMR Properties of Pnicogen Complexes $H_2XP:NXH_2$ (X = H, CH_3, NH_2, OH, F, Cl). *J. Phys. Chem. A* **115**, 13724–13731 (2011).

18. Zahn, S., Frank, R., Hey-Hawkins, E. & Kirchner, B. Pnicogen bonds: a new molecular linker? *Chem. Eur. J.* **17**, 6034–6038 (2011).

19. Moilanen, J., Ganesamoorthy, C., Balakrishna, M. S. & Tuononen, H. M. Weak interactions between trivalent pnictogen centers: Computational analysis of bonding in dimers $X_3E\cdots EX_3$ (E= Pnictogen, X= Halogen). *Inorg. Chem.* **48**, 6740–6747 (2009).

20. Solimannejad, M., Gharabaghi, M. & Scheiner, S. SH$\cdots$N and SH$\cdots$P blue-shifting H-bonds and N$\cdots$ P interactions in complexes pairing HSN with amines and phosphines. *J. Chem. Phys.* **134**, 24312 (2011).

21. Mani, D. & Arunan, E. The X–C$\cdots$Y (X = O/F, Y = O/S/F/Cl/Br/N/P) 'carbon bond' and hydrophobic interactions. *Phys. Chem. Chem. Phys.* **15**, 14377–14383 (2013).

22. Thomas, S. P., Pavan, M. S. & Guru Row, T. N. Experimental evidence for 'carbon bonding' in the solid state from charge density analysis. *Chem. Commun.* **50**, 49–51 (2014).

23. Bauzá, A., Mooibroek, T. J. & Frontera, A. Tetrel-Bonding Interaction: Rediscovered Supramolecular Force? *Angew. Chemie Int. Ed.* **52**, 12317–12321 (2013).

24. Grabowski, S. J. Tetrel bond–σ-hole bond as a preliminary stage of the S_N2 reaction. *Phys. Chem. Chem. Phys.* **16**, 1824–1834 (2014).

25. Grabowski, S. J. Triel bonds, π-hole-π-electrons interactions in complexes of boron and aluminium trihalides and trihydrides with acetylene and ethylene. *Molecules* vol. 20 11297–11316 (2015).

26. Kollman, P. A., Liebman, J. F. & Allen, L. C. Lithium bond. *J. Am. Chem. Soc.* **92**, 1142–1150 (1970).

27. Ault, B. S. & Pimentel, G. C. Matrix isolation infrared studies of lithium

bonding. *J. Phys. Chem.* **79**, 621–626 (1975).

28.   Yáñez, M., Sanz, P., Mó, O., Alkorta, I. & Elguero, J. Beryllium bonds, do they exist? *J. Chem. Theory Comput.* **5**, 2763–2771 (2009).

29.   Albrecht, L., Boyd, R. J., Mó, O. & Yáñez, M. Cooperativity between hydrogen bonds and beryllium bonds in $(H_2O)_nBeX_2$ (n = 1–3, X = H, F) complexes. A new perspective. *Phys. Chem. Chem. Phys.* **14**, 14540–14547 (2012).

30.   Eskandari, K. Characteristics of beryllium bonds; a QTAIM study. *J. Mol. Model.* **18**, 3481–3487 (2012).

31.   Martín-Sómer, A., Lamsabhi, A. M., Mó, O. & Yáñez, M. The importance of deformation on the strength of beryllium bonds. *Comput. Theor. Chem.* **998**, 74–79 (2012).

32.   Yang, X., Li, Q., Cheng, J. & Li, W. A new interaction mechanism of LiNH2 with MgH2: magnesium bond. *J. Mol. Model.* **19**, 247–253 (2013).

33.   Tama, R., Mó, O., Yáñez, M. & Montero-Campillo, M. M. Characterizing magnesium bonds: main features of a non-covalent interaction. *Theor. Chem. Acc.* **136**, 36 (2017).

34.   Grabowski, S. J. Magnesium Bonds: From Divalent Mg Centres to Trigonal and Tetrahedral Coordination. *ChemistrySelect* **3**, 3147–3154 (2018).

35.   Bader, R. F. W. *Atoms in Molecules: A Quantum Theory*. (Oxford University Press, 1990).

36.   Contreras-García, J. *et al.* NCIPLOT: a program for plotting noncovalent interaction regions. *J. Chem. Theory Comput.* **7**, 625–632 (2011).

37.   Weinhold, F., Landis, C. R. & Glendening, E. D. What is NBO analysis and how is it useful? *Int. Rev. Phys. Chem.* **35**, 399–440 (2016).

38.   Cooke, S. A. & Ohring, P. Decoding Pure Rotational Molecular Spectra for Asymmetric Molecules. *arXiv Prepr. arXiv1204.3226* (2012).

39.   Townes, C. H. & Schawlow, A. L. *Microwave spectroscopy*. (Courier

References

Corporation, 2013).

40. Kroto, H. W. *Molecular rotation spectra*. (Dover, 1992).

41. Gordy, W. & Cook, R. L. Microware molecular spectra. (1968).

42. Rosenberg, A., Ozier, I. & Kudian, A. K. Pure rotational spectrum of CH4. *J. Chem. Phys.* **57**, 568–569 (1972).

43. Bernath, P. F. *Spectra of atoms and molecules*. (Oxford university press, 2020).

44. Hainer, R. M., Cross, P. C. & King, G. W. The Asymmetric Rotor. VII. Extension of the Calculation of Energy Levels. *J. Chem. Phys.* **17**, 826–836 (1949).

45. Ray, B. S. Über die Eigenwerte des asymmetrischen Kreisels. *Zeitschrift für Phys.* **78**, 74–91 (1932).

46. Watson, J. K. G. Determination of centrifugal distortion coefficients of asymmetric-top molecules. *J. Chem. Phys.* **46**, 1935–1949 (1967).

47. Bunker, P. R. & Jensen, P. *Molecular symmetry and spectroscopy*. (NRC Research Press, 2006).

48. Kisiel, Z. http://www.ifpan.edu.pl/~kisiel/prospe.htm PROSPE–Programs for rotational spectroscopy. (2001).

49. Pickett, H. M. SPFIT/SPCAT package. (2009).

50. Pickett, H. M., Poynter, R. L. & Cohen, E. A. Submillimeter, Millimeter, and Microwave Spectral Line Catalog, accessed via World Wide Web (http://spec. jpl. nasa. gov) from the Jet Propulsion Laboratory, Pasadena. *Pasadena Calif.*

51. Novick, S. E. A beginner's guide to Pickett's SPCAT/SPFIT. *J. Mol. Spectrosc.* **329**, 1–7 (2016).

52. Maki, A. FORTRAN program ASYM82.

53. Western, C. M. PGOPHER: A program for simulating rotational, vibrational and electronic spectra. *J. Quant. Spectrosc. Radiat. Transf.* **186**, 221–242 (2017).

54. Western, C. M. PGOPHER, a program for simulating rotational structure. *Univ. Bristol* **7**, 108 (2010).

55. Arunan, E., Emilsson, T. & Gutowsky, H. S. Rotational spectra, structures, and dynamics of small $Ar_m(H_2O)_n$ clusters: The Ar–(H 2 O) 2 trimer. *J. Chem. Phys.* **116**, 4886–4895 (2002).

56. Kisiel, Z. Least-squares mass-dependence molecular structures for selected weakly bound intermolecular clusters. *J. Mol. Spectrosc.* **218**, 58–67 (2003).

57. Kraitchman, J. Determination of molecular structure from microwave spectroscopic data. *Am. J. Phys.* **21**, 17–24 (1953).

58. Watson, J. K. G., Roytburg, A. & Ulrich, W. Least-squares mass-dependence molecular structures. *J. Mol. Spectrosc.* **196**, 102–119 (1999).

References

CHAPTER

Experimental and Computational Methods

2

This page intentionally left blank.

Chapter 2: Experimental and Computational Methods

2.1   Early Days of Microwave Spectroscopy

Microwave radiation refers to electromagnetic radiation with a frequency range of 0.3 to 300 GHz. The first microwave experiment, conducted by Cleeton and Williams[1] in 1934, describes the absorption spectra of NH_3 in the 1-4 cm wavelength range (~30-7.5 GHz). The use of a magnetostatic oscillator enabled the production of light in the microwave area. A transition centred at 1.25 cm (~24 GHz) was observed due to tunnelling of NH_3 between two equilibrium geometry. In 1970, Flygare and Ekkers[2] invented the Fourier transform microwave spectrometer, which uses time-domain averaging to improve resolution and sensitivity significantly. In general, most spectroscopic methods have to compromise on one to improve the others. Flygare succeeded in improving both. In 1981, a spectrometer with a molecular beam and Fabry-Perot cavity was introduced. This design is traditionally known as Balle-Flygare[3] type spectrometers. Molecular beam expansion reduces the rotational temperature of the species to a few kelvins, which significantly improves resolution by minimizing pressure broadening. The cooling effect in molecular beams also enables the production of weakly bound complexes. The limitation of the Balle-Flygare Fourier transform microwave spectrometer is associated with the bandwidth of individual measurement, which is close to 1 MHz. Pate and co-workers[4] greatly overcame this limitation by introducing a chirped-pulse Fourier transform microwave spectrometer in 2006, which has a typical bandwidth of 12 GHz for a single measurement. The work in this Thesis used both Balle-Flygare Fourier transform microwave spectrometer[5,6] (*BF-FTMW*) (Bangalore, India) and chirped-pulse Fourier transform microwave spectrometer[7,8] (*CP-FTMW*) (Newcastle, UK). The following sections give a quick overview of both spectrometers.

2.2   Balle-Flygare Fourier Transform Microwave Spectrometer

Balle-Flygare Fourier transform microwave spectrometer (*BF-FTMW*) in Bangalore was divided into two parts: mechanical and electrical. A more extensive description of

the spectrometer's design and operation is available elsewhere [5,6]. A brief description has been provided here.

2.2.1   Mechanical Design

The spectrometer has a vacuum chamber made of stainless steel (SS 304) (see Figure 2.1). The chamber is 1000 mm long and has a diameter of 850 mm. The chamber consists of two identical aluminium mirrors mounted on three rods. This arrangement is popularly known as Fabry-Perot cavity/resonator[3]. These mirrors are highly polished, and surface roughness and radius are accurate to 1 micron. The diameter and the radius of curvature of the mirrors are 500 mm and 850 mm, respectively. Fresnel's condition limits the lower cut-off wavelength (λ). According to the condition

$$\lambda = \frac{a^2}{R}$$

here a is the mirror radius and, R is the radius of curvature. These two factors determine the lowest wavelength of the spectrometer. The lower cut-off is 3.8 GHz in the current spectrometer. However, transitions as low as 2447.8427 MHz for the Ar···H_2S[6] complex have been observed in the spectrometer. The current operating range of the spectrometer is 2-26 GHz.
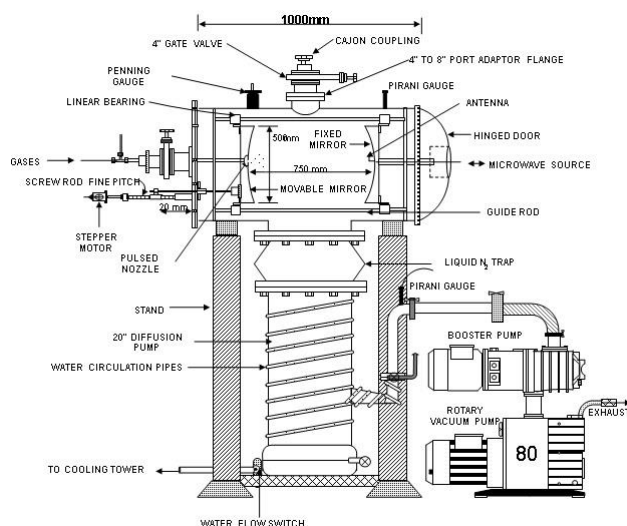
Figure 2.1. Mechanical design of pulsed nozzle Fourier transform microwave spectrometer taken with permission from Devendra Mani's Thesis[9].

One of the two mirrors is movable, and the distance can be varied between 630 mm to 730 mm. A precise pitch linear screw rod holds the moveable mirror in place. The mirror movement is controlled by a stepper motor (*103H8221-5041, Sanyo Denki, Japan)* and a stepper motor driver (*MicroLOGIX Driver MSB-403*), which has a fine pitch of 5 mm. The full rotation (i.e., fine pitch) can be carried out in 4000 steps. So, with each step mirror moves by 1.25 microns.

The following relation gives the resonant frequencies of the dominant TEM$_{00q}$ modes.

$$v = \frac{c}{2d}[(q+1) + (\frac{1}{\pi})\cos^{-1}(1 - \frac{d}{R})]$$

Here d is the distance between the mirrors, R is the radius of curvature and $(q+1)$ denotes the number of half wavelengths in the cavity.

The quality factor, Q, describes the bandwidth and duration of the microwave resonance:

$$Q = \frac{v}{\Delta v}.$$

Here Δv is the cavity bandwidth. The quality factor Q is in the order of 10^4. So, the bandwidth turned out to be~1 MHz.

The mirror has a 10 mm diameter hole in the centre. A pulsed nozzle (*General valve, USA, Series 9*) of 0.8 mm diameter is placed at this hole. The valve is connected with a stainless-steel tube of 0.25-inch outer diameter through which the sample is sent. The sample is pulsed into the cavity by opening the valve for typically one millisecond. The valve's trigger is provided through a pin connection that is sealed with an O-ring and a clamp. The stationary mirror also has a small hole at its centre. A female SMA connector, which is at the end of a coaxial cable, is placed at the mirror hole centre. An L-shaped antenna is connected to the SMA pin. The microwave power can be transmitted to and received back from the cavity through this arrangement. The same antenna is used for both sending and receiving the signal. The working frequency range of the antenna depends on its length,

$$L = \frac{\lambda}{4}.$$

A suitable antenna for a specific frequency range could be designed using the above relationship. In the current effort, five antennas cover the complete frequency range of 2-26 GHz. Figure 2.2 depicts the five antennas with their respective frequency ranges.

3-5 GHz	5-9 GHz	9-16 GHz	16-20 GHz	20-26 GHz

Figure 2.2. Antennas used in BF-FTMW spectrometer to transmit and receive the microwave signal.

The Fabry-Perot cavity is supported by a massive 20" oil diffusion pump (*Vacuum Techniques, Bangalore, India*) with a pumping speed of 10000 litres per second. The continuous running of the diffusion pump generates heat, so it is water-cooled using water circulation around the diffusion pump. A roots blower (*Boc Edwards, EH 250*) and a belt-less rotary (*Boc Edwards, E2M80*) pump support the diffusion pump. The combined backing capacity of both the pump is 4000 litres/sec. The Fabry-Perot cavity was maintained at 10^{-6} mbar by running all three pumps simultaneously. The pressure was measured using a Pirani gauge (up to 10^{-3} mbar) and a Penning gauge (up to 10^{-6} mbar).

2.2.2 **Electrical Designs**

Figure 2.3 shows electrical configuration of the spectrometer. There are two sections to the design. The first is the polarisation circuit, and the second is the detecting circuit. The microwave source is a signal generator (*Keysights, MXG, N5183 A, resolution of 0.01 Hz*). The RF output generated (ν) by the signal generator is directed to a single-pole-double-throw (SPDT) switch *(Sierra Microwave, 0.5-26.5 SFD0526-00, isolation 60 dB).* The output is either sent to a single sideband mixer (SSBM) *(Miteq, SMO-226LC1A)* or an image rejection mixer *(Miteq, IRO-0226LC1A).* During a polarisation cycle, the output is delivered to the SSBM, mixed with a function generator's (*SRS, DS345*) synchronous 30 MHz (intermediate frequency) signal. The resultant output (ν+30 MHz) is amplified by a low noise amplifier (*Miteq, JS4-02002600-30-10P)* with a gain of 30 dB. The amplified signal goes through another identical SPDT switch. Both SPDT switches work synchronously (both with polarisation and detection circuit) and are controlled by a delay generator (*BNC 575*). The delay generator sends two pulses typically in μs duration to the SPDT switches simultaneously but with different polarities. The output of the switch passes through the directional coupler (*Narda, 1.7-26.5-4227-16*), which essentially directs the signal to the antenna via a DC block. This signal polarises the molecules, and if they absorb the given frequency, molecules coherently emit microwave radiation of frequency ν+30±Δ MHz, where Δ is the offset from ν+30 MHz. The signal is detected through the same antenna and goes to the directional coupler, which sends 2.5 % of the signal to a diode detector *(Hewlett-Packard, 0.01-26.5 GHz, 8473C).* During detection, the cavity should be adjusted, which essentially entails the production of standing waves (the distance between the two mirrors should be half the integral multiple of the wavelength of radiation). For each microwave frequency, the movable mirror is adjusted accordingly with the help of a stepper motor. The LabVIEW program[10] controls the movement of the stepper motor. When the cavity is tuned, there is a dip in reflected microwave power. Figure 2.4 shows the output from oscilloscope with tuned and not tuned cavity. The rest 97.5 % of the power is used to detect the microwave transition. It first goes through a low noise amplifier (*Miteq JS4-02002600-30-10P, gain 30 dB*) via the SPDT switch. The amplified signal is mixed with the output of the signal generator (ν) via an image

rejection mixture. The IRM removes ν from ν+30±Δ MHz and provides the 30±Δ MHz signal which is sent to a bandpass filter *(Mini-Circuits, BBP-30)* and a low noise RF amplifier *(Mini-Circuits, ZFL-500LN)*. This signal is down-converted to ±Δ MHz by mixing 30 MHz from the output of the function generator in RF mixer *(Mini Circuits, ZAD-1)*. The ±Δ signal is sent to the low pass filter *(Mini-Circuits, BLP-5)* and then further amplified by another RF amplifier *(HD communications Corp., HD 17153BB)*. The resulting signal is digitised using an NI-Scope card *(National Instruments, PCI-5114, maximum sampling speed 250 MS/s.)* using a 5 MHz sampling rate. This kind of detection technique is popularly known as "double heterodyne mixing". Digitisers with a range of 2-26 GHz were not available when the Balle-Flygare spectrometer was developed, therefore the signal had to be processed at a considerably lower frequency range.

The time-domain signal is Fourier transformed to get the frequency domain signal. Coaxial arrangement of the antenna and pulsed nozzle gives doppler doublet in the frequency domain.
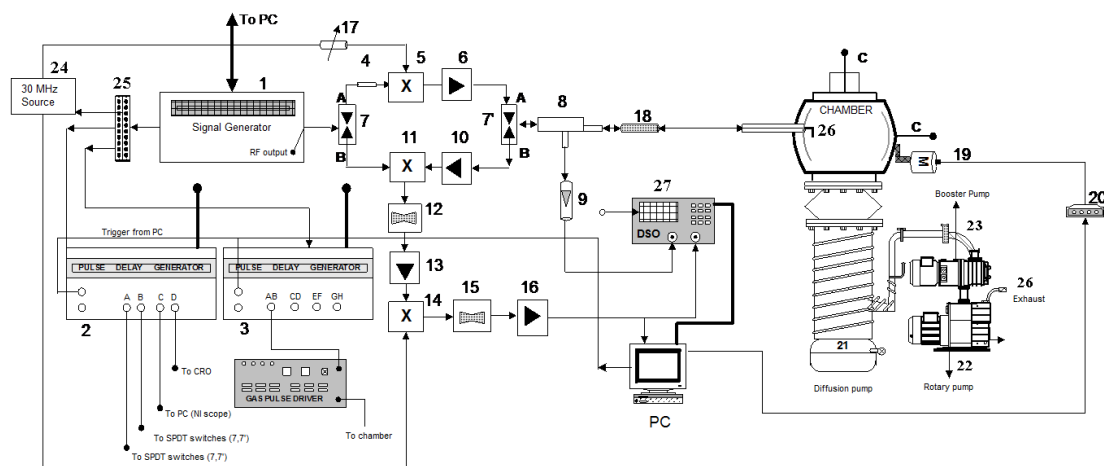
Figure 2.3. Electrical design of the pulsed nozzle Fourier transform microwave spectrometer.

 1. Signal generator *(Keysights, MXG, N5183 A)*, **2.** Delay generator *(BNC-575)*, **3**. Dealy generator *(SRS DG645)*, **4**. Attenuator *(HP, 8493C, 3dB)*; **5**. SSBM *(Mitteq, SMO-226LC1A)*, **6**. Low noise amplifier *(Miteq, JS4-02002600-30-10P)*, **7.** SPDT switch *(Sierra Microwave)*, **8.** Directional coupler *(Narda, 1.7-26.5-4227-16)*, **9.** Diode detector *(HP, 0.01-26.5 GHz, 8473C)*, **10.** Low noise amplifier *(Miteq, JS4-02002600-*

30-10P), **11.** IRM *(Miteq, IRO-0226LC1A),* **12.** Band pass flier (Mini circuits, BBP-30), **13**. RF amplifier *(Mini circuits, ZFL-500LN),* **14.**RF mixer *(Mini Circuit, ZAD-1)*, **15.** Low pass filter *(Mini circuits, BLP-5),* **16.** RF amplifier *(HD communication corporation, HD 17153BB)*, **17**. Attenuator *(Mini Circuit, ZAFT-51020).* **18.** Blocking capacitor *(HP, 11742A)*, **19**. Stepper *motor (103H8221-5041, Sanyo Denki, Japan),* **20.** Stepper driver *(*MicroLOGIX Driver MSB-403*)* **21.** Diffusion pump *(Vacuum Techniques, Bangalore, India)* **22**. Rotary pump *(Boc Edwards, E2M80)* **23**. Booster pump *(Boc Edwards, EH 250)* **24**. Distribution amplifier (SRS, FS710), **25.** Antenna (custom made) **26**. Exhaust **27.** Digital storage oscilloscope *(Tektronix TDS 2022)*
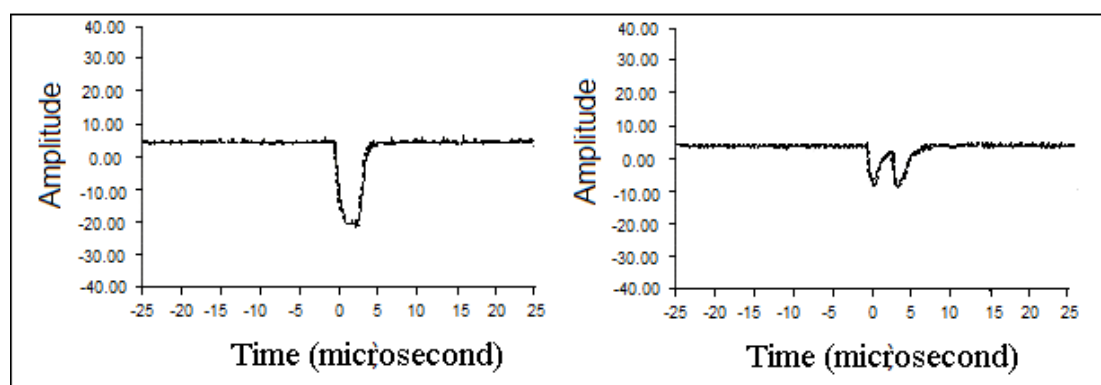
Figure 2.4. Reflected power (2.5%) signal from the cavity as viewed on the oscilloscope. The diagram shows two conditions when the cavity is not tuned (on the left) and the cavity is tuned (on the right).

2.2.3 Timing and Acquisition

In the Balle-Flygare Fourier transform microwave spectrometer (*BF-FTMW*), both molecular sample and microwave light are pulsed; two delay generators are used to control the pulsing. The *DG-645* delay generator controls molecular sample pulsing, and microwave pulsing is controlled by *BNC 575* delay generator. The sequence of pulsing is described in Figure 2.5. First, a microwave pulse with suitable pulse width is sent to the cavity. As the cavity is tuned, the microwave pulse forms a standing wave inside the cavity. The decay time of the pulse depends on the frequency of radiation. Typically, the decay time is <40 µs. As the peak-to-peak amplitude of the standing wave formed by the microwave pulse is 6-8 V, it is not feasible to record a molecular signal of few millivolts strength under such ringing. To some extent, the ringing could be reduced by adjusting the antenna. However, a delay is needed between the digitisation and the first microwave pulse to remove ringing. The delay duration is determined by the decay time of the microwave pulse.The initial digitisation is stored as noise. After

that, a gas pulse containing molecules of interest is sent to the cavity of 1 ms duration. A second microwave pulse is sent into the cavity, which polarises the sample. Usually, there is a delay between gas pulse and microwave pulse; this delay is known as "start delay". The delay generator does not introduce this delay; it is taken by the time taken for processing the program, which includes a loop to count numbers. The gas pulse typically takes 2 ms to reach the other mirror, whereas the typical acquisition time is 100 μs. Thus, multiple microwave pulses can be sent for a single gas pulse. The signal is obtained by removing the noise that was captured before the gas pulse. The entire procedure is known as "one-shot". Multiple shots were recorded to improve the signal-to-noise ratio.
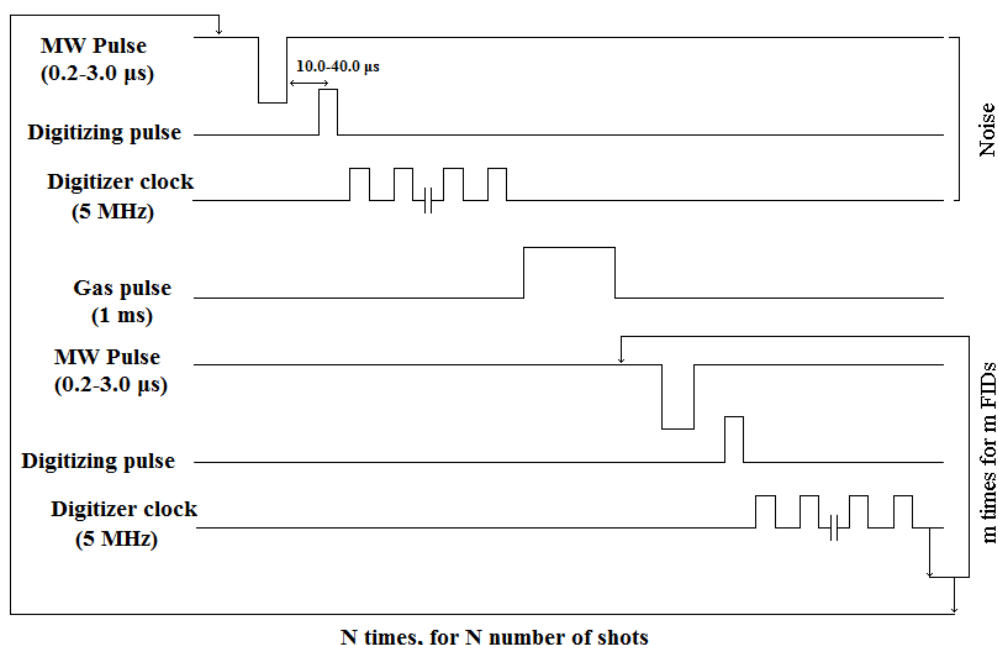
Figure 2.5. The microwave pulse and gas pulse sequences of the BF-FTMW spectrometer.

2.2.4 Software for the Spectrometer

The software code used for the spectrometer is based on LabVIEW 7.1. LabVIEW codes are called virtual instruments (VIs). The code has two separate windows, a front panel, and a block diagram. The detailed description of the LabVIEW can be found elsewhere[10].

2.2.5 Sample Preparation

The weakly bound complex of study is generated in a molecular beam using the pulsed nozzle. Usually, 1-5 % of gas samples are mixed with carrier gases, and this is done using a four-way junction. Typically, argon and helium are used as carrier gases. In the case of liquid samples, the carrier gases are flown through the bubbler containing the liquid. Four different mass flow controllers control the flow of the gases. The reagent flow meters are connected to 3-way valves to handle gases and liquids. A suitable backing pressure has been used depending upon the complex of interest. A larger complex needs more backing pressure. In helium, baking pressure typically ranges from 1.0-2.0 bar, whereas in argon, it usually has a value of 0.6-1.2 bar. Also, a typical flow rate of 200 SSCM has been used for helium carrier gases and 150 SSCM for argon.

2.3 Chirped-Pulse Fourier Transform Microwave Spectrometer

The microwave spectra of the $(H_2S)_2(H_2O)$ complex (parent species) were collected during a two-month visit to Newcastle, UK. The advantage of a chirped-pulse Fourier transform microwave spectrometer (*CP-FTMW*) over a Balle-Flygare Fourier transform microwave spectrometer (*BT-FTMW*) is the measured frequency range at a time. In the Balle-Flygare Fourier transform microwave spectrometer (*BT-FTMW*), ~1 MHz can be recorded at a time, whereas, in the chirped-pulse Fourier transform microwave spectrometer (*CP-FTMW*), 6.5-18.5 GHz spectra can be obtained at once. However, the range of the measurement is compensated by the greater sensitivity of the spectrometer. A detailed description of the spectrometer can be found elsewhere[7,8]. Only a brief description has been provided here for completeness.

2.3.1 Microwave Circuit

A schematic diagram of the microwave circuit of the spectrometer employed is presented in Figure 2.6. The excitation and detection circuits are coloured red and blue, respectively. Details of the polarisation and excitation circuits are provided in sections 2.3.1.1 and 2.3.1.2, respectively.

2.3.1.1 Excitation Circuit

A 10 GS/s arbitrary waveform generator (Component A) produces a linear frequency sweep (referred to as chirp) from 12.5 to 0.5 GHz over 1 μs. The AWG clock is referenced to a 10 MHz signal produced by frequency standard (Component B). The 12.5-0.5 GHz chirp pulse passes through a low-pass filter (Component C) and is up-converted by mixing in a triple balanced mixer (Component D) with a 19 GHz signal from a phase-locked dielectric resonant oscillator (PDRO) (Component E) to obtain a 6.5-18.5 GHz chirp pulse. Before the mixing by the triple balanced mixer (Component D), the PDRO signal passes through a cavity filter (Component F) and a power divider (Component G), having two outputs. The PDRO is phase-locked to the same 10 MHz references as the AWG. The 6.5-18.5 GHz chirp pulse is amplified by an amplifier (Component H) followed by a bandpass filter (Component I). The signal is attenuated by two 3 dB fixed attenuators (Component J). A 275 W travelling wave tube amplifier (TWTA) (Component K) amplifies the chirp before being transmitted into the vacuum chamber by a horn antenna (Component L) positioned in the spectrometer vacuum chamber. From the TWTA to the horn antenna (Component L), the chirp passes through a double-ridged waveguide (*WRD 750*) coupled to waveguide feedthrough on a bulkhead (*ATM, 750-130-3.75-G3-G3*). The amplifier has a typical 300 W power from 6.0 to 18.0 GHz and is set on maximum power.

2.3.1.2 Detection Circuit

A horn antenna (Component L) positioned in the spectrometer vacuum chamber opposite to the identical horn of the excitation circuit is used to detect the molecular free induction decay (FID) following the polarisation of the gas sample (see Figure 2.7). The signal then passes through waveguide feedthrough on a bulkhead (*ATM, 750-1303.75-G3-G3*) coupled to a double-ridged waveguide (WRD 750) to SMA coaxial adapter (*ATM, 750-251-C3*), a pin diode limiter (Component M), and a single-pole, single-throw (SPST) pin diode switch (Component N). The switch prevents the high-power microwave excitation pulse from damaging sensitive parts in the detection circuit. The signal is then amplified by a low noise amplifier (Component O), and an additional amplifier (Component P) is used to increase the dynamic range of the signal.

As the signal from molecular emission can be close to the noise level, the use of a low noise amplifier reduces the deterioration of the signal to noise (S/N) from noise sources in the following parts of the detection circuit. Therefore, it reduces the number of phase synchronised time-domain spectra that would have to be averaged to obtain the same S/N ratio. The signal is down-converted (high-side conversion) using a triple balanced mixer (Component D) by mixing with a 19 GHz from the power divider produced by the same PDRO used for the up-conversion of the chirp in the excitation circuit and then filtered with a low pass filter (Component Q). The heterodyned signal is then digitised by a 25 Gs/s oscilloscope (Component R) over 20 μs. The scope is phase-locked to a 10 MHz signal from the same source referencing the AWG and the PDRO.

2.3.1.3 Mixing

The oscilloscope used can detect frequencies in the range of 0-12.5 GHz. So, mixing of signals is necessary to get a working range of 6.5-18.5 GHz. A chirp is mixed with a 19 GHz signal from the PDRO to achieve the desired frequency range. A triple balanced mixer mixes the FID with another 19 GHz signal from the PDRO. Mixing twice is necessary to retain phase matching.

2.3.2 Resolution

The linewidth of the Newcastle *CP-FTMW* spectrometer is ~ 80 kHz which gives errors around the order of 10 kHz on peak positions. This uncertainty propagates to the fitted constants from measured spectra.

2.3.3 Sample Preparation

Gaseous samples are prepared by mixing 1-3 % of them with a carrier gas. This gas mixture is prepared in a separate small cylinder. Typically, liquid samples are put in a custom reservoir after the nozzle (see Figure 2.8). The reservoir typically contained a small quantity of liquid <0.5 ml.
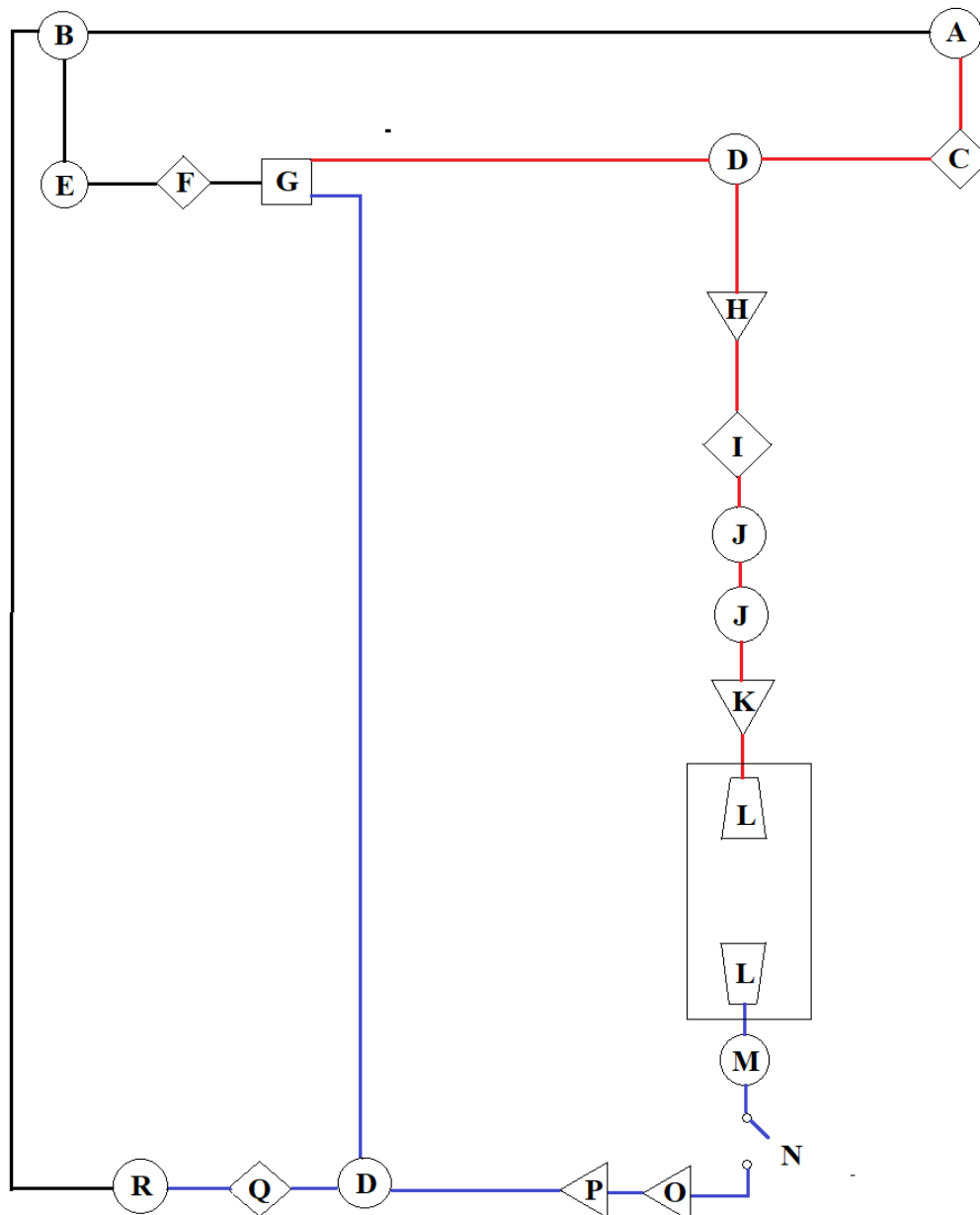
Figure 2.6. The microwave circuit of the chirped-pulse Fourier transform microwave spectrometer (CP-FTMW) at Newcastle University.

(Red lines show the polarisation circuit, and the blue line indicates the detection circuit. A) Arbitrary waveform generator AWG7105, Tektronix, B) Rubidium frequency standard, FS725, SRS C) Low pass filter, 12.2 GHz, Lorch D) Triple balanced mixer, TBO 440LWI-R, Miteq E) PDRO, XPDRO-14373, Herley, CTI F) Filter, 3C60-19000/T100-O/O, K&L Microwave G) Power divider, P218, ATM H) Amplifier, JS4-02001800, Miteq, I) Bandpass filter, 11SB10-12500/T12000-O/O,

K&L Microwave J) Attenuator, SA18S5W-03 K) TWT L) Antenna horns, 750-442-C3, ATM M) Pin diode limiter, ACLM-4539C6R1K N) SPST switch, H8753-8OD, Arra O) Low noise amplifier, AMF-5F-08001800-14-10P-R, Miteq P) Amplifier Q) Low pass filter, 11SBL-10-12500/T19000-O/O, K&L Microwave R) Oscilloscope, DPO71254, Tektronix.
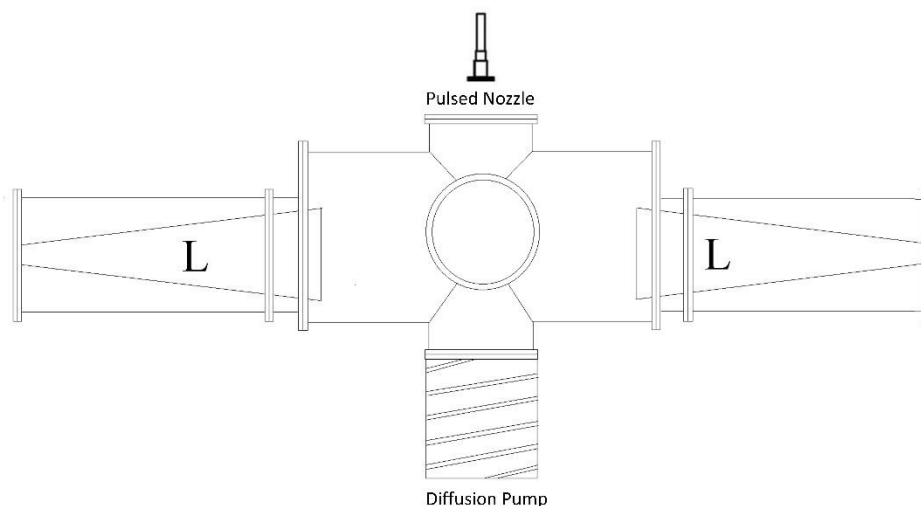
Figure 2.7. Perpendicular arrangement of gas expansion and microwave horns (L) in the chirped-pulse Fourier transform microwave spectrometer (CP-FTMW).
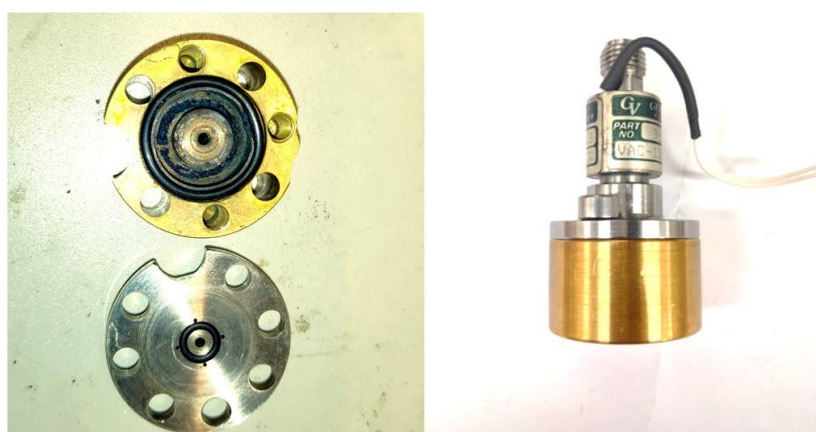
Figure 2.8. Picture of water reservoir used in the chirped-pulse Fourier transform microwave spectrometer (CP-FTMW) (on the left), assembled nozzle and reservoir (on the right).

2.4 Quantum Chemical Calculations

2.4.1 Geometry Optimisation and Binding Energy

Various quantum chemical methods have been used to gain a better understanding of the intermolecular interactions. Primarily the molecular geometries are optimised using *MP2* or *DFT* methods using Gaussian 09 suite of programs[11]. Optimised geometries provide a guess for the rotational constants (*A, B, and C*) and dipole moments about the three principal axes. The centrifugal distortion constants are also calculated from Gaussian 09 program with the *freq=vibrot* keyword. The frequency calculation on the optimised geometries has been performed to confirm that the obtained geometry corresponds to a minimum. An anharmonic correction to the frequency has been calculated using the *freq=anharmonic* keyword. Vibrationally averaged geometry was also obtained using the same keyword. The equilibrium and vibrational geometries for several complexes are reported throughout the Thesis and compared with experimentally obtained parameters. Another important property for the weakly bound complex is binding energy (*ΔE*). Binding energies of the complexes are calculated using the supermolecule approach.

$$\Delta E = E(ABC..........Q) - \sum_{a=A}^{Q} E_a$$

For a dimer:

$$\Delta E = E(AB) - [E(A) + E(B)]$$

E(A) and *E(B)* are the energies of the individual unit at their respective optimised state. The binding energies corrected for basis set superposition error and zero-point energy correction are donated as ΔE_{BSSE} and $\Delta E_{ZPE,}$ respectively. Binding energy corrected for both is denoted as $\Delta E_{BSSE+ZPE}$.

2.4.2 Atoms in Molecules (AIM) Analysis

2.4.2.1 Critical Points

Atoms in Molecules (AIM) topological analysis have been used to look deeper into the nature of chemical bonding. In 1960, Bader proposed the Atoms in Molecules (AIM)[12] theory. The AIM theory examines the distribution of electron density at each position surrounding a molecule's nuclei. The Atoms in Molecules (AIM) theory can predict the nature and characteristics of a bond based on the electron density at the bond critical point.

Any point in space where all the first-order partial derivatives of a function (electron density in our context) vanish is termed as a critical point (CP). The nature of the critical point is determined by the rank and signature of the second derivative of electron density. The rank is defined as the number of non-zero eigenvalues of the Hessian matrix. The signature is defined as the algebraic sum of the signs of the non-zero eigenvalues. A critical point is characterised by (ω, σ) where, ω is the rank and σ is the signature of the critical point. Based on this, a scalar function can have four types of critical points summarised in Table 2.1.

Table 2.1. Types and characteristics of critical points (cps) based on the rank and signature of the Hessian matrix.

(Rank, Signature)	*Types of critical points*	*Curvature*
(3,-3)	Nuclear critical point (NCP)	All negative, local maxima
(3,-1)	Bond critical point (BCP)	Two negative, one positive
(3,+1)	Ring critical point (RCP)	One negative, two positive
(3,+3)	Cage critical point (CCP)	All positive, local minima

Most of the critical points with stable nuclear configurations are of rank three. In a few exceptions, degenerate cps with rank < 3 are observed. A degenerate critical point is unstable. A small change in electron density is caused by slight displacement in nuclear configuration results to vanish or change into stable cps of rank three.

2.4.2.2 Nature of Interaction using Atoms in Molecules (AIM) Analysis

Primarily, three different criteria have been used to differentiate between closed-shell and shared-shell interactions. The nature of interactions in weakly bound complexes is primarily closed-shell type.

- *Sign of Laplacian:* Closed-shell interactions are characterised by positive Laplacian ($\nabla^2\rho > 0$), whereas negative Laplacian ($\nabla^2\rho < 0$) indicates shared-shell interaction.

- *The ratio of $|\lambda_1|/\lambda_3$:* Sosa and co-workers[13] proposed this ratio to differentiate closed- and shared-shell interactions. The $|\lambda_1|/\lambda_3$ less than 0.25 proposed as closed-shell and greater than 1 for shared shell interaction. Values between 0.25 and 1 are regarded as the interaction of intermediate kind.

- *The ratio of $|V|/G$:* Cremer and Karka[14] proposed another criterion based on potential (V) and kinetic (G) energy density ratio. For closed-shell interaction, $|V|/G < 1$ and for shared-shell $|V|/G > 2$. $|V|/G$ in between the limits proposed as intermediate kind of interaction. For the sake of simplicity, we have tabulated all these criteria in Table 2.2

Table 2.2. Atoms in Molecules (AIM) parameters to differentiate the nature of interactions.

Criterions	$\nabla^2\rho$	$|\lambda_1|/\lambda_3$	$|V|/G$
Closed (Ionic, van der Waals)	Positive	0 – 0.25	0 – 1.00
Shared (Covalent)	Negative	1 and above	2.00 and above
Intermediate	-	0.25 -1.00	1.00 – 2.00

2.4.3 **Non-covalent Interactions (NCI) Index**

The non-covalent interactions (NCI) index method, which is also known as the reduced density gradient (RDG) method, is a prevalent method for studying weak interaction, which actually deals with electron density $\rho(r)$ and reduced density gradient $s(r)$.

$$s = \frac{1}{2(3\pi^2)^{1/3}} \frac{|\nabla\rho|}{\rho^{4/3}}$$

At the bond critical point where the first derivative of electron density goes to zero [$\nabla\rho(r) = 0$], the reduced density gradient also becomes zero. So, the intra/intermolecular interaction can be identified using the plot of reduced density gradient and electron density. The sign of the second eigenvalue of the Hessian matrix (λ_2) is utilised to distinguish between types of interactions. $\lambda_2 < 0$ characterises bonding interaction; $\lambda_2 > 0$ non-bonding interaction i.e., steric repulsion. Finally, van der Waals interactions are characterised by a negligible density overlap that gives $\lambda_2 \lesssim 0$. This method, called the NCI plot, was developed by Yang's group[15]. This method has several advantages. Firstly, it applies to diverse systems, starting from chemical systems to biological systems. Secondly, this method has less computational costs than other methods. Thus, NCI analysis applied to large systems, including proteins and DNA, where analysis of intermolecular interactions is of great potential value.

Interestingly, NCI characteristics, on the other hand, are not always linked to AIM critical points. NCI properties may also be present in weak closed-shell contacts that do not have an AIM critical point, such as 1,2-ethanediol[16,17].The NCI plot for weakly bound complexes is computed using Multiwfn software[18] an open-source software.

2.4.4 Natural Bond Orbital (NBO) Analysis

Natural bond orbital analysis was developed by Weinhold[19]. It analyses intermolecular interactions from the donor-acceptor point of view. Charge transfer analysis is carried out to investigate the amount of covalency induced in the weakly bound complexes. Second-order perturbation energy is also calculated to determine the extent of perturbative stabilisation of natural orbitals due to donor-acceptor interaction. The NBO calculations are performed using NBO 6.0 software[20].

2.5 **Summary**

To summarise this Chapter, the rotational spectra of weakly bound complexes were obtained using the Balle-Flygare Fourier transform microwave spectrometer (*BF-FTMW)* and the chirped-pulse Fourier transform microwave spectrometer (Newcastle, UK) (*CP-FTMW*). A brief description of the spectrometers' design and operation has been provided. The experimentally determined geometries are supplemented by state-of-the-art quantum chemical computations. The AIM, NCI, and NBO methods were explicitly used to characterise and understand the nature of intermolecular interactions.

2.6 **References**

1.   Cleeton, C. E. & Williams, N. H. Electromagnetic waves of 1.1 cm wavelength and the absorption spectrum of ammonia. *Phys. Rev.* **45**, 234 (1934).

2.   Ekkers, J. & Flygare, W. H. Pulsed microwave Fourier transform spectrometer. *Rev. Sci. Instrum.* **47**, 448–454 (1976).

3.   Balle, T. J. & Flygare, W. H. Fabry–Perot cavity pulsed Fourier transform microwave spectrometer with a pulsed nozzle particle source. *Rev. Sci. Instrum.* **52**, 33–45 (1981).

4.   Brown, G. G. *et al.* A broadband Fourier transform microwave spectrometer based on chirped pulse excitation. *Rev. Sci. Instrum.* **79**, 53103 (2008).

5.   Arunan, E., Tiwari, A. P., Mandal, P. K. & Mathias, P. C. Pulsed nozzle Fourier transform microwave spectrometer: Ideal to define hydrogen bond radius. *Curr. Sci.* **82**, 533–540 (2002).

6.   Mandal, P. K. Indian Institute of Science,. *Ph.D. Diss. Indian Inst. Sci.* (2005).

7.   Stephens, S. L. & Walker, N. R. Determination of nuclear spin-rotation coupling constants in CF 3I by chirped-pulse Fourier-transform microwave spectroscopy. *J. Mol. Spectrosc.* **263**, 27–33 (2010).

8.   Zaleski, D. P., Stephens, S. L. & Walker, N. R. A perspective on chemistry in

transient plasma from broadband rotational spectroscopy. *Phys. Chem. Chem. Phys.* **16**, 25221–25228 (2014).

9.   Mani, D. Microwave Spectroscopic and Atoms in Molecules Theoretical Investigations on Weakly Bound Complexes: From Hydrogen Bond to'Carbon Bond'. Doctoral dissertation, Indian Institute of Science (2013).

10.   Goswami, M. Rotational Spectroscopic And Ab Initio Studies On The Weakly Bound Complexes Containing O-H⋯π And S-H⋯π Interactions. Doctoral dissertation, Indian Institute of Science (2010).

11.   Frisch, M. J. *et al.* Gaussian 09 Revision D. 01, 2009. *Gaussian Inc. Wallingford CT* (2009).

12.   Bader, R. F. W. Atoms in molecule. *A Quantum Theory* (1990).

13.   Amezaga, N. J. M., Pamies, S. C., Peruchena, N. M. & Sosa, G. L. Halogen bonding: a study based on the electronic charge density. *J. Phys. Chem. A* **114**, 552–562 (2010).

14.   Cremer, D. & Kraka, E. Chemical Bonds without Bonding Electron Density—Does the Difference Electron-Density Analysis Suffice for a Description of the Chemical Bond? *Angew. Chemie Int. Ed. English* **23**, 627–628 (1984).

15.   Contreras-García, J. *et al.* NCIPLOT: a program for plotting noncovalent interaction regions. *J. Chem. Theory Comput.* **7**, 625–632 (2011).

16.   Lane, J. R., Contreras-García, J., Piquemal, J.-P., Miller, B. J. & Kjaergaard, H. G. Are bond critical points really critical for hydrogen bonding? *J. Chem. Theory Comput.* **9**, 3263–3266 (2013).

17.   Günther, D., Boto, R. A., Contreras-Garcia, J., Piquemal, J.-P. & Tierny, J. Characterizing molecular interactions in chemical systems. *IEEE Trans. Vis. Comput. Graph.* **20**, 2476–2485 (2014).

18.   Lu, T. & Chen, F. Multiwfn: a multifunctional wavefunction analyzer. *J. Comput. Chem.* **33**, 580–592 (2012).

References

19.   Weinhold, F., Landis, C. R. & Glendening, E. D. What is NBO analysis and how is it useful? *Int. Rev. Phys. Chem.* **35**, 399–440 (2016).

20.   Glendening, E. D., Landis, C. R. & Weinhold, F. NBO 6.0: natural bond orbital analysis program. *J. Comput. Chem.* **34**, 1429–1437 (2013).

CHAPTER 3

Rotational Spectra and Structure of $(H_2S)_2$

This page intentionally left blank.

Chapter 3: Rotational Spectra and Structure of $(H_2S)_2$

3.1 Introduction

Hydrogen bonding is crucial to all life on earth. It is a lot weaker than a covalent bond, yet it is strong enough to hold water ice together. It is essential for the structure of DNA and the transmission of genetic information. In the field of intermolecular bonding, sulphur-containing compounds have attracted a lot of attention[1,2,3,4]. The simplest sulphur centred molecule, H_2S, is of particular interest due to its role as a neuromodulator[5] and its more recent identification as a room-temperature superconductor (at about 15 degrees Celsius, 267 gigapascals pressure)[6]. H_2S has always been regarded as a weaker donor and acceptor of hydrogen bonds compared to H_2O. This is primarily due to the small electronegativity difference in H and S ($\Delta \sim$ 0.38 on the Pauling scale). There have been many examples where the sulphur atom acts as the H-bond acceptor[7,8]. Also, in their book, *The Hydrogen Bond,* Pimentel and McClellan[9] specifically mentioned the S−H group as a possible H-bond donor. Recent experiments have confirmed the veracity of this possibility[4,10].

The water dimer, $(H_2O)_2$, is arguably the most experimentally and theoretically explored hydrogen-bonded species[11,12,13,14,15,16,17]. The dissociation energy of the $(H_2O)_2$, *D_0*, leading to two isolated water molecules, was measured experimentally to be 1105 ± 10 cm^{-1} (13.2 ± 0.1 kJ/mol)[18]. Only a few studies on its sulphur substituted dimer have been reported[19,20,21,22,23,24,25,26,27]. Lemke[23] has recently reported CCSD(T) calculations with complete basis set extrapolation on $(H_2S)_2$, and the dissociation energy is about 7 kJ/mol. The microwave spectrum of the $(H_2S)_2$ is interesting to examine because of clear structural differences between the condensed phases of H_2O and H_2S. In the most commonly encountered form of solid water, ice, H_2O is surrounded by four other water molecules. In isomorphs of solid H_2S[28,29], twelve H_2S molecules surround a single H_2S molecule (see Figure 3.1). A sphere could accommodate 12 different neighbours implying that each H_2S molecule interacts with neighbouring molecules through an effectively isotropic potential[30] energy surface. The

dramatic difference between the condensed phases of water and hydrogen sulphide led Pauling[28] to conclude that anisotropic hydrogen bonds mediate the structure of water ice. In contrast, the structure of solid H_2S is determined by isotropic van der Waals interactions. The thermal energy required to break the hydrogen bond along a coordinate in solids is greater than the barrier along that coordinate, resulting in an average spherical form for H_2S[31].
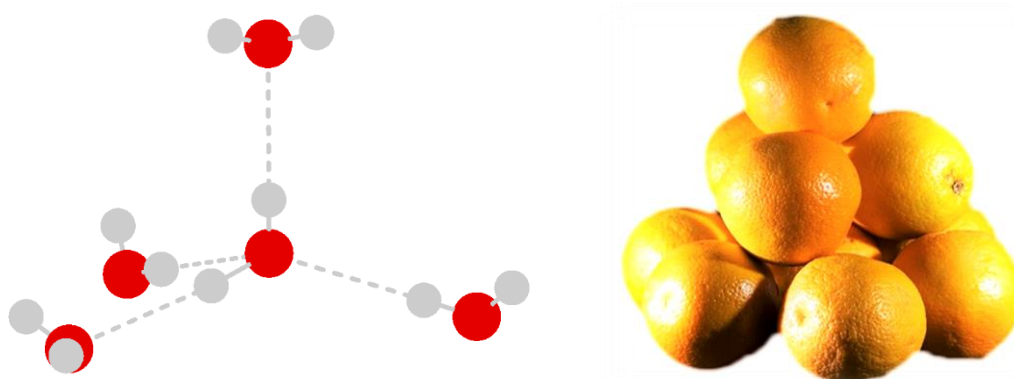
Figure 3.1. Comparison of the structures of solid ice H_2O (left, close to real) and solid H_2S (right, cartoon).

Ab initio optimised geometries of $(H_2O)_2$ and $(H_2S)_2$ are comparable, and both are hydrogen-bonded. Experimental studies on the $(H_2S)_2$ are fewer in number than those on the $(H_2O)_2$. Matrix isolation studies were not conclusive with respect to the structure of the $(H_2S)_2$ in solid N_2[32], O_2[33], Kr[34], Xe[35], and Ar[36] because H_2S readily aggregates at low temperatures to form higher oligomers and infrared shifts are much smaller than those observed for H_2O complexes. Early molecular beam electron deflection experiment by Dyke and coworkers[37] suggested that the possibility of bifurcated hydrogen bonds in $(H_2S)_2$ couldn't be ruled out (see Figure 3.2). As the authors have pointed out, "an analogy to the known $(H_2O)_2$ geometry is less obvious since $(H_2S)_2$ has weaker hydrogen bonds". Indeed, the potential energy surfaces of $(H_2O)_2$ and $(H_2S)_2$ dimers differ substantially[8], as discussed in more detail later in this Chapter.

Infrared spectroscopy of the $(H_2S)_2$ revealed that the vibrational stretch of the proton-donating S-H bond is red-shifted by 31 cm^{-1}, implying that the $(H_2S)_2$ is hydrogen-bonded[25]. A detailed description of the structure of the $(H_2S)_2$ has not yet been provided.

Linear Hydrogen Bond   *Bifurcated Hydrogen Bond*
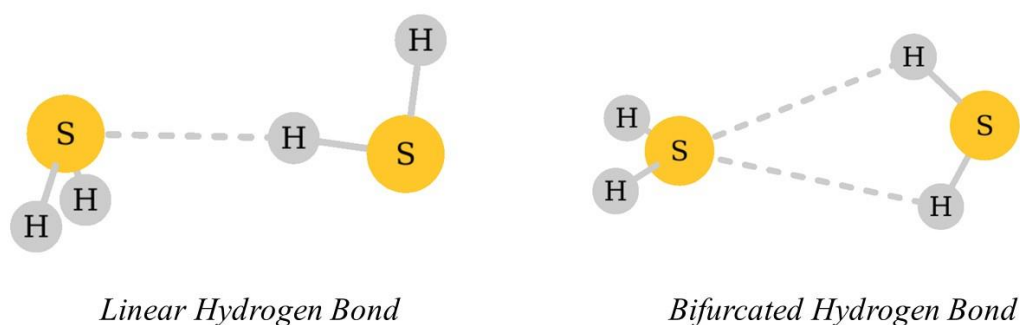
Figure 3.2. Probable structures (linear and bifurcated hydrogen bond) predicted by Dyke and coworkers[37] for $(H_2S)_2$ using molecular beam electric resonance.

3.1.1 Early Microwave Investigation

The rotational spectrum of $(H_2S)_2$ was previously observed using the Balle-Flygare[38] Fourier transform microwave spectrometer (*BF-FTMW*) at NIST[39] (around 1988-1991) and IISc[40] (around 2003-2005) (see Table 3.1). For most isotopologues of $(H_2S)_2$, a two-state pattern of *a*-type, $K_a=0$ (K_a is the vector component of rotational angular momentum along the principal axis), transitions only had been observed. A similar two-state pattern in rotational spectrum had been observed for $Ar(H_2S)_2$ and $Ar(D_2S)_2$ complexes as well[41]. Transitions with $K_a=1$ were not identified in either the NIST or the IISc studies. With only $K_a=0$ transitions, the rotational spectrum could yield only average values of $(B+C)/2$ for upper and lower states, and these were found to be 1749.3091(8) MHz and 1748.1090(8) MHz, respectively[42,43] (see Table 3.2). Figure 3.3 shows the simulated spectrum with $K_a=0$ lines for the upper state, which appear to be diatomic molecule spectra. The predicted structure would be that of a pseudo-diatomic molecule in which both H_2S are basically spherical (see Figure 3.4), which is consistent

with the obtained structure of solid H_2S, as depicted in Figure 3.1. However, given the microwave spectrum, there must be a dipole moment. The bifurcated C_{2v} structure could explain the microwave spectrum with $K_a=0$ lines. If the two H_2S molecules are freely rotating, they effectively look like a sphere, but they still can have a dipole moment (see Figure 3.5). The effective dipole moment of the bifurcated C_{2v} structure along the *a*-axis can explain the reported spectrum by Lovas and coworkers[42]. The $K_a=1$ lines are critical for reaching a firm conclusion on the structure.

Table 3.1. *Previously observed transitions for* $H^{32}SH\cdots^{32}SH_2$. *Only* $K_a=0$ *lines had been observed.*

	E₁ State		E₂ State	
J'←J"	Frequency (MHz)	Residue (MHz)	Frequency (MHz)	Residue (MHz)
1←0	3498.561(4)	3	3496.141(4)	4
2←1	6996.761(4)	3	6991.949(4)	1
3←2	10494.240(4)	-1	10487.005(4)	-2
4←3	13990.645(4)	-3	13980.969(4)	-1
5←4	17485.615(8)	-7	17473.460(8)	-6
6←5	20978.803(4)	1	20964.135(4)	1

Table 3.2. *Fitted rotational constants for* $K_a=0$ *lines for parent isotope.*

	E₁ State	E₂ State
B/MHz	1749.3091(8)	1748.1090(8)
D_J /kHz	14.94(1)	15.25(1)

$$\nu_J = 2B(J+1) - 4D(J+1)^3$$

H_2S Dimer : K_a=0 lines

3←2
10494.240

2←1
6996.761

4←3
13990.645

5←4
17485.615

1←0
3498.561

6←5
20978.803

Intensity

Frequency (MHz)
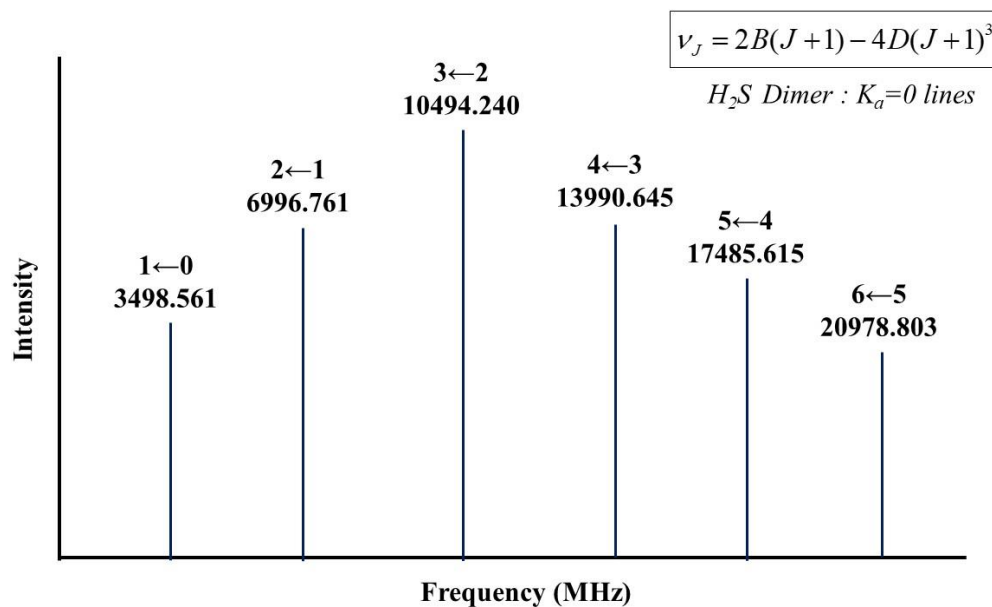
Figure 3.3: $(H_2S)_2$ spectrum from early microwave experiment (simulated spectrum for the upper state).

4.116(4)Å
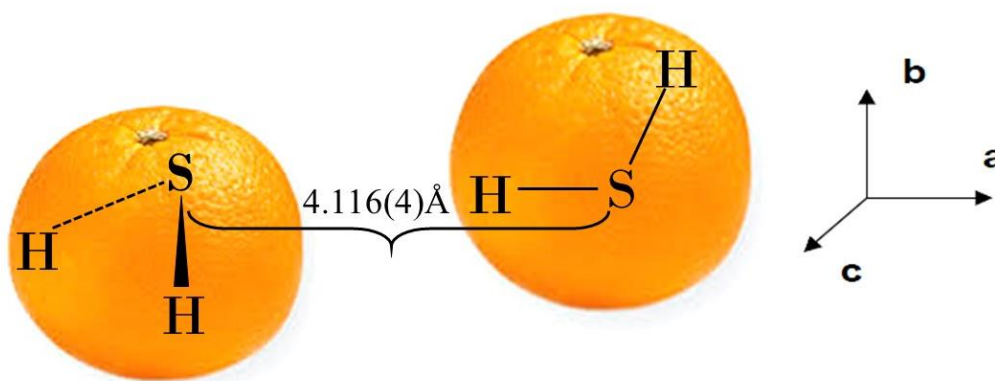
Figure 3.4. Structure of $(H_2S)_2$ derived from the K_a=0 lines of the microwave spectrum.
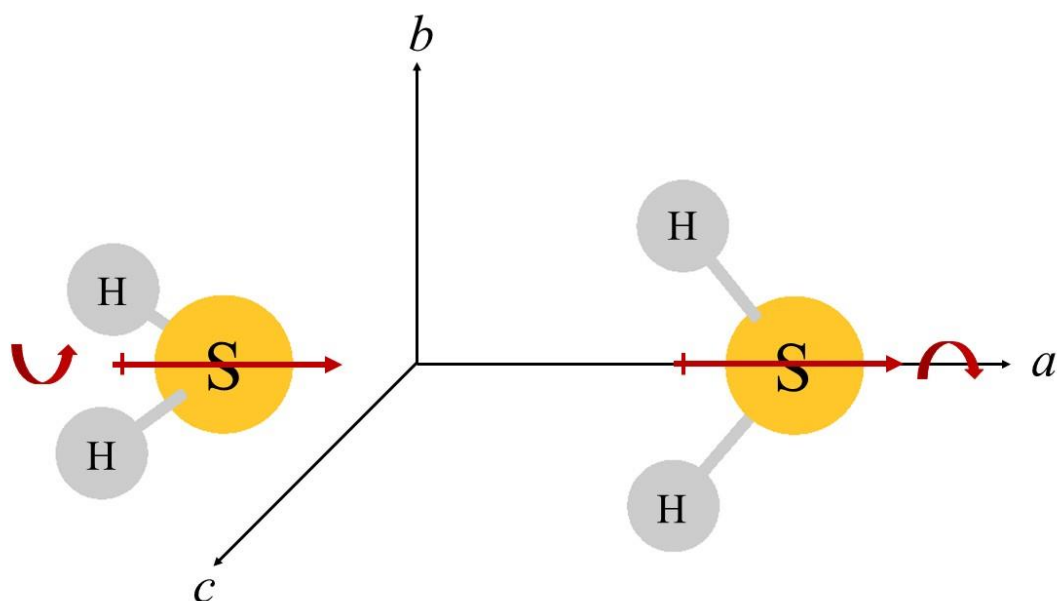
Figure 3.5. The dipole-dipole interaction structure of $(H_2S)_2$ that could explain the $K_a=0$ lines.
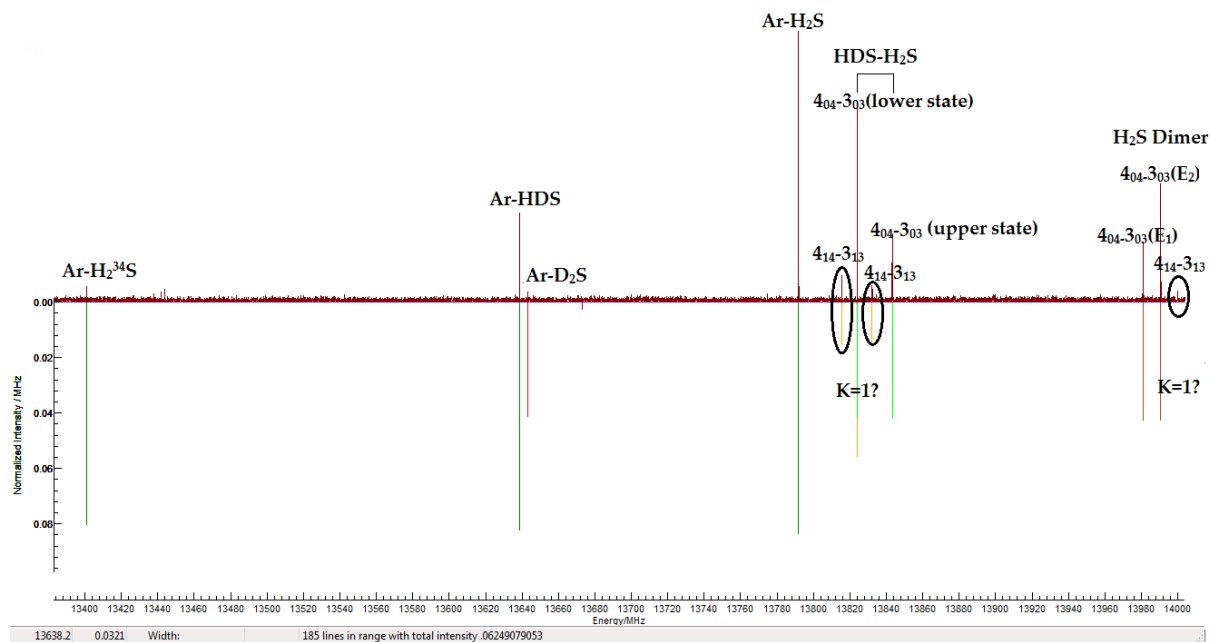
Figure 3.6. The hint of $K_a=1$ lines of $(H_2S)_2$ during rotational spectroscopic studies of $H_2S{\cdots}MI$ (M=Cu, Ag, Au) complexes by Medcraft et al.[44] using broadband microwave spectrometer at Newcastle University.

The first hint of a possibility that $K_a=1$ lines could be observed for $(H_2S)_2$ came during rotational spectroscopic studies of $H_2S \cdots MI$ (M=Cu, Ag, Au) complexes by Medcraft et al.[44] using broadband microwave spectrometer at Newcastle University[45,46] (see Figure 3.6). They found six lines that they thought were transitions of the deuterated isotopologues of $(H_2S)_2$. This motivated us to re-examine the rotational spectrum of $(H_2S)_2$. After a short period, we observed and assigned several $K_a=1$ lines for the parent and other deuterated isotopologues of $(H_2S)_2$. The spectrum of $(H_2S)_2$ was observed using the Balle-Flygare Fourier transform microwave spectrometer (*BF-FTMW)* at IISc. The following section contains the details of our experiments.

3.2   Experimental Details

The complex was formed through supersonic expansion from a pulsed valve where the gaseous sample contained helium seeded with 1 to 3 % H_2S. The He (99.999%) and H_2S (99.5%) were obtained from Bhuruka Gases Ltd. and were used without further purification. The microwave pulse was of 1.0 μs duration, and the expansion was through a 0.8 mm diameter nozzle with backing pressure ranging from 0.8 bar to 1.2 bar. Further details of the spectrometer employed can be found in Chapter 2 (section 2.2). The $K_a=0$ transitions of the parent species can be observed in our spectrometer with a single gas pulse. Whereas, for transitions having $K_a=1$, 2000 gas pulses were averaged to obtain a reasonable signal-to-noise ratio. Transitions having $K_a=1$ are significantly weaker than those having $K_a=0$, rationalising why these were not observed during previous experiments. This is due to the large A rotational constants which make their population rather small at our molecular beam temperature of ~ 3 K.

3.3   Results and Discussion

3.3.1   Search, Assignment, and Fitting

The initial searches for $K_a=1$ transitions covered the range from 10475 MHz to 10510 MHz, where $J = 3 - 2$ transitions were expected. *Ab initio* calculation at MP2/aug-cc-pVDZ level predicted that the 3_{12}-2_{11} transition is 13 MHz above the corresponding 3_{03}-

2_{02} transition. It was observed at 10508.0710 MHz, 13.8 MHz from the observed frequency of the 3_{03}-2_{02} transition (10494.2400 MHz). Similarly, the 3_{13}-2_{12} transition was predicted to be 14.5 MHz below the 3_{03}-2_{02} transition and was found at 10486.7555 MHz. Theory predicts the equal intensity of the 3_{12}-2_{11} and 3_{13}-2_{12} transitions, but it was experimentally observed that the former is more intense than the latter by a factor of three. For the lower state, we have found the 3_{13}-2_{12} and 3_{12}-2_{11} at 10479.2300 MHz and 10499.5020 MHz, respectively. The observation of these transitions allowed K_a=1 lines for other J states to be sought and identified, confirming the initial assignment. Observation and assignment of other K_a=1 lines are unambiguous for the two states, which arise due to tunnelling splitting, *vide infra* (Figure 3.7). A total of ten and seven K_a=1 transitions have been assigned for the upper and lower state. Transitions from the two states of the dimer were fitted separately using a Watson S-reduced Hamiltonian and the SPFIT[47] program of Pickett. Table 3.3 and Table 3.4 show the rotational transitions (both K_a=0 & 1) for the two states.

The rotational transitions and fits for all the other isotopologues are given in Table 3.5 to Table 3.10. Table 3.11 includes all the spectroscopic parameters. Acceptable fits with RMS residuals of the order of 0-5 kHz were obtained only after sextic distortion constants were included. While the results obtained are reasonable, a few of the centrifugal distortion constants determined for the $(H_2S)_2$ are negative, suggesting that large-amplitude motions are a pervasive feature of the system. With only K_a=0 transitions, we could evaluate only the $(B+C)/2$ rotational constant. The K_a=1 lines help us to evaluate the B and C rotational constants. When compared to experimental values, the rotational constants calculated from *ab-initio* and DFT calculations with hydrogen-bonded geometries are in excellent agreement. The A rotational constant could not be determined in this investigation since only a-dipole transitions were observed. During the fit, we set the dimer's A rotational constant to its *ab-initio* value; the value of the A rotational constant does not affect the overall fit. The B rotational constants are 1752.879(1) and 1753.102(3) MHz for the upper and lower states, respectively. The rotational constant, B, differs by 0.2231 MHz.

Similarly, the C rotational constant for upper and lower states are 1745.739(1) MHz and 1743.116(3) MHz, respectively. The difference between them is 2.623 MHz. Like parent isotopologues, a two-state pattern has been observed for ^{34}S substituted ones. The intensities of $K_a=1$ lines are very weak and have not been assigned in the present work. Supplementary data (see Table S3.1) includes the $K_a=0$ transitions for ^{34}S species.

In this work, we have assigned the $K_a=1$ lines for $D^{32}SD\cdots^{32}SDH$, $H^{32}SD\cdots^{32}SD_2$, $D^{32}SD\cdots^{32}SD_2$, $H^{32}SD\cdots^{32}SDH$. The transitions found initially at Newcastle are assigned to transitions of the $H^{32}SD\cdots^{32}SDH$ having $K_a=1$. The observations of the $K_a=1$ lines for deuterated dimers are much more feasible than the parent as a result of the lower A constant, calculated to be 49142.1785 MHz for $(D_2S)_2$ and 72259.3025 MHz for $(HDS)_2$, bringing the energy levels closer to thermal energy in the molecular beam. As the rotational constants predicted by the *ab initio* were close to the experimentally observed geometry, the spectra for all the isotopologues were predicted and located based on this geometry. Except for $D^{32}SD\cdots^{32}SDH$ and $H^{32}SD\cdots^{32}SD_2$, all isotopologues exhibit doubling of transition frequencies. No hyperfine structure could be resolved for deuterated species.

For fully deuterated species, the B rotational constants for upper and lower states are 1648.161(3) MHz and 1646.895(3) MHz, respectively. The difference in the B rotational constant is 1.2658 MHz, which is more than that of the parent. Similarly, the C rotational constant for upper and lower states are 1642.428(3) MHz and 1642.923(3) MHz, respectively. The difference between them is 0.496 MHz. Going from parent to deuterated species, the difference in B and C rotational constants for upper and lower states do not differ much.
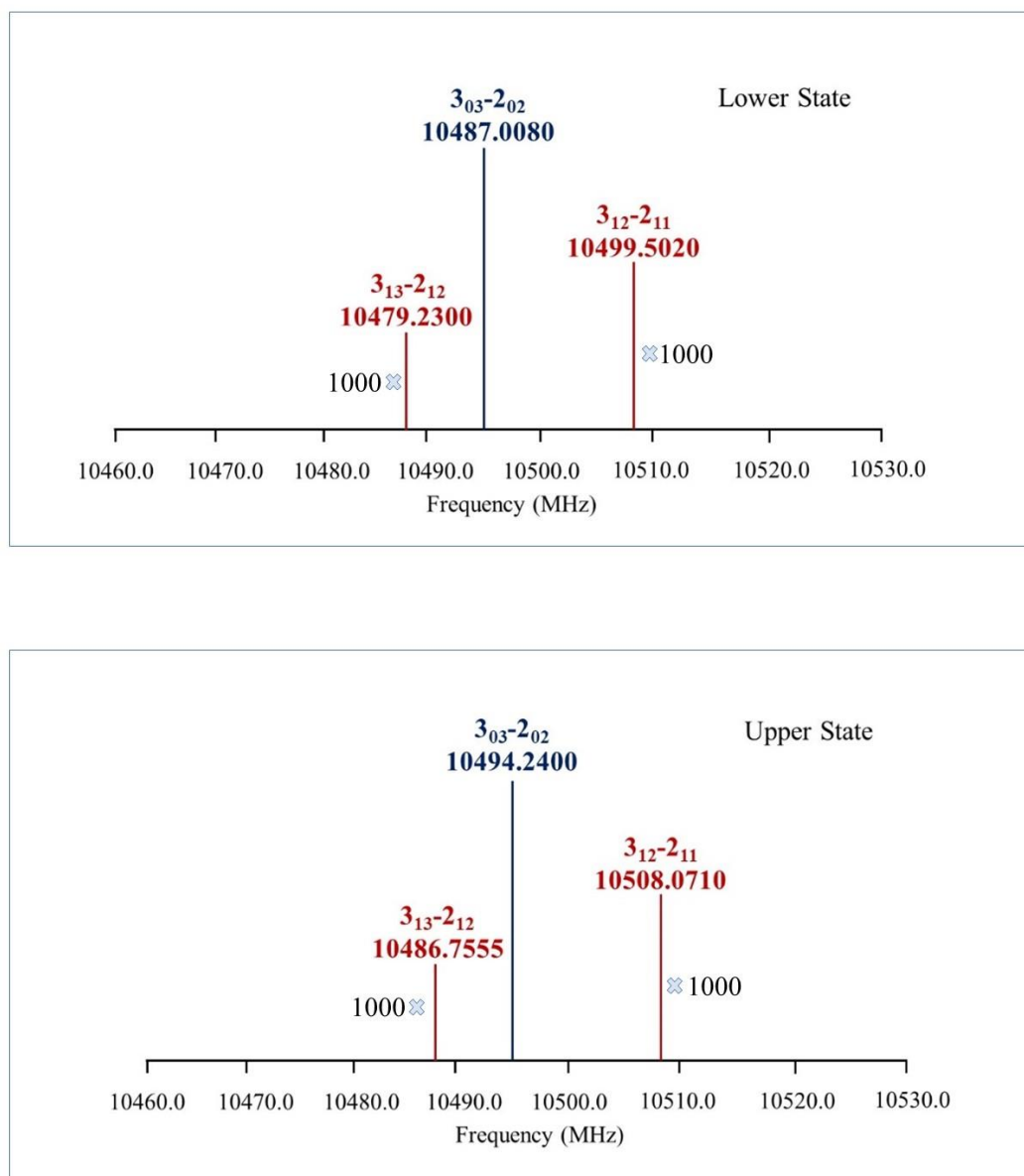
Figure 3.7. A schematic of Ka=1 lines observed for (H₂S)₂ (Top: upper state) (Bottom: lower state) showing 3₀₃-2₀₂ (Kₐ=0), 3₁₃-2₁₂ ,3₁₃-2₁₂ (Kₐ=1) transitions.

Table 3.3. Fitted rotational transitions for parent species of $(H_2S)_2$ (upper state). Quantities are in MHz.

$J'\,K_a'\,K_c'$	$J''\,K_a''\,K_c''$	Frequency (MHz)	Residual (MHz)
1 0 1	0 0 0	3498.5605	0.0025
2 1 2	1 1 1	6991.7730	0.0059
2 0 2	1 0 1	6996.7610	0.0035
2 1 1	1 1 0	7006.0220	0.0062
3 1 3	2 1 2	10486.7555	0.0016
3 0 3	2 0 2	10494.2400	0.0001
3 1 2	2 1 1	10508.0710	0.0026
4 1 4	3 1 3	13980.6620	-0.0025
4 0 4	3 0 3	13990.6459	-0.0008
4 1 3	3 1 2	14008.9690	-0.0055
5 1 5	4 1 4	17473.1350	-0.0056
5 0 5	4 0 4	17485.6150	-0.0047
5 1 4	4 1 3	17508.3490	-0.0031
6 1 6	5 1 5	20963.8270	0.0036
6 0 6	5 0 5	20978.8031	0.0028
6 1 5	5 1 4	21005.8220	0.0028

Results and Discussion

Table 3.4. Fitted rotational transitions for parent species of $(H_2S)_2$ (lower state). Quantities are in MHz.

$J' K_a' K_c'$	$J'' K_a'' K_c''$	Frequency (MHz)	Residual (MHz)
1 0 1	0 0 0	3496.1609	0.0036
2 1 2	1 1 1	6985.1597	-0.0014
2 0 2	1 0 1	6991.9510	0.0025
2 1 1	1 1 0	7001.7420	-0.0054
3 1 3	2 1 2	10479.2300	0.0012
3 0 3	2 0 2	10487.0080	-0.0001
3 1 2	2 1 1	10499.5020	0.0072
4 0 4	3 0 3	13980.9690	-0.0020
4 1 3	3 1 2	13995.6420	-0.0033
5 1 5	4 1 4	17462.5527	-0.0001
5 0 5	4 0 4	17473.4680	-0.0022
5 1 4	4 1 3	17493.2586	0.0005
6 0 6	5 0 5	20964.1353	0.0018

Table 3.5. Fitted rotational transitions for D^{32}SD$\cdots^{32}$SDH. Quantities are in MHz.

J' K$_a$' K$_c$'	J" K$_a$" K$_c$"	Frequency (MHz)	Residual (MHz)
1 0 1	0 0 0	3355.9220	-0.0044
2 1 2	1 1 1	6708.2098	-0.0174
2 0 2	1 0 1	6711.5490	0.0048
2 1 1	1 1 0	6716.3067	-0.0016
3 1 3	2 1 2	10061.5800	0.0023
3 0 3	2 0 2	10066.5440	-0.0003
3 1 2	2 1 1	10074.2004	0.0188
4 1 4	3 1 3	13414.0216	0.0094
4 0 4	3 0 3	13420.6170	-0.0011
4 1 3	3 1 2	13431.6998	-0.0177
5 1 5	4 1 4	16765.2286	0.0031
5 0 5	4 0 4	16773.4560	-0.0005
6 1 6	5 1 5	20114.9078	-0.0042
6 0 6	5 0 5	20124.7510	0.0005
6 1 5	5 1 4	20145.3311	0.0029

Results and Discussion

Table 3.6. Fitted rotational transitions for $H^{32}SD\cdots^{32}SD_2$. Quantities are in MHz.

$J'\ K_a'\ K_c'$	$J''\ K_a''\ K_c''$	Frequency (MHz)	Residual (MHz)
1 0 1	0 0 0	3357.4490	0.0045
2 0 2	1 0 1	6714.5770	0.0018
2 1 1	1 1 0	6722.0485	-0.0006
3 1 3	2 1 2	10065.7175	-0.0038
3 0 3	2 0 2	10071.0780	0.0000
3 1 2	2 1 1	10082.3848	0.0059
4 1 4	3 1 3	13419.5205	0.0024
4 0 4	3 0 3	13426.6380	-0.0013
4 1 3	3 1 2	13441.8690	-0.0056
5 1 5	4 1 4	16772.0794	0.0021
5 0 5	4 0 4	16780.9420	-0.0030
5 1 4	4 1 3	16800.2589	-0.0002
6 1 6	5 1 5	20123.0882	-0.0014
6 0 6	5 0 5	20133.6835	0.0020
6 1 5	5 1 4	20157.2538	0.0008

Table 3.7. Fitted rotational transitions for $D^{32}SD\cdots^{32}SD_2$ (upper State). Quantities are in MHz.

J' K_a' K_c'	J" K_a" K_c"	Frequency (MHz)	Residual (MHz)
1 0 1	0 0 0	3290.5189	-0.0152
2 1 2	1 1 1	6575.6901	-0.0021
2 0 2	1 0 1	6580.7398	0.0010
2 1 1	1 1 0	6587.1789	-0.0141
3 1 3	2 1 2	9862.5498	-0.0025
3 0 3	2 0 2	9870.3021	0.0091
3 1 2	2 1 1	9879.8857	0.0043
4 1 4	3 1 3	13148.2420	0.0007
4 0 4	3 0 3	13158.8634	0.0004
4 1 3	3 1 2	13171.4835	0.0036
5 0 5	4 0 4	16446.1203	-0.0032
5 1 4	4 1 3	16461.6300	0.0047
6 0 6	5 0 5	19731.7480	0.0007
6 1 5	5 1 4	19749.9505	-0.0038

Table 3.8. Fitted rotational transitions for $D^{32}SD\cdots^{32}SD_2$ (lower State). Quantities are in MHz.

J' K_a' K_c'	J" K_a" K_c"	Frequency (MHz)	Residual (MHz)
1 0 1	0 0 0	3288.7550	-0.0098
2 1 2	1 1 1	6572.8510	-0.0135
2 0 2	1 0 1	6577.2150	0.0076
2 1 1	1 1 0	6582.6610	0.0006
3 0 3	2 0 2	9865.0070	0.0020
3 1 2	2 1 1	9873.2519	0.0047
4 1 4	3 1 3	13144.2565	0.0159
4 0 4	3 0 3	13151.8330	-0.0023
4 1 3	3 1 2	13162.9395	-0.0024
5 1 5	4 1 4	16428.8980	-0.0073
5 0 5	4 0 4	16437.3740	-0.0022
5 1 4	4 1 3	16451.4430	-0.0042
6 0 6	5 0 5	19721.3070	0.0015
6 1 5	5 1 4	19738.4685	0.0025

Table 3.9. Fitted rotational transitions for $H^{32}SD\cdots^{32}SDH$ (upper state). Quantities are in MHz.

J' K_a' K_c'	J" K_a" K_c"	Frequency (MHz)	Residual (MHz)
2 1 2	1 1 1	6917.3525	-0.0051
2 0 2	1 0 1	6922.8830	0.0014
2 1 1	1 1 0	6929.1290	-0.0034
3 0 3	2 0 2	10383.5520	0.0002
3 1 2	2 1 1	10392.9370	0.0084
4 1 4	3 1 3	13832.2536	0.0025
4 0 4	3 0 3	13843.2960	-0.0012
4 1 3	3 1 2	13855.7960	-0.0046
5 0 5	4 0 4	17301.8100	0.0002

Table 3.10. Fitted rotational transitions for H^{32}SD···^{32}SDH (lower state). Quantities are in MHz.

J' K$_a$' K$_c$'	J" K$_a$" K$_c$"	Frequency (MHz)	Residual (MHz)
2 0 2	1 0 1	6913.2000	0.0018
3 1 3	2 1 2	10362.8180	-0.0100
3 0 3	2 0 2	10369.0570	0.0004
3 1 2	2 1 1	10375.2440	0.0112
4 1 4	3 1 3	13815.7270	0.0050
4 0 4	3 0 3	13824.0250	-0.0010
4 1 3	3 1 2	13832.2600	-0.0015
5 1 5	4 1 4	17267.4330	0.0019
5 0 5	4 0 4	17277.8060	-0.0044
5 1 4	4 1 3	17288.1000	-0.0055
6 0 6	5 0 5	20730.1170	0.0036

Table 3.11. Fitted constants of several isotopologues of $(H_2S)_2$.

Parameter	$H^{32}SH-^{2}SH_2$ (Upper)	$H^{32}SH-^{32}SH_2$ (Lower)	$D^{32}SD-^{32}SDH$	$H^{32}SD-^{32}SD_2$	$D^{32}SD-^{32}SD_2$ (Upper)	$D^{32}SD-^{32}SD_2$ (Lower)	$H^{32}SD-^{32}SDH$ (Upper)	$H^{32}SD-^{32}SDH$ (Lower)
A /MHz (Theo)	95185.7560	95185.7560	58762.6595	58200.69515	49142.17845	49142.17845	72259.33052	72259.33052
B /MHz	1752.879(1)	1753.102(3)	1679.945(3)	1681.501(1)	1648.161(3)	1646.895(3)	1733.767(1)	1730.466(1)
C /MHz	1745.739(1)	1743.116(3)	1676.033(3)	1675.996(1)	1642.428(3)	1642.923(3)	1727.879(1)	1726.331(1)
D_J /kHz	14.92(1)	15.23(1)	12.86(3)	13.07(1)	13.63(2)	13.43(2)	12.832(2)	12.34(1)
D_{JK} /kHz	-537.5(8)	-363.5(9)	-148.(2)	-480.2(7)	-192.(2)	-112.(2)	-90.8(6)	4.4(5)
d_1 /kHz	-0.489(9)	-59.8(1)	4.02(2)	0.655(7)	0.60(5)	-2.32(3)		
H_{JK} /kHz	-0.51(1)	1.59(2)	4.16(3)	0.83(1)	-2.10(5)	3.36(4)		
h_1 /kHz	----	1.069(2)						
σ /kHz	3.8	3.1	8.7	3.0	6.5	7.2	4.0	5.5
#N	16	13	15	15	14	14	9	11

3.3.2 A Detailed Comparison between Experiment and Theory

This section compares the experimentally obtained rotational and centrifugal distortion constant with theoretically calculated ones. Two methods are used to determine theoretical rotational constants. In the first set of calculations, rotational constants are calculated from equilibrium geometry (see Table 3.12). In the second set, rotational constants are calculated from vibrationally averaged geometry (see Table 3.13).

3.3.2.1 Equilibrium Rotational Constants from Theory

The rotational constants derived using dispersion corrected B3LYP functionals, and those measured experimentally are quite comparable. In addition, the *ab initio* van der Waals functional, wb97xd, agrees well with the experiment.

Table 3.12. Equilibrium rotational constants calculated from different theory and basis sets.

Methods	A	B	C
DFT			
B3LYP//6-311++(d,p)	97582.040	1689.323	1681.793
D2-B3LYP//6-311++g(d,p)	96863.882	1750.849	1742.679
D2-B3LYP//6-311++g(df,p)	97273.387	1741.099	1733.181
D3-B3LYP//6-311++g(d,p)	96664.775	1749.564	1741.203
D3-B3LYP//6-311++g(df,p)	97028.932	1738.534	1730.426
wb97xd//6-311++g(d,p)	97844.909	1751.859	1743.756
MP2			
MP2/6-311++g(d,p)	106171.113	1690.169	1684.360
MP2//aug-cc-pVDZ	97293.252	1790.948	1781.766
MP2//aug-cc-pVTZ	96942.906	1795.208	1785.922
MP2//aug-cc-pVQZ	97294.261	1791.099	1781.912
Experiment			
Upper State		1752.879(1)	1745.739(1)
Lower State	-	1753.102(3)	1743.116(3)

The DFT results with a 6-311++g(df,p) basis somewhat underestimate the equilibrium rotational constants. However, the rotational constants are well determined by a 6-311++(d,p) basis. On the other hand, the MP2 method overestimates the rotational constant with Dunning basis[48] (aug-cc-pVDZ, aug-cc-pVTZ, and aug-cc-pVQZ) and underestimates with Pople 6-311++g(d,p) basis.

3.3.2.2 Vibrationally Averaged Rotational Constants from Theory

The vibrationally averaged rotational constants obtained using the B3LYP functionals without dispersion correction significantly underestimate the results. Grimme's D2[49] and D3[50], which take care of dispersion correction, provide an excellent match. Here, the wb97xd functional also underestimates the experimental rotational constants. In the MP2 method with a larger basis, the vibrationally averaged rotational constants agree well with the experimental ones.

Table 3.13. Vibrationally averaged rotational constants calculated from different theory and basis sets.

Methods	A	B	C
DFT			
B3LYP//6-311++(d,p)	102659.055	1615.404	1608.575
D2-B3LYP//6-311++g(d,p)	95344.856	1762.320	1753.486
D2-B3LYP//6-311++g(df,p)	95877.225	1747.657	1739.156
D3-B3LYP//6-311++g(d,p)	95140.877	1746.431	1737.667
D3-B3LYP// 6-311++g(df,p)	94265.811	1744.730	1735.719
wb97xd//6-311++g(d,p)	86760.638	1701.297	1690.438
MP2			
MP2/6-311++g(d,p)	110231.165	1673.075	1669.077
MP2//aug-cc-pVDZ	91159.799	1732.139	1723.741
MP2//aug-cc-pVTZ	102600.194	1764.785	1758.469
Experiment			
Upper State		1752.879(1)	1745.739(1)
Lower State	-	1753.102(3)	1743.116(3)

DFT techniques with dispersion correction, in general, replicate experimental *B* and *C* rotational constants quite well. The recent localised molecular orbital energy

decomposition shows dispersion interaction contribute about 16.4% of the total energy[27].

3.3.2.3 Rotational Constants of Isotopologues of $(H_2S)_2$

After obtaining a good match with experimental rotational constants at the D3-B3LYP method with a 6-311G++(d,p) basis, we have calculated the rotational constants of the isotopologues of the $(H_2S)_2$ using the same method and basis set. These calculations help us to assign the correct isotopologues. All the measured values are in excellent agreement with the experiments, as shown in Table 3.14.

3.3.2.4 Centrifugal Distortion Constant

Microwave spectroscopy also provides additional helpful knowledge about the centrifugal distortion constants of the molecules/complexes. Table 3.15 provides the centrifugal distortion constants of $(H_2O)_2$ and $(H_2S)_2$ dimer. The experimentally measured centrifugal distortion constants, D_J, for upper and lower states of $(H_2S)_2$ are 14.92(1) kHz and 15.23(1) kHz, respectively, which are much greater than theoretically anticipated values. Whereas the centrifugal distortion constants for $(H_2O)_2$ calculated at MP2 level with Dunning basis reproduce the experimental value with minimal error. These findings strongly suggest that more rigorous theoretical attention to $(H_2S)_2$ is needed. The magnitudes of these constants are, crudely, inversely proportional to the square of the molecular mass. In Table 3.16, we have listed the experimentally obtained centrifugal distortion constant of several weakly bound complexes of H_2S. The $Ar(H_2S)$[51], $Ar_2(H_2S)$[52], and $CO(H_2S)$[53] complexes have slightly higher centrifugal distortion constant compared to $(H_2S)_2$. Interestingly, $Ar(H_2S)_2$ complex has a centrifugal distortion constant of 20.4 (4) kHz, similar to that of $(H_2S)_2$. It is clear that the large amplitude vibrational motions leading to the centrifugal distortion in $(H_2S)_2$ are not significantly affected by the addition of Ar. Similar observations have been made comparing all the vibrational modes of $(H_2O)_2$ and $Ar(H_2O)_2$ presented in Chapter 5 (section 5.3.1). Similar values can be found in $C_2H_4(H_2S)$[54], $HF(H_2S)$[55] complexes as well.

Table 3.14. Rotational constants evaluated at D3-B3LYP-6311G++(d,p) for isotopologues of $(H_2S)_2$.

#	Isotopologues		A/MHz	B/MHz	C/MHz
01	$H^{32}SH{\cdots}^{32}SH_2$	Theory	96664.775	1749.564	1741.203
		Expt.		1753.102(3)	1743.116(3)
02	$D^{32}SD{\cdots}^{32}SDH$	Theory	59656.769	1682.006	1664.260
		Expt.		1679.945(3)	1676.033(3)
03	$H^{32}SD{\cdots}^{32}SD_2$	Theory	59334.0048	1677.3874	1672.7185
		Expt.		1681.501(1)	1675.996(1)
04	$D^{32}SD{\cdots}^{32}SD_2$	Theory	49964.9662	1647.4846	1634.4937
		Expt.		1646.895(3)	1642.923(3)
05	$H^{32}SD{\cdots}^{32}SDH$	Theory	73594.5746	1731.2652	1725.7666
		Expt.		1730.466(1)	1726.331(1)
06	$H^{34}SH{\cdots}^{32}SH_2$	Theory	96550.4791	1702.2236	1694.2736
		Expt.		1699.468(2)*	
07	$H^{32}SH{\cdots}^{34}SH_2$	Theory	96588.3591	1700.0961	1692.1775
		Expt.		1700.321(1)*	
08	$H^{34}SD{\cdots}^{32}SD_2$	Theory	59298.9950	1629.5437	1625.1107
		Expt.		1635.167(1)*	
09	$H^{32}SD{\cdots}^{34}SD_2$	Theory	59186.3228	1636.0116	1631.4580
		Expt.		1631.464(3)*	
10	$D^{34}SD{\cdots}^{32}SD_2$	Theory	49888.4983	1602.6897	1590.3154
		Expt.		1600.490(2)*	

* *(B+C)/2* values have been provided.

Table 3.15. Centrifugal distortion constants, D_J, calculated for $(H_2O)_2$ and $(H_2S)_2$ at different levels of theory. The experimental values are also provided.

Methods	$(H_2O)_2$	$(H_2S)_2$
D2-B3LYP//6-311++g(d,p)	33.441	3.373
D2-B3LYP//6-311++g(df,p)	33.343	3.378
D3-B3LYP//6-311++g(d,p)	31.486	4.057
D3-B3LYP//6-311++g(df,p)	31.441	4.053
wb97xd//6-311++g(d,p)	32.508	4.072
MP2/6-311++g(df,p)	35.635	4.538
MP2//aug-cc-pVDZ	39.486	4.386
MP2//aug-cc-pVTZ	40.122	4.962
*Experiment	44(4)	15.23(1)

Table 3.16. Centrifugal distortion constants, D_J, of different H_2S complexes. Values are in kHz.

Methods	Experimental
$(H_2S)_2$	15.23(1)
$Ar(H_2S)$	46.2(4)[51]
$Ar(H_2S)_2$	20.4(4)[41]
$Ar_2(H_2S)$	41.34(2)[52]
$CO(H_2S)$	36.08(2)[53]
$C_2H_4(H_2S)$	14.30(2)[54]
$HF(H_2S)$	15.1(2)[55]

3.3.3 Structure

The structure of the complex was determined using two different methods, one involving substitution analysis by Kraitchman[56] and the other involving Kisiel's fitting program STRFIT[57]. In both cases, the structures of the free monomers were assumed to be unchanged upon complexation, and rotational constants from the lower state were

used. Kraitchman equations were used to find the $R(S_a - S_d)$, donor-acceptor sulphur atoms distance.

3.3.3.1 Kraitchman's Analysis

The position of the substituted atom can be determined using Kraitchman analysis[56]. The rotational constants of the various isotopologues vary depending on the location of the substitution. Using the planer moments of inertia relations (given in Chapter 1, section 1.4.2), we have evaluated the coordinates of S_a, H_1, S_d, H_3 (see Table 3.17). It is important to note that Kraitchman's analysis only provides the magnitude of the coordinates; the *ab-initio* calculation is used to decide the signs of the coordinates. Also, for a small value of coordinate, Kraitchman's analysis may give imaginary values. These values are kept at zero for further analysis. The limitation of the substitution analysis is apparent from the imaginary |b| coordinate for the S_a, H_1, and S_d. These atoms are very close to the b principal axis of the complex, as can be seen in Figure 3.8, which results in this imaginary coordinate. We should keep in mind that hydrogens of $(H_2S)_2$ are affected by large amplitude motions. Thus, the vibrationally averaged geometry is not the same in the deuterated structure because deuterium will undergo smaller motions than the hydrogen atoms.

Table 3.17. Coordinates derived from Kraitchman's analysis for $(H_2S)_2$. Values are in Å.

	|a|	|b|	|c|
S_a	2.047(1)	0.0	0.469(3)
H_1	2.311(1)	0.0	1.302(1)
H_2	-	-	-
S_d	2.065(1)	0.0	0.470(3)
H_3	2.325(1)	0.215(7)	1.262(1)
H_4	-	-	-

Kraitchman's equation gives the distance of the substituted atom from the centre of mass.

$$|r| = \left[(\frac{1}{2\mu})(\Delta I_a + \Delta I_b + \Delta I_c) \right]^{\frac{1}{2}}$$

Here, μ is the reduced mass of the substitution, and ΔI is the change in moment of inertia upon substitution. Using the aforementioned equation, the distances of S_a, H_1, S_d, and H_3 atoms from the centre of mass were computed. The distances of the S_a and S_d from the centre of mass were found to be 2.047(1) Å and 2.066(1) Å, respectively (see Table 3.18). The results of the DFT estimation are in near agreement with these two distances. The distance between two sulphur atoms is found out to be 4.113(1) Å. The S_a-S_d distance calculated at D3-B3LYP/6-311G++(d,p) is 4.119 Å, with only 0.1% of error. Karka and coworkers[58] calculated the S_a-S_d distance to be 4.138 Å at the CCSD(T)/aug-cc-PVTZ level. Kraitchman's analysis provides reliable results only for heavy atoms. The distance from cm to H_1 atom is about 0.1 Å longer than expected by theory, while substitution analysis for H_4 atoms yields a surprisingly good result.
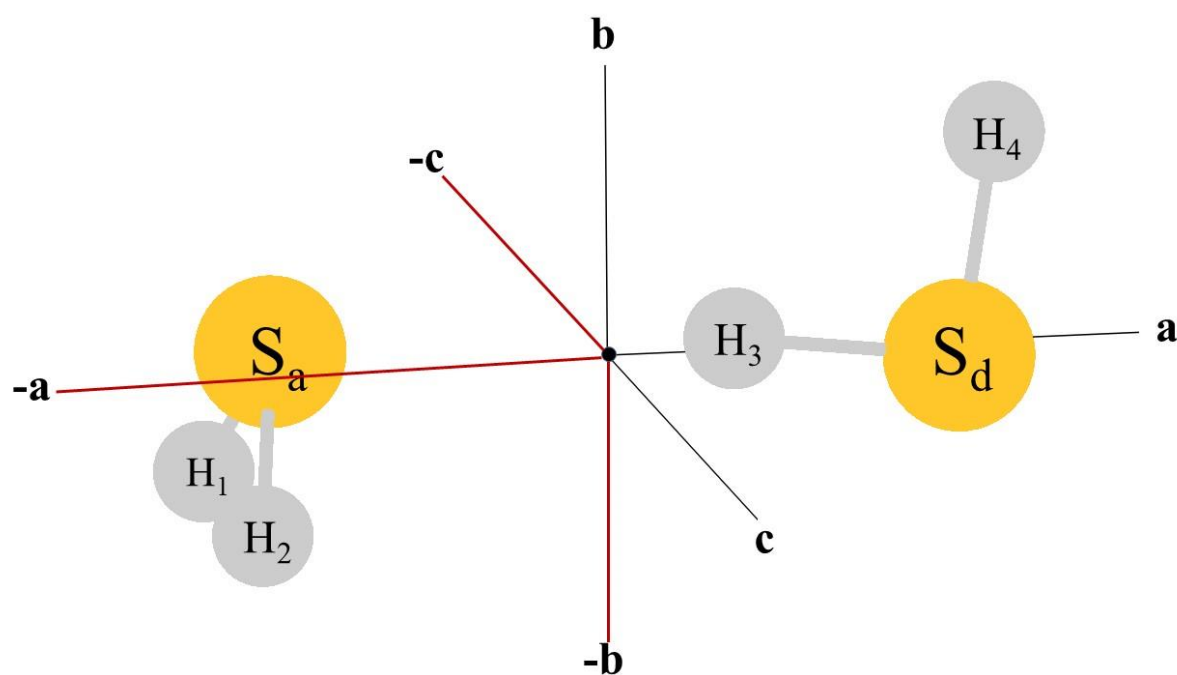
Figure 3.8. Labelling of the atoms used in the structural analysis for $(H_2S)_2$. The approximate orientations of the principal axes are shown in the figure. The c principal axis is perpendicular to the plane of the paper.

Table 3.18. Distances of atoms from the centre of mass evaluated using D3-B3LYP/6-311G++(d,p) method and Kraitchman's Analysis. Values are in Å.

Atom	D3-B3LYP/ 6-311G++(d,p)	Experiment
S_a	2.020	2.047(1)
H_1	2.574	2.651(1)
H_2	2.574	-
S_d	2.099	2.066(1)
H_3	2.626	2.654(1)
H_4	0.757	-

3.3.3.2 Ground State Structure (r_0) from STRFIT

The three parameters (1) $r(H_4 \cdots S_a)$, the hydrogen bond distance, (2) $\theta(S_d$-$H_4 \cdots S_a)$, the angle between the S_d–H_4 donor and acceptor sulphur atom, and (3), the angle between the symmetry axis of the proton-accepting H_2S with respect to intermolecular bond (ϕ) were determined using Kisiel's STRFIT program. The dihedral angle between the planes of the two H_2S molecules was initially set at 90°. Table 3.19 shows the fitted parameters from STRFIT as well as the Kraitchman values. The hydrogen bond distance in the $(H_2S)_2$ was determined to be 2.778(9) Å . The angle between $(S_d$-$H_4 \cdots S_a)$ is 175(7)°, which suggests that the hydrogen bond is almost linear. (Figure 3.9). Based on the experimental structure reported here, clearly, the $(H_2S)_2$ is hydrogen-bonded. The recent recommendation by IUPAC on hydrogen bonding[59,60] suggests that directionality is the defining property for hydrogen bonding. In particular, the hydrogen bond angle is close to 180°. In $(H_2S)_2$, the tilt between the acceptor H_2S moiety and the intermolecular axis is found out to be $\varphi = 78(4)$°. In Table 3.20, we have compared the structural parameters obtained from Kraitchman and STRFIT with high-level quantum chemistry calculation. DFT method with wb97xd and dispersion corrected B3LYP functionals provided excellent agreement with the experimental geometry. Dispersion correction is crucial for $(H_2S)_2$ to obtain a good match.

Table 3.19. Structural parameters derived from the Kraitchman analysis and STRFIT fit for $(H_2S)_2$. Values are in Å.

Parameters	Kraitchman r_s	STRFIT r_0 with r_0 H$_2$S*
$R(S_a \cdots S_d)$/Å	4.113(1)	-
$r(H_4 \cdots S_a)$ /Å	-	2.778(9)
$\theta(S_d\text{-}H_4 \cdots S_a)^\circ$ /degree	-	175(7)
φ° / degree	-	78(4)
σ /uÅ^2	-	1.1

Table 3.20. Structural parameters obtained from experiment and theory for $(H_2S)_2$. Theoretical values are from the MP2/aug-cc-pVQZ, wb97xd//6-311++g(d, p), D2-B3LYP//6-311++g(d, p), D3-B3LYP//6-311++g(d, p) respectively. Values are in Å.

Parameters	Equilibrium				Expt.
	MP2 aug-cc-pVQZ	wb97xd//6-311++g(d, p)	D2-B3LYP//6-311++g(d, p)	D3-B3LYP//6-311++g(d, p)	
$R(S_a \cdots S_d)$/Å	4.081	4.114	4.116	4.119	4.113(1)
$r(H_4 \cdots S_a)$ /Å	2.752	2.772	2.767	2.772	2.778(9)
$\theta(S_d\text{-}H_4 \cdots S_a)^\circ$ /degree	172	174	175	174	175(7)
φ° / degree	87	75	76	77	78(4)

R(O-O) = 2.976(30) Å

58(6)°

$r(H\cdots O)^* = 2.029$ Å

-51(6)°

$\theta(O\text{-}H\cdots O)^* = 171°$

R(S – S) = 4.113(1) Å

φ = 78(4)°

$r(H\cdots S) = 2.777(9)$ Å

$\theta(S\text{-}H\cdots S) = 176(7)°$
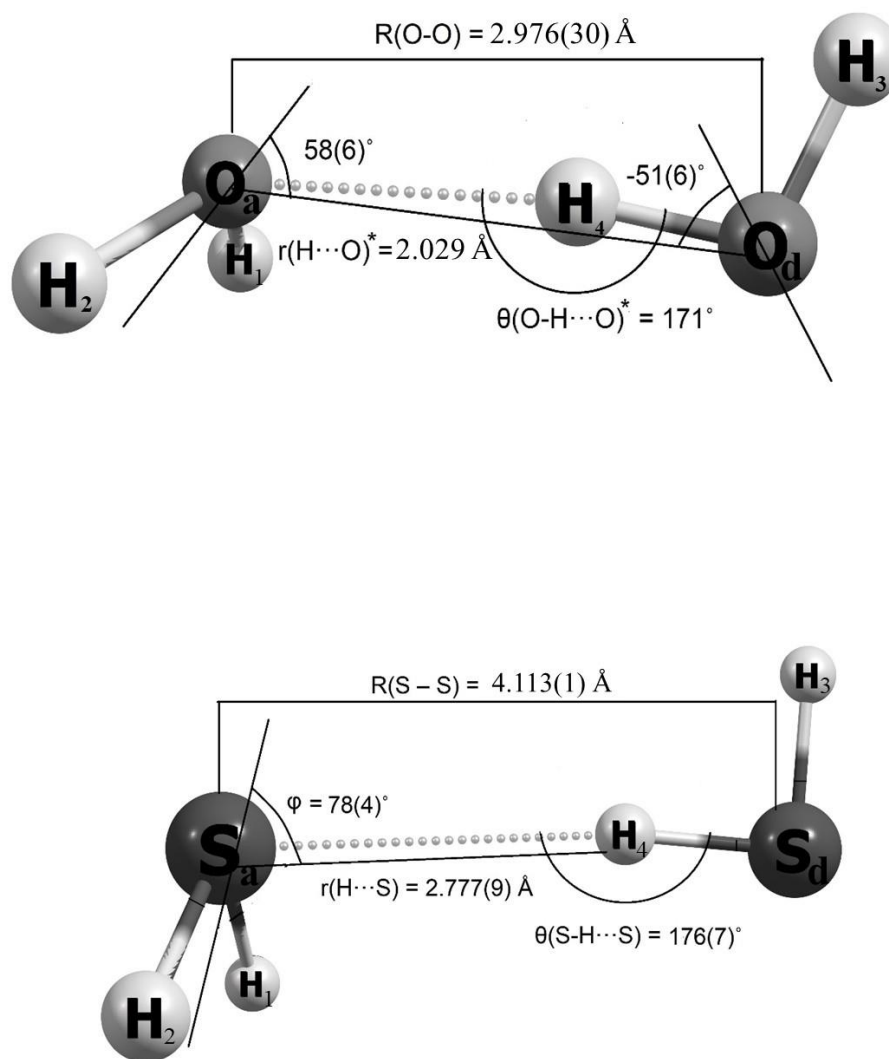
*Figure 3.9. (H2O)2 (top) and (H2S)2 (bottom) structure from the experiment. *Vibrationally averaged geometry calculated at MP2/aug-cc-pVDZ level.*

3.3.4 **Structure Comparison: $(H_2O)_2$ versus $(H_2S)_2$**

The structural parameters of $(H_2O)_2$ and $(H_2S)_2$ have been compared in this section (Table 3.21). The hydrogen bond length of two dimers reveals that $(H_2O)_2$ is more tightly bound than $(H_2S)_2$. The $H_4 \cdots S_a$ hydrogen bond length is almost 0.7 Å longer than the $H_4 \cdots O_a$ hydrogen bond. The sum of the van der Waals[61] radii of O and H atom is 2.72 Å which is 0.6 Å more than the hydrogen bond distance in $(H_2O)_2$. In comparison, the sum of the van der Waals radii of S and H atom is 3.00 Å and 0.2 Å more than the hydrogen bond distance in $(H_2S)_2$. Dyke and co-workers[62] had found the $(H_2O)_2$ structure, using molecular beam electric resonance spectroscopy, with an oxygen-oxygen distance $R(O_a\text{-}O_d)$ of 2.976(30) Å. In the $(H_2S)_2$, the $S_a\text{-}S_d$ distance is 1.1 Å longer than the $O_a\text{-}O_d$ distance.

Intriguingly, the hydrogen bond in $(H_2S)_2$ is closer to linearity. In general, the stronger the bond closer it to linearity. The proton-accepting water axis is 58(6)° with respect to $R(O_a\text{-}O_d)$, and the proton-donating water axis is at -51(6)° with respect to $R(O_a\text{-}O_d)$. In $(H_2S)_2$, the tilt between the acceptor H_2S moiety and the intermolecular axis is found out to be $\varphi = 78(4)°$. So, the H_2S acceptor has rigidly pyramidal geometry, while the H_2O acceptor has an approximately tetrahedral configuration at O_a. This discrepancy has also been observed with H_2O and H_2S complexes in previous studies as well[63].

Table 3.21. Comparison of structural parameters of $(H_2O)_2$ and $(H_2S)_2$.

$(H_2O)_2$	Parameters	$(H_2S)_2$	Parameters
$R(O_a\text{-}O_d)$ /Å	2.976(30)[62]	$R(S_a\text{-}S_d)$/Å	4.113(1)
$r(H_4 \cdots O_a)$ /Å	2.029*	$r(H_a \cdots S_a)$ /Å	2.778(9)
$\theta(O_d\text{-}H_4 \cdots O_a)°$ /degree	171*	$\theta(S_d\text{-}H_4 \cdots S_a)°$ /degree	175(7)
$\varphi°$ / degree	58(6)[12]	$\varphi°$ / degree	78(4)

*Vibrationally averaged geometry calculated at MP2/aug-cc-pVDZ level.

3.3.5 **Force Field**

There are two measures of the strength of the interaction of two molecules B and A in a complex B$\cdots$A (for dimer both are same) that are commonly employed, namely, the dissociation energy (i.e., the energy required to dissociate the complex into B and A) and the intermolecular stretching force constant k_σ. Various expressions are available for determining k_σ for a complex B$\cdots$A from its quartic centrifugal distortion constants, either D_J or Δ_J depending on the symmetry and the reduction used. The quartic distortion constants are functions only of quadratic force constants and molecular geometry. The diatomic model[64,65], which assumes that B and A may be approximated as point masses, give the most straightforward expression. However, a more sophisticated approach was developed for polyatomic linear, symmetric-top, and asymmetric-top complexes[66]. Recently, Walker and Legon[67] proposed a two force constant model for complexes of the type B$\cdots$MX, in which B is a simple Lewis base of at least C_{2v} symmetry and MX is any diatomic molecule lying along a C_n axis (n $\geq$ 2) of B. This model does not strictly apply to complexes of C_s symmetry but may be expected to give good results because of the near-prolate symmetry and the line between the heavy atoms nearly coincident with the *a*-inertial axis. We have evaluated the force constant both using diatomic approximation and two force constant model.

3.3.5.1 Diatomic Approximation

In recent years stretching force constants have been obtained for many weakly bound dimers. In some instances, such force constants have been computed using the well-established approach of vibrational wavenumbers associated with the stretching modes of a weakly bound dimer. The intermolecular stretching frequency (ω_s) in $(H_2S)_2$ was calculated using pseudo-diatomic approximation. In the pseudo-diatomic model, each monomer is treated as a point mass and found to give satisfactory results only when moments of inertia of the constituent monomers are small. From intermolecular stretching frequency, we can evaluate the force constant (k_s) associated with the bond. By continuing to treat the $(H_2S)_2$ complex as a pseudo-diatomic molecule, an estimate of the depth of the effective potential well (ε) can be made. Here we assume the

Lennard-Jones 6/12 potential can describe the interaction. In the next section, we have calculated binding energy from much accurate *ab-initio* calculation and compared it with diatomic approximation.

$$V(r) = \varepsilon[(\frac{r_e}{r})^{12} - 2(\frac{r}{r_e})^6]$$

The depth of the well is represented by ε here, and it occurs at the equilibrium distance *(r_e)*. Expanding this potential in a Taylor series at $r=r_e$ gives

$$V(r) = -\varepsilon + \frac{36\varepsilon}{r_e^2}(r-r_e)^2 - \frac{252\varepsilon}{r_e^3}(r-r_e)^3 + \frac{1113\varepsilon}{r_e^4}(r-r_e)^4 + ...$$

The harmonic force constant is related to the quadratic term of the potential by

$$\frac{1}{2}k_c = \frac{36\varepsilon}{r_e^2}$$

Moreover, well depth can be found by rearrangement.

$$\varepsilon = \frac{1}{72}r_e^2 k_c$$

Table 3.22 provides the intermolecular stretching frequency (ω_s), force constant (k_s), and well depth of the potential (ε) of $(H_2S)_2$ and its isotopologues. Intermolecular stretching frequency has been found out to be 40 cm^{-1} with force constant of 1.603 N/m. The potential well depth for the interaction was found to be 2.2 kJ/mol. The force constants appear reasonably consistent with sulphur substitution but differ significantly in going from hydrogen to deuterium. This indicates a coupling between the modes. The lighter isotope, hydrogen, undergo larger amplitude vibrations than deuterium and thus samples more of the potential surface. Diatomic approximation yields an equilibrium distance (r_e) of 4.119 Å between the monomers. Karka and coworkers[58] have calculated a considerably more accurate stretching frequency and force constant. They have reported the local mode force constant and frequency associated with two monomer units to be 2.1 N/m and 125 cm^{-1}, respectively. Furthermore, their calculation reports force constant for $H_4 \cdots S_a$ (H-bond) as 4.6 N/m.

Table 3.22. Intermolecular stretching frequencies, force constants, and binding energies of isotopologues of $(H_2S)_2$ calculated using diatomic approximation.

Isotopologues	ω_s (cm^{-1})	k_s (N/m)	ε (kJ/mol)
H^{32}SH$\cdots^{32}$SH$_2$ (Upper)	40.0	1.603	2.2
H^{32}SH$\cdots^{32}$SH$_2$ (Lower)	39.5	1.568	2.2
D^{32}SD-^{32}SDH	40.4	1.709	2.4
H^{32}SD$\cdots^{32}$SD$_2$	40.1	1.685	2.3
D^{32}SD$\cdots^{32}$SD$_2$ (Upper)	38.1	1.542	2.1
D^{32}SD$\cdots^{32}$SD$_2$ (Lower)	38.4	1.565	2.2
H^{32}SD$\cdots^{32}$SDH (Upper)	42.4	1.854	2.5
H^{32}SD$\cdots^{32}$SDH (Lower)	43.2	1.920	2.6
H^{34}SH$\cdots^{32}$SH$_2$ (Upper)	39.2	1.581	2.2
H^{34}SH$\cdots^{32}$SH$_2$ (Lower)	38.8	1.551	2.2
H^{32}SH$\cdots^{34}$SH$_2$ (Upper)	39.6	1.615	2.2
H^{32}SH$\cdots^{34}$SH$_2$ (Lower)	39.0	1.566	2.2
H^{34}SD$\cdots^{32}$SD$_2$ (Upper)	40.0	1.718	2.4
H^{34}SD$\cdots^{32}$SD$_2$ (Lower)	40.3	1.747	2.4
H^{32}SD$\cdots^{34}$SD$_2$	39.4	1.664	2.3
D^{34}SD$\cdots^{32}$SD$_2$	37.3	1.514	2.1

3.3.5.2 Two-Force Constant Model

The experimentally determined force constants are calculated by applying a model developed by Walker and Legon[67], which accounts for contributions to the centrifugal distortion constants from both the S_d–H_4 and $S_a\cdots H_4$ bonds. The force constants of these bonds are denoted by F_{11} and F_{22}, respectively,

$$hD_J = \frac{1}{2}\left\{\frac{\hbar^4}{I_{bb}^4}\right\}\left\{(m_1 a_1)^2 \left(F^{-1}\right)_{11} + (m_1 a_1 + m_2 a_2)^2 (F^{-1})_{22}\right\}$$

where m_1 and m_2 are the masses of the sulphur (S_d) and hydrogen atoms, respectively. The principal axis coordinates of the sulphur (S_d) and hydrogen atoms are a_1 and a_2, respectively. This model allows the calculation of either F_{11} or F_{22}, provided the other is known by assuming the cross term, F_{12}, is negligible. Even where neither parameter is accurately known, a reasonable estimate will allow an approximate value and uncertainty limits to be assigned to the other. To estimate F_{22} for HSH· · ·SH$_2$, F$_{11}$ complex is assumed to equal to that of the S-H bond in isolated H$_2$S molecule, and the r$_0$ values of geometrical parameters are used to determine the principal axis coordinates. Table 3.23 provides the estimated F_{22} values of H-bond calculated assuming different F_{11} values. The F_{22} values are almost independent of F_{11} values in the provided range (see Figure 3.10). We highlight that due to the simplicity of the model, this technique may not yield high accuracy.

Table 3.23. Variation of F_{22} (N/m) as a function of the assumed value of F_{11} (N/m) for (H$_2$S)$_2$.

Methods	F_{11} (N/m)	F_{22} (Expt) (N/m)
MP2//aug-cc-pVQZ	446.716	1.435
wb97xd//6-311++g(d,p)	459.811	1.435
D2-B3LYP//6-311++g(d,p)	414.554	1.436
D3-B3LYP//6-311++g(d,p)	415.085	1.436
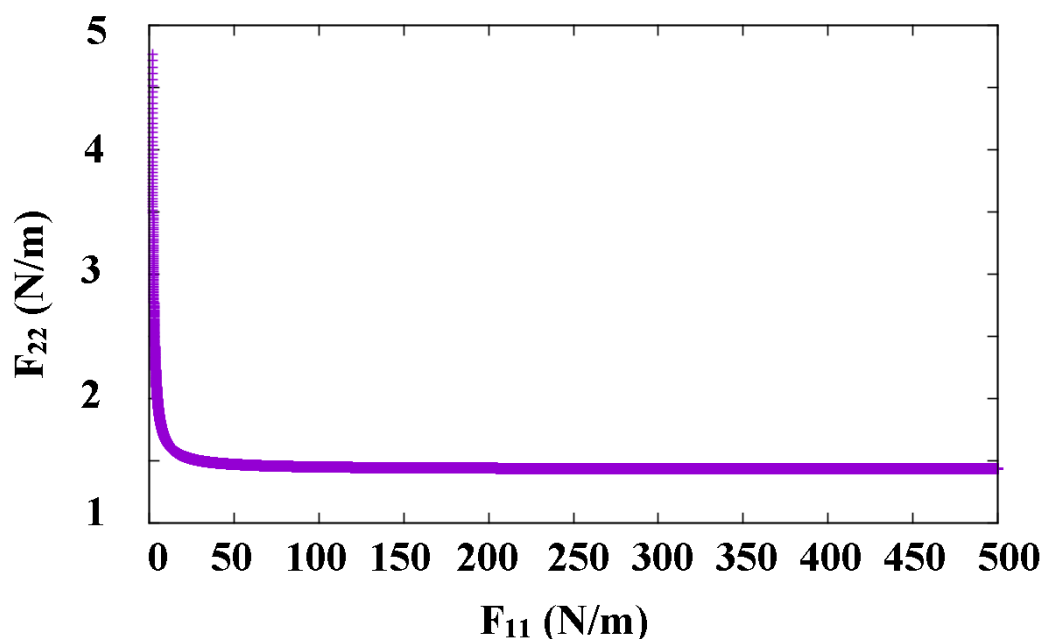
Figure 3.10: Variation of F_{22} as a function of the assumed value of F_{11} for (H₂S)₂.

3.3.6 Binding Energy

Binding energy (ΔE) is an important parameter for a hydrogen-bonded complex. Basis set superposition error (BSSE) corrected stabilisation energies ΔE_{BSSE}, and BSSE and zero-point corrected stabilisation energies $\Delta E_{BSSE+ZPE}$ are calculated using various methods and basis sets. For the binding energy of (H₂S)₂, only two experimental measurements exist: a D_0 value of 7.1 ± 1.3 kJ/mol published over forty years ago[68], and a more recent binding energy value of $D_e = 7.1 \pm 0.1$ kJ/mol obtained using cavity-enhanced absorption spectroscopy (CEAS)[69]. The D_0 value for (H₂S)₂ is close to the measured dissociation energy for (H₂O)₂ ($D_0 = 13.2 \pm 0.1$ kJ/mol)[18], implying that (H₂S)₂ is moderately strongly bound, though less loosely than (H₂O)₂. Recently, Lemke[23] reported a comprehensive analysis of (H₂S)₂ binding energy at the CCSD(T) with the complete basis set limit. The binding energy evaluated at CCSD(T)/CBS is found out to be 7.096 kcal/mol, which is in excellent agreement with the experimentally obtained binding energy. The binding energy of (H₂S)₂ has also been estimated using DFT and MP2 methods in this Chapter (see Table 3.24). The BSSE corrected binding energy calculated at D2-B3LYP//6-311++g(df,p) and wb97xd//6-311++g(d,p) is in fact in perfect agreement with the experimental and CCSD(T)/CBS results. In fact, in a

recent study, the wb97xd proved to be excellent functional to reproduce the experimental binding energy and geometrical parameter of $(H_2S)_2$[70]. In the previous section, we have calculated the binding energy of $(H_2S)_2$ with diatomic approximation. The diatomic approximation binding energy of 2.2 kJ/mol significantly underestimates experimental binding energy (7.1 kJ/mol), indicating that a hydrogen bond binds the $(H_2S)_2$.

Table 3.24. Binding energy calculated for $(H_2S)_2$ at different levels of theory. Values are in kJ/mol.

Methods	ΔE	ΔE_{BSSE}	$\Delta E_{BSSE+ZPE}$
D2-B3LYP//6-311++g(d,p)	9.2	6.3	2.5
D2-B3LYP//6-311++g(df,p)	8.8	7.1	2.1
D3-B3LYP//6-311++g(d,p)	10.0	8.4	3.8
D3-B3LYP//6-311++g(df,p)	10.0	7.9	3.3
wb97xd//6-311++g(d,p)	8.8	7.1	2.1
MP2//aug-cc-pVDZ	10.0	6.3	2.1
MP2//aug-cc-pVTZ	8.8	7.5	3.3
MP2//aug-cc-pVQZ	8.4	7.5	3.8
*CCSD(T)//CBS(D,T,Q)[23]		7.1	4.6
Cavity-enhanced absorption spectroscopy (CEAS)[69]		7.1 ± 0.1	
Diatomic approximation		2.2	

ΔE is the binding energy obtained as a difference between the sum of monomers and dimers. ΔE_{BSSE} is the counterpoise corrected binding energy. $\Delta E_{BSSE+ZPE}$ is counterpoise and zero-point energy corrected binding energy.

3.3.7   **Potential Energy Surface**

There is a substantial difference between the potential energy surface of $(H_2O)_2$ and $(H_2S)_2$. So far, we have concentrated on the experimentally observed hydrogen-bonded C_s global minimum. Recently, a comprehensive study by Tschumper and coworkers[71] reported twelve low-energy configurations of $(H_2S)_2$. Out of twelve $(H_2S)_2$ configurations, harmonic vibrational frequency computations confirm three as minima, four as transition states, and five as higher-order saddle points. Only one minimum was found in the $(H_2O)_2$, reflecting the sharp difference in the potential energy surfaces of $(H_2O)_2$ and $(H_2S)_2$. Figure 3.11 depicts the three minima of the $(H_2S)_2$.

1   **2**   **3**
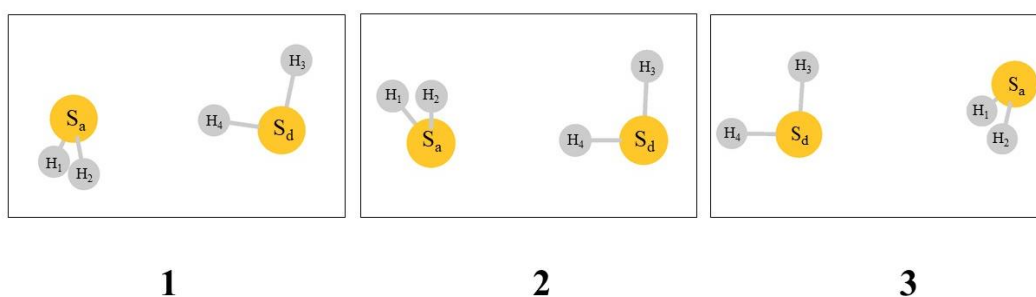
Figure 3.11. Three minima found in $(H_2S)_2$ potential energy surface. The first two minima were found in our calculations previously. The third structure is taken from Tschumper and coworkers[71].

The energy differences between the three different minima are small. Structure 1 and structure 2 are hydrogen-bonded structures, and the only difference is the dihedral angle between the two-monomer unit. Structure 1 is referred to as trans, while structure 2 is referred to as the cis. Structure 1 is the global minima. Tschumper and coworkers[71] found that the energy difference between the trans and cis is 0.4 kJ/mol at CCSD(T) CBS method. The interconversion barrier for the trans and cis form is found to be 4.0 kJ/mol[72]. The *B* and *C* rotational constants are somewhat lower in the cis form than in the trans form. The experimental rotational constants match the trans from better. The S_a-S_d distance in cis form is elongated by 0.011 Å. Both the cis and trans forms have the same hydrogen bond distance. At the same time, the hydrogen bond angle is slightly more linear in cis. In terms of the *b*-dipole moment, there is a significant difference between the two. The *b*-dipole in cis form is almost ten times larger than in trans form. We only observed *a*-dipole transitions in the experiment. The *b*-dipole transitions

cannot be obtained in the frequency range of 2-26 GHz. The trans conformer is not even a stationary point on the $(H_2O)_2$ potential energy surface[72]. Interestingly, the stable conformer of the dipole-bound anion of the water dimer is cis-$(H_2O)_2^-$. Consequently, the trans-$(H_2O)_2^-$ is found to be unstable against electron autodetachment[73].

Structure 3 is a minimum on the $(H_2S)_2$ potential energy surface, with an energy of only 0.2 kJ/mol higher than the global minimum[71]. In the $(H_2O)_2$ potential energy surface, the structure is a second-order saddle point. Structure 3 has drastically different rotational constants than structures 1 and 2 (see Table 3.25). Structure 3 has a dipole moment similar to structure 1. Structure 3 is not hydrogen-bonded, and it has $S_a \cdots S_d$ interaction, confirmed by Atoms in Molecules (AIM) calculations. The S_a-S_d distance is 3.773 Å, almost 0.3 Å shorter compared to its hydrogen-bonded counterparts (see Table 3.26). Interestingly a recent report shows[70], the hydrogen bonding between H_2S molecules disappears as confinement increases, and sulphur–sulphur interactions emerge. Inside C_{60}, the $(H_2S)_2$ is bound by a covalent bond between two sulphur atoms.

Table 3.25. Rotational constants and dipole moment components of cis and trans conformers calculated at the D3-B3LYP/6-311++g(d,p).

	Structure 1 (Trans)	Structure 2 (Cis)	Structure 3
A/MHz	96664.717	97903.312	116833.076
B/MHz	1749.563	1737.785	2063.330
C/MHz	1741.203	1729.927	2059.008
$|\mu_a|$/D	1.576	1.834	1.670
$|\mu_b|$/D	0.256	2.136	0.295
$|\mu_c|$/D	0.001	0.012	0.000
ΔE/kJ/mol CCSD(T)/CBS	0.0	0.4	0.2

The relative energies are taken from Tschumper and coworkers[71].

Table 3.26. Structural parameters of there (H$_2$S)$_2$ minima compared to that of the experiment.

(H$_2$O)$_2$	Structure 1 (Trans)	Structure 2 (Cis)	Structure 3	Experiment
R(S$_a$-S$_d$)/Å	4.119	4.130	3.773	4.113(1)
r(H$_a\cdots$S$_a$) /Å	2.772	2.779	-	2.778(9)
θ(S$_d$-H$_4\cdots$S$_a$) ° /degree	174	178	-	175(7)
φ° / degree	77	71	-	78(4)

3.3.8 Dynamics: Assuming (H$_2$O)$_2$ like Tunnelling Paths

We looked at possible tunnelling paths and splitting for the (H$_2$S)$_2$ in this part. The tunnelling splitting in (H$_2$S)$_2$ was calculated using (H$_2$O)$_2$ tunnelling pathways as a reference[74]. Different pathways can lead to different barrier heights that strongly influence the tunnelling splitting. The three most popular hydrogen atom motions in the (H$_2$O)$_2$ are acceptor-acceptor interchange, donor-acceptor interchange, and donor-donor interchange. In (H$_2$O)$_2$, the donor-donor interchange does not result in tunnelling splitting. The acceptor-acceptor and donor-acceptor interchange tunnelling splitting are ~200 GHz and ~20 GHz, respectively. A detailed description of the (H$_2$O)$_2$ tunnelling pathways can be found in Chapter 5 (section 5.1). Smith et al.[75], established the pathways that would permit each of the four hydrogens to participate in the H-bonding. The barrier for (H$_2$O)$_2$ tunnelling pathways is listed in Table 3.27.

Table 3.27. Calculated barriers for different tunnelling dynamics in (H$_2$O)$_2$. Values are in cm^{-1}.

	MP2/6-311+G(2df,2p)	MP4/6-311+G(2df,2p)
Acceptor tunnelling	206	206
Interchange Motion	311	304
Donor tunnelling	682	658

We assume that the $(H_2S)_2$ has similar tunnelling paths as $(H_2O)_2$ and calculated the associated barrier for each. The $(H_2S)_2$ transition states (see Figure 3.12) for different tunnelling motions are optimised at MP2/aug-cc-pVDZ level of theory, and electronic energies are calculated at MP4 (full)/aug-cc-PVDZ and CCSD (t, full)/aug-cc-pVDZ level. Table 3.28 lists the values for $(H_2S)_2$ transition state energies for different tunnelling motions at different levels of theory. The optimised internals for the transition states are provided in the supplementary information (see Table S3.10). The barrier for the $(H_2S)_2$ is much smaller compared to the $(H_2O)_2$. The acceptor tunnelling barrier for $(H_2O)_2$ is nearly three times that of $(H_2S)_2$. In $(H_2O)_2$, the donor-acceptor and donor-donor tunnelling barriers are twice as high as in $(H_2S)_2$. The lower barrier leads to increased tunnelling splitting in $(H_2S)_2$. Until now, none of these tunnelling motions have been seen in $(H_2S)_2$. Using a periodic potential[76], we have calculated the donor-acceptor interchange tunnelling splitting in $(H_2S)_2$, which is discussed in the following section. It should be again emphasised that these calculations are done to get an estimate of tunnelling splitting, assuming $(H_2S)_2$ tunnelling pathways are comparable to $(H_2O)_2$ tunnelling paths. This may not be the case; as we have shown in the previous section (3.3.7), there is a significant difference between the potential energy surfaces of $(H_2O)_2$ and $(H_2S)_2$.

Table 3.28. Calculated barriers for different tunnelling dynamics in $(H_2S)_2$. Values are in cm^{-1}.

$(H_2S)_2$	MP2/ aug-cc-pVDZ	MP4(full)/ aug-cc-pVDZ	CCSD(t,full)/ aug-cc-pVDZ
Acceptor tunnelling	46	49	43
Interchange Motion	151	200	171
Donor tunnelling	312	375	308

| Acceptor Tunnelling | Interchange Tunnelling cyclic | Donor Tunnelling bifurcated |
| [C_1] | [C_i] | [C_{2v}] |
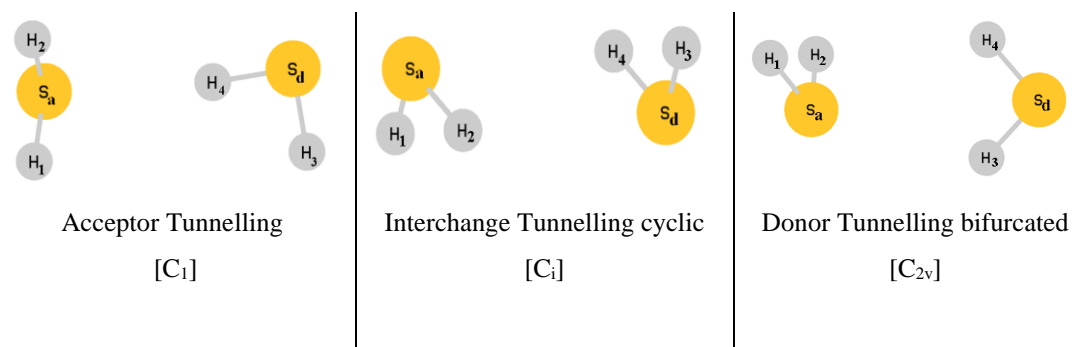
Figure 3.12. $(H_2O)_2$ like transition state for $(H_2S)_2$ for different tunnelling motion.

3.3.8.1 Modelling Donor-Acceptor Interchange Tunnelling Splitting using Periodic Potentials

To simulate the interchange tunnelling motion in $(H_2S)_2$, we adopted the methodology used in water dimer[77] and acetylene dimer[78]. The interchange conversion is depicted as a concerted geared internal rotation of the two H_2S units around their C_2 axis, similar to $(H_2O)_2$ interchange conversion[77]. The transition state resembles the C_i symmetry found in the *ab initio* calculation mentioned above. With this model, approximate tunnelling Hamiltonian takes the form,

.

$$\boldsymbol{B}p^2 + \frac{V_4}{2}(1 - \cos 4\phi)$$

$$p = -\mathrm{i}\frac{\partial}{\partial \alpha}$$

Where V_4 is the barrier for interconversion, ϕ is the internal rotation angle and $\boldsymbol{B} = b_0/2$. Here b_0 is the zero-point B rotational constant of H_2S. For H_2S $b_0 = 9.016$ cm^{-1} and D_2S $b_0 = 4.512$ cm^{-1}. The Hamiltonian matrix is set up in the free-rotor basis diagonalised to obtain eigenvalues.

$$|m\rangle = \frac{e^{im\alpha}}{(2\pi)^{\frac{1}{2}}}$$

For $(H_2S)_2$, we cannot observe the donor-acceptor tunnelling splitting. In this work, we have used the barrier from 140 cm^{-1} to 200 cm^{-1} to predict the tunnelling splitting associated with $(H_2S)_2$ interchange motion. Tunnelling splitting ranges from around 70

GHz-30 GHz, depending on the barrier heights. Our spectrometer *(BT-FTMW, Bangalore)* works in the 2-26 GHz frequency range. Assuming $(H_2S)_2$ similarly interchanges its donor and acceptor like $(H_2O)_2$; then the tunnelling splitting would not be observable in our spectrometer range.

A similar approach has been taken for $(D_2S)_2$ where $B = 2.256$ cm^{-1}. A barrier was varied from 140 cm^{-1} to 200 cm^{-1} corresponding values of the tunnelling splitting are given in Table 3.29. These range from approximately 2-6 GHz and are potentially measurable. However, given the large variations, observing them would be a big challenge, and we have not observed any transitions so far.

Table 3.29. Barrier (cm^{-1}) and corresponding splitting (GHz) for $(H_2S)_2/(D_2S)_2$ interchange tunnelling motion.

Barrier (cm^{-1})	Splitting (GHz)	
	$(H_2S)_2$	$(D_2S)_2$
140	70.6	6.3
151	60.8	5.1
170	47.3	4.1
180	41.6	3.4
200	32.4	1.8

3.3.8.2 Mathieu's Differential Equation

The energy level corresponding to the periodic potential functions with only one term could be determined by solving Mathieu's differential equation.

$$y'' + (b - s\cos^2 x)y = 0$$

The parameters of the equation are now related to the tunnelling Hamiltonian (section 3.3.8.1) as follows:

$$V_n = \frac{n^2 \boldsymbol{B} s}{4}, E = \frac{n^2 \boldsymbol{B} b}{4}, 2x = n\phi + \pi,$$

The values of b are listed in Mathieu's table[79] for corresponding values of s. For a particular V_n, if $\boldsymbol{B}$, is known we can determine the energy levels. The values calculated from the free rotor basis and Mathieu's differential equation are almost identical (see Table 3.29 and Table 3.30).

Table 3.30. Barrier (cm^{-1}) and corresponding tunnelling splitting (GHz) for $(H_2S)_2$ interchange tunnelling motion obtained using Mathieu's tables.

Barrier (cm^{-1})	Splitting (GHz)	
	$(H_2S)_2$	$(D_2S)_2$
140	70.7	6.3
151	60.6	5.2
170	47.2	4.1
180	41.4	3.3
200	32.8	1.8

3.3.9 Atoms in Molecules (AIM) Analysis

Following the confirmation of the structure, Atoms in Molecules (AIM)[80] calculations were used to investigate the existence and nature of the intermolecular interactions present in the $(H_2S)_2$. The wavefunctions for the Atoms in Molecules (AIM) calculations have been evaluated using MP2/aug-cc-pVDZ and MP2/aug-cc-pVTZ level of theory. The calculations are performed with AIMALL[81] and AIM2000[82] programs. For a complex to be hydrogen-bonded, Carroll and Bader[83,84] suggested several conditions based on electron density topology. Koch and Popelier[85] outlined eight requirements for C-H···O hydrogen bonds in a helpful overview. We begin the discussion by examining the Koch and Popelier[85] criteria for $(H_2S)_2$ and $(H_2O)_2$. The calculated parameters based on the Koch and Popelier[85] criteria are provided in Table 3.31.

3.3.9.1 Koch and Popelier Criteria

(1) Topology: The presence of a bond critical point (BCP) and the bond path between hydrogen (H_4) and sulphur (S_a) is the first criterion, and this is satisfied in the $(H_2S)_2$

(see Figure 3.13). IUPAC[59] also highlights this criterion as one of the characteristics of hydrogen bond formation.

(2) *The Charge Density at the Bond Critical Point*

According to the second criterion, the electron density, $\rho(r)$, at the bond critical point (BCP) should be within the range of 0.002-0.034 au. The electron density at the BCP for $(H_2S)_2$ is 0.0107 au, within the hydrogen bond limit. Bader showed that electron density at the bond critical point is a good indicator of the strength of the bonds[80]. At the hydrogen bond critical point, the electron density for $(H_2O)_2$ is nearly twice that of $(H_2S)_2$, which indicates a stronger hydrogen bond in $(H_2O)_2$. Also, the bond path is almost linear in both complexes.
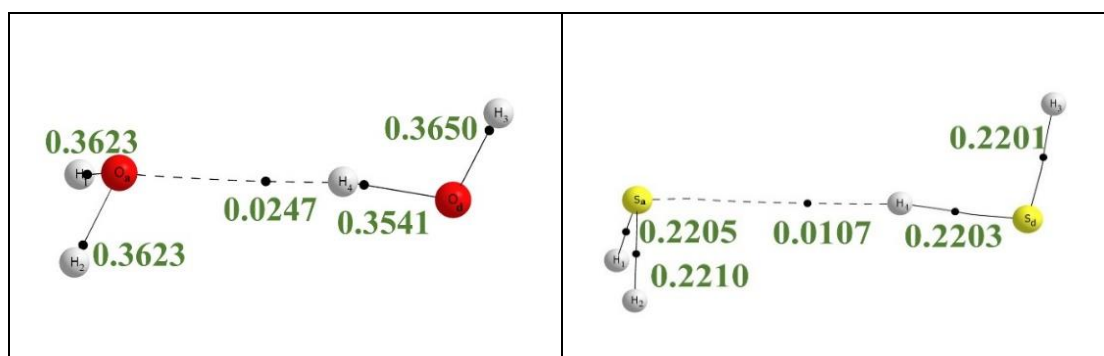
Figure 3.13. Atoms in Molecules (AIM) topology study for (H₂O)₂ (left) and (H₂S)₂ (right). The black dots refer to the bond critical point. The dotted line shows the hydrogen bond path.

(3) *The Laplacian of the Charge Density at the Bond Critical Point*

The third necessary criterion focuses on another local property, the Laplacian of the charge density $(\nabla^2\rho)$ evaluated at the bond critical point. The recommended range for $\nabla^2\rho$ is 0.024-0.139 au (allowing for small differences in basis set). For $(H_2S)_2$, $\nabla^2\rho$ is within the recommended range. The, $\nabla^2\rho$ values at the bond critical point are positive in both $(H_2O)_2$ and $(H_2S)_2$, suggesting charge depletion between the two atoms. This is expected for closed-shell interactions.

(4) *Mutual Penetration of Hydrogen and Acceptor Atom*

According to the fourth criterion, the H atom and the H-bond acceptor atom should have positive mutual penetration. This criterion was found to be the necessary and sufficient condition for the H-bonding. Mutual penetration is the difference between the non-bonded and bonded radii of both the acceptor and the bonded H atom added together. The distance between the nucleus and the point where the electron density value is 0.001 au, along the bond path, is known as non-bonded radii. Hence, in monomers, the distance should be determined in the direction of the bonded partner's approach. For hydrogen-bonded complexes, the binding energy is strongly correlated to the mutual penetration. Mutual penetration, with significant positive values, confirm the hydrogen bonding between S_a and H_4 $(H_2S)_2$. Mutual penetration for $(H_2O)_2$, as expected, is slightly larger than $(H_2S)_2$. In the supplementary information (see Table S3.11), a detailed computation of this parameter is provided.

(5) *Loss of Charge of the Hydrogen Atom*

According to the fifth hydrogen bonding criterion, the hydrogen atom should lose charge during complex formation. This is determined by subtracting the population on the monomer atom, N(monomer), from the population on the atom in the complex, N(complex). The results are shown in Table 3.31. It is clear that the $(H_2S)_2$ has a significantly larger $|\Delta N|$ than $(H_2O)_2$.

(6) *Energetic Destabilisation of the Hydrogen Atom*

Hydrogen should destabilise during complex formation, according to the sixth criterion. This criterion is also satisfied by $(H_2S)_2$. The ΔE value is almost similar in both dimers.

(7) *Decrease of Dipolar Polarisation of the Hydrogen Atom*

According to the seventh criterion, the magnitude of dipolar polarisation of hydrogen (M) should decrease during complex formation. The atomic first moment slightly decreases upon formation of complex formation in $(H_2S)_2$. This decrease is significantly more in $(H_2O)_2$.

(8) *Decrease of the Hydrogen Atom's Volume*

The change in atomic volume after complex formation is the final criterion. Koch and Popelier[85] observed a decrease in the atomic volume of H for C-H···O hydrogen bonds. It is observed in all hydrogen-bonded complexes in the previously reported work[86]. The reduction in H atom volume upon complex is also observed in the case of $(H_2S)_2$.

Table 3.31. The Koch and Popelier[85] criteria were applied to the S-H···S hydrogen bond in $(H_2S)_2$. For comparison, the values are provided for O-H···O hydrogen bond in $(H_2O)_2$. Values are in au.

#	Criteria	Conditions	$(H_2O)_2$	$(H_2S)_2$
1	Presence of BCP	Yes	Yes	Yes
2	$\rho(r)$	0.002-0.034	0.0247	0.0107
3	$\nabla^2\rho$	0.024-0.139	0.0819	0.0270
4	$\Delta r(H) + \Delta r(O/S)$	Positive	1.1	0.9
5	ΔN	Negative	-0.0376	-0.0464
6	ΔE	Positive	0.0219	0.0222
7	$\Delta|M|$	Negative	-0.0384	-0.0023
8	ΔV	Negative	-7.3	-3.0

$\rho(r)$: electron density at BCP, $\nabla^2\rho$: Laplacian of electron density, $\Delta r(H) + \Delta r(O/S)$: mutual penetration, ΔN: population difference, ΔE: atomic energy difference, $\Delta|M|$: difference in dipolar polarisation, ΔV: difference in atomic volume. The differences are between monomers and dimers.

Overall, it is clear that the eight criteria found by Koch and Popelier[85] for C-H···O hydrogen bonds are satisfied by S-H···S hydrogen bond in $(H_2S)_2$.

3.3.9.2 Nature of Interaction from Atoms in Molecules (AIM) Analysis

In both the dimers, $\nabla^2\rho$ is positive, indicating closed-shell interactions. The ratios of the first ($|\lambda_1|$) and third eigenvalues (λ_3) of the Hessian matrix are 0.238 and 0.204, respectively for $(H_2O)_2$ and $(H_2S)_2$. According to the criteria by Sosa and coworkers[87]

the value less than 0.25 is regarded as closed-shell interaction. Also, the ratio of potential ($|V|$) and kinetic (G) energy density <1.0 suggests closed-shell interaction[88]. The $|V|$/G ratio for $(H_2O)_2$ is slightly greater than 1.0, and for $(H_2S)_2$ is 0.885 (see Table 3.32).

Table 3.32. The $|\lambda_1|/\lambda_3$, $|V|/G$ from Atoms in Molecules (AIM) analysis. Wavefunctions used for the calculations are evaluated at the MP2/aug-cc-pVTZ. The values for $(H_2O)_2$ are provided for comparison. Values are in au.

	λ_1	λ_2	λ_3	$|\lambda_1|/\lambda_3$	V	G	$|V|/G$
$(H_2O)_2$	-0.0369	-0.0360	0.1548	0.238	-0.0213	0.0209	1.019
$(H_2S)_2$	-0.0093	-0.0093	0.0456	0.204	-0.0054	0.0061	0.885

3.3.10 **Non-covalent Interactions (NCI) Index**

Non-covalent interactions (NCI) index developed by Yang's group[89,90], employs quantum-mechanical electron density to identify intermolecular bonds. From NCI analysis, we can conclude that the weak interactions of HOH···OH$_2$ and HSH···SH$_2$ belong to hydrogen bonding. The 'spike' at the scatter diagram shows that the interaction strength in $(H_2O)_2$ is stronger than that $(H_2S)_2$ (see Figure 3.14). The findings of the non-covalent interactions (NCI) index match those of the Atoms in Molecules (AIM) study.
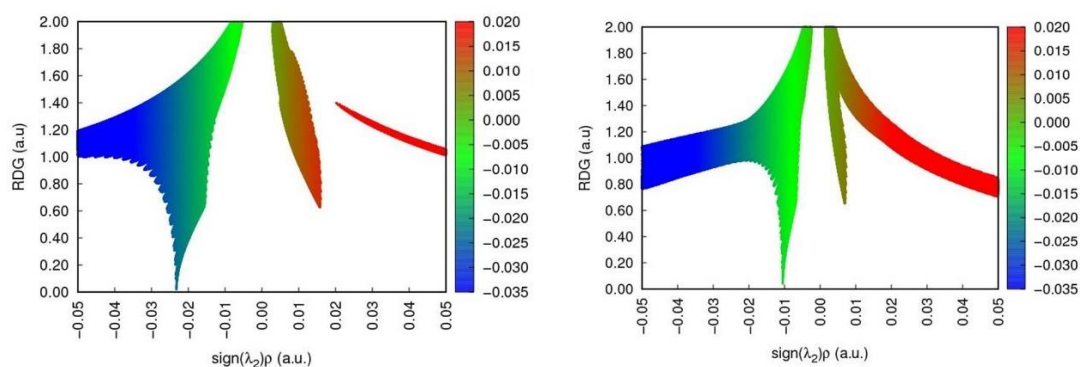
Figure 3.14. Non-covalent interactions (NCI) index plots for $(H_2O)_2$ (top) and $(H_2S)_2$ (bottom). The troughs in the plot arise due to O-H···O (Top) and S-H···S (Bottom) hydrogen bond.

3.3.11 **Natural Bond Orbital (NBO) Analysis**

We performed a natural bond orbital (NBO) study on $(H_2S)_2$ using the NBO 6.0 program[91] and compared the results to $(H_2O)_2$. The hydrogen bond is often referred to as $n \rightarrow \sigma^*$ interaction[92]. In both the dimers, $n \rightarrow \sigma^*$ interaction is a major source of stabilisation of the hydrogen bond geometry, as measured by second-order perturbation energy. The second-order perturbation energy for $(H_2O)_2$ is nearly twice that of the $(H_2S)_2$, meaning $(H_2O)_2$ has a stronger hydrogen bond (see Table 3.33). Figure 3.15 depicts the interacting natural orbitals of both the dimers.

In monomer and dimer, we looked at the occupation numbers[93] for both $n(LP)$ and σ^* NBOs. The occupation number in $n(LP)$ NBO decreases for both $(H_2O)_2$ and $(H_2S)_2$ compared to their respective monomers. Coincidentally, this difference (Δ) is the same for both the dimers. On the other hand, occupation number in σ^* NBO increases confirming $n \rightarrow \sigma^*$ charge transfer (see Table 3.34). The nature of the interaction is similar for both the hydrogen-bonded $(H_2O)_2$ and $(H_2S)_2$.

Table 3.33. Interacting natural bond orbitals with the respective second-order perturbation energy calculated at MP2/aug-cc-pVTZ level of theory.

Interaction	Second-order perturbation energy (kJ/mol)
$n_{O_a} \rightarrow \sigma^*_{O_d\text{-}H_4}$	30.5
$n_{S_a} \rightarrow \sigma^*_{S_d\text{-}H_4}$	16.4
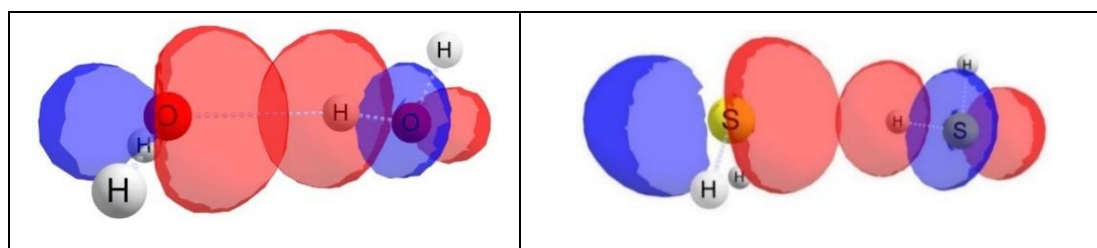
Figure 3.15. Interacting natural bond orbitals in $(H_2O)_2$ and $(H_2S)_2$.

Table 3.34. NBO population analysis for $(H_2O)_2$ and $(H_2S)_2$.

Donor					
H$_2$O Monomer	H$_2$O Dimer	Δ	H$_2$S Monomer	H$_2$S Dimer	Δ
n_O	n_{O_a}		n_S	n_{S_a}	
1.9979	1.9894	0.0085	1.9963	1.9878	0.0085
Acceptor					
$\sigma^*_{O\text{-}H}$	$\sigma^*_{O_d\text{-}H_4}$		$\sigma^*_{S\text{-}H}$	$\sigma^*_{S_d\text{-}H_4}$	
0.00000	0.0091	0.0091	0.0015	0.0102	0.0087

3.4 **Summary**

Finally, despite the fact that the microwave spectrum of the $(H_2S)_2$ was studied three decades ago, only $K_a=0$ lines were found. This would suggest that the H$_2$S is spherical in the dimer. The observation and assignment of $K_a=1$ lines are crucial in demonstrating that the $(H_2S)_2$ is hydrogen-bonded and that the interaction is not isotropic. Based on the criterion established by Goswami and Arunan[94], the mismatch in behaviour of H$_2$S in solid and in our experimental condition can be interpreted. In solids, the thermal energy along a coordinate that can break the hydrogen bond is greater than the barrier along that coordinate, resulting in an isotropic structure. When the temperature decreases significantly, the thermal motion becomes restrained, leading to the observation of the hydrogen-bonded geometry in our case. The thermal motion is inhibited when the temperature drops considerably, resulting in the observation of the hydrogen-bonded geometry. As a result, whereas H$_2$S stays gaseous at normal temperature and each H$_2$S has 12 neighbours when frozen at -85.5°C, the $(H_2S)_2$ demonstrates hydrogen bonding at lower temperatures. D$_2$S exhibits anisotropic packing and is hydrogen-bonded even in crystals, according to Loveday et al.[29] In comparison to H$_2$S, they used D$_2$S, which has substantially shorter oscillations due to thermal vibrations. The microwave spectrum revealed the first unequivocal experimental confirmation that the $(H_2S)_2$ is hydrogen-bonded[95]. AIM, NCI, and NBO calculations also support the hydrogen-bonded geometry of $(H_2S)_2$. The potential

energy surfaces of $(H_2S)_2$ and $(H_2O)_2$ are substantially different, which could lead to very different tunnelling dynamics in $(H_2S)_2$.

3.5 References

1. Biswal, H. S. & Wategaonkar, S. Sulfur, not too far behind O, N, and C: SH⋯π hydrogen bond. *J. Phys. Chem. A* **113**, 12774–12782 (2009).

2. Biswal, H. S., Bhattacharyya, S., Bhattacherjee, A. & Wategaonkar, S. Nature and strength of sulfur-centred hydrogen bonds: laser spectroscopic investigations in the gas phase and quantum-chemical calculations. *Int. Rev. Phys. Chem.* **34**, 99–160 (2015).

3. Biswal, H. S. Hydrogen bonds involving sulfur: new insights from ab initio calculations and gas phase laser spectroscopy. in *Noncovalent forces* 15–45 (Springer, 2015).

4. Mishra, K. K. *et al.* Observation of an Unusually Large IR Red-Shift in an Unconventional S–H⋯S Hydrogen-Bond. *J. Phys. Chem. Lett.* **12**, 1228–1235 (2021).

5. Kimura, H. Hydrogen sulfide as a neuromodulator. *Mol. Neurobiol.* **26**, 13–19 (2002).

6. Snider, E. *et al.* Room-temperature superconductivity in a carbonaceous sulfur hydride. *Nature* **586**, 373–377 (2020).

7. Biswal, H. S., Shirhatti, P. R. & Wategaonkar, S. O−H⋯O versus O−H⋯S hydrogen bonding. 2. Alcohols and thiols as hydrogen bond acceptors. *J. Phys. Chem. A* **114**, 6944–6955 (2010).

8. Michielsen, B., Verlackt, C., van der Veken, B. J. & Herrebout, W. A. C–H⋯X (X= S, P) hydrogen bonding: The complexes of halothane with dimethyl sulfide and trimethylphosphine. *J. Mol. Struct.* **1023**, 90–95 (2012).

9. Pimentel, G. C. & McClellan, A. L. The hydrogen bond. (1960).

10. Lobo, I. A., Robertson, P. A., Villani, L., Wilson, D. J. D. & Robertson, E. G.

Thiols as Hydrogen Bond Acceptors and Donors: Spectroscopy of 2-Phenylethanethiol Complexes. *J. Phys. Chem. A* **122**, 7171–7180 (2018).

11. Dyke, T. R. & Muenter, J. S. Microwave spectrum and structure of hydrogen bonded water dimer. *J. Chem. Phys.* **60**, 2929–2930 (1974).

12. Dyke, T. R., Mack, K. M. & Muenter, J. S. The structure of water dimer from molecular beam electric resonance spectroscopy. *J. Chem. Phys.* **66**, 498–510 (1977).

13. Fraser, G. T., Suenram, R. D. & Coudert, L. H. Microwave electric-resonance optothermal spectroscopy of $(H_2O)_2$. *J. Chem. Phys.* **90**, 6077–6085 (1989).

14. Fraser, G. T., Suenram, R. D., Coudert, L. H. & Frye, R. S. Electric-resonance optothermal spectrum of $(H_2O)_2$: Microwave spectrum of the K= 1-0 subband for the E2±states. *J. Mol. Spectrosc.* **137**, 244–247 (1989).

15. Fraser, G. T., Suenram, R. D. & Coudert, L. H. Microwave electric-resonance optothermal spectroscopy of $(H_2O)_2$. *J. Chem. Phys.* **90**, 6077–6085 (1989).

16. Mukhopadhyay, A., Cole, W. T. S. & Saykally, R. J. The water dimer I: Experimental characterization. *Chem. Phys. Lett.* **633**, 13–26 (2015).

17. Mukhopadhyay, A., Xantheas, S. S. & Saykally, R. J. The water dimer II: Theoretical investigations. *Chem. Phys. Lett.* **700**, 163–175 (2018).

18. Rocher-Casterline, B. E., Chng, L. C., Mollner, A. K. & Reisler, H. Communication: Determination of the bond dissociation energy (D_0) of the water dimer, $(H_2O)_2$, by velocity map imaging. *J. Chem. Phys.* **134**, 1–5 (2011).

19. Kollman, P., McKelvey, J., Johansson, A. & Rothenberg, S. Theoretical Studies of Hydrogen-Bonded Dimers. Complexes Involving HF, H_2O, NH_3, CHl, H_2S, PH_3, HCN, HNC, HCP, CH_2NH, H_2CS, H_2CO, CH_4, CF_3H, C_2H_2, C_2H_4 C_6H_6, F-and H_3O^+. *J. Am. Chem. Soc.* **97**, 955–965 (1975).

20. Kerns, R. C. & Allen, L. C. Cyclic and Bifurcated Hydrogen Bonds. *J. Am. Chem. Soc.* **100**, 6587–6594 (1978).

References
_____

21.   de Oliveira, G. & Dykstra, C. E. Large basis set study of the stability of (H2S)2: the importance of 3d functions in weak interaction of second row molecules. *Chem. Phys. Lett.* **243**, 158–164 (1995).

22.   Amos, R. D. Structures, harmonic frequencies and infrared intensities of the dimers of H_2O and H_2S. *Chem. Phys.* **104**, 145–151 (1986).

23.   Lemke, K. H. Structure and binding energy of the H_2S dimer at the CCSD(T) complete basis set limit. *J. Chem. Phys.* **146**, (2017).

24.   Pradeep, T. & Rao, C. N. R. An ultraviolet photoelectron spectroscopic study of the H_2S dimer , a van der Waals molecule *. **185**, 496–500 (1991).

25.   Bhattacherjee, A., Matsuda, Y., Fujii, A. & Wategaonkar, S. The intermolecular S-H···Y (Y=S,O) hydrogen bond in the H_2S dimer and the H_2S-MeOH complex. *ChemPhysChem* **14**, 905–914 (2013).

26.   Albertí, M., Amat, A., Aguilar, A. & Pirani, F. Molecular dynamics simulations of small clusters and liquid hydrogen sulfide at different thermodynamic conditions. *J. Phys. Chem. A* **120**, 4749–4757 (2016).

27.   Sarkar, S. & Bandyopadhyay, B. Cooperative nature of the sulfur centered hydrogen bond: investigation of $(H_2S)_n$ (n= 2–4) clusters using an affordable yet accurate level of theory. *Phys. Chem. Chem. Phys.* **21**, 25439–25448 (2019).

28.   Pauling, L. *The Nature of the Chemical Bond,* (3rd edition, pp. 465) (Cornell University Press, 1960).

29.   Loveday, J. S., Nelmes, R. J., Klotz, S., Besson, J. M. & Hamel, G. Pressure-induced hydrogen bonding: structure of D_2S phase I′. *Phys. Rev. Lett.* **85**, 1024–1027 (2000).

30.   Arunan, E. & Mani, D. Dynamics of the chemical bond: Inter- and intra-molecular hydrogen bond. *Faraday Discuss.* **177**, 51–64 (2015).

31.   Goswami, M. & Arunan, E. The hydrogen bond: A molecular beam microwave spectroscopist's view with a universal appeal. *Phys. Chem. Chem. Phys.* **11**,

8974–8983 (2009).

32. Tursi, A. J. & Nixon, E. R. Infrared spectra of Matrix-isolated hydrogen sulfide in solid nitrogen. *J. Chem. Phys.* **53**, 518–521 (1970).

33. Woodbridge, E. L., Tso, T. L., McGrath, M. P., Hehre, W. J. & Lee, E. K. C. Infrared spectra of matrix-isolated monomeric and dimeric hydrogen sulfide in solid O_2. *J. Chem. Phys.* **85**, 6991–6994 (1986).

34. Tsujii, H., Takizawa, K. & Koda, S. IR spectra of hydrogen bonding of H_2S doped in Kr solids. *Chem. Phys.* **285**, 319–326 (2002).

35. Koga, K., Takami, A. & Koda, S. IR spectra of H_2S isolated in free-standing crystals of Kr and Xe. *Chem. Phys. Lett.* **293**, 180–184 (1998).

36. Pacansky, J. & Calder, V. Matrix-Isolation Spectra of H_2S and D_2S: An Example of the Application of the Uncoupled Oscillator Approximation. *J. Chem. Phys.* **53**, 4519–4524 (1970).

37. Odutola, J. A., Viswanathan, R. & Dyke, T. R. Molecular beam electric deflection behavior and polarity of hydrogen-bonded complexes of ROH, RSH, and RNH. *J. Am. Chem. Soc.* **101**, 4787–4792 (1979).

38. Balle, T. J. & Flygare, W. H. Fabry-Perot cavity pulsed Fourier transform microwave spectrometer with a pulsed nozzle particle source. *Rev. Sci. Instrum.* **52**, 33–45 (1981).

39. Lovas, F. J. & Suenram, R. D. Pulsed beam Fourier transform microwave measurements on OCS and rare gas complexes of OCS with Ne, Ar, and Kr. *J. Chem. Phys.* **87**, 2010–2020 (1987).

40. Arunan, E., Tiwari, A. P., Mandal, P. K. & Mathias, P. C. Pulsed nozzle Fourier transform microwave spectrometer: Ideal to define hydrogen bond radius. *Current Science* vol. 82 533–540 (2002).

41. Mandal, P. K., Goswami, M. & Arunan, E. Pulsed nozzle Fourier transform microwave spectroscopic and ab initio investigationson the weakly bound Ar-$(H_2S)_2$ trimer. *J. Indian Inst. Sci.* **85**, 353 (2013).

References
───────────────────────────────────────

42.   F. J. Lovas, R. D. Suenram, and L. H. C. No Title. *43rd Int.Symp. Mol. Spectrosc.* (1988).

43.   Mandal, P. K. Rotational Spectra of Weakly Bound Complexes and 'Hydrogen Bond Radius' Doctoral dissertation, Indian Institute of Science (2005).

44.   Medcraft, C., Bittner, D. M., Tew, D. P., Walker, N. R. & Legon, A. C. Geometries of $H_2S\cdots MI$ (M = Cu, Ag, Au) complexes studied by rotational spectroscopy: The effect of the metal atom. *J. Chem. Phys.* **145**, (2016).

45.   Stephens, S. L. & Walker, N. R. Determination of nuclear spin–rotation coupling constants in CF_3I by chirped-pulse Fourier-transform microwave spectroscopy. *J. Mol. Spectrosc.* **263**, 27–33 (2010).

46.   Zaleski, D. P., Stephens, S. L. & Walker, N. R. A perspective on chemistry in transient plasma from broadband rotational spectroscopy. *Phys. Chem. Chem. Phys.* **16**, 25221–25228 (2014).

47.   Pickett, H. M. The fitting and prediction of vibration-rotation spectra with spin interactions. *J. Mol. Spectrosc.* **148**, 371–377 (1991).

48.   Dunning, T. H. Gaussian basis sets for use in correlated molecular calculations. I. The atoms boron through neon and hydrogen. *J. Chem. Phys.* **90**, 1007–1023 (1989).

49.   Grimme, S. Semiempirical GGA-type density functional constructed with a long-range dispersion correction. *J. Comput. Chem.* **27**, 1787–1799 (2006).

50.   Grimme, S., Antony, J., Ehrlich, S. & Krieg, H. A consistent and accurate ab initio parametrization of density functional dispersion correction (DFT-D) for the 94 elements H-Pu. *J. Chem. Phys.* **132**, 154104 (2010).

51.   Viswanathan, R. & Dyke, T. R. The microwave and radiofrequency spectrum of $H_2S\cdot$ Ar. *J. Chem. Phys.* **82**, 1674–1681 (1985).

52.   Mandal, P. K., Ramdass, D. J. & Arunan, E. Rotational spectra and structure of the Ar_2–H_2S complex: pulsed nozzle Fourier transform microwave spectroscopic

and ab initio studies. *Phys. Chem. Chem. Phys.* **7**, 2740–2746 (2005).

53. Xu, Y., Arboleda, P. & Jäger, W. Microwave spectroscopic study of the CO–H₂S complex. *J. Mol. Spectrosc.* **229**, 47–53 (2005).

54. Goswami, M., Neill, J. L., Muckle, M., Pate, B. H. & Arunan, E. Microwave, infrared-microwave double resonance, and theoretical studies of C₂H₄···H₂S complex. *J. Chem. Phys.* **139**, 104303 (2013).

55. Willoughby, L. C., Fillery-Travis, A. J. & Legon, A. C. An investigation of the rotational spectrum of H₂S···HF by pulsed-nozzle, Fourier-transform microwave spectroscopy: Determination of the hyperfine coupling constants χ aa (³³S), χD aa, and DH (D) F aa. *J. Chem. Phys.* **81**, 20–26 (1984).

56. Kraitchman, J. Determination of molecular structure from microwave spectroscopic data. *Am. J. Phys.* **21**, 17–24 (1953).

57. Kisiel, Z. Least-squares mass-dependence molecular structures for selected weakly bound intermolecular clusters. *J. Mol. Spectrosc.* **218**, 58–67 (2003).

58. Martins, J. B. L. *et al.* Computational analysis of vibrational frequencies and rovibrational spectroscopic constants of hydrogen sulfide dimer using MP2 and CCSD (T). *Spectrochim. Acta Part A Mol. Biomol. Spectrosc.* **239**, 118540 (2020).

59. Arunan, E. *et al.* Definition of the hydrogen bond (IUPAC Recommendations 2011). *Pure Appl. Chem.* **83**, 1637–1641 (2011).

60. Arunan, E. *et al.* Defining the hydrogen bond: An account (IUPAC Technical Report). *Pure Appl. Chem.* **83**, 1619–1636 (2011).

61. Batsanov, S. S. Van der Waals Radii of Elements. *Inorg. Mater. Transl. from Neorg. Mater. Orig. Russ. Text* **37**, 871–885 (2001).

62. Odutola, J. A. & Dyke, T. R. Partially deuterated water dimers: Microwave spectra and structure. *J. Chem. Phys.* **72**, 5062–5070 (1980).

63. Legon, A. C. & Walker, N. R. What's in a name?'Coinage-metal'non-covalent

bonds and their definition. *Phys. Chem. Chem. Phys.* **20**, 19332–19338 (2018).

64. Novick, S. E., Davies, P., Harris, S. J. & Klemperer, W. Determination of the structure of ArHCl. *J. Chem. Phys.* **59**, 2273–2279 (1973).

65. Balle, T. J., Campbell, E. J., Keenan, M. R. & Flygare, W. H. A new method for observing the rotational spectra of weak molecular complexes: KrHCl. *J. Chem. Phys.* **72**, 922–932 (1980).

66. Millen, D. J. Determination of stretching force constants of weakly bound dimers from centrifugal distortion constants. *Can. J. Chem.* **63**, 1477–1479 (1985).

67. Bittner, D. M., Walker, N. R. & Legon, A. C. A two force-constant model for complexes B··· M–X (B is a Lewis base and MX is any diatomic molecule): Intermolecular stretching force constants from centrifugal distortion constants D_j or Δ_J. *J. Chem. Phys.* **144**, 74308 (2016).

68. Lowder, J. E., Kennedy, L. A., Sulzmann, K. G. P. & Penner, S. S. Spectroscopic studies of hydrogen bonding in H_2S. *J. Quant. Spectrosc. Radiat. Transf.* **10**, 17–23 (1970).

69. Ciaffoni, L. *et al.* Line strength and collisional broadening studies of hydrogen sulphide in the 1.58 μm region using diode laser spectroscopy. *Appl. Phys. B* **92**, 627–633 (2008).

70. Kumar, A. & Kumar, P. Formation of unexpected S–S covalent bonds in H_2S dimers under confinement. *Phys. Chem. Chem. Phys.* **23**, 5963–5968 (2021).

71. Perkins, M. A., Barlow, K. R., Dreux, K. M. & Tschumper, G. S. Anchoring the hydrogen sulfide dimer potential energy surface to juxtapose $(H_2S)_2$ with $(H_2O)_2$. *J. Chem. Phys.* **152**, 214306 (2020).

72. Fernández-Alarcón, A. *et al.* The nature of the intermolecular interaction in $(H_2X)_2$ (X= O, S, Se). *Phys. Chem. Chem. Phys.* **23**, 10097–10107 (2021).

73. Chen, H.-Y. & Sheu, W.-S. Dipole-bound anion of water dimer: Theoretical ab-initio study. *J. Chem. Phys.* **110**, 9032–9038 (1999).

74. Fraser, G. T. (H$_2$O)$_2$: spectroscopy, structure and dynamics. *Int. Rev. Phys. Chem.* **10**, 189–206 (1991).

75. Smith, B. J., Swanton, D. J., Pople, J. A., Schaefer III, H. F. & Radom, L. Transition structures for the interchange of hydrogen atoms within the water dimer. *J. Chem. Phys.* **92**, 1240–1247 (1990).

76. Lewis, J. D., Malloy Jr, T. B., Chao, T. H. & Laane, J. Periodic potential functions for pseudorotation and internal rotation. *J. Mol. Struct.* **12**, 427–449 (1972).

77. Karyakin, E. N., Fraser, G. T. & Suenram, R. D. Microwave spectrum of the K a= 1← 0 rotation-tunnelling band of (D$_2$O)$_2$. *Mol. Phys.* **78**, 1179–1189 (1993).

78. Fraser, G. T. *et al.* Infrared and microwave investigations of interconversion tunneling in the acetylene dimer. *J. Chem. Phys.* **89**, 6028–6045 (1988).

79. Laboratory, U. S. N. B. of S. C. *Tables Relating to Mathieu Functions: Characteristic Values, Coefficients, and Joining Factors*. vol. 59 (US Department of Commerce, National Bureau of Standards, 1967).

80. Bader, R. F. W. *Atoms in Molecules: A Quantum Theory*. (Oxford University Press, 1990).

81. Keith, T. A. AIMAll (Version 14.11. 23). *TK Gristmill Software, Overl. Park KS, USA* (2014).

82. Biegler-Konig, F. & Schonbohm, J. AIM2000 Program Package, Ver. 2.0. *Univ. Appl. Sci. Bielefeld* (2002).

83. Carroll, M. T. & Bader, R. F. W. An analysis of the hydrogen bond in BASE-HF complexes using the theory of atoms in molecules. *Mol. Phys.* **65**, 695–722 (1988).

84. Carroll, M. T., Chang, C. & Bader, R. F. W. Prediction of the structures of hydrogen-bonded complexes using the Laplacian of the charge density. *Mol. Phys.* **63**, 387–405 (1988).

85.   Koch, U. & Popelier, P. L. A. Characterization of CHO hydrogen bonds on the basis of the charge density. *J. Phys. Chem.* **99**, 9747–9754 (1995).

86.   Shahi, A. & Arunan, E. Hydrogen bonding, halogen bonding and lithium bonding: an atoms in molecules and natural bond orbital perspective towards conservation of total bond order, inter- and intra-molecular bonding. *Phys. Chem. Chem. Phys.* **16**, 22935–22952 (2014).

87.   Amezaga, N. J. M., Pamies, S. C., Peruchena, N. M. & Sosa, G. L. Halogen bonding: a study based on the electronic charge density. *J. Phys. Chem. A* **114**, 552–562 (2009).

88.   Cremer, D. & Kraka, E. Chemical Bonds without Bonding Electron Density—Does the Difference Electron-Density Analysis Suffice for a Description of the Chemical Bond? *Angew. Chemie Int. Ed. English* **23**, 627–628 (1984).

89.   Contreras-García, J. *et al.* NCIPLOT: a program for plotting noncovalent interaction regions. *J. Chem. Theory Comput.* **7**, 625–632 (2011).

90.   Johnson, E. R. *et al.* Revealing noncovalent interactions. *J. Am. Chem. Soc.* **132**, 6498–6506 (2010).

91.   Glendening, E. D., Landis, C. R. & Weinhold, F. NBO 6.0: natural bond orbital analysis program. *J. Comput. Chem.* **34**, 1429–1437 (2013).

92.   Reed, A. E., Curtiss, L. A. & Weinhold, F. Intermolecular interactions from a natural bond orbital, donor-acceptor viewpoint. *Chem. Rev.* **88**, 899–926 (1988).

93.   Reed, A. E., Weinstock, R. B. & Weinhold, F. Natural population analysis. *J. Chem. Phys.* **83**, 735–746 (1985).

94.   Goswami, M. & Arunan, E. The hydrogen bond: a molecular beam microwave spectroscopist's view with a universal appeal. *Phys. Chem. Chem. Phys.* **11**, 8974 (2009).

95.   Das, A. *et al.* The H_2S Dimer is Hydrogen-Bonded: Direct Confirmation from Microwave Spectroscopy. *Angew. Chemie Int. Ed.* **57**, 15199–15203 (2018).

3.6 **Supplementary Information**

Table S3.1. Observed rotational transitions for ^{34}S and deuterated isotopologues (K_a =0 lines)

$H^{34}SH\text{-}^{32}SH_2$				
$J' \leftarrow J''$	Upper	Residual	Lower	Residual
$2 \leftarrow 1$	6801.761(4)	1	6797.406(4)	-2
$3 \leftarrow 2$	10201.784(4)	0	10195.244(4)	3
$4 \leftarrow 3$	13600.780(4)	-1	13592.028(4)	-1
$5 \leftarrow 4$	16998.405(4)	1	--	--
$(B_0 + C_0)/2$	1700.5543(4)		1699.468(2)	
$(D_J)_0$ (kHz)	14.28(1)		14.52(7)	
$H^{32}SH\text{-}^{34}SH_2$				
$1 \leftarrow 0$	3402.259(4)	1	--	--
$2 \leftarrow 1$	6804.185(4)	0	6800.826(4)	3
$3 \leftarrow 2$	10205.432(4)	0	10200.368(4)	-2
$4 \leftarrow 3$	13605.671(4)	-1	13598.877(4)	-2
$5 \leftarrow 4$	17004.570(4)	2	16996.006(4)	1
$(B_0 + C_0)/2$	1701.157(1)		1700.321(1)	
$(D_J)_0$ (kHz)	13.99(4)		14.41(3)	
$H^{34}SD\text{-}^{32}SD_2$				
$3 \leftarrow 2$	9813.855(10)	0	9809.713(10)	2
$4 \leftarrow 3$	13083.775(10)	0	13078.272(10)	-2
$5 \leftarrow 4$	16352.524(10)	0	16345.688(10)	0
$(B_0 + C_0)/2$	1635.8620(1)		1635.167(1)	
$(D_J)_0$ (kHz)	12.191(3)		11.97(3)	
$H^{32}SD\text{-}^{34}SD_2$				
$3 \leftarrow 2$	9787.387(10)	0		
$4 \leftarrow 3$	13048.563(10)	-1		
$5 \leftarrow 4$	16308.461(10)	0		

Continued Table S3.1…

	1631.4643(3)			
	12.464(7)			
$(B_0 + C_0)/2$	1631.4643(3)			
$(D_J)_0$ (kHz)	12.464(7)			
D^{34}SD-^{32}SD$_2$				
$3 \leftarrow 2$	9606.752(4)	2	9601.544(4)	2
$4 \leftarrow 3$	12807.525(4)	-3	12800.604(4)	-3
$5 \leftarrow 4$	16007.044(4)	1	15998.430(4)	1
	1601.3617(15)		1600.4899(16)	
	13.15(4)		12.94(4)	
$(B_0 + C_0)/2$	1601.362(2)		1600.49(2)	
$(D_J)_0$ (kHz)	13.15(4)		12.9(4)	

Table S3.2. Vibrationally averaged coordinates of $(H_2S)_2$, optimised at D3-B3LYP-6311G++(d,p) level.

Atom	x(Å)	y(Å)	z(Å)
S_a	-2.044539	0.111226	0.000147
H_1	-1.835579	-0.862612	-0.931583
H_2	-1.845151	-0.860253	0.930822
S_d	2.095029	-0.094625	-0.000315
H_3	2.623585	1.097295	0.003502
H_4	0.833219	0.374972	0.004116

Table S3.3. Vibrationally averaged coordinates of $(H_2S)_2$, optimised at wb97xd/6-311G++(d,p) level.

Atom	x(Å)	y(Å)	z(Å)
S_a	-2.081375	0.127414	-0.020068
H_1	-2.145422	-1.176518	-0.683145

Continued Table S3.1…

H_2	-1.277609	-0.727640	1.279922
S_d	2.134814	-0.097528	-0.020045
H_3	2.332088	1.168825	0.967246
H_4	0.822779	0.045460	-0.217907

Table S3.4. Equilibrium geometry coordinates of $(H_2S)_2$, optimised at D3-B3LYP-6311G++(d,p) level.

Atom	x(Å)	y(Å)	z(Å)
S_a	-2.013237	0.107522	0.000131
H_1	-2.240914	-0.793157	-0.976895
H_2	-2.239772	-0.795362	0.975387
S_d	2.100863	-0.089966	-0.000034
H_3	2.320333	1.240155	0.000582
H_4	0.758329	0.067462	-0.000626

Table S3.5. Equilibrium geometry coordinates of $(H_2S)_2$, optimised at wb97xd/6-311G++(d,p).

Atom	x(Å)	y(Å)	z(Å)
S_a	-2.009390	0.106471	0.006055
H_1	-2.230235	-0.719928	-1.029885
H_2	-2.301011	-0.839982	0.913629
S_d	2.100154	-0.090049	-0.001376
H_3	2.317342	1.235824	0.009496
H_4	0.761673	0.061330	0.031891

Table S3.6. Equilibrium geometry coordinates of $(H_2S)_2$, optimised at aug-cc-pVQZ level of theory.

Atom	x(Å)	y(Å)	z(Å)
S_a	-2.005368	0.105874	0.000214
H_1	-2.055880	-0.814893	-0.964717
H_2	-2.055092	-0.818682	0.961556
S_d	2.070750	-0.086848	-0.000048
H_3	2.318683	1.224126	0.000522
H_4	0.746171	0.105037	-0.000011

Table S3.7. Normal mode analysis of $(H_2S)_2$ calculated at wb97xd/6-311++g(d,p), D3-B3LYP/6-311++g(d,p), and MP2/aug-cc-pVQZ levels of theory.

Modes(cm^{-1})	wb97xd/ 6-311++g(d,p)	D3-B3LYP/ 6-311++g(d,p)	MP2/ aug-cc-pVQZ
1	76	57	37
2	101	75	63
3	125	87	73
4	164	94	80
5	238	205	160
6	316	313	282
7	1221	1204	1212
8	1232	1218	1218
9	2727	2635	2731
10	2777	2672	2771
11	2796	2684	2786
12	2810	2689	2791

37
Intermolecular Vibration

63
Intermolecular Vibration

73
Intermolecular Vibration

80
Intermolecular Vibration

160
Intermolecular Vibration

282
Intermolecular Vibration

1212
Acceptor bending

1218
Donor bending

2731
Donor sym. stretch

2771
Acceptor sym. stretch

2786
Donor asym. stretch

2791
Acceptor asym. stretch
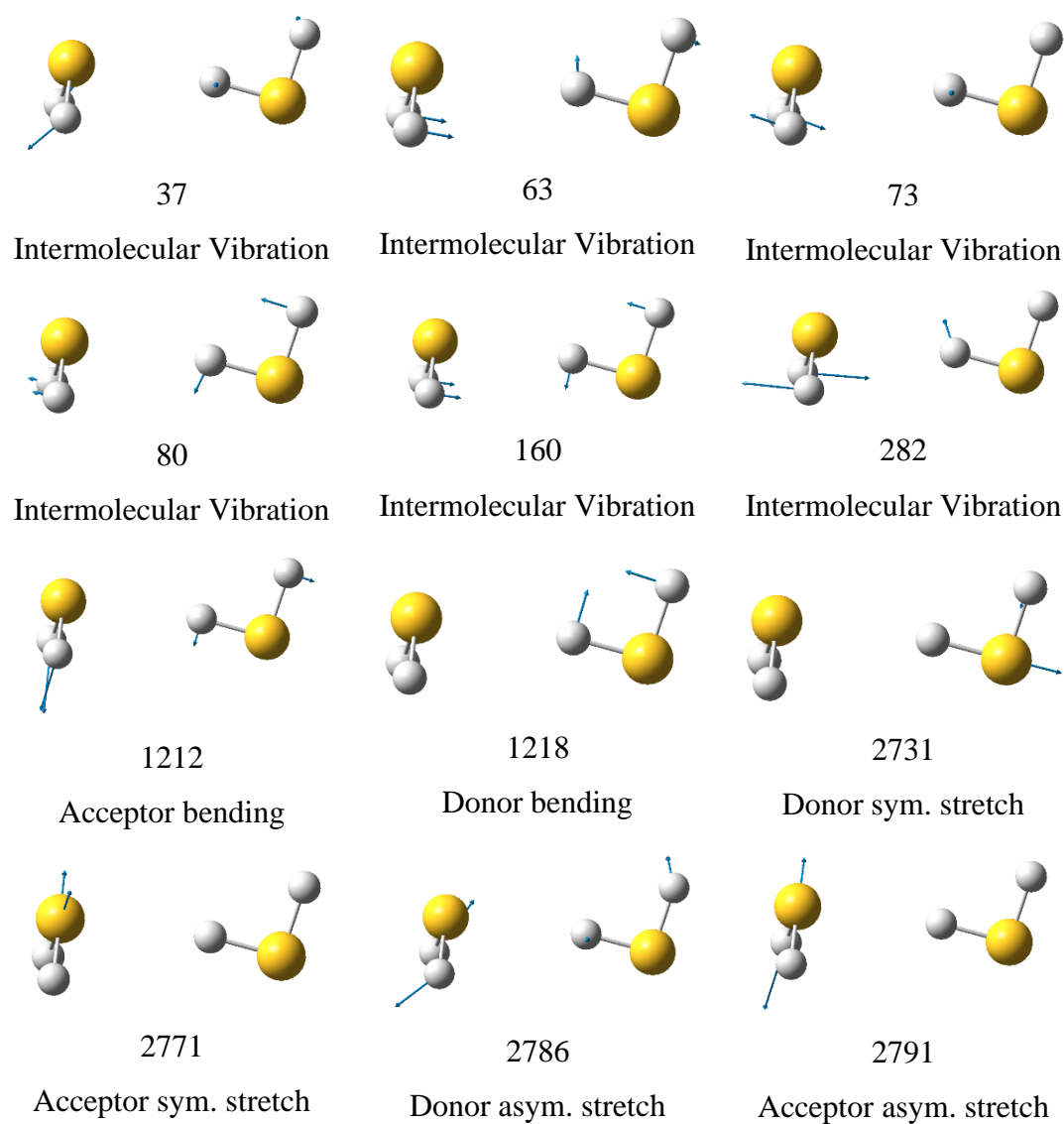
Figure S3.1. Displacements for normal modes of (H₂S)₂. Values are in cm⁻¹. Normal modes are calculated at the MP2/ aug-cc-pVQZ level of theory.

Table S3.8. Intermolecular force constant calculated using different approximate formulae. Values are in N/m.

Method	Force Constant (N/m)
$k = \dfrac{16\pi^2 \mu_D B_D{}^3}{D_J}$	1.56752
$k = \dfrac{16\pi^2 \mu_D B_D{}^3}{D_J}(1 - \dfrac{B_D}{B_{HA}})$	1.55528
$k = \dfrac{16\pi^2 \mu_D B_D{}^3}{D_J}(1 - \dfrac{B_D}{B_{HA}} - \dfrac{B_D}{B_B})$	1.54731
$k = \dfrac{8\pi^2 \mu_D}{D_J}[B_D^3(1-b) + C_D^3(1-c) - \dfrac{1}{4}(B_D - C_D)^2(B_D + C_D)(2-b-c)]$	1.54733
$k = \dfrac{8\pi^2 \mu_D}{\Delta_J}[B_D^3(1-b) + C_D^3(1-c)]$	1.54735

Table S3.9. Total energies of the transition states for different anticipated tunnelling dynamics of $(H_2S)_2$. Values are in au.

	MP2/ aug-cc-pVDZ	MP4(full)/ aug-cc-PVDZ	CCSD(t,full)/ aug-cc-pVDZ
$(H_2S)_2$, Minima	-797.71018768	-797.72773176	-797.77069919
Acceptor tunnelling	-797.70997972	-797.72751003	-797.77050286
Interchange Motion	-797.70949876	-797.72681966	-797.76991886
Donor tunnelling	-797.70876578	-797.72602425	-797.76929722

Table S3.10. Optimised internals for different transition states of $(H_2S)_2$ at MP2/aug-cc-pVDZ level. Distances are reported in Å, and angles are reported in degrees.

	AA	DA	DD
$R(S_aH_4)$	2.76524	3.14075	3.39593
$R(S_aS_d)$	4.11031	4.04552	4.11947
$R(S_aH_2)$	1.35029	1.35082	1.34969
$R(S_aH_1)$	1.35016	1.34983	1.34969
$R(S_dH_4)$	1.35323	1.35082	1.34942
$R(S_dH_3)$	1.34956	1.34983	1.34948
$A(S_aH_4S_d)$	172.319	123.451	113.242
$A(H_1S_aH_2)$	92.422	92.626	92.645
$A(H_4S_dH_3)$	92.638	92.626	91.442
$A(H_1S_aH_4)$	95.488	103.924	90.186
$A(H_2S_aH_4)$	90.782	56.550	90.239
$D(H_2S_aH_4S_d)$	-12.524	-0.001	-133.749
$D(H_1S_aH_4S_d)$	-105.032	-83.846	133.605
$D(S_aH_4S_dH_3)$	131.597	-104.973	0.044

Table S3.11. Mutual penetration of hydrogen and acceptor atom for $(H_2O)_2$ and $(H_2S)_2$. Radii of bonded [r(H) and r(O/S)], non-bonded [r_0(H) and r(O/S)] atoms, differences between them [$\Delta r(H)$, $\Delta r(O/S)$] and summation of both differences i.e., mutual penetration [$\Delta r(H) + \Delta r(O/S)$]. Values are in Å.

	$R_0(H)$	r(H)	$\Delta r(H)$	$r_0(O/S)$	r(O/S)	Δ r(O/S)	$\Delta r(H)+$ $\Delta r(O/S)$
$(H_2O)_2$	1.2	0.7	0.5	1.9	1.3	0.6	1.1
$(H_2S)_2$	1.4	1.0	0.4	2.3	1.8	0.5	0.9

Supplementary Information

CHAPTER

4

Rotational Spectra, Structure and Dynamics

of $(H_2S)_2(H_2O)$ Complex

This page intentionally left blank.

Chapter 4: Rotational Spectra, Structure and Dynamics of $(H_2S)_2$ (H_2O) Complex

4.1 Introduction

Distinct physical properties of H_2O and H_2S under ambient settings have long been recognised as a result of their significantly different hydrogen-bonding capabilities[1]. In Chapter 3, we have conclusively shown $(H_2S)_2$ is hydrogen-bonded similar to $(H_2O)_2$ at very low temperature[2]. We will need a vast amount of experimental data to figure out the microscopic distinctions between the two. The complex formed by water with hydrogen sulphide, H_2O–H_2S, is an interesting example of their hydrogen bonding abilities. Consequently, two possible hydrogen-bonded structures are possible. In one of the structures, HOH$\cdots$SH$_2$, the water molecule acts as a proton donor, and in the second one, $H_2O\cdots$HSH, it acts as a proton acceptor[3,4]. There are two possible hydrogen-bonded structures. The water molecule serves as a proton donor in one of the structures, HOH$\cdots$SH$_2$, and as a proton acceptor in the other, HSH$\cdots$OH$_2$. These two structures were found to be isoenergetic[5].

Microsolvation of small molecules is of prime importance in atmospheric and interstellar chemistry. There have been very few studies on the microsolvation of H_2S[6] and protonated H_2S molecule[7]. In this Chapter, we have looked at the microwave spectra of $(H_2S)_2(H_2O)$ complex and its isotopologues using chirped-pulse and Balle-Flygare microwave spectrometers. It is worth mentioning that microwave spectroscopy would not be able to detect $(H_2O)_3$ and $(H_2S)_3$ complexes due to the lack of dipole moment. Using a distributed multipole analysis, Gregory et al.[8] determined the dipole moments of $(H_2O)_n$ (n=2-6 and 8) at the MP2/aug-cc-pVDZ level of theory. The estimated total dipole moment for the (*ab initio* asymmetric equilibrium structure of the) water trimer was 1.071 D. However, no dipole moment was observed experimentally due to the facile torsional averaging. In $(H_2S)_3$, we also have similar torsional averaging due to symmetry (see Figure 4.1 and Table 4.1). Though the

microwave spectra of Ar(H$_2$S)$_2$ were known, the rotational constants are consistent with a T-shaped heavy atom vibrationally averaged geometry[9]. Using Fourier transform microwave spectroscopy, Kisiel et al.[10] found the (H$_2$O)$_2$(HCl) cluster and established a cyclic structure in which one of the water molecules in the water trimer is replaced by HCl. Similarly, the structure of the (HCl)$_2$(H$_2$O)[11] molecule has also been determined using a chirped-pulse Fourier transform microwave spectrometer (*CP-FTMW*). At the onset, we anticipate the structure of the (H$_2$S)$_2$(H$_2$O) complex will be similar to (HCl)$_2$(H$_2$O) complex as the masses of HCl and H$_2$S are close to each other. A two inversion tunnelling states have been observed for (HCl)$_2$(H$_2$O) with 1:3 relative intensity for the parent molecule[11]. *Ab-initio* calculation suggests the cyclic structure of (H$_2$S)$_2$(H$_2$O) complex with three hydrogen bonds. Also, we expect some cooperative effect in three hydrogen bonds. We obtained a few assigned lines during the (H$_2$S)$_2$ experiment as some H$_2$O is always present in the gas tubes. These lines were first considered to belong to the Ne(H$_2$S)$_2$ complex since neon was used as a carrier gas; however, they are also present when argon is used as a carrier gas. With the use of Ar as a carrier gas, nearly all of the known clusters produced by Ar + H$_2$O + H$_2$S were observed at the same time. The key to identification of new cluster has been the exclusion of lines of the known species. Novik's bibliography[12] was found to be useful in this regard. Rotational constants for Ar(H$_2$S)$_2$, (HCl)$_2$(H$_2$O) and (H$_2$S)$_2$(H$_2$O) are provided in Table 4.2 for comparison.
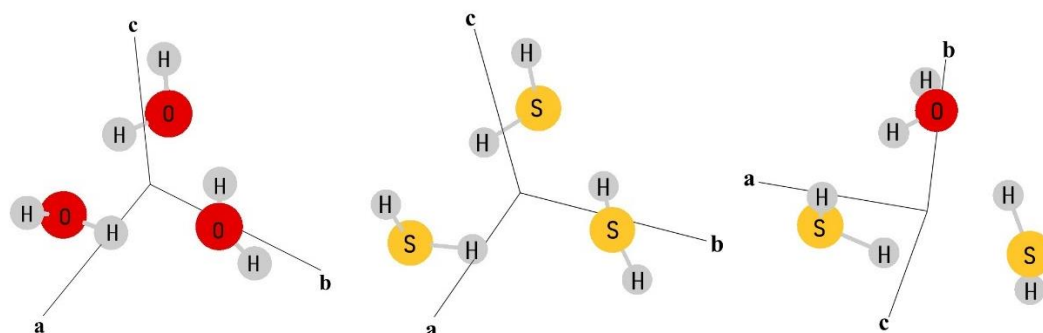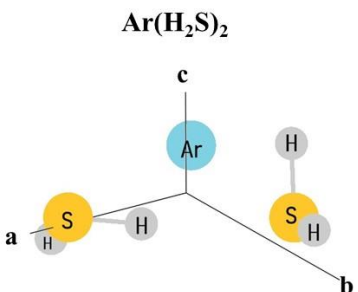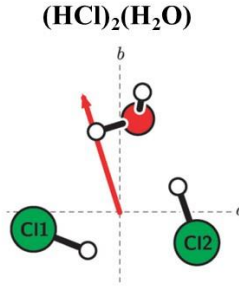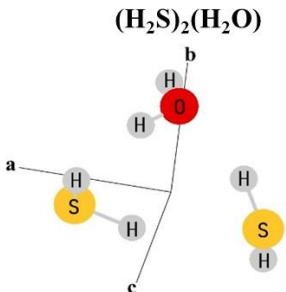
Figure 4.1. Ab-initio structures of (H$_2$O)$_3$, (H$_2$S)$_3$, (H$_2$S)$_2$(H$_2$O) with principal axes.

Table 4.1. Dipole moment components of $(H_2O)_3$, $(H_2S)_3$, and $(H_2S)_2(H_2O)$.

	$|\mu_a|$/D	$|\mu_b|$/D	$|\mu_c|$/D	Effective dipole
$(H_2O)_3$	0.007	0.120	1.116	Zero
$(H_2S)_3$	0.020	0.035	0.753	Zero
$(H_2S)_2(H_2O)$	1.331	1.067	0.390	Non-Zero

Table 4.2. Rotational constants with the principal axes for $Ar(H_2S)_2$, $(HCl)_2(H_2O)$ and $(H_2S)_2(H_2O)$.

$Ar(H_2S)_2$

Mandal, P. K., et al. (2013). *Journal of the Indian Institute of Science, 85*(6), 353.

$(HCl)_2(H_2O)$

Kisiel, H., et al. (2011). *Physical Chemistry Chemical Physics, 13*(31), 13912-13919.

$(H_2S)_2(H_2O)$

Current Study

Rotational Constants	$Ar(H_2S)_2$	$(H^{35}Cl)_2(H_2^{16}O)$	$(H_2^{32}S)_2(H_2^{16}O)$
A	1810.410(6)	4719.3194(4)	4346.6556
B	1596.199(9)	2066.4883(3)	1767.3302
C	844.814(2)	1435.0378(2)	1279.8416

The experimental rotational constants for the lower state of $Ar(H_2S)_2$ and the strong state of $(HCl)_2(H_2O)$ are given here. Theoretical rotational constants are computed at B3LYP/6-311G++g(2d,2p) for $(H_2S)_2(H_2O)$.

Recent neon matrix isolation experiment by Tremblay et al.[13] identifies $(H_2S)_2(H_2O)$ complex. For $(H_2S)_2(H_2O)$, the band observed at 2567.4 cm^{-1} is correlated with proton donor (PD) vibrations in the $(H_2S)_2$ perturbed by H_2O (see Table 4.3). The PD vibration for $(H_2S)_2$ in the neon matrix is 2596.5 cm^{-1}. Wategaonkar and coworkers[14] found the PD vibration frequency of $(H_2S)_2$ 2590 cm^{-1} in the gas phase. In the gas phase, the symmetric (v_1) and antisymmetric (v_3) modes of the H_2S monomer are known to appear at 2614 and 2628 cm^{-1} respectively[15,16,17]. In the neon matrix, two stretching modes v_1 and v_3 for the H_2S monomer were not observed, so gas-phase values were used to calculate the shifts. The H-bonded S-H stretch in the $(H_2S)_2$ is thus red-shifted by 31 cm^{-1} with respect to the central frequency of the v_1 and v_3 modes of the H_2S monomer[14] (discussed in Chapter 3, section 3.1). Similarly, in the $(H_2S)_2(H_2O)$ complex, the H-bonded S-H stretch for the S-H$\cdots$S interaction is red shifted by 53.6 cm^{-1}.

Table 4.3. Frequency shifts for $(H_2S)_2$ and $(H_2S)_2(H_2O)$ complex. Values are in cm^{-1}.

	H_2S $(v_1 + v_3)/2$	$(H_2S)_2$ $v_{S-H}{}^b$	Δv	$(H_2S)_2(H_2O)$ $v_{S-H}{}^b$ (For S-H$\cdots$S bond)	Δv
Calculated	2783	2730	53	2692	91
Gas Phase[14]	2621.0	2590	31	-	-
Neon Matrix[13]	-	2596.5	24.5	2567.4	53.6

4.2 Experimental Details

The spectrum of the parent complex was recorded in the 6.5–18.5 GHz region with the chirped-pulse Fourier transform microwave spectrometer (*CP-FTMW*) at Newcastle University, UK, in the configuration described in detail elsewhere[18,19]. The procedure for recording broadband microwave spectra was as follows. First, the sample was polarised using a microwave chirp that sweeps from 6.5 to 18.5 GHz in 1 μs. Secondly, the free induction decay (FID) of the molecular emission following the polarisation was recorded over a time period of 20 μs. During the expansion of each gas pulse, this sequence was repeated eight times. The FID was mixed down with the signal from a 19

GHz local oscillator and then digitised using a 100 GS/s digital oscilloscope. The Fourier transform used herein employed a high-resolution window function, resulting in line widths of transitions in the frequency domain spectrum of approximately 100 kHz at FWHM. This line width corresponds to an estimated accuracy of 10 kHz in measuring line centre frequencies. The spectra used for most of the analysis were obtained by averaging over 1 million free-induction decays. The H_2S cylinder from Sigma Aldrich was used for the experiment. A small sample of H_2S gas is introduced in the sample tank; the remaining portion is filled with argon, maintained at a constant pressure of 2 bar. For water, a bespoke reservoir was used. The reservoir was placed after the nozzle. The reservoir typically contained a small quantity of water, ~ 0.2 mL, to seed the molecular beam with water. A block was used throughout the experiment to improve efficiency. Also, the block allows a small amount of water to enter the beam, which facilities the $(H_2S)_2(H_2O)$ formation.

The spectra for the isotopologues were obtained in the Indian Institute of Science, Bangalore, with the help of the Balle-Flygare Fourier transform microwave spectrometer (*BF-FTMW*)[20]. A mixture of 3% H_2S in Ar carrier gas was expanded from back pressure of 0.7 atm into an evacuated Fabry-Perot cavity[21]. The H_2S cylinder is bought from Chemix gases, Bangalore. The isotopes ($H_2^{18}O$, D_2O) used in the experiment were bought from Cambridge Isotope Laboratory Inc. The ^{34}S signals have been obtained in the natural abundance (4%). In the experiment, we have obtained the *a* and *b* dipole transitions. The optimum pulse width for *a*- and *b*-dipole transitions are found to be 0.3 µs and 0.8 µs, respectively.

4.3 Results and Discussion

4.3.1 Rotational Spectra and Fitted Spectroscopic Constants

As mentioned in the experimental section, the rotational spectrum for the parent molecule was recorded in Newcastle using a chirped-pulse Fourier transform microwave spectrometer (*CP-FTMW*). Two states were observed for the parent species. A total of 35 and 24 transitions for the strong state and weak state have been fitted independently using the Watson S Hamiltonian and SPFIT program of Pickett[22]. For

the parent species, rotational transitions with quantum numbers ranging from 0 to 6 for J and 0 to 3 for K_a were obtained. Figure 4.2 depicts a portion of the chirped-pulse spectra with assigned transitions. The bottom panel shows the magnification of a-dipole 3_{03}-2_{02} and b-dipole 3_{13}-2_{02} transitions. Transitions of $(H_2O)_2$, $(H_2S)_2$, and H_2O-H_2S complexes dominate the raw chirped-pulse spectra.

The $(H_2O)_2$ and $(H_2S)_2$ lines are 100 and ten times stronger, respectively than the $(H_2S)_2(H_2O)$ complex. In the $(H_2S)_2(H_2O)$ complex, the a-dipole transitions are relatively stronger than the b-dipole transitions. Most of the assigned transitions were R-type. The key characteristic that distinguishes the $(H_2S)_2(H_2O)$ transitions is the two-splitting pattern with a roughly 1:3 intensity. This feature was not surprising because it is typical of the existence of a clustered water molecule in an environment with minimal barriers to reorientation motions. The intermolecular potential of such clusters has two energetically equivalent minima. The cluster between these minima can be interconverted using a combination of inversion and tunnelling movements while the water hydrogen atoms are switched. As a result of the occurrence of two equivalent minima, the lowest vibrational energy levels take the form of a doublet. The relative intensities of rotational transitions in these states are governed by nuclear spin statistical weights from exchanging hydrogen atoms. The Fermi–Dirac statistics are applicable to H_2O. The corresponding weight of symmetric and antisymmetric wavefunctions are 3 and 1, respectively. The ground rotational state is symmetric, and it needs anti-symmetric spin state to ensure that the total wave function is anti-symmetric to exchange of the two H atoms. As a consequence, the state with the weakest transitions is the actual ground state. Similar spectra were found for ^{34}S isotopologues as well. The Bose-Einstein statistics are applied to a clustered D_2O, resulting in relative intensities of 2 : 1 in favour of the ground state. Only one state of HDO was observed. We haven't found any evidence of tunnelling dynamics caused by H_2S molecules. In the $(H_2S)_2$, two states were seen, which were most likely quenched in the $(H_2S)_2(H_2O)$ complex. We used the abbreviations W and S for weak and strong.
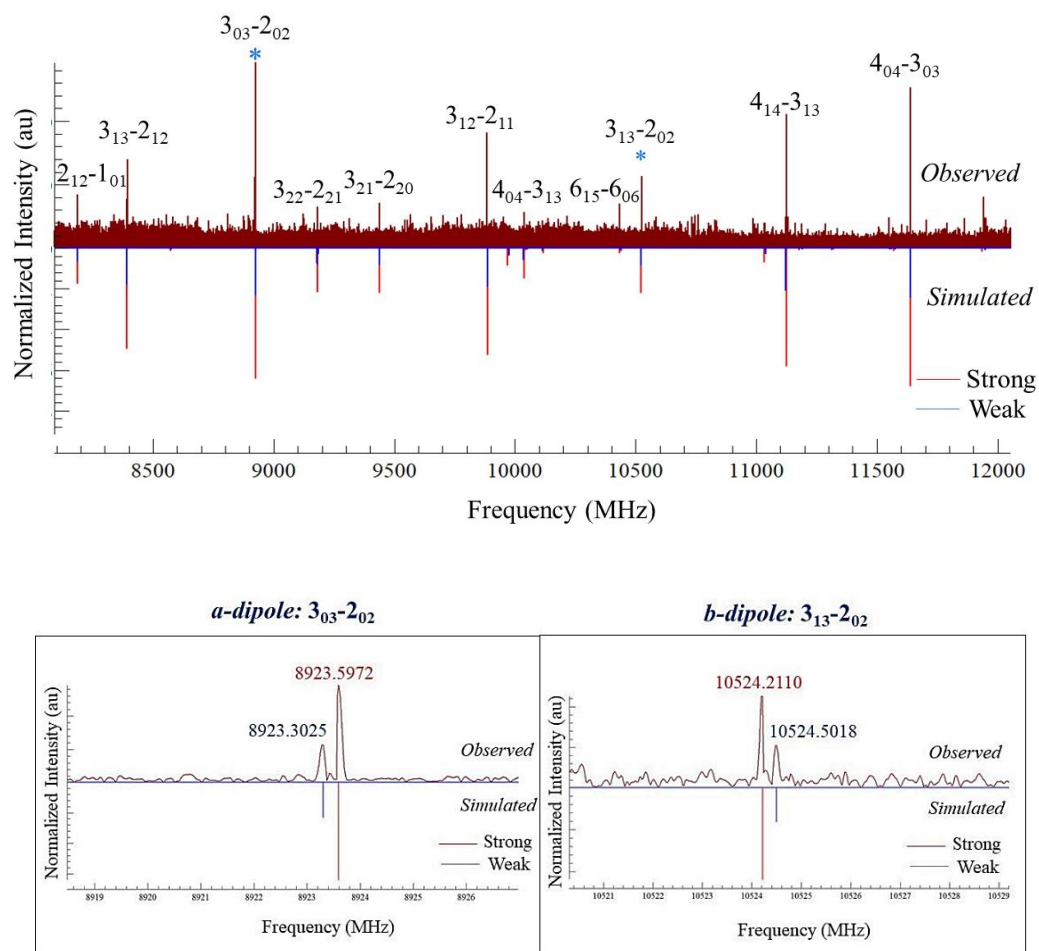
Figure 4.2. A portion of the spectrum for $(H_2S)_2(H_2O)$ is displayed. The spectrum was recorded in the argon carrier gas. A magnified version of the $3_{03}\text{-}2_{02}$ and $3_{13}\text{-}2_{02}$ transitions are shown in the bottom panel, which clearly indicates two states.
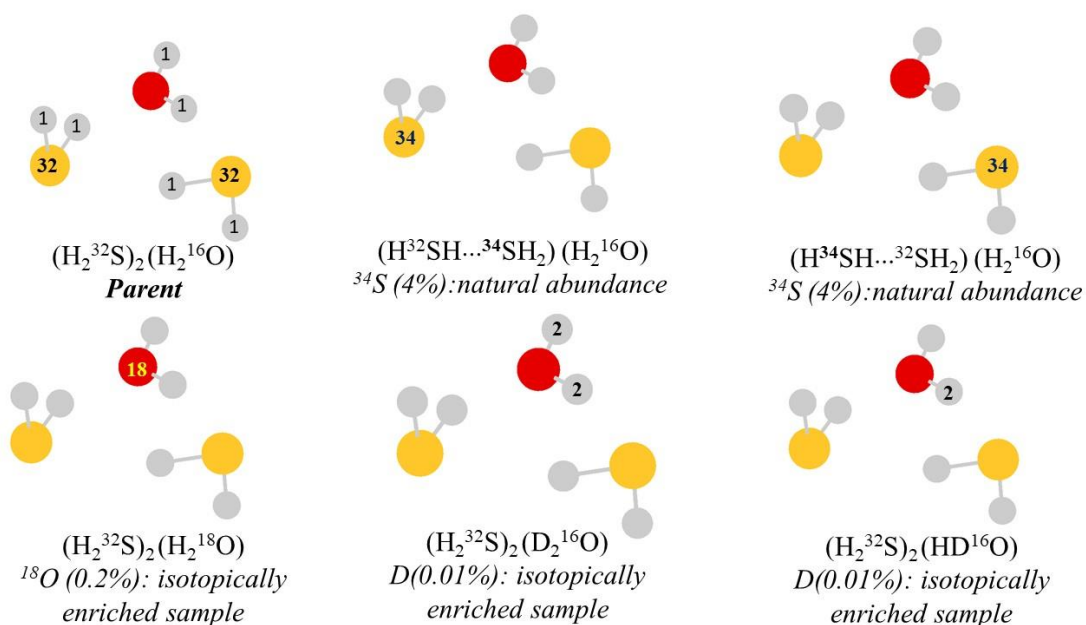
Figure 4.3. Parent and isotopologues observed in this study for (H₂S)₂(H₂O) complex. The chirped-pulse Fourier transform microwave spectrometer (CP-FTMW) was used to get the spectra of the parent species. The Balle-Flygare Fourier transform microwave spectrometer (BF-FTMW) was used to obtain its isotopologues.

Figure 4.3 depicts all the isotopologues observed in this study. Table 4.4 to Table 4.15 contain the entire sets of observed transitions and fits for the parent and its isotopologues. Table 4.16 also includes combined spectroscopic parameters from the fit. All the transitions could be fitted within the experimental accuracy.

Table 4.4. Fitted rotational transitions for the parent species of $(H_2{}^{32}S)_2(H_2{}^{16}O)$.

J' Kₐ' Kc'	J" Kₐ" Kc"	Dipole	Frequency (MHz) (S)	Residual (MHz)	Frequency (MHz) (W)	Residual (MHz)
1 1 1	0 0 0	b	5624.6871	0.0002	5625.5713	-0.0105
2 0 2	1 0 1	a	6055.1043	-0.0017	6055.0254	-0.0023
2 1 1	1 1 0	a	6620.2883	-0.0081	6620.3579	0.0007
3 0 3	2 1 2	b	6792.5931	0.0033	-	-
2 2 0	2 1 1	b	7749.9311	-0.0076	-	-
2 1 2	1 0 1	b	8186.1093	-0.0018	-	-
3 1 3	2 1 2	a	8393.2075	-0.0014	8392.7148	0.0090
3 0 3	2 0 2	a	8923.5972	0.0023	8923.3025	-0.0012
3 2 2	2 2 1	a	9181.2725	0.0012	-	-
3 2 1	2 2 0	a	9438.4822	-0.0007		
3 1 2	2 1 1	a	9884.7564	-0.0043	9884.8260	0.0027
4 0 4	3 1 3	b	10037.8490	0.0013	-	-
6 1 5	6 0 6	b	10434.1021	0.0018	10441.0730	0.0031
3 1 3	2 0 2	b	10524.2110	-0.0029	10524.5081	0.0030
4 1 4	3 1 3	a	11124.1623	0.0022	11123.1910	-0.0030
4 0 4	3 0 3	a	11638.4710	0.0042	11637.7846	-0.0024
4 1 4	3 0 3	b	12724.7775	-0.0017	12724.3899	0.0008
4 2 2	3 2 1	a	12789.7708	-0.0019	12789.6953	-0.0042
4 1 3	3 1 2	a	13087.6370	0.0074	13087.7853	-0.0003
5 0 5	4 1 4	b	13140.6947	-0.0003	-	-
5 1 5	4 1 4	a	13814.3997	-0.0013	13812.9826	-0.0016
5 0 5	4 0 4	a	14227.0041	-0.0032	14225.8734	0.0040
2 2 0	1 1 1	b	14869.1810	0.0013	-	-
5 1 5	4 0 4	b	14900.7168	0.0034	-	-
5 2 4	4 2 3	a	15153.0777	-0.0069	15153.0008	0.0014
5 3 3	4 3 2	a	15477.9763	0.0009	-	-
5 3 2	4 3 1	a	15590.6786	-0.0017	-	-

Continued Table 4.4…

6 0 6	5 1 5	b	16081.4390	-0.0041	16080.1327	-0.0019
5 1 4	4 1 3	a	16197.8290	-0.0020	16198.3965	-0.0003
5 2 3	4 2 2	a	16224.4149	0.0000	16224.9316	-0.0017
6 1 6	5 1 5	a	16470.6520	-0.0005	16469.1655	0.0017
6 0 6	5 0 5	a	16755.1576	0.0024	16753.8492	0.0008
3 2 2	2 1 1	b	16865.0840	0.0064	16869.8036	0.0000
6 1 6	5 0 5	b	17144.3631	0.0045	17142.8817	0.0041
6 2 5	5 2 4	a	18069.9798	0.0005	18070.6723	-0.0046

Table 4.5. Fitted rotational constants (strong & weak state) of $(H_2{}^{32}S)_2(H_2{}^{16}O)$.

Constants	S	W
A/MHz	4344.342(3)	4345.102(4)
B/MHz	1779.9860(8)	1780.030(1)
C/MHz	1281.053(1)	1281.021(1)
D_J/kHz	33.17(3)	36.99(4)
D_K/kHz	664.7(5)	486.4(8)
D_{JK}/kHz	-45.3(1)	-50.1(1)
d_1/kHz	1.50(1)	3.03(1)
d_2/kHz	2.153(6)	2.011(6)
H_J/kHz	0.5674(5)	0.6429(6)
N	34	24
RMS/kHz	4.1	4.7

Table 4.6. Fitted rotational transitions (strong & weak state) of $(H^{32}SH \cdots ^{34}SH_2)(H_2O)$ isotopologue.

J' K_a' K_c'	J'' K_a'' K_c''	Dipole	Frequency (MHz) (S)	Residual (MHz)	Frequency (MHz) (W)	Residual (MHz)
2 0 2	1 0 1	a	5904.7351	0.0053	5904.7702	-0.0050
2 1 1	1 1 0	a	6441.3573	-0.0035	6441.1644	0.0105
5 1 4	5 0 5	b	7755.8836	-0.0021	7750.6456	-0.0011
2 2 0	2 1 1	b	7831.6432	0.0001	7833.3808	-0.0001
3 1 3	2 1 2	a	8194.7755	-0.0002	8194.8792	0.0007
3 0 3	2 0 2	a	8711.3238	0.0073	8711.5005	-0.0037
3 1 2	2 1 1	a	9620.4849	-0.0002	9619.9496	-0.0051
6 1 5	6 0 6	b	10081.0370	0.0008	10070.4791	0.0000
3 1 3	2 0 2	b	10369.9701	0.0031	10370.5393	-0.0019
4 1 4	3 1 3	a	10861.8607	-0.0085	10862.5267	-0.0029
4 0 4	3 0 3	a	11372.6289	0.0020	11373.2907	0.0066
4 1 4	3 0 3	b	12520.5070	-0.0127	12521.5656	-0.0011
4 1 3	3 1 2	a	12742.7812	0.0037	12741.7596	0.0042
5 0 5	4 1 4	b	12758.0840	-0.0005	12759.3900	-0.0091
5 0 5	4 0 4	a	13905.9721	-0.0053	13907.6949	0.0132
5 1 5	4 0 4	b	14633.5916	0.0115	14635.7010	-0.0058

Table 4.7. Fitted rotational constants (strong & weak state) of $(H^{32}SH \cdots ^{34}SH_2)(H_2O)$ isotopologue.

Constants	S	W
A/MHz	4321.18(2)	4321.89(2)
B/MHz	1729.500(4)	1729.548(4)
C/MHz	1253.313(6)	1253.281(2)
D_J/kHZ	32.66(4)	32.75(4)
D_K/kHz	288.3(3)	258.7(3)
D_{JK}/kHz	-77.0(7)	-30.9(8)
d_1/kHz	8.91(7)	4.81(7)
d_2/kHz	1.4(1)	0.9(1)
N	16	16
RMS/kHz	8.1	8.2

Table 4.8. Fitted rotational transitions (strong & weak state) of ($H^{34}SH \cdots ^{32}SH_2$)($H_2O$) isotopologue.

J' K_a' K_c'	J'' K_a'' K_c''	Dipole	Frequency (MHz) (S)	Residual (MHz)	Frequency (MHz) (W)	Residual (MHz)
2 0 2	1 0 1	a	5909.3406	0.0017	5909.3716	0.0033
2 1 1	1 1 0	a	6448.1455	-0.0002	6448.1156	0.0023
2 2 0	2 1 1	b	7812.3663	0.0000	7816.6781	0.0000
5 1 4	5 0 5	b	7771.0365	-0.0008	7765.5712	-0.0034
3 1 3	2 1 2	a	8199.3700	-0.0021	8199.8859	-0.0015
3 0 3	2 0 2	a	8716.9813	0.0028	8717.2131	0.0026
3 1 2	2 1 1	a	9630.1893	0.0004	9629.8446	0.0004
6 1 5	6 0 6	b	10102.7272	0.0002	10090.7877	0.0008
3 1 3	2 0 2	b	10366.7498	-0.0014	10368.2621	0.0028
4 1 4	3 1 3	a	10867.7698	-0.0012	10869.0816	-0.0040
4 0 4	3 0 3	a	11378.4762	0.0035	11379.4200	-0.0106
4 1 4	3 0 3	b	12517.5383	-0.0054	12520.1306	-0.0038
4 1 3	3 1 2	a	12754.7572	0.0017	12753.9005	0.0063
5 0 5	4 1 4	b	12772.8495	-0.0075	12773.7794	-0.0035
5 0 5	4 0 4	a	13911.9362	0.0082	13914.4950	0.0084

Table 4.9. Fitted rotational constants (strong & weak state) of ($H^{34}SH \cdots ^{32}SH_2$)($H_2O$) isotopologue.

Constants	S	W
A/MHz	4317.12(1)	4317.86(1)
B/MHz	1731.722(3)	1731.762(3)
C/MHz	1253.673(2)	1253.643(2)
D_J/kHZ	32.02(3)	32.98(3)
D_K/kHz	299.6(2)	183.(2)
D_{JK}/kHz	-26.8(5)	-44.1(7)
d_1/kHz	7.00(5)	2.00(6)
d_2/kHz	1.01(7)	1.03(9)
N	15	15
RMS/kHz	5.2	6.7

Table 4.10. Fitted rotational transitions (strong & weak state) of the $(H_2{}^{32}S)(H_2{}^{32}S)(H_2{}^{18}O)$ isotopologue.

$J'\,K_a'\,K_c'$	$J''\,K_a''\,K_c''$	Dipole	Frequency (MHz) (S)	Residual (MHz)	Frequency (MHz) (W)	Residual (MHz)
2 0 2	1 0 1	*a*	5977.7613	-0.0007	5977.7440	-0.0078
2 1 1	1 1 0	*a*	6589.2724	-0.0001	6589.2668	-0.0029
2 2 0	2 1 1	*b*	6795.5834	0.0000	6797.1530	0.0000
3 1 3	2 1 2	*a*	8247.9310	0.0028	8247.9281	0.0008
3 0 3	2 0 2	*a*	8769.7292	0.0001	8769.7243	0.0122
3 1 2	2 1 1	*a*	9825.5445	-0.0003	9825.4154	0.0067
6 1 5	6 0 6	*b*	10711.0494	0.0001	10716.9052	0.0002
3 1 3	2 0 2	*b*	10042.0767	0.0062	10042.7752	-0.0011
4 1 4	3 1 3	*a*	10913.1996	0.0014	10913.0829	-0.0056
4 0 4	3 0 3	*a*	11384.0884	0.0010	11384.0533	0.0072
4 1 4	3 0 3	*b*	12185.5272	-0.0123	12186.1438	-0.0089
4 1 3	3 1 2	*a*	12979.6254	-0.0004	12979.5073	-0.0043
5 0 5	4 1 4	*b*	13069.5591	-0.0066	13068.5679	-0.0108
5 0 5	4 0 4	*a*	13871.0279	0.0100	13870.6985	0.0133

Table 4.11. Fitted rotational constants (strong & weak state) of $(H_2{}^{32}S)(H_2{}^{32}S)(H_2{}^{18}O)$ isotopologue.

Constants	S	W
A/MHz	4019.450(9)	4020.20(1)
B/MHz	1779.537(3)	1779.579(4)
C/MHz	1251.364(2)	1251.335(3)
D_J/kHz	33.05(4)	34.54(6)
D_K/kHz	509. (2)	547(2)
D_{JK}/kHz	-31.2(6)	-37.0(8)
d_1/kHz	7.18(6)	4.90(9)
d2/kHz	8.24(8)	1.0(1)
N	15	15
RMS/kHz	7.1	10.3

Results and Discussion

Table 4.12. Fitted Rotational transitions (strong & weak state) of $(H_2{}^{32}S)(H_2{}^{32}S)(D_2O)$ isotopologue.

J' K_a' K_c'	J" K_a" K_c"	Dipole	Frequency (MHz) (S)	Residual (MHz)	Frequency (MHz) (W)	Residual (MHz)
2 0 2	1 0 1	a	5952.3066	-0.050	5952.3557	-0.0001
5 1 4	5 0 5	b	8117.3453	0.0039	8120.4018	-0.0050
3 1 3	2 1 2	a	8212.7549	-0.0019	8212.7446	-0.0024
3 0 3	2 0 2	a	8728.0041	0.0028	8728.0799	-0.0031
3 1 2	2 1 1	a	9789.1569	-0.0097	9789.5070	0.0153
3 1 3	2 0 2	b	9944.7766	-0.0011	9944.9648	0.0012
4 1 4	3 1 3	a	10866.9499	0.0074	10866.7755	-0.0065
4 0 4	3 0 3	a	11326.2025	0.0086	11326.1713	-0.0051
4 1 4	3 0 3	b	12083.7223	0.0033	12083.6604	-0.0022
4 1 3	3 1 2	a	12928.3760	0.0010	12929.1335	-0.0026
5 0 5	4 1 4	b	13044.1062	0.0057	13043.7267	-0.0025
5 0 5	4 0 4	a	13801.6160	-0.0096	13801.2157	0.0003
5 1 5	4 0 4	a	14228.2684	0.0018	14227.6979	0.0008
5 1 4	4 1 3	a	15937.9399	-0.0058	15939.3402	0.0073

Table 4.13. Fitted rotational constants (strong & weak state) of the $(H_2{}^{32}S)(H_2{}^{32}S)(D_2O)$ isotopologue.

Constants	S	W
A/MHz	3949.45(9)	3949.63(9)
B/MHz	1773.876(5)	1773.862(5)
C/MHz	1245.232(2)	1245.246(2)
D_J/kHz	23.1(3)	21.8(3)
D_K/kHz	251.(82)	236.(79)
D_{JK}/kHz	-6.(3)	-11.(3)
d_1/kHz	-3.8(1)	-2.0(1)
d_2/kHz	-1.5(3)	-2.4(3)
N	15	15
RMS/kHz	8.0	7.8

Table 4.14. Fitted Rotational transitions of the $(H_2^{32}S)(H_2^{32}S)(HDO)$ isotopologue.

J' K_a' K_c'	J" K_a" K_c"	Dipole	Frequency (MHz) (S)	Residual (MHz)
1 1 1	0 0 0	*a*	5532.4436	-0.0012
2 0 2	1 0 1	*a*	6029.9399	0.0006
5 1 4	5 0 5	*b*	7956.1451	-0.0002
3 1 3	2 1 2	*a*	8356.4962	0.0024
3 0 3	2 0 2	*a*	8881.2703	0.0008
3 1 2	2 1 1	*a*	9849.5170	-0.0017
6 1 5	6 0 6	*b*	10374.1234	0.0002
3 1 3	2 0 2	*b*	10407.9466	0.0056
4 1 4	3 1 3	*a*	11073.4172	-0.0054
4 0 4	3 0 3	*a*	11576.0345	-0.0036
4 1 4	3 0 3	*b*	12600.0935	-0.0007
4 1 3	3 1 2	*a*	13035.1525	0.0003
5 0 5	4 1 4	*b*	13119.6702	0.0112
5 0 5	4 0 4	*a*	14143.6992	-0.0159
2 2 0	1 1 1	*b*	14614.6974	0.0000
5 1 5	4 0 4	*a*	14770.7807	0.0080

Table 4.15. Fitted rotational constants of $(H_2^{32}S)(H_2^{32}S)(HDO)$.

Constants	One state
A/MHz	4258.00(1)
B/MHz	1774.869(5)
C/MHz	1274.590(2)
D_J/kHz	24.27(6)
D_K/kHz	163.5(2)
D_JK/kHz	-39.2(5)
d_1/kHz	-8.89(8)
d_2/kHz	1.04(1)
N	16
RMS/kHz	8.1

Table 4.16. Fitted rotational constants and distortion constants for all the parent and isotopologues of $(H_2S)_2(H_2O)$.

	$(H_2{}^{32}S)_2(H_2{}^{16}O)$		$(H^{32}SH\cdots^{34}SH_2)(H_2{}^{16}O)$		$(H^{34}SH\cdots^{32}SH_2)(H_2{}^{16}O)$		$(H_2{}^{32}S)_2(H_2{}^{18}O)$		$(H_2{}^{32}S)_2(D_2O)$		$(H^{32}S)_2HDO$
	W	S	W	S	W	S	W	S	W	S	-
A/MHz	4345.102(4)	4344.342(2)	4321.89(2)	4321.18(2)	4317.86(1)	4317.12(1)	4020.20(1)	4019.450(9)	3949.63(9)	3949.45(9)	4258.00(1)
B/MHz	1780.030(1)	1779.9859(7)	1729.548(4)	1729.500(4)	1731.762(3)	1731.722(3)	1779.579(4)	1779.537(3)	1773.862(5)	1773.876(5)	1774.869(5)
C/MHz	1281.021(1)	1281.0533(9)	1253.281(2)	1253.313(6)	1253.643(2)	1253.673(2)	1251.335(3)	1251.364(2)	1245.246(2)	1245.232(2)	1274.590(2)
D_J/kHz	36.99(4)	33.17(3)	32.75(4)	32.66(4)	32.98(3)	32.02(3)	34.54(6)	33.05(4)	21.8(3)	23.1(3)	24.27(5)
D_K/kHz	486.4(8)	664.7(5)	258.7(3)	288.3(3)	183.(2)	299.6(2)	547(2)	509.(2)	236.(79)	251.(82)	163.(2)
D_{JK}/kHz	-50.1(1)	-45.21(4)	-30.9(8)	-77.0(7)	-44.1(7)	-26.8(5)	-37.0(8)	-31.2(6)	-11.(3)	-6.(3)	-39.2(6)
d_1/kHz	3.03(1)	1.497(9)	4.81(7)	8.91(7)	2.00(6)	7.00(5)	4.90(9)	7.18(6)	-2.0(1)	-3.8(1)	-8.89(8)
d_2/kHz	2.011(6)	2.153(4)	0.9(1)	1.4(1)	1.03(9)	1.01(7)	1.0(1)	8.24(8)	-2.4(3)	-1.5(3)	1.04(1)
H_1/kHz	0.6429(6)	0.5674(4)									
N_{lines}	24	35	16	16	15	15	15	15	15	15	16
σ_{fit}/kHz	4.7	4.1	8.2	8.1	6.7	5.2	10.3	7.1	7.8	8.0	8.1

4.3.2   **Comparison with Theory and Experiment**

Ab initio and DFT quantum chemical calculations were utilised to optimise the structure of the $(H_2S)_2(H_2O)$ complex. Table 4.17 displays the optimised rotational constants derived from these computations. Harmonic frequency calculations revealed that the cyclic structure is the minimum in the potential energy surface. Three different basis sets are used in the calculations: 6-311++g(2d,2p), aug-cc-pVDZ, and aug-cc-pVTZ with DFT and MP2 methods. All the calculations are performed using *opt=tight* and *freq=vibrot* keywords using Gaussian 09, Revision D.01[23]. The rotational constants calculated with the DFT method are in excellent agreement with the experimental ones.

Table 4.17. Rotational constants calculated from different theory and basis sets.

Methods	*A*	*B*	*C*
DFT			
B3LYP//6-311++g(2d,2p)	4346.6556	1767.3302	1279.8416
B3LYP//aug-cc-pVDZ	4338.8490	1777.5616	1284.1678
B3LYP//aug-cc-pVTZ	4309.7504	1746.5266	1265.3998
MP2			
MP2/6-311++g(2d,2p)	4438.2985	1827.2779	1317.9229
MP2//aug-cc-pVDZ	4342.5525	1859.2728	1325.9713
MP2//aug-cc-pVTZ	4411.5731	1882.9670	1344.1264
Experiment			
Weak State	4345.102(4)	1780.030(1)	1281.021(1)
Strong State	4344.342(2)	1779.9859(7)	1281.0533(9)

opt=tight and freq=vibrot keywords have been used for optimisation and frequency calculations.

Results and Discussion

In weakly bound complexes, the discrepancy between theory and experiment occurs more frequently in distortion constants, as the large amplitude intermolecular vibrations are not calculated accurately. We have estimated centrifugal distribution constants using the B3LYP and MP2 methods and compared them to the experiment. The distortion constants estimated from theory, D_J, D_K, and D_{JK}, are in sharp contrast to the experiment. The estimated distortion constants for $(H_2S)_2$ in Chapter 3 (section 3.3.2.4) are similarly lower than the experimental values. The D_J for $(H_2S)_2$ and $Ar(H_2S)_2$ were determined to be 15.227(11) and 20.4(4) kHz, respectively[2,9]. For $(H_2O)_2$, the experimental D_J is found to be 44(4) kHz[24]. The D_J for the ground vibrational state of $(H_2S)_2(H_2O)$ complex in the current investigation is 36.99(4) kHz. As mentioned previously, in weakly bound complexes, the discrepancy between theory and experiment occurs more frequently in distortion constants, as the large amplitude intermolecular vibrations are not calculated accurately.

Table 4.18. *Theoretical and experimental centrifugal distortion constants for* $(H_2S)_2(H_2O)$.

Distortion Constants	B3LYP// aug-cc-pVDZ	MP2// aug-cc-pVDZ	Weak State	Strong State
D_J/kHz	3.31	2.92	33.17(3)	36.99(4)
D_K/kHz	33.23	22.10	664.7(5)	486.4(8)
D_{JK}/kHz	-4.02	-0.478	-45.3(1)	-50.1(1)
d_1/kHz	-1.12	-0.746	1.50(1)	3.03(1)
d_2/kHz	-0.13	-0.110	2.153(6)	2.011(6)

4.3.3 **Rotational Constants of Isotopologues**

The rotational constants of six distinct isotopologues have been determined for $(H_2S)_2(H_2O)$. As stated in the preceding section, the computed rotational constants with the B3LYP functional match the experimental findings well. Furthermore, using the B3LYP/aug-cc-pVDZ level, we have calculated the rotational constants of the isotopologues. These computations assist us in assigning the appropriate isotopologues. The observed and computed rotational constants of all isotopologues of $(H_2S)_2(H_2O)$ are given in Table 4.19.

Table 4.19. Theoretical and experimental rotational constants of isotopologues $(H_2S)_2(H_2O)$.

#	Isotopologues		A/MHz	B/MHz	C/MHz
01	$(H_2{}^{32}S)_2(H_2{}^{16}O)$	Theory	4338.8490	1777.5616	1284.1678
		Expt.	4344.342(2)	1779.9859(7)	1281.0533(9)
02	$(H^{32}SH...^{34}SH_2)(H_2{}^{16}O)$	Theory	4316.3551	1726.9323	1255.6576
		Expt.	4321.18(2)	1729.500(4)	1253.313(6)
03	$(H^{34}SH...^{32}SH_2)(H_2{}^{16}O)$	Theory	4312.1430	1728.7053	1256.2397
		Expt.	4317.12(1)	1731.722(3)	1253.673(2)
04	$(H_2{}^{32}S)_2(H_2{}^{18}O)$	Theory	4017.2507	1777.4870	1254.4149
		Expt.	4019.450(9)	1779.537(3)	1251.364(2)
05	$(H_2{}^{32}S)_2(D_2{}^{16}O)$	Theory	3943.1887	1771.7722	1244.7533
		Expt.	3949.45(9)	1773.876(5)	1245.232(2)
06	$(H_2{}^{32}S)_2(HD^{16}O)$	Theory	4246.2554	1773.1482	1273.6595
		Expt.	4258.00(1)	1774.869(5)	1274.590(2)

4.3.4 **Structure**

The Kraitchman substitution (r_s) analysis[25] using the experimental rotational constants of the parent and the singly substituted isotopologues allows for the direct structural study of the complex. The labelling of the atoms in the $(H_2S)_2(H_2O)$ complex, along with the approximate locations of the principal axes, are shown in Figure 4.4. Using rotational constants (strong state) of the singly substituted isotopologues, we calculated the coordinates for S_1, S_2, O_3, and H_4 atoms (Table 4.20). It should be noted that coordinates with small values are associated with larger uncertainties. For example, the c- and a-coordinates of S_1 and O_3, respectively. The sign of the coordinates is not provided by Kraitchman's analysis. The appropriate signs are determined by comparing with computational results. The coordinates of the heavy atoms S_1, S_2, and O_3 are well known. Kraitchman's technique was generally inefficient at identifying the coordinate of lighter isotopes.
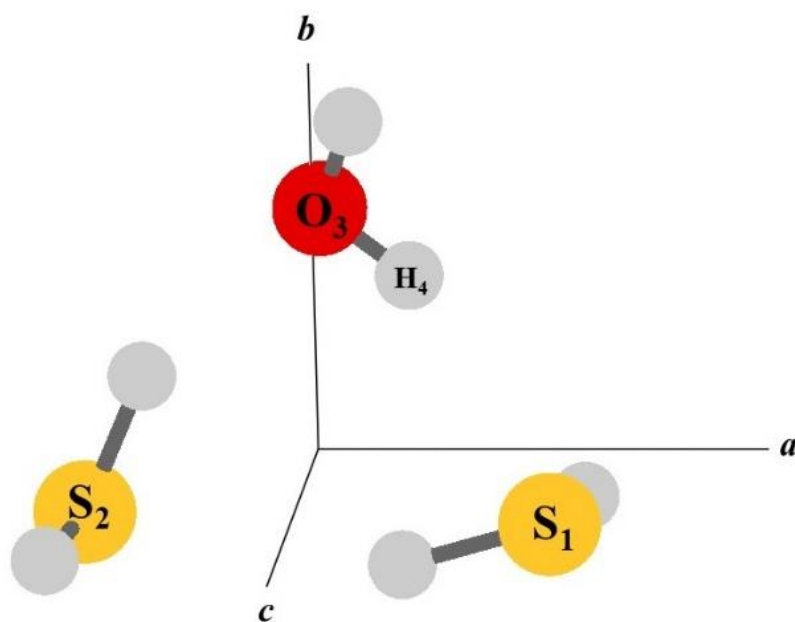
Figure 4.4. Labelling of the atoms used in Kraitchman's analysis. The approximate locations of the principal axes are shown in the figure. The c principal axis is perpendicular to the plane of the paper.

Table 4.20. The experimentally derived Kraitchman substitution coordinates for the S_1, S_2, O_3, and H_4. The values in parentheses denote the uncertainties associated with the coordinates. The calculated coordinates are at the B3LYP/aug-cc-pVDZ level.

Angstrom		*a*	*b(db)*	*c(dc)*
S_1	Calculated	2.017	-0.656	0.087
	Expt.	2.008(1)	0.621(2)	0.09(2)
S_2	Calculated	-2.066	-0.591	-0.083
	Expt.	2.047(1)	0.535(3)	0.218(7)
O_3	Calculated	0.063	2.149	-0.046
	Expt.	0.08(2)	2.184(1)	0.178(8)
H_4	Calculated	0.837	1.565	0.020
	Expt.	0.478(3)	1.332(1)	0.776(2)

More efficient use of the available rotational constants is to determine the ground state, r_0 structural coordinates. For this, the non-linear least-square fitting method STRFIT[26] was employed. To get the r_0 structure of the complex, the internal coordinates were directly fitted to the moments of inertia. Despite the fact that the structure is formally defined by 3N-6=18 coordinates, it was feasible to significantly lower this number by numerous simplifications. The H_2O and H_2S subunits were assumed to remain unchanged on complexation and were taken to be described by their r_0 parameters[27,28]. The theory suggests the H_4, H_5, and H_6 lie very near the $S_1S_2O_3$ plane. These atoms were all assumed to be coplanar with the heavy atoms initially. The six-independent set of rotational constants (of the strong state) for the six isotopes were used to derive structural parameters of $(H_2S)_2(H_2O)$ complex. No constraints were imposed during the fitting. The STRFIT was used to fit the parameters $r[S_2\text{-}O_3]$, $r[S_1\text{-}H_4]$, $\theta(S_1S_5O_3)$, $\theta(H_6S_2H_5)$, and $\theta(S_1H_4O_6)$. A reasonably good structural match was found, with a standard deviation of 0.250 amuÅ^2. The fitted parameters from substitution analysis (r_s) and STRFIT (r_0) and their deviations are shown in Table 4.21. Figure 4.5 illustrates the structural parameters of the $(H_2S)_2(H_2O)$ complex.

Results and Discussion

The S-S distance[2] in $(H_2S)_2$ was 4.113(1) Å. The $(H_2S)_2(H_2O)$ complex has an $r_s(S_1\text{-}S_2)$ distance of 4.067(2) Å, which is 0.046 Å smaller than the r_s(S-S) distance in $(H_2S)_2$. Theoretical calculations also suggested shortening the S-S distance. The experimental S-S distance in $Ar(H_2S)_2$ complex is found to be 4.053 Å from the lower state rotational constants[9]. The other two heavy atom distance $r_s(S_1\text{-}O_3)$ and $r_s(S_2\text{-}O_3)$ are 3.412 (11) Å and 3.454 (11) Å, respectively. A similar comparison for OH···S and SH···O heavy atom lengths in dimers and $(H_2S)_2(H_2O)$ complex cannot be done since experimental geometry data for HOH···SH_2 and HSH···OH_2 were unavailable. DFT computations revealed that the O-S distances in HOH···SH_2, and HSH···OH_2 dimers are 3.508 and 3.581 Å, respectively. The experimental O-S distances in $(H_2S)_2(H_2O)$ for O-H···S and S-H···O interactions are 3.412 (11) and 3.454 (11) Å, respectively. So, the DFT calculation suggests the contraction of $r(S_1\text{-}O_3)$ and $r(S_2\text{-}O_3)$ bond distances in the $(H_2S)_2(H_2O)$ complex, indicating a cooperative effect (see Figure 4.6).

STRFIT calculates the $r_0(S_2\text{-}O_3)$ distance as well; the r_0 and r_s values are quite close. The hydrogen bond distances for $r_s(S_1\text{-}H_4)$ and $r_0(S_1\text{-}H_4)$ are 2.573(5) and 2.496 (24) Å, respectively. The estimated B3LYP $r(S_1\text{-}H_4)$ hydrogen bond distance of 2.516 Å is in closer accord with the r_0 distance. The hydrogen bond length is significantly less than the sum of the van der Waals radii of sulphur and hydrogen, 3.0. Å[29]. Furthermore, $r_s(O_3\text{-}H_4)$ = 1.339(8) Å, which is significantly greater than the O-H distance in the free water molecule. There is no evidence from *ab initio* results for substantial lengthening (0.367 Å) of the $(O_3\text{-}H_4)$ bond on complexation, which must be due to ground state averaging across the anharmonic tunnelling potential. Due to large amplitude motion, the coordinates of the heavy atoms S_1, S_2, and O_3 should be altered far less than the atom H_4. Also, the $\theta_0(H_6S_2H_5)$ is found to be 56(5)°, whereas the DFT calculation suggests 75.6°. The hydrogen bond angle $\theta_0(S_1H_4O_6)$ is close to linearity, 168°. Overall, the comparison of the experimental geometries with the DFT geometries reveals remarkable agreement (Table 4.21).

Table 4.21: Fitted structural parameters obtained from r_s, r_0, and B3LYP/aug-cc-pVDZ for $(H_2S)_2(H_2O)$.

Parameters	Experimental		Theoretical
	r_s	r_0	B3LYP/ aug-cc-pVDZ
$r[S_1\text{-}S_2]$ Å	4.067(2)	-	4.088
$r[S_1\text{-}O_3]$ Å	3.412(11)	-	3.421
$r[S_2\text{-}O_3]$ Å	3.454(11)	3.482(25)	3.470
$r[S_1\text{-}H_4]$ Å	2.573(5)	2.496(24)	2.516
$r[O_3\text{-}H_4]$ Å	1.339(8)	-	0.972
$\theta(S_1S_2O_3)$ degree	53.2(2)	-	53.1
$\theta(S_1S_5O_3)$ degree	72.64(5)	72.95(7)	72.8
$\theta(S_2S_1O_3)$ degree	54.2(3)	-	54.2
$\theta(H_6S_2H_5)$ degree	-	56(5)	75.6
$\theta(S_1H_4O_6)$ degree	-	168(3)	155
σ /uÅ^2		0.250	
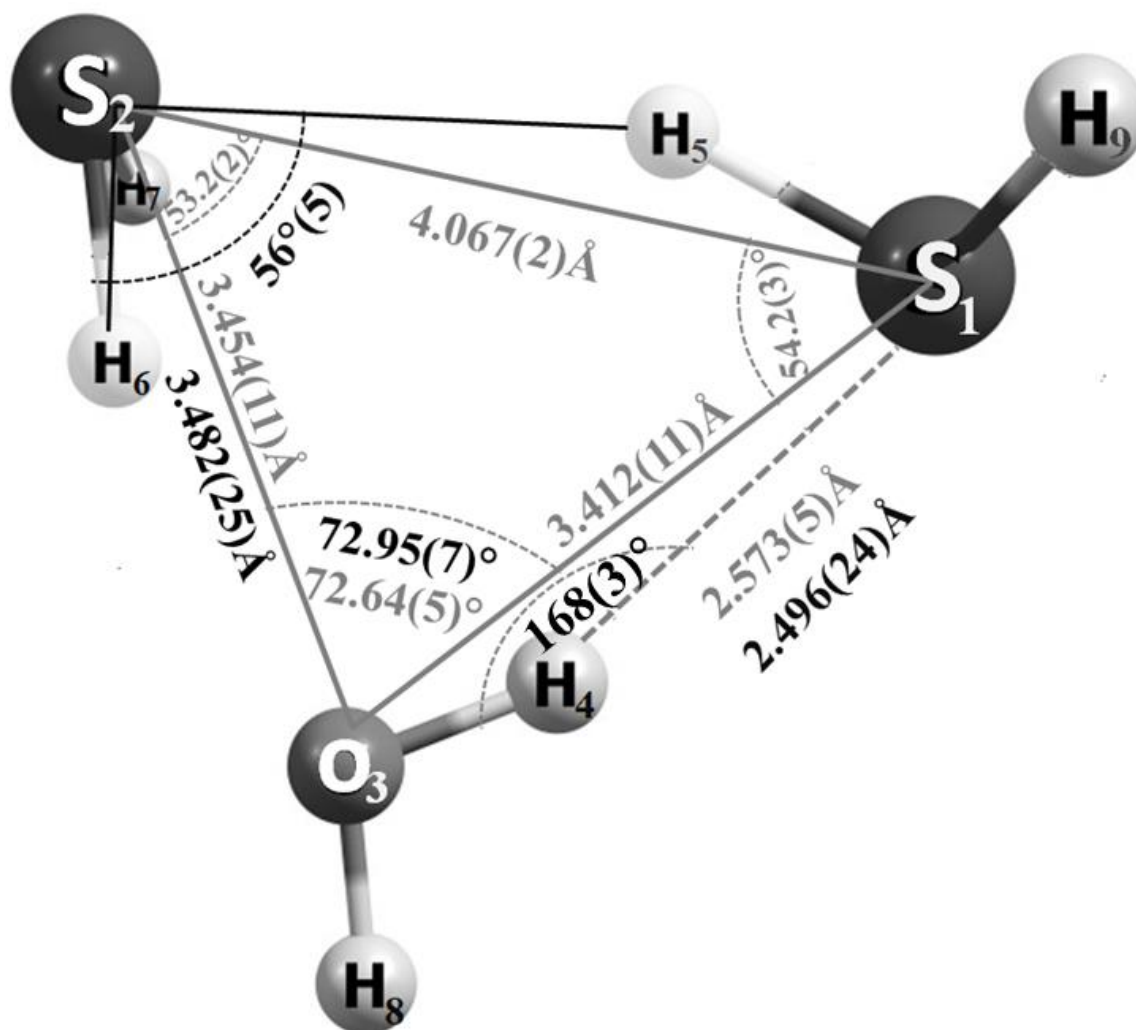
Figure 4.5. Structural parameters for (H2S)2(H2O) complex. The values in black are derived from the fitting of the r0 structure to the experimentally derived moments of inertia of all the isotopologues. The grey values are from substitution analysis (rs structure).
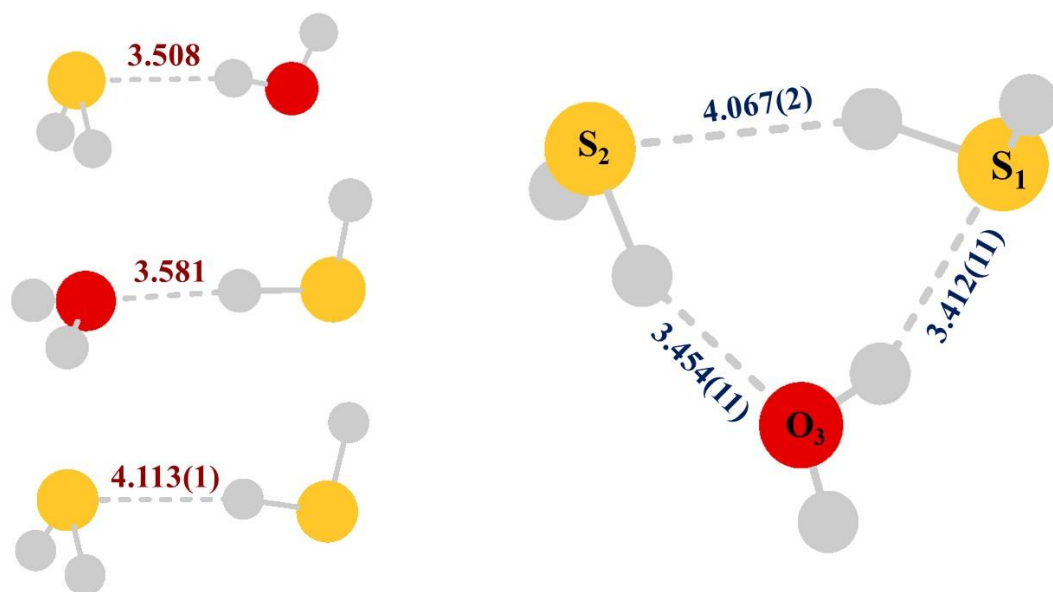
Figure 4.6. Heavy atom distances (in Å) in HSH···OH$_2$, HOH···SH$_2$, HSH···SH$_2$ and $(H_2S)_2(H_2O)$. The distances between heavy atoms decrease in the $(H_2S)_2H_2O$ complex, indicating hydrogen bonding cooperation. Values are in Å.

4.3.5 Inertial Defect

Inertial defect ($\Delta = I_c - I_b - I_a$) is an important parameter to understand the structure and dynamics of the complex. The inertial defects for all the isotopologues are significantly small. They do not change much with the substitutions, which obviously indicates that the structure is effectively planar with all the heavy atoms lying in the same plane. The inertial defects do not change at all by the $^{34}S_1$, $^{34}S_2$, ^{18}O substitution, which clearly tells that the two sulphur and oxygen atoms are lying in the *ab* inertial plane of the complex. However, the location of the two hydrogen atoms of H$_2$O may not be very precise. The inertial defect is found to be -6.93 μÅ^2 for $(H_2S)_2(HDO)$ (referred to as D in Table 4.22), despite the fact that the DFT value is identical to the parent. This difference can easily be attributed to the vibrational effects, especially where an atom as light as hydrogen is involved. The inertial defect of $(H_2S)_2(D_2O)$ (referred to as D$_2$ in Table 4.22) differs from that of the parent because the non-bonded hydrogen atom can shuttle in and out of the plane without encountering any significant barriers.

Table 4.22. Inertial defects for isotopologues of (H₂S)₂(H₂O). Values are in a.m.u.Å².

$\Delta(\mu\mathring{A}^2)$	*Parent*	$^{34}S_1$	$^{34}S_2$	^{18}O	*D*	D_2
Strong	-5.75	-5.78	-5.93	-5.87	-6.93	-7.01
Weak	-5.71	-5.74	-5.89	-5.83	-	-7.01
DFT(B3LYP)	-7.23	-7.23	-7.23	-7.23	-7.23	-7.37

4.3.6   Internal Motion of H₂O in (H₂S)₂(H₂O) Complex

Except for the (H₂S)₂(HDO), all isotopologues show a doubling of transition frequencies due to the large amplitude motion of the H₂O moiety. This type of doubling could be caused by the interchange of equivalent hydrogens in H₂O around its C₂ axis. It should be noted that none of these motions alters the *a*-and *b*-dipoles of the complex. Hence, it is expected that any of these motions would give rise to a semi-rigid rotor spectrum for the *a*-dipole and the *b*-dipole transitions, which can be fitted without the inclusion of any additional tunnelling splitting term in the Hamiltonian. In reality, as previously stated, both series can be fitted independently. Hence, we cannot measure the tunnelling splitting directly from the spectra. The quenching of the observed splitting in the (H₂S)₂(HDO) complex confirms that the splitting is caused by the H₂O rotating internally around its C₂ symmetry axis. In principle, water protons can be exchanged by rotating the water over a "low" barrier or tunnelling through a "high" barrier. The Ar-H₂O[30], Ar-HCN-H₂O[31] systems support a low barrier model for the interchange of the water protons. One argument is that the substitution with D₂O should significantly reduce the splitting between the two states for the high barrier model. The rotational constant differences are reported for the isotopologues are reported in Table 4.23. The magnitude of the splitting drops roughly four-fold when we go from (H₂S)₂(H₂O) to (H₂S)₂(D₂O). This indicates that in nature, the internal rotation of H₂O in (H₂S)₂(H₂O) is hindered. This is to be expected, given that the motion requires the breaking of the hydrogen bonds. The splitting, on the other hand, is unaffected by sulphur or oxygen atom substitutions.

Table 4.23. Experimentally derived differences in the rotational constants between the stronger and the weaker series for $(H_2S)_2(H_2O)$ and its isotopologues.

Difference in Rotational Constant	Parent	$^{34}S(1)$	$^{34}S(2)$	^{18}O	D_2
$\Delta|A|$/MHz	0.76	0.74	0.71	0.75	0.18
$\Delta|B|$/MHz	0.0441	0.040	0.048	0.041	0.014
$\Delta|C|$/MHz	0.0323	0.030	0.032	0.030	0.014

Figure 4.7 shows a potential energy curve (rigid scan) for H_2O rotation along the C_2 symmetry axis at the B3LYP/aug-cc-pVDZ level. The potential energy barrier at the MP2/aug-cc-pVDZ level of theory is 1501 cm^{-1}, which is far too large to impede the potential of this rotation. Based on frequency calculations, one mode has been identified at 505 cm^{-1} (ZPE = 253 cm^{-1}) associated to the rotation of H_2O on its C_2 symmetry axis. As a result, along this coordinate, the barrier height is nearly six times greater than the zero-point energy.
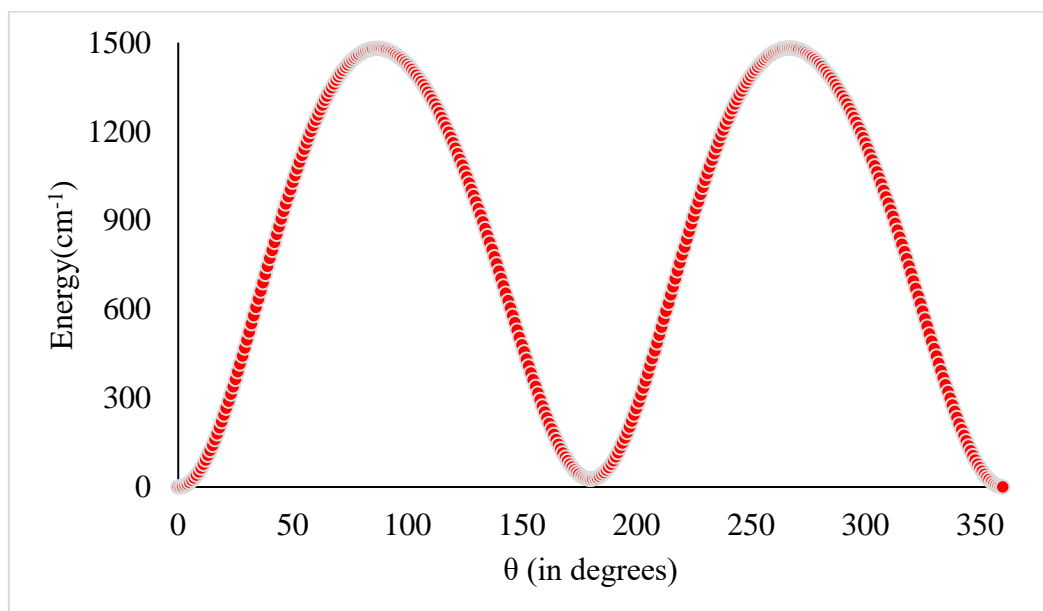
Figure 4.7. Barrier for C_2 rotation of water in the $(H_2S)_2(H_2O)$ complex. A rigid scan was performed at B3LYP/aug-cc-pVDZ level.

Results and Discussion

Table 4.24 shows the barrier for C_2 rotation of water for the different weakly bound complexes. The barrier and splitting magnitudes for phenylacetylene-water[32], propargyl alcohol-water[33], and $(H_2S)_2(H_2O)$ complexes are comparable. This is not surprising because a rotation of the H_2O molecule in these complexes would cause the hydrogen bonds to break. Since H_2O acts as a hydrogen bond acceptor in the Ar-HCN-H_2O[30] complex, rotation around the C_2 axis does not break the hydrogen bond, accounting for its low barrier.

Table 4.24. Barrier for C_2 rotation of water in weakly bound complexes.

Complexes	Method	Barrier (cm^{-1})
Phenylacetylene-Water[32]	MP2/aug-cc-pVDZ	1186
Propargyl alcohol-Water[33]	MP2/6-311++G(d,p)	1505
Ar-HCN-H$_2$O[31]	MMC	25
$(H_2S)_2(H_2O)$	B3LYP/aug-cc-pVDZ	1480
	MP2/aug-cc-pVDZ	1501

4.3.7   Binding Energy

We have calculated the binding energy of the $(H_2S)_2(H_2O)$ complex using the supermolecule approach. The intermolecular binding energy (ΔE) is defined as a difference between the total energy of the complex and the energies of the constituent molecules. For the complex binding energy is calculated as follows:

$$E_{int}=[E(H_2S)_2(H_2O)]-[\ E(H_2S)+E(H_2S)+E(H_2O)]$$

Basis set superposition error (BSSE) has been corrected using the counterpoise method. The basis set corrected energy is denoted by $\Delta E_{BSSE.}$ The binding energy was also corrected for zero-point energy (ZPE). The BSSE and ZPE corrected energy is represented as $\Delta E_{BSSE+ZPE}$.

We have also calculated the binding energies of the HSH⋯SH$_2$, HOH⋯SH$_2$, HSH⋯OH$_2$. The binding energies calculated for HOH⋯SH$_2$ and HSH⋯OH$_2$ are 14.4 and 13.4 kJ/mol respectively. The difference in binding energies between these

complexes is reduced when the BSSE energy is included. However, the HSH$\cdots$OH$_2$ became more stable, once the zero-point energy correction was introduced[5]. As discussed in Chapter 3 (section 3.3.6), the binding energy of $(H_2S)_2$ with zero-point and BSSE correction was found to be 1.9 kJ/mol.

 The binding energy $\Delta E_{BSSE+ZPE}$ of the complex is determined to be 15.3 kJ/mol, about 4 kJ/mol higher than the sum of the binding energies of the $(H_2S)_2$, HOH$\cdots$SH$_2$ and HSH$\cdots$OH$_2$. So, the binding energy of the $(H_2S)_2(H_2O)$ deviates from additivity, indicating the existence of a cooperative effect in hydrogen bonding in the complex (See Table 4.25).

Table 4.25. Binding energy of $(H_2S)_2(H_2O)$ compared with the isolated dimer interactions. Binding energies are calculated at the MP2/aug-cc-pVDZ level of theory.

System	ΔE(kJ/mol)	ΔE_{BSSE}(kJ/mol)	$\Delta E_{BSSE+ZPE}$(kJ/mol)
HSH$\cdots$SH$_2$	9.8	6.5	1.9
HOH$\cdots$SH$_2$	14.4	10.7	4.3
HSH$\cdots$OH$_2$	13.4	10.4	5.0
Total			**11.2**
$(H_2S)_2(H_2O)$	38.9	29.1	15.3

4.3.8 **Atoms in Molecules (AIM) Analysis**

The Atoms in Molecules (AIM) topological study has been used to understand the nature of interactions in the $(H_2S)_2(H_2O)$ complex. Three intermolecular bond critical points (BCP) have been located for the complex corresponding to S-H$\cdots$S, O-H$\cdots$S and S-H$\cdots$O hydrogen bonds. We estimated the electron density (ρ), Laplacian of electron density ($\nabla^2\rho$), $|\lambda_1|/\lambda_3$ and $|V|/G$ ratio at the bond critical point. These parameters have also been estimated for HSH$\cdots$SH$_2$, HOH$\cdots$SH$_2$ and HSH$\cdots$OH$_2$ dimer complexes. Table 4.26 shows the electron density for dimers and subsequent interactions in $(H_2S)_2(H_2O)$, as well as the associated differences ($\Delta\rho$). Bader[34, 35] showed that electron density at the bond critical point is a good indicator of the strength of the bonds. For the dimers electron density at the BCP for S-H$\cdots$S, O-H$\cdots$S and S-H$\cdots$O interactions

are 0.0105, 0.0137, and 0.0155 au respectively. When moving from dimers to $(H_2S)_2(H_2O)$, the electron density at the BCP rises by about 0.001 au for the above-mentioned interactions. In essence, this also supports the cooperativity effect in hydrogen bonding (see Figure 4.8).

Table 4.26. Properties calculated from the Atoms in Molecules (AIM) analysis. Wave functions used for the calculations are evaluated at the MP2/aug-cc-pVDZ. Trimer refers to the $(H_2S)_2(H_2O)$ complex, whereas dimer refers to the HSH⋯SH_2, HOH⋯SH_2 and HSH⋯OH_2 complexes.

Dimers	$\rho_{dimer}(au)$	$(H_2S)_2(H_2O)$	$\rho_{trimer}(au)$	$\Delta\rho(au)$
HSH⋯SH$_2$	0.0105	S-H⋯S	0.0115	0.0010
HOH⋯SH$_2$	0.0137	O-H⋯S	0.0147	0.0010
HSH⋯OH$_2$	0.0155	S-H⋯O	0.0166	0.0011
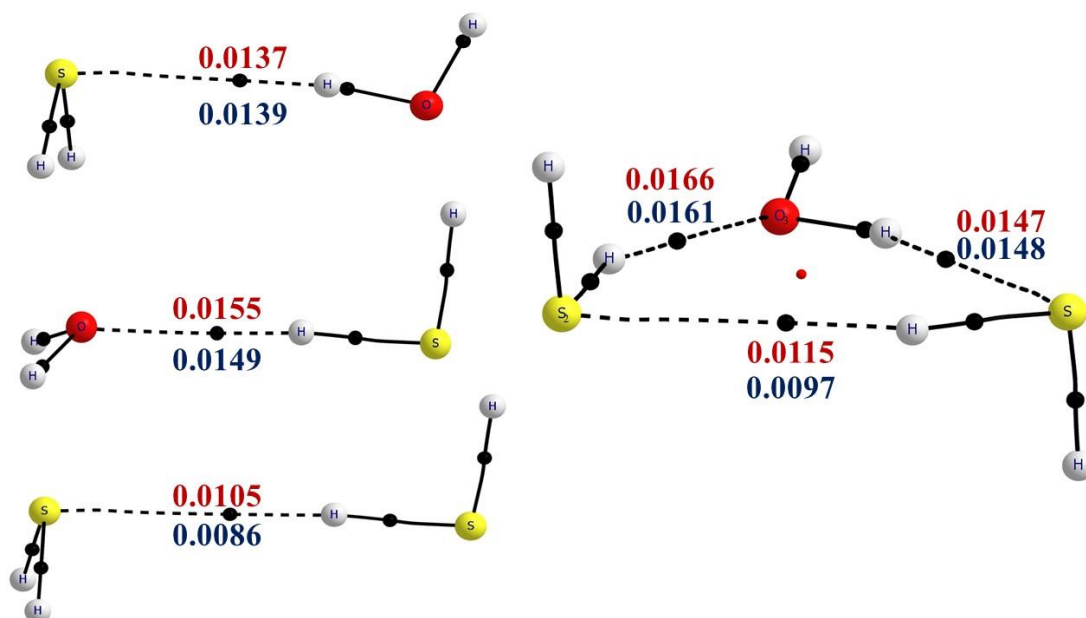
Figure 4.8. Atoms in Molecules (AIM) topological analysis of HSH⋯SH_2, HOH⋯SH_2, HSH⋯OH_2 and $(H_2S)_2(H_2O)$. The black dots show the bond critical points (BCP). The blue and red values represent electron density at the bond critical point computed using the B3LYP and MP2 methods.

We have also compared the $\nabla^2\rho$, $|\lambda_1|/\lambda_3$[36] and $|V|/G$[37] for the S-H···S, O-H···S and S-H···O interactions in dimers and (H2S)2(H2O) complex (see Table 4.27, Table 4.28, Table 4.29). The wavefunctions were determined at MP2/aug-cc-pVDZ and B3LYP/aug-cc-pVDZ levels. As previously stated, $\rho(r)$ increases from dimer to (H2S)2(H2O) complex for hydrogen bonding interactions. Similarly, the Laplacian of electron density ($\nabla^2\rho$), $|\lambda_1|/\lambda_3$ and $|V|/G$ also increases in the (H2S)2(H2O) complex.

*Table 4.27. Parameters calculated at **S-H•••S** bond critical point for the (H2S)2 and (H2S)2(H2O) at MP2 and B3LYP method. Values are in au.*

S-H•••S	(H2S)2	(H2S)2(H2O)	(H2S)2	(H2S)2(H2O)
	MP2/aug-cc-pVDZ		**B3LYP/aug-cc-pVDZ**	
$\rho(r)$	0.0105	0.0115	0.0086	0.0097
$\nabla^2\rho$	0.0245	0.0257	0.0197	0.0211
$|\lambda_1|/\lambda_3$	0.2067	0.2154	0.2036	0.2143
$|V|/G$	0.9474	0.9516	0.8636	0.9167

*Table 4.28. Parameters calculated at **O-H•••S** bond critical point for the HOH···SH2 and (H2S)2(H2O) at MP2 and B3LYP method. Values are in au.*

O-H•••S	HOH···SH2	(H2S)2(H2O)	HOH···SH2	(H2S)2(H2O)
	MP2/aug-cc-pVDZ		**B3LYP/aug-cc-pVDZ**	
$\rho(r)$	0.0137	0.0147	0.0139	0.0148
$\nabla^2\rho$	0.0344	0.0358	0.0306	0.0331
$|\lambda_1|/\lambda_3$	0.2118	0.2120	0.2266	0.2263
$|V|/G$	0.9091	0.9286	0.9143	0.9221

*Table 4.29. Parameters calculated at **S-H•••O** bond critical point for the HSH···OH$_2$ and (H$_2$S)$_2$(H$_2$O) at MP2 and B3LYP method. Values are in au.*

S-H•••O	HSH···OH$_2$	(H$_2$S)$_2$(H$_2$O)	HSH···OH$_2$	(H$_2$S)$_2$(H$_2$O)
	MP2/aug-cc-pVDZ		**B3LYP/aug-cc-pVDZ**	
$\rho(r)$	0.0155	0.0166	0.0149	0.0161
$\nabla^2\rho$	0.0462	0.0511	0.0414	0.0456
$|\lambda_1|/\lambda_3$	0.2114	0.2104	0.2199	0.2210
$|V|/G$	0.9735	0.9840	0.9703	0.9732

4.3.9 **Non-covalent Interactions (NCI) Index**

In addition to the traditional topological analysis tools of the chemical bond (AIM analysis), Yang and coworkers[38] offered a novel methodology called NCI analysis in 2010. This technique, which is similarly based on the electron density (ED) topology, allows for identifying and visualising weak interaction zones in 3D real space by giving chemically intuitive iso-surfaces of the reduced density gradients (abbreviated as RDG). The RDG versus sign $(\lambda_2)*\rho$ plot is known as the NCI plot. For HSH···SH$_2$, HOH···SH$_2$ and HSH···OH$_2$ dimer we have observed one spike each for S-H···S, O-H···S, and S-H···O hydrogen bonds (see Figure 4.9). The (H$_2$S)$_2$(H$_2$O) shows four spikes; three belong to the hydrogen bonds, and the fourth one belongs to the ring critical point (RCP). The results of the non-covalent interactions (NCI) index are consistent with the findings of the Atoms in Molecules (AIM) investigation.
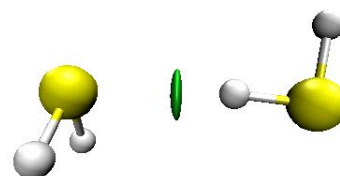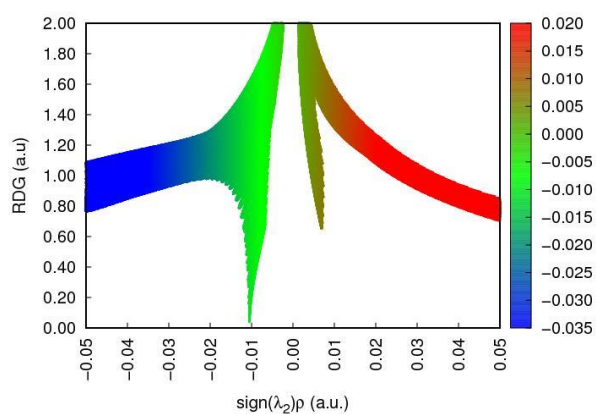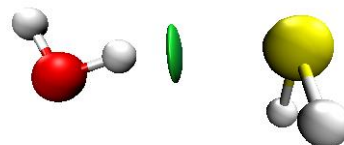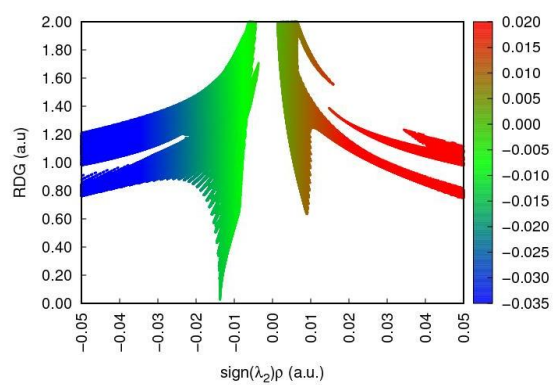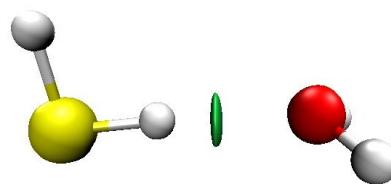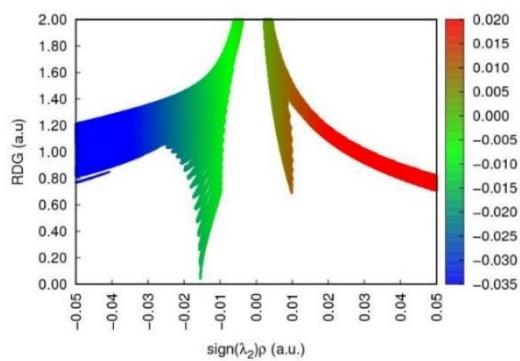
Continued Figure 4.9…
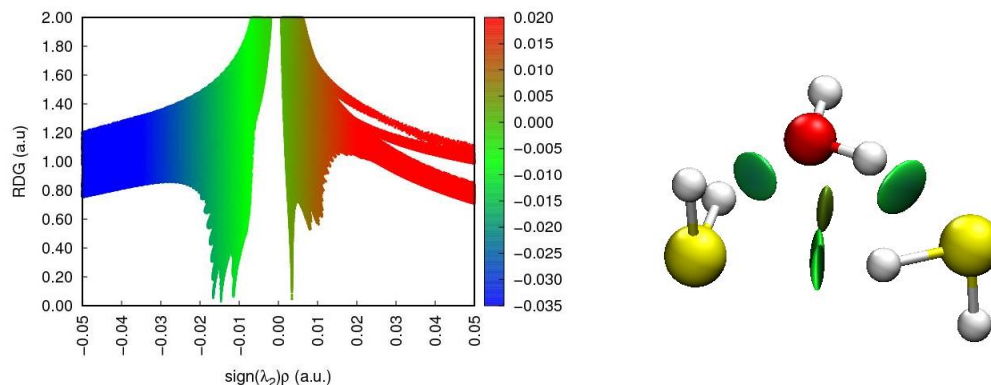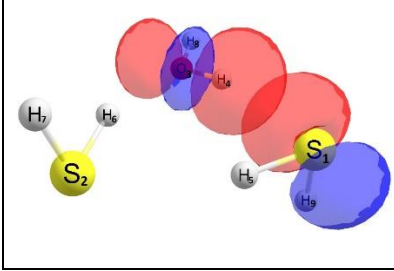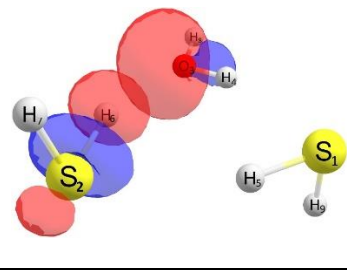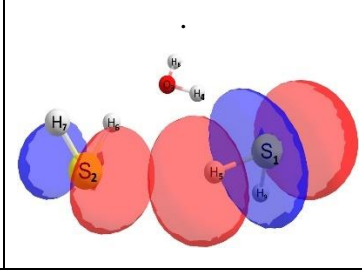
Figure 4.9. Non-covalent interactions (NCI) index plot for HSH⋯OH$_2$, HOH⋯SH$_2$, HSH⋯SH$_2$ and (H$_2$S)$_2$(H$_2$O).

4.3.10 Natural Bond Orbital (NBO) Analysis

To get a distinct viewpoint on bonding, we used natural bond orbital (NBO) analysis. The electronic wavefunction is interpreted in terms of occupied Lewis and non-Lewis localised orbitals in the NBO analysis[39]. The existence of off-diagonal components of the Fock matrix in the NBO basis can be used to detect delocalisation effects. Second-order perturbation theory is used to estimate the strengths of these delocalisation interactions. In (H$_2$S)$_2$(H$_2$O)$_2$, n $\rightarrow$ σ* interaction is a significant source of stabilisation of the hydrogen bonds. The second-order perturbation energy calculated at MP2/aug-cc-pVDZ level of the S-H⋯S, O-H⋯S, and S-H⋯O hydrogen bonding interactions were 22.8, 23.1, and 29.1 kJ/mol respectively (see Table 4.30). The B3LYP/aug-cc-pVDZ wavefunction has a consistent trend with MP2/aug-cc-pVDZ wavefunction. The second-order perturbation energy is a measure of interaction strength of the hydrogen bonds, which indicates O-H⋯S interaction is stronger than S-H⋯O interaction in the (H$_2$S)$_2$(H$_2$O) complex.

Table 4.30. Second order perturbation energies calculated at MP2 and DFT method for the O-H•••S, S-H•••O and S-H•••S interaction in the $(H_2S)_2(H_2O)$ complex. Values are in kJ/mol.

O-H⋯S	S-H⋯O	S-H⋯S
$n_{S_1} \rightarrow \sigma^*_{H_4-O_3}$	$n_{O_3} \rightarrow \sigma^*_{H_6-S_2}$	$n_{S_2} \rightarrow \sigma^*_{H_5-S_1}$
MP2/aug-cc-pVDZ		
29.1	23.1	22.8
B3LYP/aug-cc-pVDZ		
25.8	19.1	14.8

4.4 **Summary**

In summary, the rotational spectra of $(H_2S)_2(H_2O)$ were recorded with the help of chirped-pulse Fourier transform microwave spectrometer (*CP-FTMW*) and Balle-Flygare Fourier transform microwave spectrometer (*BF-FTMW)*. The various observables are available from the analysis of the rotational spectrum of $(H_2S)_2(H_2O)$ lead to a very self-consistent picture of the geometry of the complex. We have observed S-H⋯S, O-H⋯S and S-H⋯O hydrogen-bonded interactions in the complex. This geometry contains numerous characteristics that indicate the cooperative nature of the intermolecular interaction. The break with axial molecular symmetry and the simplified internal dynamics allowed us to investigate $(H_2S)_2(H_2O)$ at a level of structural detail that has not yet been possible for $(H_2O)_3$ and $(H_2S)_3$ with rotational spectroscopy. Rotational spectroscopy has revealed key features concerning the makeup of clusters with precise details of their internal motion. Nevertheless, the understanding of the properties of these three smallest clusters is now quite extensive, and the ground has been prepared for a search for similar/heavier species.

4.5 **References**

1. Pauling, L. *The Nature of the Chemical Bond,*. (Cornell University Press, 1960).

2. Das, A. *et al.* The H_2S Dimer is Hydrogen-Bonded: Direct Confirmation from Microwave Spectroscopy. *Angew. Chemie Int. Ed.* **57**, 15199–15203 (2018).

3. Lovas, F. J. *Private communication*.

4. Dreux, K. M. & Tschumper, G. S. Examination of the structures, energetics, and vibrational frequencies of small sulfur-containing prototypical dimers,$(H_2S)_2$ and H_2O/H_2S. *J. Comput. Chem.* **40**, 229–236 (2019).

5. Mandal, P. K. Rotational Spectra of Weakly Bound Complexes and 'Hydrogen Bond Radius' Doctoral dissertation, Indian Institute of Science (2005).

6. Maeda, S. & Ohno, K. Microsolvation of Hydrogen Sulfide: Exploration of $H_2S \cdot (H_2S)_n$ and $SH^- \cdot H_3O^+ \cdot (H_2O)_{n-1}$ (n= 5− 7) Cluster Structures on Ab Initio Potential Energy Surfaces by the Scaled Hypersphere Search Method. *J. Phys. Chem. A* **112**, 2962–2968 (2008).

7. Hattori, K., Wang, D. & Fujii, A. Influence of the microsolvation on hemibonded and protonated hydrogen sulfide: infrared spectroscopy of $[(H_2S)_n(X)_1]+$ and $H^+ (H_2S)_n(X)_1$(n=1 and 2, X= water, methanol, and ethanol). *Phys. Chem. Chem. Phys.* **21**, 16064–16074 (2019).

8. Gregory, J. K., Clary, D. C., Liu, K., Brown, M. G. & Saykally, R. J. The water dipole moment in water clusters. *Science.* **275**, 814–817 (1997).

9. Mandal, P. K., Goswami, M. & Arunan, E. Pulsed nozzle Fourier transform microwave spectroscopic and ab initio investigationson the weakly bound Ar-$(H_2S)_2$ trimer. *J. Indian Inst. Sci.* **85**, 353 (2013).

10. Kisiel, Z. *et al.* Structure and properties of the weakly bound trimer $(H_2O)_2HCl$ observed by rotational spectroscopy. *J. Chem. Phys.* **112**, 5767–5776 (2000).

11.   Kisiel, Z., Lesarri, A., Neill, J. L., Muckle, M. T. & Pate, B. H. Structure and properties of the $(HCl)_2H_2O$ cluster observed by chirped-pulse Fourier transform microwave spectroscopy. *Phys. Chem. Chem. Phys.* **13**, 13912–13919 (2011).

12.   Novick, S. E. Bibliography of Rotational Spectra of Weakly Bound Complexes. *Bibliogr. Rotational Spectra Weakly Bound Complexes*.

13.   Soulard, P. & Tremblay, B. Vibrational study in neon matrix of H_2S-H_2O, H_2S-$(H_2O)_2$, and $(H_2S)_2$-H_2O complexes. Identification of the two isomers: HOH-SH_2 (H_2O proton donor) and HSH-OH_2 (H_2S proton donor). *J. Chem. Phys.* **151**, 124308 (2019).

14.   Bhattacherjee, A., Matsuda, Y., Fujii, A. & Wategaonkar, S. The intermolecular S-H$\cdots$Y (Y=S,O) hydrogen bond in the H_2S dimer and the H_2S-MeOH complex. *ChemPhysChem* **14**, 905–914 (2013).

15.   Lechuga-Fossat, L., Flaud, J.-M., Camy-Peyret, C. & Johns, J. W. C. The spectrum of natural hydrogen sulfide between 2150 and 2950 cm$-$ 1. *Can. J. Phys.* **62**, 1889–1923 (1984).

16.   Gillis, J. R. & Edwards, T. H. Analysis of $2\nu_2$, ν_2, and ν_3 of H_2S. *J. Mol. Spectrosc.* **85**, 55–73 (1981).

17.   Brown, L. R. *et al.* The Absorption Spectrum of H_2S Between 2150 and 4260 cm$-$ 1: Analysis of the Positions and Intensities in the First ($2\nu_2$, ν_1, and ν_3) and Second ($3\nu_2$, $\nu_1+ \nu_2$, and $\nu_2+ \nu_3$) Triad Regions. *J. Mol. Spectrosc.* **188**, 148–174 (1998).

18.   Stephens, S. L. & Walker, N. R. Determination of nuclear spin-rotation coupling constants in CF_3I by chirped-pulse Fourier-transform microwave spectroscopy. *J. Mol. Spectrosc.* **263**, 27–33 (2010).

19.   Zaleski, D. P., Stephens, S. L. & Walker, N. R. A perspective on chemistry in transient plasma from broadband rotational spectroscopy. *Phys. Chem. Chem. Phys.* **16**, 25221–25228 (2014).

20.   Arunan, E., Tiwari, A. P., Mandal, P. K. & Mathias, P. C. Pulsed nozzle Fourier

References

transform microwave spectrometer: Ideal to define hydrogen bond radius. *Curr. Sci.* **82**, 533–540 (2002).

21. Balle, T. J. & Flygare, W. H. Fabry-Perot cavity pulsed Fourier transform microwave spectrometer with a pulsed nozzle particle source. *Rev. Sci. Instrum.* **52**, 33–45 (1981).

22. Pickett, H. M. SPFIT/SPCAT package. (2009).

23. Frisch, M. J. *et al.* Gaussian 09 Revision D. 01, 2009. *Gaussian Inc. Wallingford CT* (2009).

24. Dyke, T. R., Mack, K. M. & Muenter, J. S. The structure of water dimer from molecular beam electric resonance spectroscopy. *J. Chem. Phys.* **66**, 498–510 (1977).

25. Kraitchman, J. Determination of molecular structure from microwave spectroscopic data. *Am. J. Phys.* **21**, 17–24 (1953).

26. Kisiel, Z. Least-squares mass-dependence molecular structures for selected weakly bound intermolecular clusters. *J. Mol. Spectrosc.* **218**, 58–67 (2003).

27. De Lucia, F. C., Helminger, P., Gordy, W., Morgan, H. W. & Staats, P. A. Millimeter-and submillimeter-wavelength spectrum and molecular constants of T_2O. *Phys. Rev. A* **8**, 2785 (1973).

28. Cook, R. L., De Lucia, F. C. & Helminger, P. Molecular force field and structure of hydrogen sulfide: Recent microwave results. *J. Mol. Struct.* **28**, 237–246 (1975).

29. Batsanov, S. S. Van der Waals Radii of Elements. *Inorg. Mater. Transl. from Neorg. Mater. Orig. Russ. Text* **37**, 871–885 (2001).

30. Cohen, R. C. & Saykally, R. J. Determination of an improved intermolecular global potential energy surface for Ar–H_2O from vibration–rotation–tunneling spectroscopy. *J. Chem. Phys.* **98**, 6007–6030 (1993).

31. Gutowsky, H. S., Hoey, A. C., Tschopp, S. L., Keen, J. D. & Dykstra, C. E.

Rotational spectrum and structure of an $(H_2O–HCN)$–Ar trimer. *J. Chem. Phys.* **102**, 3032–3040 (1995).

32.   Goswami, M. & Arunan, E. Microwave spectroscopic and theoretical studies on the phenylacetylene$\cdots H_2O$ complex: C–H$\cdots$ O and O–H$\cdots$ π hydrogen bonds as equal partners. *Phys. Chem. Chem. Phys.* **13**, 14153–14162 (2011).

33.   Gnanasekar, S. P. Rotational Spectroscopic and Computational Studies on Inter/Intramolecular Bonding. Doctoral dissertation, Indian Institute of Science (2020).

34.   Bader, R. F. W. Atoms in Molecules: A Quantum Theory: Oxford Univ. Press. (1990).

35.   Keith, T. A. AIMAll (Version 14.11. 23). *TK Gristmill Software, Overl. Park KS, USA* (2014).

36.   Amezaga, N. J. M., Pamies, S. C., Peruchena, N. M. & Sosa, G. L. Halogen bonding: a study based on the electronic charge density. *J. Phys. Chem. A* **114**, 552–562 (2009).

37.   Cremer, D. & Kraka, E. Chemical Bonds without Bonding Electron Density—Does the Difference Electron-Density Analysis Suffice for a Description of the Chemical Bond? *Angew. Chemie Int. Ed. English* **23**, 627–628 (1984).

38.   Contreras-García, J. *et al.* NCIPLOT: a program for plotting noncovalent interaction regions. *J. Chem. Theory Comput.* **7**, 625–632 (2011).

39.   Glendening, E. D., Landis, C. R. & Weinhold, F. NBO 6.0 : natural bond orbital analysis program. *J. Comput. Chem.* **34**, 1429–1437 (2013).

4.6 **Supplementary Information**

Table S4.1. Coordinates of equilibrium geometry of $(H_2S)_2(H_2O)$, optimised at B3LYP-6-311++g(2d,2p) level.

Atom	x(Å)	y(Å)	z(Å)
S_1	2.024321	-0.652847	0.086512
H_5	0.737027	-1.046939	0.011825
H_9	2.191504	-0.728418	-1.242792
O_3	0.066494	2.151805	-0.068034
H_4	0.829857	1.562278	0.021451
H_8	0.294824	2.954082	0.408505
S_2	-2.071982	-0.592332	-0.080703
H_6	-1.527524	0.637724	0.012433
H_7	-2.295069	-0.670294	1.239912

Table S4.2. Coordinates of equilibrium geometry of $(H_2S)_2(H_2O)$, optimised at B3LYP-aug-cc-pVDZ level.

Atom	x(Å)	y(Å)	z(Å)
S_1	2.017657	-0.655435	0.086952
H_5	0.711606	-1.040496	0.009315
H_9	2.194443	-0.754465	-1.254567
O_3	0.062210	2.148793	-0.047348
H_4	0.836254	1.564754	0.022004
H_8	0.356714	3.010696	0.268639
S_2	-2.066554	-0.591527	-0.082735
H_6	-1.526000	0.655818	0.013181
H_7	-2.288354	-0.675272	1.252750

Table S4.3. Coordinates of equilibrium geometry of $(H_2S)_2(H_2O)$, optimised at B3LYP-aug-cc-pVTZ level.

Atom	x(Å)	y(Å)	z(Å)
S_1	2.035934	-0.656023	0.086545
H_5	0.745018	-1.047697	0.013207
H_9	2.211215	-0.753327	-1.243385
O_3	0.065275	2.160015	-0.059412
H_4	0.831781	1.572002	0.016273
H_8	0.327942	2.989494	0.349702
S_2	-2.084694	-0.593551	-0.081847
H_6	-1.543892	0.639642	0.024549
H_7	-2.314102	-0.687051	1.239771

Table S 4.4. Coordinates of equilibrium geometry of $(H_2S)_2(H_2O)$, optimised at MP2-6-311++g(2d,2p) level.

Atom	x(Å)	y(Å)	z(Å)
S_1	-1.989350	-0.651504	-0.086393
H_5	-0.700865	-1.000847	-0.009993
H_9	-2.153300	-0.750939	1.231346
O_3	-0.067652	2.125038	0.052166
H_4	-0.835579	1.546719	-0.033470
H_8	-0.354919	2.976666	-0.280473
S_2	2.037394	-0.584222	0.080982
H_6	1.509275	0.640215	-0.016974
H_7	2.307891	-0.640498	-1.221181

Table S4.5. Coordinates of equilibrium geometry of (H₂S)₂(H₂O), optimised at MP2-aug-cc-pVDZ level.

Atom	x(Å)	y(Å)	z(Å)
S_1	-1.978974	-0.651614	-0.085325
H_5	-0.670589	-1.002883	-0.012717
H_9	-2.141434	-0.743896	1.252193
O_3	-0.038521	2.145709	0.029170
H_4	-0.824751	1.577213	-0.033891
H_8	-0.362024	3.036942	-0.153043
S_2	2.014348	-0.598009	0.083997
H_6	1.507305	0.654720	-0.020054
H_7	2.233677	-0.693801	-1.244600

Table S4.6. Coordinates of equilibrium geometry of (H₂S)₂(H₂O), optimised at MP2-aug-cc-pVTZ level.

Atom	x(Å)	y(Å)	z(Å)
S_1	-1.962922	-0.653019	-0.083303
H_5	-0.661355	-0.984341	-0.033312
H_9	-2.094647	-0.745526	1.244088
O_3	-0.054375	2.130006	0.032077
H_4	-0.824876	1.545619	-0.023495
H_8	-0.389055	3.006362	-0.178877
S_2	2.006077	-0.586996	0.082437
H_6	1.505025	0.654860	-0.015559
H_7	2.209426	-0.676792	-1.235606

Table S 4.7. Normal mode frequencies of $(H_2S)_2(H_2O)$. Frequencies are calculated B3LYP/aug-cc-pVDZ, MP2/aug-cc-pVDZ level of theory.

Modes (cm^{-1})	B3LYP/ aug-cc-pVDZ	MP2/ aug-cc-pVDZ	Experiment Ref[13]
1	61.66	72.77	
2	83.00	80.52	
3	102.05	111.66	
4	116.72	116.01	
5	123.82	129.60	
6	149.68	150.56	
7	167.55	168.20	
8	203.37	201.72	
9	257.09	259.80	
10	315.07	323.99	
11	430.15	453.23	
12	510.38	505.13	
13	1184.18	1199.02	1187.1
14	1189.46	1199.68	1187.1
15	1618.84	1626.30	
16	2589.01	2682.97	2567.4
17	2609.35	2704.35	2579.4
18	2672.85	2761.58	
19	2677.29	2764.97	
20	3677.30	3709.38	
21	3870.56	3897.04	

This page intentionally left blank

CHAPTER 5

Microwave Measurements of Proton Tunnelling Splitting and Structure of $Ar(H_2O)_2$

This page intentionally left blank

Chapter 5: Microwave Measurements of Proton Tunnelling Splitting and Structure of Ar(H$_2$O)$_2$

5.1 Introduction

Accurate determination of the tunnelling splitting is of prime importance to have a rigorous description of the intermolecular potential energy surface in weakly bound complexes. Microwave spectroscopy has helped enormously in getting the accurate structure of such complexes, popularly stabilised by hydrogen bonds [1–3]. However, in the most fundamental hydrogen-bonded system H$_2$O dimer, spectroscopists had to deal with the large amplitude motions which enable tunnelling between multiple minima in the potential energy hypersurface. There have been an enormous amount of study involving water dimer structure[4,5] tunnelling pathways [6,7,8,9,10,11,12,13,14,15], barrier[16,17,18] and splitting[19,20,21,22,23,24]. The H$_2$O dimer primarily undergoes three kinds of tunnelling motions, namely acceptor-acceptor (AA), donor-acceptor (DA), and donor-donor (DD) tunnelling. These motions lead to eight-fold degeneracy in the ground vibrational level, and these levels are split into six. The rotational states of A′ symmetry give rotational-tunnelling sublevels A$_1^+$, B$_1^+$, E$^+$, A$_2^-$, B$_2^-$, and E$^-$ symmetry while rotational states of A″ symmetry give sublevels of A$_1^-$, B$_1^-$, E$^-$, A$_2^+$, B$_2^+$, and E$^+$ symmetry. The overall selection rules are A$_1^+$↔A$_1^-$, B$_1^+$↔B$_1^-$, A$_2^+$↔A$_2^-$, B$_2^+$↔B$_2^-$, and E$^+$↔E$^-$. The statistical weights for these states of the (H$_2$O)$_2$ and (D$_2$O)$_2$ levels are given in Figure 5.1 (for A′ rotational state). The first huge splitting is due to the acceptor-acceptor tunnelling motion, the splitting being about 200 GHz in (H$_2$O)$_2$ and 9 GHz for (D$_2$O)$_2$. These levels split further into three levels each due to the donor–acceptor interchange tunnelling, leading to a doubly degenerate E state flanked by the A and B states. This splitting is about 22 GHz for (H$_2$O)$_2$ and 1 GHz for (D$_2$O)$_2$. The donor-acceptor tunnelling reverses the sign of *a*-dipole. This happens as the selection rules permit lower ↔ upper transitions when the tunnelling motion changes the dipole moment. Hence, only the E states have rigid-rotor like spectrum and the A and B states have the tunnelling splitting

spectra. The donor-donor tunnelling does not result in any splitting of energy levels, it changes the relative energies.
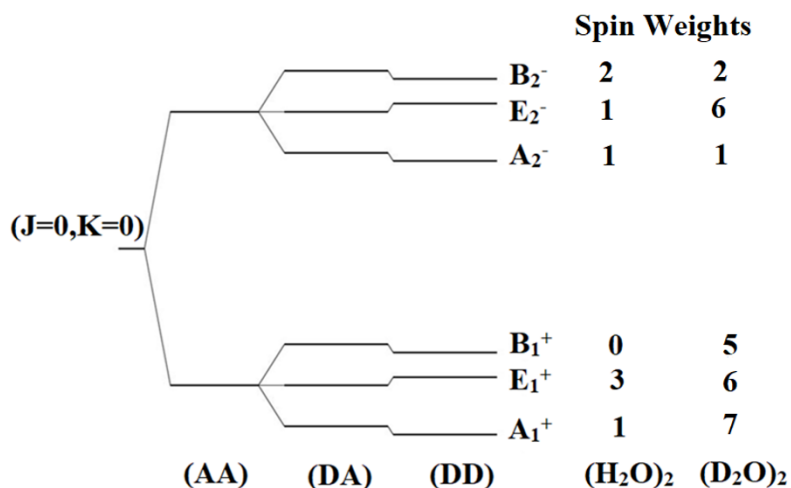
Figure 5.1. Energy level diagram for $(H_2O)_2$. The numbers represent the spin statistical weights of each of the six $(H_2O)_2$ and $(D_2O)_2$ states.
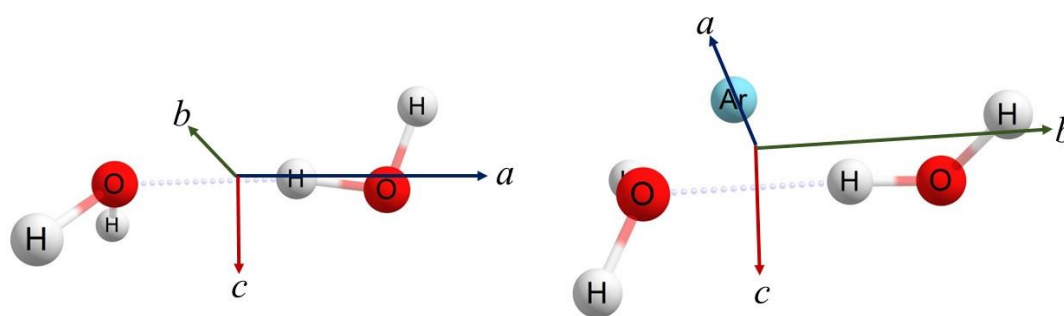
Figure 5.2. Structures and principal axes of $(H_2O)_2$ and $Ar(H_2O)_2$ complexes. In these two systems, the a-axis and b-axis are swapped.

The $(H_2O)_3$ cannot be studied using rotational spectroscopy owing to its zero or low effective dipole moment. Kisiel recorded the rotational spectra of a series of $HX(H_2O)_2$ (X=Cl, Br)[25,26] complexes by replacing one of the H_2O to HX (X=Cl, Br) as it

introduces two non-zero dipole moment components. Similarly, the incorporation of argon (Ar) in $(H_2O)_2$ also introduces a new dipole along the dimer b-axis (a-axis in the $Ar(H_2O)_2$, see Figure 5.2). As the b-dipole moment does not change during the donor-acceptor interchange tunnelling, in these complexes, A and B states could have a rigid-rotor like spectra unlike in $(H_2O)_2$. Here, HCl/, -HBr/, -Ar acts as electrophore, which allows us to obtain the rotational spectra of non-polar molecules similar to a chromophore in electronic spectroscopy.

The A rotational constant for $Ar(H_2O)_2$, $HBr(H_2O)_2$, and $HCl(H_2O)_2$ are 6253, 6770, and 6875 MHz compared to the B rotational constant of 6160.7 MHz for $(H_2O)_2$. A careful look at the A rotational constant for $HBr(H_2O)_2$, and $HCl(H_2O)_2$ indicates that the $(H_2O)_2$ geometry has altered significantly with the addition of HCl/HBr. Addition of Ar does not appear to have led to such significant changes in the $(H_2O)_2$ geometry. Clearly, Ar can be an electrophore that does not affect the molecule/complex significantly. In the broader context, a systemic study of $Ar_m(H_2O)_n$, $Ar_2(H_2O)$, $Ar_3(H_2O)$, $Ar(H_2O)_3$[27] systems using high-resolution microwave spectroscopy helps us to understand the dynamics and the bulk interactions with argon atoms with water molecules.

In the previous rotational spectroscopic investigation[28], $Ar(D_2O)_2$, A_1, E_1, B_1 states have been observed. The a-dipole transitions for A_1, E_1, B_1 states give a rigid rotor-like spectrum, as the donor-acceptor tunnelling does not reverse the sign of the a-dipole. The b-dipole transitions for the A_1 and B_1 states are shifted by 106 MHz from the E_1 state. However, that investigation did not report the A_1 and B_1 states of $Ar(H_2O)_2$.

In $Ar(H_2O)_2$, the B_1 state transitions will be missing due to its zero-spin statistical weight (See Figure *5.3*). The A_1 state b-dipole transitions are expected to have a large tunnelling splitting of 4-5 GHz and so far, eluded the experimental detection. Furthermore, the ordering of the energy levels in the case of b-dipole transitions depends on the K_p quantum number, which also made the observation of b-dipole A_1 state transitions difficult. The b-dipole transitions with K_p' even, the transition frequencies increase in the order $A_1 > E_1 > B_1$, whereas, for K_p' odd, the order is reversed with $B_1 > E_1 > A_1$ (see Figure 5.3). Figure 5.4 depicts an overview of the different states

and splitting found for $(H_2O)_2$ and $Ar(H_2O)_2$ and their completely deuterated isotopologues using stick diagrams. This Chapter reports the successful search and observation of A_1 state for the $Ar(H_2O)_2$ complex and a re-look at its structure. The vector components of rotational angular momentum along the main axis are indicated by Kp and Ko in this Chapter rather than Ka and Kc. This is done to adhere to the nomenclature in reference 28, which reports the initial work on the $Ar(H_2O)_2$ complex. With this introduction, we turn our attention to the experimental details and the results.
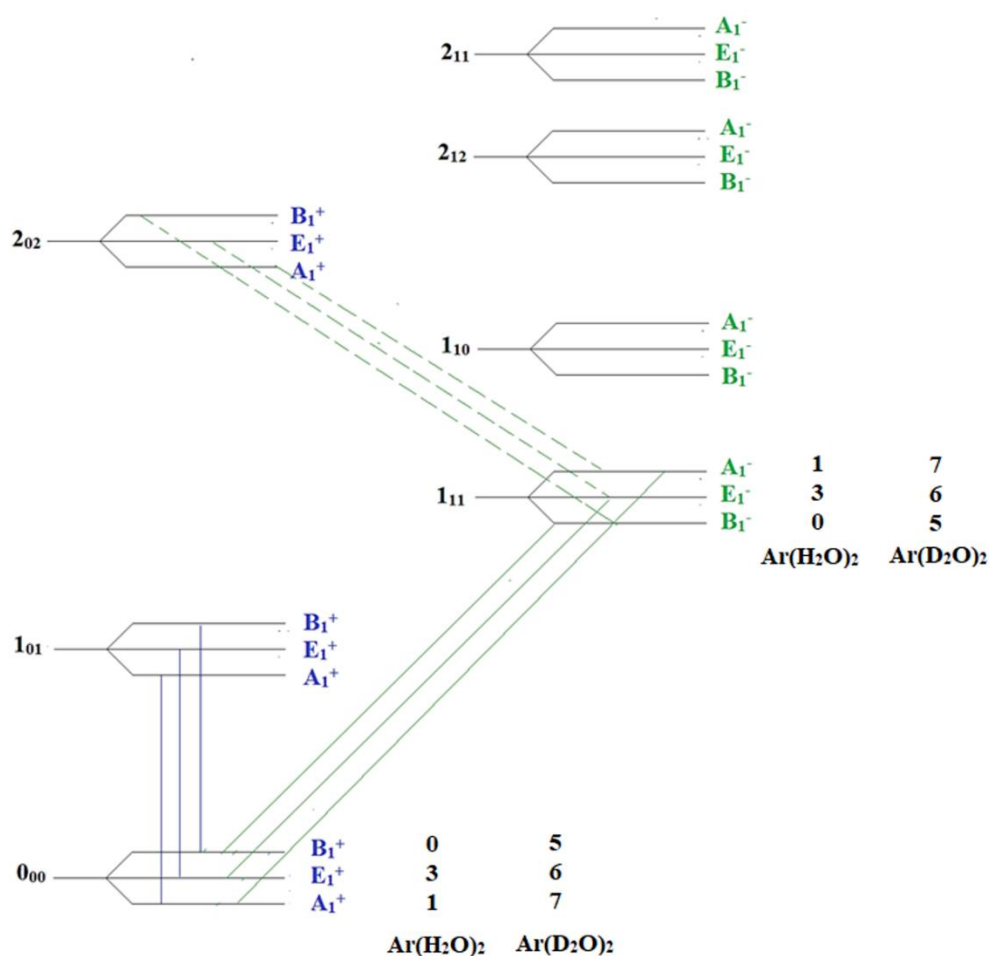
Figure 5.3. Energy level diagram for Ar(H₂O)₂ complex. The solid blue line represents rigid-rotor-like a-dipole transitions. Green solid lines denote the b-dipole Kp' even transitions. The green dotted line indicates the b-dipole Kp' odd transitions.

Stick Diagrams	Systems

$(H_2O)_2/(D_2O)_2$

1

$E_1(3)$

a-dipole

$B_1(0)$ 22554 $A_1(1)$

Frequency (MHz)

2

b-dipole

Frequency (MHz)

3

$A_1(7)$

$E_1(6)$ a-dipole

$B_1(5)$

1172

Frequency (MHz)

4

b-dipole

Frequency (MHz)
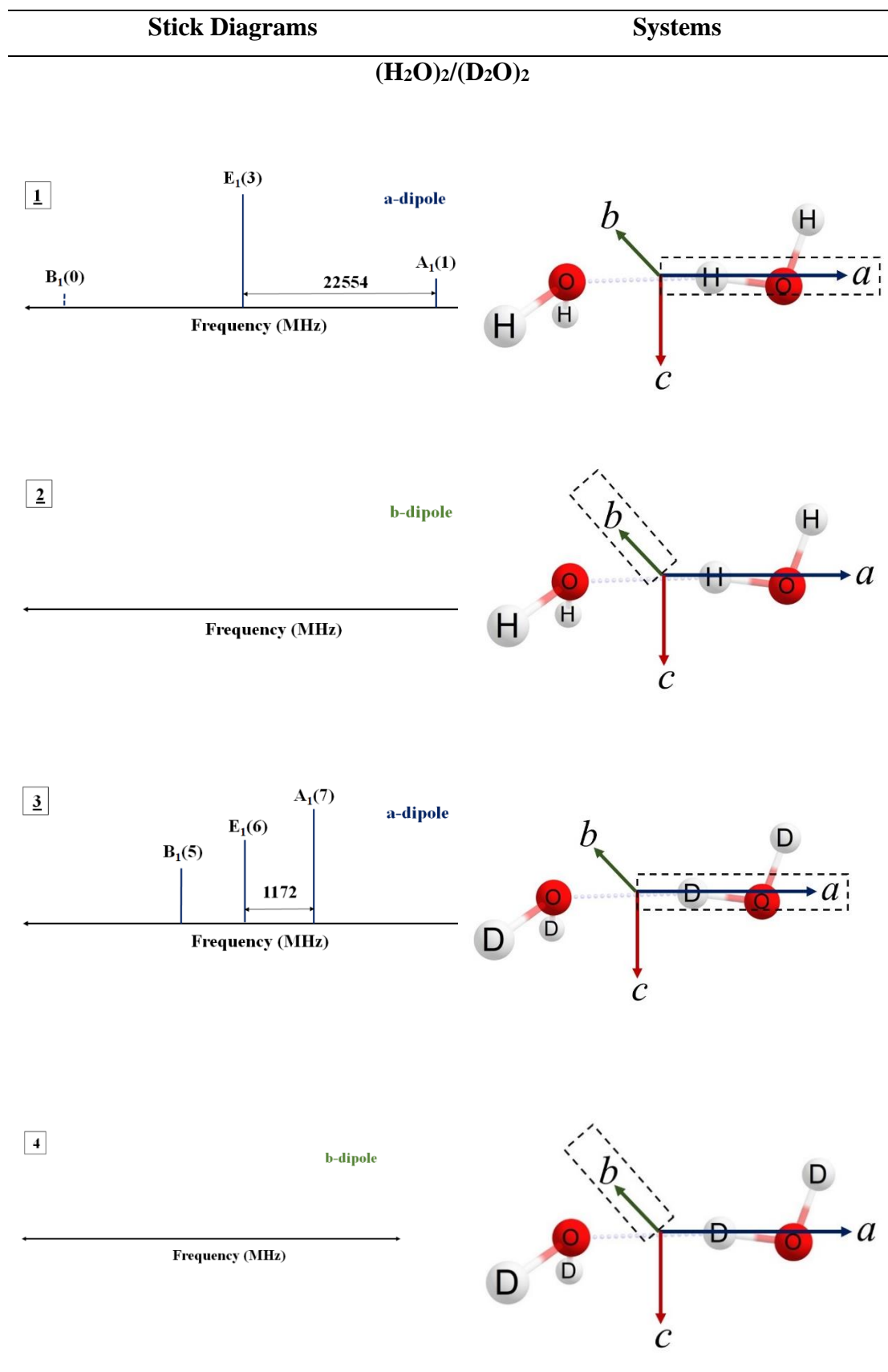
Ar(H₂O)₂/Ar(D₂O)₂
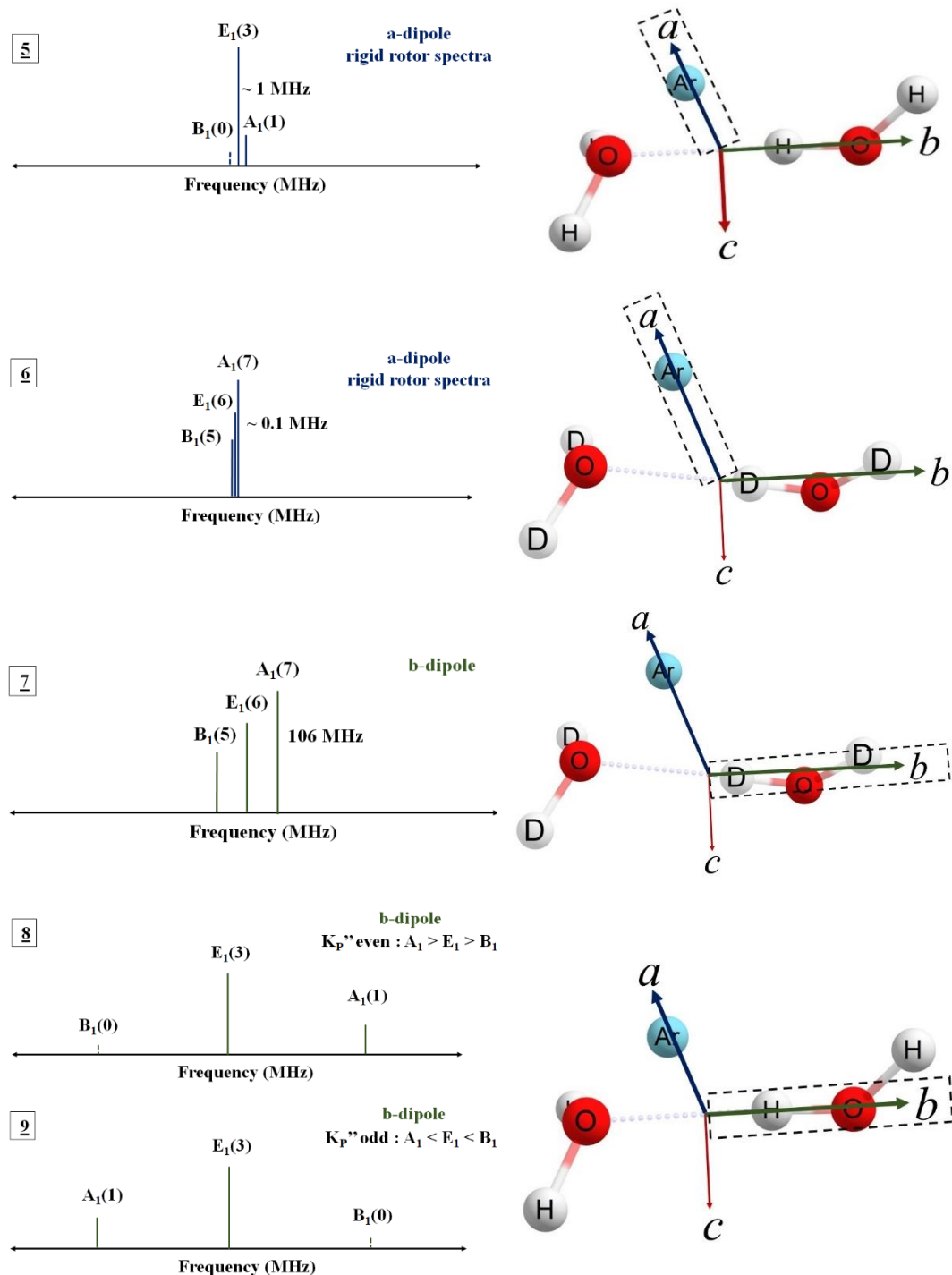
Figure 5.4. Stick diagram showing A_1, B_1, and E_1 states of $(H_2O)_2$, $Ar(H_2O)_2$, and their fully deuterated counterparts.

Detailed caption: The number after the state specifies the spin weights of that state. The dotted states are having zero spin weight and are absent in the experimental spectra. The intensities of the transitions are drawn according to their spin weights. The relative magnitude of the splitting is not accurate to scales. (1) The A_1 states of $(H_2O)_2$ are split from E_1 states by about 22554 MHz for a-dipole transitions. B_1 states are not observed due to their zero-spin weight. (2) $(H_2O)_2$ has no dipole moment along the b-axis, so the b-dipole transitions are not present in the pure microwave spectra. (3) The A_1, B_1, and E_1 states are observed for $(D_2O)_2$; the splitting observed was 1172 MHz. (4) The b-dipole transitions are absent due to zero-dipole along the b-axis in $(D_2O)_2$. (5) Rigid rotor spectra were observed for $Ar(H_2O)_2$ a-dipole transitions, as the direction of a-dipole was unchanged during tunnelling motion. (6) Similarly, a-dipole $Ar(D_2O)_2$ shows rigid-rotor spectra. (7) The b-dipole transitions of $Ar(D_2O)_2$ show tunnelling splitting spectra with 106 MHz splitting. (8) In this work, the b-dipole A_1 states are observed for $Ar(H_2O)_2$; for Kp," even, A_1 states are observed above the E_1 state. (9). For Kp" odd. A_1 states are observed below the E_1 state.

5.2   Experimental Details

The $Ar(H_2O)_2$ rotational-tunnelling spectra were observed with the Balle-Flygare Fourier transform microwave spectrometer (*BF-FTMW)* described in detail elsewhere[29]. Argon was used as the carrier gas and bubbled through H_2O kept at ambient conditions. The backing pressure was typically 0.8 atm, and the nozzle diameter was 0.8 mm. The flow rate of Ar was kept at 150 SCCM, and 1% of it was flown through a bubbler containing water sample. Around 3000 free induction decays (FIDs) were recorded per gas pulse. At a sampling rate of 5 MHz, 256 points were collected for each FID during the search for rotational transitions. Once a signal was observed, it was further averaged with 512 or 1024 points to improve the resolution. A microwave pulse of 0.2 μs duration was found to be the optimum for both the *b*-dipole transitions.

5.3 Results and Discussion

5.3.1 Periodic Potential and Normal Mode Analysis

To simulate the donor-acceptor interchange tunnelling motion in $Ar(H_2O)_2$ complex, we adopted the methodology used in water dimer and acetylene dimer[30] using periodic potential functions[31,32]. We start with the wave equation,

$$-\boldsymbol{B}\frac{d^2\psi}{d\phi^2} + V\psi = E\psi$$

$$\text{where, } V = \frac{1}{2}V_n(1-\cos n\phi)$$

and $\boldsymbol{B}$ is the internal rotational constant, ϕ is the phase angle, and V_n is an n-fold barrier. With four equivalent minima and maxima, a four-fold potential (V_4) has been used. Torsional coordinate depends on reduced mass and the shape of the potential. Force constant depends on the second derivative of the minimum; the energy difference between the minimum and the saddle point gives the barrier. We assume that the presence of argon does not affect the tunnelling path for donor-acceptor interchange tunnelling, but it increases the barrier for the motion. This approximation can be justified by comparing the vibrational mode for donor-acceptor interchange tunnelling[33] (see Figure 5.5), which remains unchanged as we go from $(H_2O)_2$ to $Ar(H_2O)_2$. Table 5.1 provides all the normal modes of $(H_2O)_2$ and $Ar(H_2O)_2$, also normal mode frequencies with anharmonic correction are given supplementary information (Table S5.7).

With this approximation of the internal rotational constant, $\boldsymbol{B}$ is taken as $b_0/2$. Here b_0 (7.260 cm^{-1}) is the zero-point B rotational constant of H_2O. The Hamiltonian matrix is set up in the free-rotor basis and diagonalised to obtain the eigenvalues and tunnelling splitting.

127 cm^{-1} 127 cm^{-1}
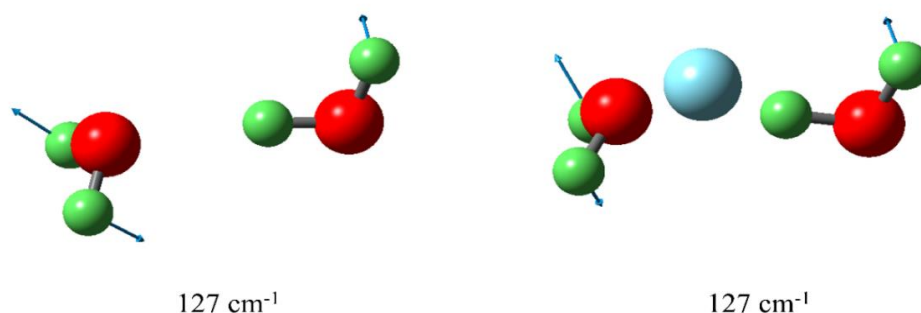
Figure 5.5. Vibrational mode for the donor-acceptor interchange tunnelling in the $(H_2O)_2$ *and* $Ar(H_2O)_2$ *remains unchanged. Calculated at MP2/aug-cc-pVDZ level.*

Table 5.1. Comparison of normal mode frequencies between $(H_2O)_2$ *&* $Ar(H_2O)_2$. *Frequencies are calculated using MP2/aug-cc-pVDZ and MP2/aug-cc-pVTZ level of theory. The labelling of normal modes is according to* $(H_2O)_2$.

Modes (cm^{-1})	$(H_2O)_2$	$Ar(H_2O)_2$	Difference (cm^{-1})	$(H_2O)_2$	$Ar(H_2O)_2$	Difference (cm^{-1})
	MP2/aug-cc-pVDZ			**MP2/aug-cc-pVTZ**		
ν_{12}	127	127	0	127	130	3
ν_{11}	148	153	5	146	155	9
ν_8	151	156	5	155	161	6
ν_7	185	185	0	184	190	6
ν_6	355	365	1	359	375	16
ν_{10}	639	635	-4	629	627	-2
ν_5	1624	1622	-2	1629	1628	-1
ν_4	1643	1643	0	1650	1651	-1
ν_3	3704	3701	-3	3719	3713	-6
ν_2	3796	3795	-1	3814	3811	-3
ν_1	3904	3903	-1	3915	3914	-1
ν_9	3926	3924	-2	3935	3931	-4
	Modes Involving Argon					
		20			26	
		35			53	
		67			66	

We have calculated the *ab-initio* barrier for donor-acceptor interchange motion in $(H_2O)_2$ and $Ar(H_2O)_2$ using the Gaussian 09[34] suite of the program (see Table 5.2). The *ab-initio* barrier for the exchange motion in $Ar(H_2O)_2$ is around 25 cm^{-1} higher than that in $(H_2O)_2$. So, we expect the donor-acceptor tunnelling splitting in the complex will be less than that of the dimer. Also, it can be seen that the *ab-initio* barrier in the dimer is almost 100 cm^{-1} less compared to what has been evaluated using the experiment. The comparison between theory and experiment is difficult because of the lack of knowledge of the reduced mass for the motion and shape of the tunnelling potential. The barrier heights and resulting tunnelling splitting in $Ar(H_2O)_2$ are given in Table 5.3. To simulate the tunnelling splitting, we have used a scaled barrier for $Ar(H_2O)_2$. The ratio of the $Ar(D_2O)_2$ and $(D_2O)_2$ barrier (642/402=1.597) is multiplied with the experimental $(H_2O)_2$ barrier (437 cm^{-1}) to get the scaled V_4 potential of 697.89 cm^{-1}. The tunnelling splitting corresponding to the scaled barrier is estimated to be 4263 MHz.

Table 5.2. Ab-initio barriers for donor-acceptor interchange motion in $(H_2O)_2$ and $Ar(H_2O)_2$. Values are in cm^{-1}.

	MP2/ 6-311++G(2d,2p)	MP2/ 6-311++G(2df,2p)	Experiment
$(H_2O)_2$	312	303	437*
$Ar(H_2O)_2$	335	328	698**

*Reference [17], **Reference [28]

Table 5.3. Barrier heights (cm⁻¹) and resulting tunnelling splitting (GHz) for Ar(H₂O)₂.

Barrier(cm⁻¹)	Splitting (GHz)
590	8.159
642	5.939
690	4.462
695	4.333
698(Scaled Barrier)	**4.263**
700	4.208
710	3.946

Internal rotational constant has been kept constant at 7.260 cm⁻¹.

5.3.2 Rotational Transitions and Constants

We started looking for the 4_{13}-4_{04} transition corresponding to the A_1 state with this prediction in hand. The E_1 state, 4_{13}-4_{04} transition, appears at 8556.6560 MHz. The 4_{13}-4_{04} transition ($K_p'' =$ even) for the A_1 state appears at a higher frequency than the E_1 state. Based on our model, we expect the A_1 state b-dipole 4_{13}-4_{04} transition around 12819.6560 MHz. We have observed a transition at 12814.9930 MHz.

On the other hand, we have failed to observe the corresponding B_1 state around the 4293 MHz regions owing to its zero spins statistical weight. Next, we planned for the A_1 state 3_{03}-2_{12} (K_p''=odd) transition. The E_1 state, 3_{03}-2_{12} transition occurs at 8948.9970 MHz. A_1 state will be at a lower frequency than the E_1 state for the 3_{03}-2_{12} transition. We have found the 3_{03}-2_{12} transition of the A_1 state at 4690.164 MHz, 4258.833 MHz downshifted from the E_1 state (see Figure 5.6). We have observed a total of 15 b-dipole A_1 state transitions of Ar(H₂O)₂ (see Table 5.4). We have fitted the transitions using the ASYM82 program with the semirigid rotor Watson Hamiltonian. To fit all the transitions simultaneously, the transitions with K_p' even manifold were intentionally

changed to a higher frequency than E_1 state by adding the appropriate tunnelling splitting frequency. For example, the 3_{03}-2_{12} transitions appear at 4690.1640 MHz with a tunnelling splitting value of 4258.8330 MHz. We have added 4258.8330 MHz to the E_1 state 3_{03}-2_{12} transition (8948.9970 MHz) to artificially increase the frequency to 13207.8300 MHz. This exercise has been done to all the $K_p{'}$ even transitions. Acceptable fit with RMS deviation of 9 kHz has been obtained for the b-dipole A_1 state (see Table 5.5) transitions. Previously reported root-mean-square deviation for the a-dipole A_1 state rigid rotor-like transitions was 456 kHz, almost two orders of magnitude higher than the experimental accuracy[28]. The large uncertainty was attributed to some unidentified coupling. The coupling does not appear to influence the b-dipole A_1 state transitions.
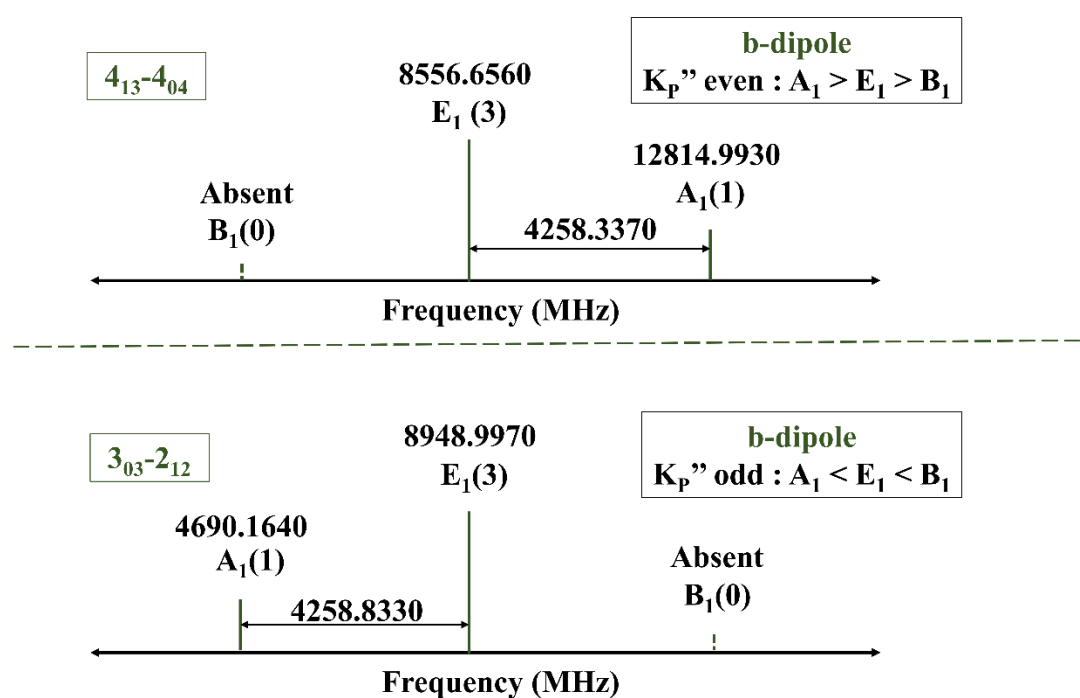
Figure 5.6. Stick diagram showing tunnelling splitting for the b-dipole lines in Ar(H₂O)₂. B₁ states have a zero-spin weight, so not observed in the experiment. E₁ states are from reference [28]. *A₁ states are observed in the current investigation. These states can be above or below the E₁ state depending on even or odd Kₚ".*

Table 5.4. Observed transitions and splitting for Ar(H₂O)₂. Values are in MHz.

J	K_p'	K_o'	J	K_p''	K_o''	B₁	*E₁	**A₁	Splitting
1	1	0	1	0	1	-	4513.4475	8770.7725	4257.3250
2	1	1	2	0	2	-	5286.2665	9544.3510	4258.0845
1	1	1	0	0	0	-	7992.0870	12250.0505	4257.9635
3	1	2	3	0	3	-	6592.2621	10851.0100	4258.7479
4	1	3	4	0	4	-	8556.6560	12814.9930	4258.3370
5	1	4	5	0	5	-	11239.4573	15496.3711	4256.9138
2	1	2	1	0	1	-	11469.6750	15728.6500	4258.9750
						**A₁	*E₁	B₁	
3	0	3	2	1	2	4690.1640	8948.9970	-	4258.8330
5	0	5	4	1	4	13442.8500	17699.4466	-	4256.5966
5	2	4	5	1	5	13654.5390	17912.2243	-	4257.6853
2	2	1	2	1	2	9282.0200	13539.7957	-	4257.7757
3	2	2	3	1	3	10361.857	14619.4198	-	4257.5628
4	2	3	4	1	4	11821.8292	16077.0396	-	4255.2104
2	2	0	2	2	1	7298.4152	11558.4226	-	4260.0068
4	0	4	3	1	3	9158.3203	13416.5099	-	4258.1896

*E₁ states are observed previously[28]. **A₁ states are observed in the current work.

Experimentally observed tunnelling splitting is 4257.41(4) MHz is in good agreement with the theoretically predicted value of 4263 MHz. The experimental barrier corresponding to the observable splitting is found out to be 698 cm⁻¹, which is in apparent disagreement with the calculated *ab-initio* one (see Table 5.2). The magnitude of the donor-acceptor tunnelling splitting in Ar(H₂O)₂ is almost five times less than that of free water dimer (22 GHz). The obtained rotational constants for the A₁ state are similar to the E₁ state rotational constants. In Table 5.6 the experimentally observed rotational constants are compared with the theoretically evaluated ones. The equilibrium *A* and *B* rotational constants deviate almost 250 MHz and 100 MHz from the theoretically predicted constants, while the *C* rotational constant is in close

agreement. Not surprisingly, vibrationally averaged rotational constants are in better agreement with the experimentally obtained rotational constants.

Table 5.5. Fitted b-dipole A_1 state rotational transitions for $Ar(H_2O)_2$. Values are in MHz.

J'	K_a'	K_c'	J''	K_a''	K_c''	Observed	Deviation
1	1	0	1	0	1	8770.7725	-0.0052
2	1	1	2	0	2	9544.3510	0.0096
1	1	1	0	0	0	12250.0505	0.0017
3	1	2	3	0	3	10851.0100	0.0128
4	1	3	4	0	4	12814.9930	-0.0220
5	1	4	5	0	5	15496.3711	0.0078
2	1	2	1	0	1	15728.6500	0.0047
3	0	3	2	1	2	13207.8300	0.0062
5	0	5	4	1	4	21956.0432	-0.0026
5	2	4	5	1	5	22169.9096	-0.0016
2	2	1	2	1	2	17797.5714	-0.0095
3	2	2	3	1	3	18876.9826	0.0062
4	2	3	4	1	4	20332.2500	0.0004
2	2	0	2	1	1	15818.4300	0.0044
4	0	4	3	1	3	17674.6995	0.0090

RMS deviation of 15 measurements = 8.7 kHz

Table 5.6. Equilibrium, vibrationally averaged and experimental rotational constants for Ar(H₂O)₂.

Constants	Calculated Equilibrium MP2/aug-cc-pVDZ	Calculated Equilibrium MP2/aug-cc-pVTZ	Calculated Vib. avg MP2/aug-cc-pVDZ	Calculated Vib. avg MP2/aug-cc-pVTZ	Experimental
A/MHz	6507.632	6497.190	6120.376	6237.796	6252.963(5)
B/MHz	2316.617	2502.389	2468.389	2544.881	2428.7831(6)
C/MHz	1720.760	1819.110	1758.542	1804.584	1739.6825(6)
d_1/kHz			-13.33	-8.40	-3.88(8)
d_2/kHz			-3.12	-2.64	26.0(3)
d_j/kHz			38.6	23.10	25.71(8)
d_{jk}/kHz			167	177	46(2)
d_k/kHz			-115	-154	-171(8)
h_k					6.29(4)
v				4263	4257.41(4)
rms					9
$\#N$					15

5.3.3 Structure

Table 5.7 provides experimental and theoretically calculated vibrational averaged rotational constants for all the isotopologues. These experimental rotational constants have been used to obtain the structural parameters of the Ar(H₂O)₂ complex. The comparison with theoretical rotational constants helps us to label the isotopologues correctly. The distance between the two oxygen atoms was obtained in the previous work[28]. In this work, we have refined the Ar(H₂O)₂ structure with additional structural parameters and critically compared with the (H₂O)₂ structure.

Kraitchman analysis (r_s) was used to find the distance between the two water dimer units (O_d-O_a) with parent and the singly substituted isotopologues. The distance between the two oxygen atoms in Ar(H₂O)₂ is found out to be 2.946(1) Å (see Table

5.8), which is shorter compared to the water dimer O_d-O_a distance of 2.976(30) Å. The distance between the centre of mass of water dimer and argon atom [Ar-cm(H$_2$O)$_2$] was determined previously as 3.315 Å[28]. The substitution analysis provides only the O_d-O_a distance as the single atom oxygen substitutions are only available.

Table 5.7. Experimental and vibrationally averaged rotational constants calculated at MP2/aug-cc-pVTZ level for all the isotopologues. Rotational constants are in MHz. Inertial defects are in a.m.u.Å^2.

	Ar-H$_2$^{16}O$_a$-H$_2$^{16}O$_d$	Ar-H$_2$^{18}O$_a$-H$_2$^{16}O$_d$	Ar-H$_2$^{16}O$_a$-H$_2$^{18}O$_d$	Ar-H$_2$^{18}O$_a$-H$_2$^{18}O$_d$	Ar-D$_2$^{16}O$_a$-D$_2$^{16}O$_d$
	Experimental				
A	6253.031(2)	5974.807(3)	5938.234(2)	5649.460(2)	5517.465(3)
B	2428.2309(4)	2356.997(1)	2366.5266(8)	2305.5919(7)	2280.931(1)
C	1739.3335(2)	1680.9227(9)	1682.8493(7)	1628.4011(5)	1614.0259(8)
Δ	1.6178	1.6542	1.6525	1.6997	-0.0462
	Ab-initio (MP2/aug-cc-pVTZ)				
A	6237.796	5941.3005	5912.1093	5617.4820	5468.8591
B	2544.881	2443.8797	2450.2159	2387.4655	2360.5260
C	1804.584	1738.6154	1739.2936	1681.9937	1660.6272
Δ	0.448	-1.177	-1.175	-1.181	-2.176

Table 5.8. Kraitchman substitution coordinates (r_s) for the substituted atoms of Ar(H$_2$O)$_2$ complex. Values are in Å. When computing the distance, the imaginary c-coordinates are assumed to be zero.

	|a|	|b|	|c|
O$_a$	1.771(9)	1.427(1)	0.11*i(1)
O$_d$	1.642(1)	1.516(1)	0.11*i(1)
R(O$_a$-O$_d$)		2.946(1)	

Kisiel's STRFIT program[35] was used to fit four other structural parameters of Ar(H$_2$O)$_2$, using four different isotopologues Ar(D$_2$O)$_2$, Ar(H$_2$^{18}O-H$_2$O), Ar(H$_2$O-H$_2$^{18}O),

$Ar(H_2^{18}O)_2$ (see Table 5.9). The ground state rotational constants are fitted directly to the moments of inertia in a non-linear least square procedure. The r_0 fit has been carried out by two means; in one case, the structural values of both the H_2O monomer, i.e., the O-H bond length and the ∠HOH angle, are kept at 0.965 Å and 104.8° respectively (Fit 2, column 3, Table 5.9). In the other case the geometrical values of O-H bond length and the ∠HOH angle have been taken from the vibrationally averaged geometry in the $Ar(H_2O)_2$ complex (Fit 3, column 4, Table 5.9). Lastly, the r_m^1 (mass-weighted technique developed by Watson) was utilised. which takes the vibrational-rotational interaction term into account (Fit 4, column 5, Table 5.9).

The tilt between the acceptor H_2O moiety and the intermolecular axis is fixed at the vibrationally averaged value of 48° in $Ar(H_2O)_2$. In free H_2O dimer; this tilt is 58°(6). This is done since the present parameter and rotational constant combinations do not allow for the simultaneous fitting of all five variables. Four parameters, such as (distance between $O_a \cdots H_4$, the angle between $\angle O_d\text{-}H_4 \cdots O_a$, the distance between $Ar\text{-}O_d$, the angle between $\angle Ar\text{-}O_d\text{-}O_a$) have been evaluated. The hydrogen bond distance $O_a \cdots H_4$ is 2.000(15) Å from r_0 fit, assuming r_0 H_2O monomer geometries (Fit 1). The r_0 fit with calculated H_2O monomer geometries led us to 2.033(37) Å, close to the *ab-initio* $O_a \cdots H_4$ distance calculated at MP2/aug-cc-pVDZ level. The primary difference between the two r_0 fit arises due to different assumed $O_d\text{-}H_4$ donor bond distances in monomer geometry. In Fit 2, the $O_d\text{-}H_4$ distance in the donor water monomer unit is kept at 0.942 Å (vibrationally averaged value). In contrast, in Fit 3, the distance was assumed to be 0.965 Å. interestingly, adding a vibrational-rotation co-efficient (Fit 4, r_m^1) along the a-inertial axis (c_a) decreases the deviation of fit by almost an order of magnitude. The $O_d\text{-}H_4 \cdots O_a$ angle is close to linearity as expected in highly directional hydrogen bonds and matches well with *ab-initio* calculations. Fit 4 dramatically reduces the uncertainty in determining the $\angle O_d\text{-}H_4 \cdots O_a$ angle. The other two parameters are, related to the argon's position with respect to the water dimer. The distance between the $Ar\text{-}O_d$ is ~ 3.597 Å, and the $\angle Ar\text{-}O_d\text{-}O_a$ angle is found out to be ~ 67° irrespective of the nature of fit. As the inertial defect of the complex is close to zero, we can assume a simple triangle with two water spheres and an Argon, which allows us to determine

the Ar-O_a and ∠Ar-O_a-O_d angle using the law of cosines. The Ar-O_a and ∠Ar-O_a-O_d angle is determined to be 3.652 Å and 65° respectively. We used the experimental values from Fit 3 to compare with the *ab-initio* values. The parameters derived from these fits are pretty close to each other. Table 5.10 clearly indicates the vibrationally averaged parameters are in excellent match with experimental values.

Table 5.9. Fitted structural parameters for Ar(H_2O)$_2$ complex. The errors in the fitted value are shown in the parentheses.

Parameters	Fit 1 r_s	Fit 2 r_0 with r_0 H_2O	Fit 3 r_0 with calc. H_2O	Fit 4 r_m^1
[O_d-O_a]/Å	2.946(1)	-	-	-
[O_a···H_4]/Å	-	2.000(15)	2.033(37)	2.083(9)
∠ O_d-H_4···O_a/degree	-	174(28)	169(26)	172(4)
[Ar-O_d]/Å	-	3.598(77)	3.597(64)	3.597(8)
∠Ar-O_d-O_a/degree	-	67(3)	67(2)	66.5(3)
c_a/ uÅ^2	-	-	-	-0.367(14)
σ /uÅ^2	-	1.6	1.3	0.3

Fit 1 refers to the Kraitchman analysis,

Fit 2 and Fit 3 are the r_0 structural fit with r_0 H_2O monomer and vibrationally averaged H_2O monomer in the Ar(H_2O)$_2$ complex.

Fit 4 is similar to Fit 3 but with an additional vibrational-rotation coefficient.

Table 5.10. Structural parameters derived from Ar(H₂O)₂ along with the theoretically predicted values. Theoretical values are from the MP2/aug-cc-pVDZ level of theory.

Parameters	Equilibrium		Vib. Average		Expt.
	MP2 aug-cc-pVDZ	MP2 aug-cc-pVTZ	MP2 aug-cc-pVDZ	MP2 aug-cc-pVTZ	
$[O_d\text{-}O_a]$/Å	2.911	2.899	2.979	2.958	2.946(1)
$[O_a \cdots H_4]$/Å	1.949	1.944	2.042	2.027	2.033(37)
$\angle\, O_d\text{-}H_4 \cdots O_a$/degree	169	168	169	169	169(26)
$[Ar\text{-}O_d]$/Å	3.782	3.582	3.581	3.535	3.597(64)
$\angle Ar\text{-}O_d\text{-}O_a$/degree	62	65	67	66	67(2)
$[Ar\text{-}O_a]$/Å	3.549	3.519	3.645	3.577	*3.652
$\angle Ar\text{-}O_a\text{-}O_d$/degree	71	67	65	65	#65
$Ar\text{-}cm(H_2O)_2$	3.322	3.428	3.389	3.418	**3.315

* Evaluated using the law of cosines from experimental parameters, ** taken from reference [28].

cm refers to the centre of mass.

We compare a few other structural parameters in the $(H_2O)_2$ and $Ar(H_2O)_2$ in Table 5.11. The $H_4 \cdots O_a$ hydrogen bond distance is comparable in both $(H_2O)_2$ and $Ar(H_2O)_2$. Interestingly, the $O_d\text{-}O_a$ distance in the complex [2.946(1)] is shorter than that of the dimer 2.976(30) Å. The experimental difference in $O_d\text{-}O_a$ distance is well supported by theory. Also, hydrogen bond is more deviated from linearity in $Ar(H_2O)_2$ complex (see Figure 5.7).

Table 5.11. Structural changes in (H₂O)₂ upon the formation of Ar(H₂O)₂.

	System	$[O_d\text{-}O_a]$/Å	$[O_a\cdots H_4]$/Å	$\angle\ O_d\text{-}H_4\cdots O_a$/ degree
MP2/aug-cc-pVTZ	$(H_2O)_2$	2.965	2.026	172.0
	$Ar(H_2O)_2$	**2.958**	**2.027**	**168.8**
Experiment	$(H_2O)_2$	2.976(30)	-	-
	$Ar(H_2O)_2$	**2.946(1)**	**2.033(37)**	**169(26)**

Hydrogen bond parameters for some similar weakly bound complexes have been given in Table 5.12. These parameters clearly suggest that they are almost unchanged between $(H_2O)_2$ and $Ar(H_2O)_2$. In $HCl(H_2O)_2$[25] and $HBr(H_2O)_2$[26], the $O_d\text{-}O_a$ distance almost reduces by 0.16 Å compared to that of $(H_2O)_2$. Hydrogen bond distance is also significantly shorter in $HCl(H_2O)_2$ and $HBr(H_2O)_2$ compared to $(H_2O)_2$.

Table 5.12. Hydrogen bond structural parameters for similar complexes.

System	$[O_d\text{-}O_a]$/Å	$[O_a\cdots H_4]$/Å	$\angle\ O_d\text{-}H_4\cdots O_a$/ degree
$Ar(H_2O)_2$	**2.946(1)**	**2.033(37)**	**169(26)**
$HCl(H_2O)_2$[25]	2.810(2)	1.934(2)	149.5(4)
$HBr(H_2O)_2$[26]	2.817(2)	1.917(1)	154.0(3)
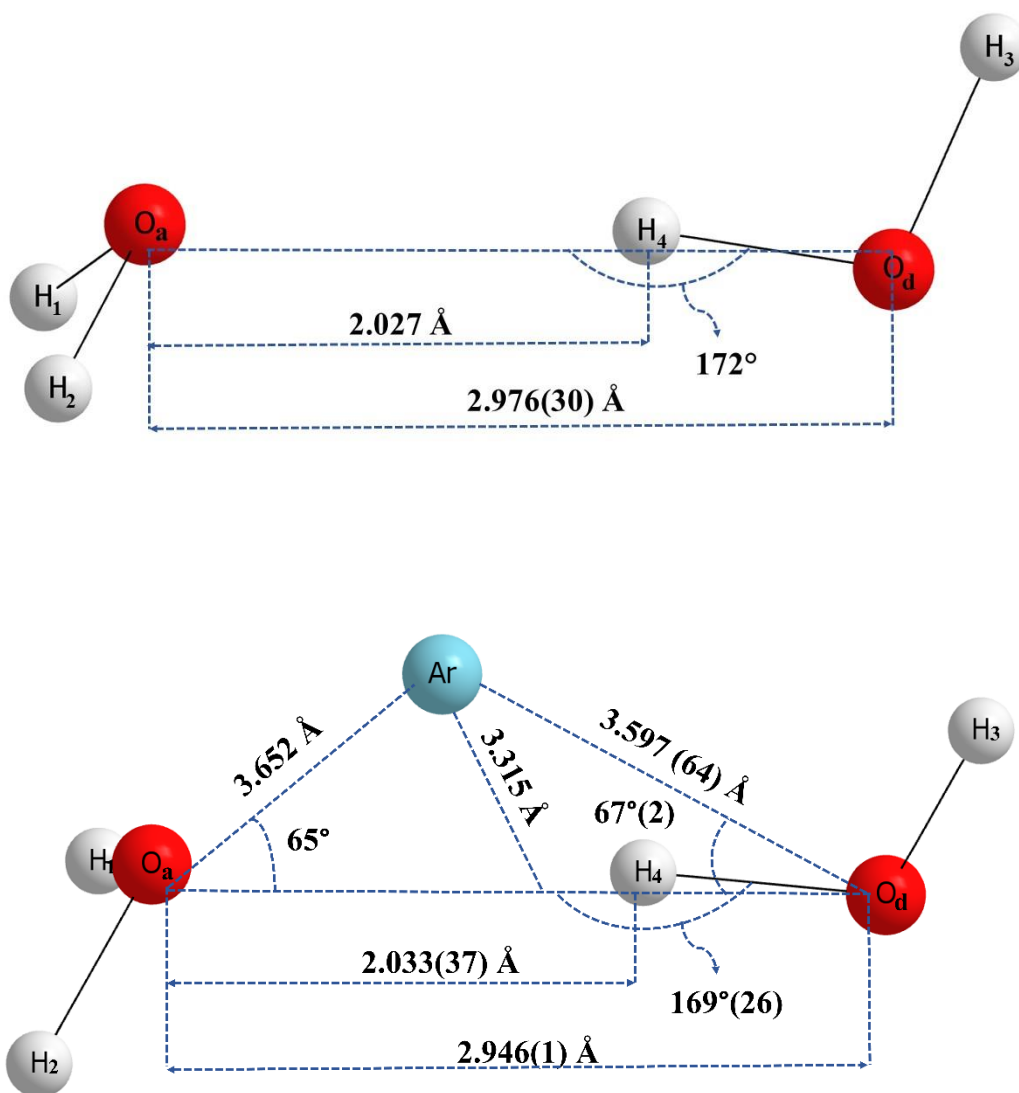
Figure 5.7. Structure of $(H_2O)_2$ and $Ar(H_2O)_2$ derived from the experiment.

5.3.4 **Binding Energy**

We have calculated the binding energy of the complex using the supermolecule approach. The intermolecular binding energy (ΔE) is defined as a difference between the total energy of the complex and the energies of the constituent molecules. For the $Ar(H_2O)_2$ complex binding energy is calculated as follows:

$$E_{int}=[E(Ar(H_2O)_2)]-[E(Ar)+E(H_2O)+E(H_2O)]$$

Basis set superposition error (BSSE) has been corrected using the counterpoise method. The basis set corrected energy is denoted by ΔE_{BSSE}. The binding energy was also corrected for zero-point energy (ZPE). The BSSE and ZPE corrected energy is represented as $\Delta E_{BSSE+ZPE}$. At the MP2/ aug-cc-pVDZ level of theory, the Ar $(H_2O)_2$ complex is almost 1 kJ/mol more strongly bound than the $(H_2O)_2$. This difference is 1.5 kJ/mol at MP2/aug-cc-pVTZ (see Table 5.13). The extra stabilisation in the $Ar(H_2O)_2$ comes from the additional interaction of the $(H_2O)_2$ unit with the Argon atom. Detailed nature of these interactions is investigated in the next section with the help of AIM, NCI and NBO analysis.

Table 5.13. Binding energy of $(H_2O)_2$ and $Ar(H_2O)_2$ calculated at MP2/aug-cc-pVDZ and MP2/aug-cc-pVTZ level of theory with BSSE and zero-point energy (ZPE) correction. Values are given in kJ/mol.

Methods	ΔE	ΔE_{BSSE}	$\Delta E_{BSSE+ZPE}$
MP2//aug-cc-pVDZ			
$(H_2O)_2$	22.0	18.5	9.4
$Ar(H_2O)_2$	25.2	20.1	10.5
MP2//aug-cc-pVTZ			
$(H_2O)_2$	21.7	19.7	11.0
$Ar(H_2O)_2$	25.4	22.2	12.5

5.3.5 Atoms in Molecules (AIM) Analysis

The Atoms in Molecules (AIM) topological study have been used to understand the differences in $(H_2O)_2$ and $Ar(H_2O)_2$ in terms of the bonding perspective. We have compared the properties calculated at the $H_4 \cdots O_a$ hydrogen bond critical point in $(H_2O)_2$, and $Ar(H_2O)$. Bader[36,37] showed that electron density at the bond critical point is a good indicator of the strength of the bonds. The wavefunctions for the Atoms in Molecules (AIM) calculations have been evaluated at MP2/aug-cc-pVDZ and MP2/aug-cc-pVTZ level of theory (see Table 5.14). The values obtained using two different basis sets are consistent with each other. We have used the values obtained from the MP2/aug-cc-pVTZ level of theory for further discussion and comparison.

The electron density at the BCP for $O_a \cdots H_4$ interaction remains similar for both [0.0247 au for $(H_2O)_2$ and 0.0249 au for $Ar(H_2O)_2$] which indicates the hydrogen bond is almost unaffected in going from $(H_2O)_2$ to $Ar(H_2O)_2$. Two additional interactions in $Ar(H_2O)_2$ make the complex 1.5 kJ/mol more stable than that of the $(H_2O)_2$. The $Ar \cdots H_1$ interaction has 0.0058 au electron density at the bond critical point, and the weak $O_d \cdots Ar$ interaction has 0.0031 au electron density at BCP (see Figure 5.8). The electron density is within the range proposed by Koch and Popelier for the C-H$\cdots$O hydrogen bond (0.002 au-0.034 au)[38]. The $(O_d \cdots Ar)$ interaction falls within the electron density range of hydrogen-bonded systems. Also, the other parameters such as the gradient of electron density $(\nabla^2\rho)$, the Hessian eigenvalues $(\lambda_1, \lambda_2, \lambda_3)$, potential energy density (V), kinetic energy density (G) are similar in magnitude for both $(H_2O)_2$ and $Ar(H_2O)_2$ (see Table 5.14). The positive $(\nabla^2\rho)$, $|\lambda_1|/\lambda_3$ ratio < 0.250 and $|V|/G$ ratio <1.000 indicate that all interactions are of the closed-shell type. The $|V|/G$ ratio calculated at $O_a \cdots H_4$ bond critical point using MP2/aug-cc-pVTZ level falls in the intermediate range (1.019) for both $(H_2O)_2$ and $Ar(H_2O)_2$. The $Ar \cdots H_1$ and $O_d \cdots Ar$ interactions have low $|V|/G$ ratio and $|\lambda_1|/\lambda_3$ ratio, indicative of closed-shell interaction.
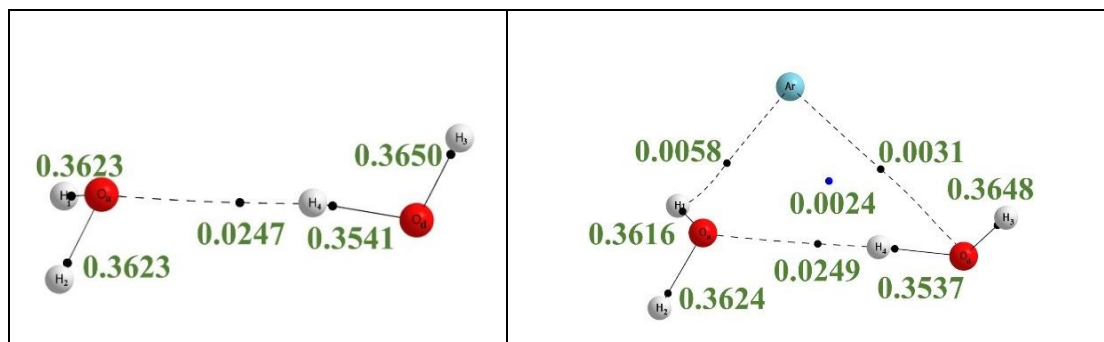
Figure 5.8. Atoms in Molecules (AIM) topology study for (H₂O)₂ (right) and Ar(H₂O)₂ (left). The black dots and blue dots refer to the bond critical point and ring critical point, respectively.

Table 5.14. Properties calculated from Atoms in Molecules (AIM) analysis. Wave functions used for the calculations are evaluated at the MP2/aug-cc-pVDZ and MP2/aug-cc-pVTZ levels of theory. Values are in au.

	$\rho(r)$	$\nabla^2\rho$	λ_1	λ_2	λ_3	$|\lambda_1|/\lambda_3$	V	G	|V|/G
				MP2/aug-cc-pVDZ level					
				Properties at the Oₐ•••H₄ BCP					
(H₂O)₂	0.0238	0.0870	-0.0300	-0.0295	0.1464	0.205	-0.0174	0.0196	0.888
Ar(H₂O)₂	0.0239	0.0866	-0.0302	-0.0294	0.1462	0.207	-0.0175	0.0196	0.893
				Properties at the Ar•••O_d BCP					
Ar(H₂O)₂	0.0023	0.0092	-0.0015	-0.0013	0.0120	0.125	-0.0013	0.0018	0.722
				Properties at the Ar•••H₁ BCP					
Ar(H₂O)₂	0.0055	0.0211	-0.0048	-0.0045	0.0304	0.158	-0.0037	0.0045	0.822
				MP2/aug-cc-pVTZ level					
				Properties at the Oₐ•••H₄ BCP					
(H₂O)₂	0.0247	0.0819	-0.0369	-0.0360	0.1548	0.238	-0.0213	0.0209	1.019
Ar(H₂O)₂	0.0249	0.0822	-0.0371	-0.0362	0.1554	0.239	-0.0214	0.0210	1.019
				Properties at the Ar•••O_d BCP					

Continued Table 5.14…

Ar(H$_2$O)$_2$	0.0031	0.0121	-0.0021	-0.0017	0.0159	0.132	-0.0017	0.0023	0.739

Properties at the Ar•••H$_1$ BCP									
Ar(H$_2$O)$_2$	0.0058	0.0232	-0.0052	-0.0044	0.0328	0.159	-0.0034	0.0046	0.739

5.3.6 Non-covalent Interactions (NCI) Index

The other interactions in the Ar(H$_2$O)$_2$ complex are confirmed by the non-covalent index (NCI) plot. Non-Covalent Index (NCI)[39,40,41] plots were obtained using Multiwfn 3.6[42] with two functions. The function 1 (on the *X*-axis) is the multiplication of the sign of the second Eigenvalue (λ_2) of electron density Hessian matrix with the electron density (ρ) [(sign (λ_2*ρ)], and function 2 (on *Y*-axis) reduced density gradient. (RCP). One trough has been observed for the O$_a$···H$_4$ hydrogen bond in (H$_2$O)$_2$. In contrast, Ar(H$_2$O)$_2$ shows two more additional interactions, similar to what was found in the AIM analysis, along with one ring critical point (RCP) (see Figure 5.9) . Atoms in Molecules (AIM) and NCI plots agree with each other.
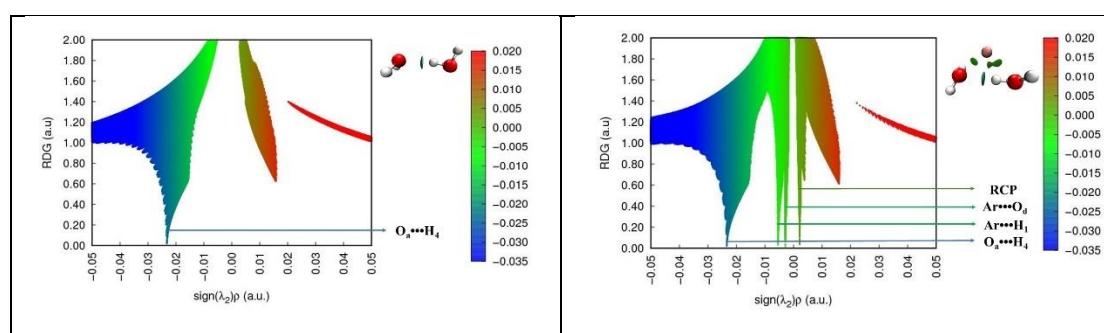
Figure 5.9. Non-covalent interactions (NCI) index plots for (H$_2$O)$_2$ (on left) and Ar(H$_2$O)$_2$ (on right). The additional trough are observed in Ar(H$_2$O)$_2$ due to other interactions (Ar···H$_1$, Ar···O$_d$, and RCP).

5.3.7 **Natural Bond Orbital (NBO) Analysis**

We have carried out natural bond orbital (NBO) analysis for $Ar(H_2O)_2$ complex using NBO 6.0 software[43]. Figure 10 shows two major stabilization interactions in the $Ar(H_2O)_2$ complex. The first one is the, $n_{O_a} \rightarrow \sigma^*_{O_d-H_4}$ which is the typical H-bond interaction present in hydrogen bonded complexes. The $Ar(H_2O)_2$ complex has a second-order perturbation energy of 41.5 kJ/mol at the MP2/aug-cc-pVDZ level, which is similar to $(H_2O)_2$ (see Table 5.15). At MP2/aug-cc-pVTZ level, we have observed slightly favourable $n_{O_a} \rightarrow \sigma^*_{O_d-H_4}$ interaction for the $Ar(H_2O)_2$ complex.

An additional $n_{Ar} \rightarrow \sigma^*_{O_a-H_1}$ interaction has been found in $Ar(H_2O)_2$ complex, with 2.4 kJ/mol second-order perturbation energy. Unlike, AIM and NCI analysis, NBO analysis does not show any significant second order perturbation energy for the $Ar \cdots O_d$ interaction.

$$n_{O_a} \rightarrow \sigma^*_{O_d-H_4} \qquad\qquad n_{Ar} \rightarrow \sigma^*_{O_a-H_1}$$
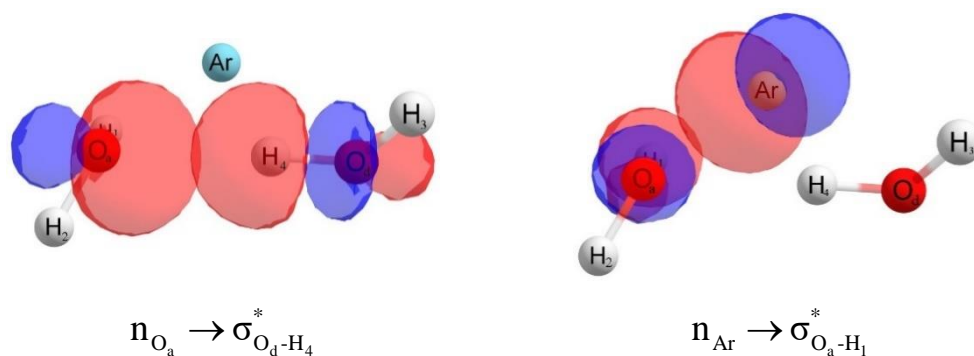
Figure 5.10. Interacting natural bond orbitals in Ar(H₂O)₂ complex.

Table 5.15. Interacting natural bond orbitals with the respective second-order perturbation energies calculated at MP2/aug-cc-pVDZ and MP2/aug-cc-pVTZ level of theory. Values are in kJ/mol.

Interaction	$Ar(H_2O)_2$	
	MP2/ aug-cc-pVDZ	MP2/ aug-cc-pVTZ
$n_{O_a} \rightarrow \sigma^*_{O_d-H_4}$	41.5	30.9
$n_{Ar} \rightarrow \sigma^*_{O_a-H_1}$	2.4	0.9
	$(H_2O)_2$	
$n_{O_a} \rightarrow \sigma^*_{O_d-H_4}$	41.5	30.3

In Table 5.16, occupation number for donor lone pair (n_{O_a}) and acceptor antibonding orbital ($\sigma^*_{O_d-H_4}$) have been provided for H_2O monomer, $(H_2O)_2$, and $Ar(H_2O)_2$. Hydrogen bonding is often interpreted as $n \rightarrow \sigma^*$ interaction, so we expect the occupation number of n_{O_a} NBO will decrease after the formation of $(H_2O)_2$ and $Ar(H_2O)_2$. Similarly, the occupation number $\sigma^*_{O_d-H_4}$ will increase after the formation of the complexes. We have found this both in $(H_2O)_2$ and $Ar(H_2O)_2$. The population difference in $(H_2O)_2$ (dimer) and $Ar(H_2O)_2$ (trimer) is denoted as $\Delta_{Mono-Dimer}$ and $\Delta_{Mono-Trimer}$, respectively. The $\Delta_{Mono-Trimer}$ is slightly higher for both the donor and acceptor orbital indicating slightly feasible charge transfer.

Table 5.16. NBO Population analysis for H_2O, $(H_2O)_2$ (referred to as dimer) and $Ar(H_2O)_2$ (referred to as trimer).

Donor					
Monomer	Dimer	$\Delta_{\text{Mono-Dimer}}$	Monomer	Trimer	$\Delta_{\text{Mono-Trimer}}$
n_O	n_{O_a}		n_{O_a}	n_{O_a}	
1.99792	1.98950	**-0.00842**	1.99792	1.98910	**-0.00882**
Acceptor					
$\sigma^*_{O\text{-}H}$	$\sigma^*_{O_d\text{-}H_4}$		$\sigma^*_{O_d\text{-}H_4}$	$\sigma^*_{O_d\text{-}H_4}$	
0.00000	0.00901	**0.00901**	0.00000	0.00932	**0.00932**

5.4 **Summary**

In summary, the present observation of the *b*-dipole A_1 state transitions of the $Ar(H_2O)_2$ facilitates the direct measurement of the proton tunnelling splitting. A simple one-dimensional tunnelling model with scaled potential almost accurately predicts the tunnelling splitting. We expect these results will motivate renewed theoretical initiatives to use these precision spectroscopic data to construct accurate intermolecular potentials. The hydrogen bond in $(H_2O)_2$ remains unaffected in $Ar(H_2O)_2$. Also in this Chapter, we have refined the structural parameters of $Ar(H_2O)_2$ and compared with the $(H_2O)_2$. Two additional interactions are identified in $Ar(H_2O)_2$ using Atoms in Molecules (AIM) and non-covalent interactions (NCI) index.

5.5 **References**

1. Legon, A. C. Tetrel, pnictogen and chalcogen bonds identified in the gas phase before they had names: A systematic look at non-covalent interactions. *Phys. Chem. Chem. Phys.* **19**, 14884–14896 (2017).

2. Juanes, M., Saragi, R. T., Caminati, W. & Lesarri, A. The Hydrogen Bond and Beyond: Perspectives for Rotational Investigations of Non-Covalent

Interactions. *Chem. Eur. J.* (2019).

3.   Gnanasekar, S. P. & Arunan, E. Molecular Beam and Spectroscopic Techniques: Towards Fundamental Understanding of Intermolecular Interactions/Bonds, *Intermolecular Interactions in Crystal, Ed* Novoa, J. J, The Royal Society of Chemistry (2018).

4.   Dyke, T. R., Mack, K. M. & Muenter, J. S. The structure of water dimer from molecular beam electric resonance spectroscopy. *J. Chem. Phys.* **66**, 498–510 (1977).

5.   Dyke, T. R. & Muenter, J. S. Microwave spectrum and structure of hydrogen bonded water dimer. *J. Chem. Phys.* **60**, 2929–2930 (1974).

6.   Zwart, E., Ter Meulen, J. J., Meerts, W. L. & Coudert, L. H. The submillimeter rotation tunneling spectrum of the water dimer. *J. Mol. Spectrosc.* **147**, 27–39 (1991).

7.   Zwart, E., Ter Meulen, J. J. & Meerts, W. L. The submillimeter rotation tunneling spectrum of $(D_2O)_2$. *Chem. Phys. Lett.* **173**, 115–121 (1990).

8.   Vaillant, C. L. & Cvitaš, M. T. Rotation-tunneling spectrum of the water dimer from instanton theory. *Phys. Chem. Chem. Phys.* **20**, 26809–26813 (2018).

9.   Karyakin, E. N., Fraser, G. T. & Suenram, R. D. Microwave spectrum of the K a= 1← 0 rotation-tunnelling band of $(D_2O)_2$. *Mol. Phys.* **78**, 1179–1189 (1993).

10.   Busarow, K. L. *et al.* Measurement of the perpendicular rotation-tunneling spectrum of the water dimer by tunable far infrared laser spectroscopy in a planar supersonic jet. *J. Chem. Phys.* **90**, 3937–3943 (1989).

11.   Bartashevich, E. & Tsirelson, V. A comparative view on the potential acting on an electron in a molecule and the electrostatic potential through the typical halogen bonds. *J. Comput. Chem.* **39**, 573–580 (2018).

12.   Coudert, L. H. & Hougen, J. T. Analysis of the microwave and far infrared spectrum of the water dimer. *J. Mol. Spectrosc.* **139**, 259–277 (1990).

13. Hougen, J. T. A generalized internal axis method for high barrier tunneling problems, as applied to the water dimer. *J. Mol. Spectrosc.* **114**, 395–426 (1985).

14. Coudert, L. H. & Hougen, J. T. Tunneling splittings in the water dimer: Further development of the theory. *Journal of Molecular Spectroscopy* vol. 130 86–119 (1988).

15. Coudert, L. H. & Hougen, J. T. Tunneling splittings in the water dimer: Further development of the theory. *J. Mol. Spectrosc.* **130**, 86–119 (1988).

16. Taketsugu, T. & Wales, D. J. Theoretical study of rearrangements in water dimer and trimer. *Mol. Phys.* **100**, 2793–2806 (2002).

17. Karyakin, E. N., Fraser, G. T., Lovas, F. J., Suenram, R. D. & Fujitake, M. Donor–acceptor interchange tunneling in HDO–DOH and the higher energy HDO–HOD isotopomer. *J. Chem. Phys.* **102**, 1114–1121 (1995).

18. Smith, B. J., Swanton, D. J., Pople, J. A., Schaefer III, H. F. & Radom, L. Transition structures for the interchange of hydrogen atoms within the water dimer. *J. Chem. Phys.* **92**, 1240–1247 (1990).

19. Harker, H. A. *et al.* Toward a precise determination of the acceptor switching splitting in the water dimer. *Mol. Phys.* **105**, 497–512 (2007).

20. Coudert, L. H., Lovas, F. J., Suenram, R. D. & Hougen, J. T. New measurements of microwave transitions in the water dimer. *J. Chem. Phys.* **87**, 6290–6299 (1987).

21. Suenram, R. D., Fraser, G. T. & Lovas, F. J. Microwave spectrum of $(D_2O)_2$. *J. Mol. Spectrosc.* **138**, 440–449 (1989).

22. Fraser, G. T., Suenram, R. D. & Coudert, L. H. Microwave electric-resonance optothermal spectroscopy of $(H_2O)_2$. *J. Chem. Phys.* **90**, 6077–6085 (1989).

23. Fraser, G. T., Suenram, R. D., Coudert, L. H. & Frye, R. S. Electric-resonance optothermal spectrum of $(H_2O)_2$: Microwave spectrum of the K= 1-0 subband for the $E_2^{\pm}$ states. *J. Mol. Spectrosc.* **137**, 244–247 (1989).

24. Watanabe, Y., Taketsugufoot, T. & Wales, D. J. An ab initiostudy of tunneling splittings in the water dimer. *J. Chem. Phys.* **120**, 5993–5999 (2004).

25. Kisiel, Z. *et al.* Structure and properties of the weakly bound trimer $(H_2O)_2HCl$ observed by rotational spectroscopy. *J. Chem. Phys.* **112**, 5767–5776 (2000).

26. Kisiel, Z. *et al.* Structure and properties of the weakly bound cyclic trimer $(H_2O)_2$ HBr observed by rotational spectroscopy. *J. Chem. Phys.* **119**, 5907–5917 (2003).

27. Arunan, E., Emilsson, T. & Gutowsky, H. S. Rotational Spectra, Structure, and Dynamics of Ar_m-$(H_2O)_n$ Clusters: Ar_2-H_2O, Ar_3-H_2O, Ar-$(H_2O)_2$, and Ar-$(H_2O)_3$. *J. Am. Chem. Soc.* **116**, 8418–8419 (1994).

28. Arunan, E., Emilsson, T. & Gutowsky, H. S. Rotational spectra, structures, and dynamics of small Ar_m-$(H_2O)_n$ clusters: The Ar-$(H_2O)_2$ trimer. *J. Chem. Phys.* **116**, 4886–4895 (2002).

29. Arunan, E., Tiwari, A. P., Mandal, P. K. & Mathias, P. C. Pulsed nozzle Fourier transform microwave spectrometer: Ideal to define hydrogen bond radius. *Current Science* vol. 82 533–540 (2002).

30. Fraser, G. T. *et al.* Infrared and microwave investigations of interconversion tunneling in the acetylene dimer. *J. Chem. Phys.* **89**, 6028–6045 (1988).

31. Lewis, J. D., Malloy Jr, T. B., Chao, T. H. & Laane, J. Periodic potential functions for pseudorotation and internal rotation. *J. Mol. Struct.* **12**, 427–449 (1972).

32. Lewis, J. D. & Laane, J. Periodic potential energy functions with sine and cosine terms. *J. Mol. Spectrosc.* **65**, 147–154 (1977).

33. Watanabe, Y., Taketsugu, T. & Wales, D. J. An ab initio study of tunneling splittings in the water dimer. *J. Chem. Phys.* **120**, 5993–5999 (2004).

34. Frisch, M. J. *et al.* Gaussian 09 Revision D. 01, 2009. *Gaussian Inc. Wallingford CT* (2009).

References

35. Kisiel, Z. Least-squares mass-dependence molecular structures for selected weakly bound intermolecular clusters. *J. Mol. Spectrosc.* **218**, 58–67 (2003).

36. Bader, R. F. W. Atoms in Molecules: A Quantum Theory: Oxford Univ. Press. (1990).

37. Keith, T. A. AIMAll (Version 14.11. 23). *TK Gristmill Software, Overl. Park KS, USA* (2014).

38. Koch, U. & Popelier, P. L. A. Characterization of CHO hydrogen bonds on the basis of the charge density. *J. Phys. Chem.* **99**, 9747–9754 (1995).

39. Johnson, E. R. *et al.* Revealing noncovalent interactions. *J. Am. Chem. Soc.* **132**, 6498–6506 (2010).

40. Contreras-García, J. *et al.* NCIPLOT: a program for plotting noncovalent interaction regions. *J. Chem. Theory Comput.* **7**, 625–632 (2011).

41. Contreras-García, J., Yang, W. & Johnson, E. R. Analysis of hydrogen-bond interaction potentials from the electron density: integration of noncovalent interaction regions. *J. Phys. Chem. A* **115**, 12983–12990 (2011).

42. Lu, T. & Chen, F. Multiwfn: a multifunctional wavefunction analyzer. *J. Comput. Chem.* **33**, 580–592 (2012).

43. Glendening, E. D., Landis, C. R. & Weinhold, F. NBO 6.0: natural bond orbital analysis program. *J. Comput. Chem.* **34**, 1429–1437 (2013).

5.6 Supplementary Information

Table S5.1. Coordinates of vibrationally averaged of Ar(H$_2$O)$_2$ complex, optimised at MP2/aug-cc-pVDZ level.

Atom	x(Å)	y(Å)	z(Å)
O$_a$	-1.474263	-1.572744	-0.094734
H$_1$	-0.594226	-1.776509	-0.201336
H$_2$	-1.720024	-2.029553	0.598068
O$_d$	-1.626232	1.396990	0.082049
H$_3$	-2.280859	1.751048	-0.368808
H$_4$	-1.691734	0.456349	-0.025104
Ar	1.732401	0.157074	0.005304

Table S5.2. Coordinates of vibrationally averaged geometry of Ar(H$_2$O)$_2$ complex, optimised at MP2/aug-cc-pVTZ level.

Atom	x(Å)	y(Å)	z(Å)
O$_a$	1.683901	1.504171	-0.040876
H$_1$	0.837558	1.745302	-0.096162
H$_2$	1.988969	1.995526	0.602842
O$_d$	1.711831	-1.452515	0.033910
H$_3$	2.335680	-1.826497	-0.403226
H$_4$	1.820581	-0.518529	-0.029374
Ar	-1.535241	-0.055876	0.000920

Table S5.3. Coordinates of equilibrium geometry of Ar(H₂O)₂ complex, optimised at MP2/aug-cc-pVDZ level.

Atom	x(Å)	y(Å)	z(Å)
O_a	-1.400700	1.479670	0.104381
H_1	-0.461312	1.570168	-0.105957
H_2	-1.847889	2.011626	-0.567196
O_d	-1.787598	-1.397341	-0.110006
H_3	-2.265848	-1.736082	0.656518
H_4	-1.753109	-0.435745	0.034631
Ar	1.768586	-0.114922	0.001500

Table S5.4. Coordinates of equilibrium geometry of Ar(H₂O)₂ complex, optimised at MP2/aug-cc-pVDZ level

Atom	x(Å)	y(Å)	z(Å)
O_a	1.648612	1.455740	-0.054824
H_1	0.695957	1.585940	0.004379
H_2	1.996980	1.917324	0.714159
O_d	1.757962	-1.439470	0.051824
H_3	2.371426	-1.797350	-0.594815
H_4	1.843603	-0.478542	-0.037728
Ar	-1.537693	-0.037465	-0.000747

Table S5.5. Vibrationally averaged rotational constants calculated from different theory and basis sets. Experimental rotational constants are from the E state.

Methods	A/MHz	B/MHz	C/MHz
D2-B3LYP//6-311++g(d,p)	6240.124	2700.454	1897.701
D3-B3LYP//6-311++g(d,p)	6540.147	2372.178	1744.011
M06-2X//6-311++g(3df,3pd)	6263.966	2048.409	1551.927
MP2/6-311++g(3d,3p)	6182.832	2413.752	1734.190
wb97xd//6-311++g(d,p)	6642.045	2977.103	2113.516
b97d//6-311++g(d,p)	6623.791	1770.544	1384.994
MP2//aug-cc-pVDZ	6120.376	2468.389	1758.542
MP2(full)//aug-cc-pVDZ	6027.618	2571.440	1809.696
MP2//aug-cc-pVTZ	6237.796	2544.881	1804.584
*Experiment	6253.031(2)	2428.2309(4)	1739.3335(2)

Table S5.6. Mulliken, APT, AIM and NBO charges on $Ar(H_2O)_2$ calculated at MP2/aug-cc-pVTZ level of theory.

Atoms	Mulliken	APT	AIM	NBO
O_a	-0.431	-0.557	-1.222	-0.946
H_1	0.236	0.283	0.620	0.479
H_2	0.208	0.269	0.618	0.476
O_d	-0.501	-0.593	-1.257	-0.966
H_3	0.191	0.244	0.596	0.459
H_4	0.300	0.357	0.643	0.497
Ar	-0.003	-0.002	0.002	0.001

Table S5.7. Anharmonic frequencies of $(H_2O)_2$ & $Ar(H_2O)_2$ were calculated at MP2/aug-cc-pVTZ level of theory. The labellings of normal modes are according to $(H_2O)_2$

Modes(cm^{-1})	$(H_2O)_2$	$Ar(H_2O)_2$	Difference (cm^{-1})
ν_{12}	86	80	-6
ν_{11}	125	119	-6
ν_8	117	123	6
ν_7	140	139	-1
ν_6	304	320	16
ν_{10}	503	492	-11
ν_5	1586	1583	-3
ν_4	1597	1597	0
ν_3	3583	3577	-6
ν_2	3646	3644	-2
ν_1	3740	3740	0
ν_9	3755	3751	-4
Modes involving Ar		32	
		48	
		50	

$\nu_{12=}86/80$

$\nu_{11=}125/119$

$\nu_8=117/123$

$\nu_7=140/139$

$\nu_6=304/320$

$\nu_{10}=503/492$

$\nu_5=1586/1583$

$\nu_4=1597/1597$

$\nu_3=3583/3577$

$\nu_2=3646/3644$

$\nu_1=3740/3740$

$\nu_9=3755/3751$

32

48

50
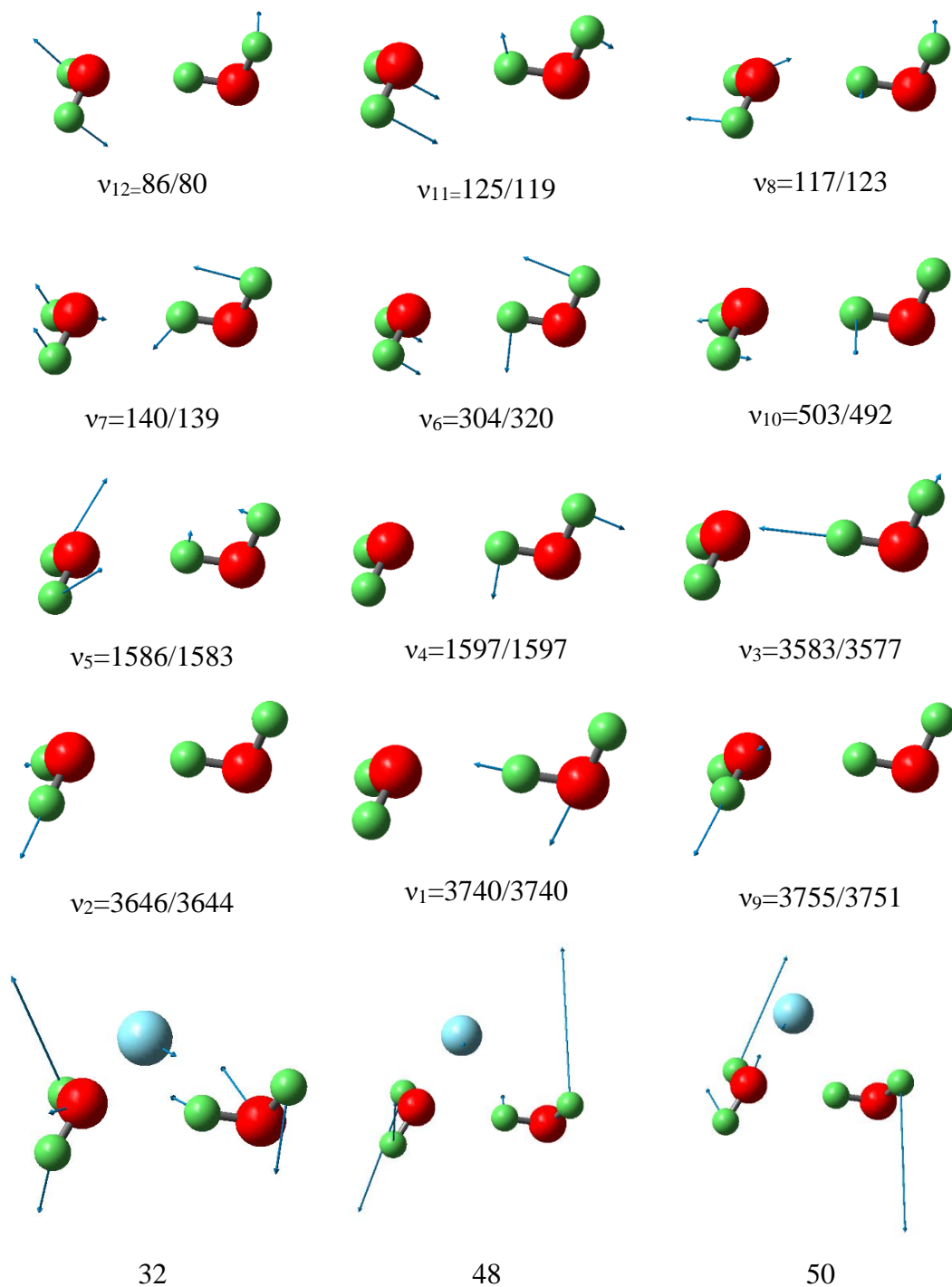
Figure S5.1. Displacements for anharmonic normal modes of $(H_2O)_2/Ar(H_2O)_2$. Values are in cm^{-1}.

This page intentionally left blank.

CHAPTER

6

Periodic Table of Intermolecular Bonding

This page intentionally left blank.

Chapter 6: Periodic Table of Intermolecular Bonding

6.1 Introduction

The years 2019 and 2020 were celebrated for two historical landmark discoveries in chemistry. Dmitri Mendeleev published the first recognizable form of the Periodic Table in 1869 by listing the elements in rows or columns in order of atomic weights, 2019 marked as the 150th anniversary of the Periodic Table. On the other hand, Wendell M. Latimer and Worth H. Rodebush's paper[1] in 1920, which was credited by Linus Pauling in his classic book[2] as the first to mention hydrogen bond, celebrated its 100th anniversary in 2020. Until hydrogen bonding was well recognised, all intermolecular interactions were called van der Waals interactions, as the equation was the first to formally recognize attractive forces between molecules. Today we know that the study of intermolecular bonding does not limit to hydrogen bonds, and it extends to other elements. Non-covalent interactions have been well accepted as the description of all these interactions, as it was commonly accepted that a covalent bond would not exist between molecules[3]. In this context, the Periodic Table provides a consistent and systematic description of intermolecular bonds formed by the various groups of elements.

In the last two decades, there have been enormous efforts to identify, name, and define intermolecular bonding. These efforts are well justified by looking at the importance of intermolecular bonding in the various fields of basic science and crystal engineering. For example, a carbon bond could play a stabilizing role in the intermediate to S_N2 reaction, as pointed out by Mani and Arunan[4]. Soon after the discovery of carbon bond[5], intermolecular interactions involving other congeners of group 14 have been studied, and two different research groups simultaneously came up with the name 'Tetrel bond[6,7] for group 14 elements. As discussed in the Chapter 1, the other groups of p-block are now given a name for each in terms of intermolecular bonding, such as Triel bonds[8] (group 13), and Pnictogen bond (group 15)[9,10,11,12], Chalcogen bond[13,14,15,16] (group 16), Halogen bond[17,18,19,20,21] (group 17), Aerogen bond[22,23](renamed as noble gas bond)

(group 18) (see Figure 6.1). Apart from the p-block elements, intermolecular bonds involving transitions metals have also been recognised[24,25]; a common name for group 10 and group 11 (known as metal-coinage bond[26]) is proposed as Regium bond[27]. More recently, the new name Spodium bond is recommended for group 12[28,29].

Other than hydrogen bonds, amongst the group 1 metals, lithium and sodium bonds are reported in the literature. Kollman, Liebman, and Allen[30] theoretically predicted lithium bond in the early 1970s. Ault and Pimentel[31] demonstrated its existence with the help of matrix isolation experiments. There have been some theoretical reports on sodium bonding as well[32,33,34]. To the best of our knowledge, intermolecular bonding involving the remaining members of group 1 has not yet been investigated. Besides hydrogen bond, Alkorta recently proposes to call the intermolecular bond formed by group 1 metals as Alkali bonds[29].

The dissimilarities in bonding nature in hydrogen and the rest of the members are noted by many. Shahi and Arunan[35] showed the extrapolation of binding energy versus electron density (at the bond critical point) plot for Li-bond leads towards the ionic bond. In contrast, H-bond leads towards covalent bonds[35] as the slopes for Li bond and H-bond are significantly different. Hydrogen is unique, and its position in the Periodic Table is debatable. Various forms of the Periodic Table also highlighted this fact. Figure 6.2 shows the three different forms of the modern Periodic Table from the International Union of Pure and Applied Chemistry (IUPAC), American Chemical Society (ACS) & Royal Society of Chemistry (RSC). IUPAC Periodic Table is the simplest one; only the Lanthanides and Actinides are coloured. The RSC Periodic Table is more colourful. Each group is marked with a different colour. Interestingly hydrogen is marked with a different colour though it belongs to the group 1 element. On the other hand, a similar colour with a slightly different shade was used for the alkali and alkaline earth metals. ACS Periodic Table is more thoughtful, and it differentiates elements based on their nature, such as metals, non-metals, metalloids. Both RSC and ACS Periodic Tables reflect the uniqueness of hydrogen in the Periodic Table from the rest of the group congeners. Hydrogen bonding is dissimilar from its group congeners when it forms an

intermolecular bond with a Lewis acceptor. The uniqueness and versatility of hydrogen bonds have motivated the International Union of Pure and Applied Chemistry (IUPAC)[36,37] to redefine the hydrogen bond comprehensively in 2011.

In group 2, intermolecular bonding involving beryllium[38,39,40,41,42], magnesium[43,44,45,46], and calcium[47] have been theoretically investigated in the last decade. Beryllium bond was identified while studying the interaction of BeX_2 (X=H, F, Cl, OH) with different Lewis bases[38]. Beryllium bond has been used to turn the conventional bases into gas-phase superacids[48], exergonic and spontaneous formation of radicals[49] and design anion-sponges[50]. Magnesium bond was proposed in $LiNH_2 \cdots HMgX$ (X=OH, F, Cl, Br, CH_3, OH, and NH_2) complexes[43]. Due to its relevance in cell biology and synthetic organic chemistry (Grignard reagents), the precise nature of the magnesium bond was studied. Calcium bond was studied in view of acidity enhancements[47]. There have been several reports on π-beryllium[51], π-magnesium[52] bond, mutual cooperativity of Be[39,53,54,55,56] and Mg-Bond[46,57] with other weak intermolecular bonds. Alkorta and Legon[58] recently called the group 2 bond as 'Alkaline earth bonds' and defined the intermolecular bonding in group 2 as *"An alkaline-earth non-covalent bond occurs when there is evidence of a net attractive interaction between an electrophilic region associated with an atom of an element, E{II}, in a molecular entity and a nucleophilic region (e.g., an n-pair or π-pair of electrons) in another, or the same, molecular entity, where E{II} is an element of Group II in the Periodic Table."*

Interestingly, the previous studies on beryllium and the rest of the group 2 members, in terms of their homonuclear dimers and clusters, infer that the bonding nature of beryllium is remarkably different from its other congeners[59]. In group 2 elements, the formal bond order of homonuclear dimers turned out to be zero. However, these dimers have been observed experimentally. The trends in measured spectroscopic parameters such as bond dissociation energies, ground-state vibrational frequencies, and force constants are quite obvious for group 1 dimers. However, the trend is ambiguous for group 2 homonuclear dimers. In going from beryllium dimer (D_e= 929.7 cm^{-1}) to magnesium dimer (D_e= 403.0cm^{-1}), bond dissociation energy decreases by a factor of

almost two which is also reflected in the force constant values (k [Be$_2$]=19.46 Nm^{-1} k [Mg$_2$]=1.85Nm^{-1}) of the dimers[60,61]. The striking conflict in the beryllium and magnesium is not merely in terms of their dimers; higher clusters also reflect the same. In going from dimer to cyclic trimer, the bond energy increases by a factor of three (Be$_3$=25.9 kcal/mol, Mg$_3$=7.12 kcal/mol)[62]. Be$_4$ and Mg$_4$ also show different characteristics, like Mg$_4$ has a smaller electron affinity than Be$_4$. The smaller affinities of the magnesium cluster appear to be due to the greater repulsive nature of their potential surfaces[63]. The small size, high charge density, greater electronegativity, and ability to form strong covalent bonds help beryllium to form complexes, even in a zero-valent state with the aid of non-heterocyclic carbene[64]. This kind of zero-valent species is not known for other congeners of alkaline earth metals.

This Chapter looks beyond hydrogen bonding and explores other intermolecular interactions across the Periodic Table. For each main group element, the slopes of the binding energy versus electron density (at the bond critical point) plots were obtained. The slopes for Li, Na, Be, Mg, Ca-bonds were found out to be comparable, whereas the slope for the hydrogen bond remains distinctly different. Hence, instead of alkali and alkaline earth bonds for group 1 and group 2, we propose to call intermolecular bonding involving both groups (except H) as *"alkalene bond"*.

Figure 6.1. The Periodic Table in its modern version, with various names of intermolecular bonds (in black). A common name for Group 1 (except hydrogen, hydrogen bond remains unique among its group congeners) and Group 2 has been proposed as the 'alkalene bond' (in red).
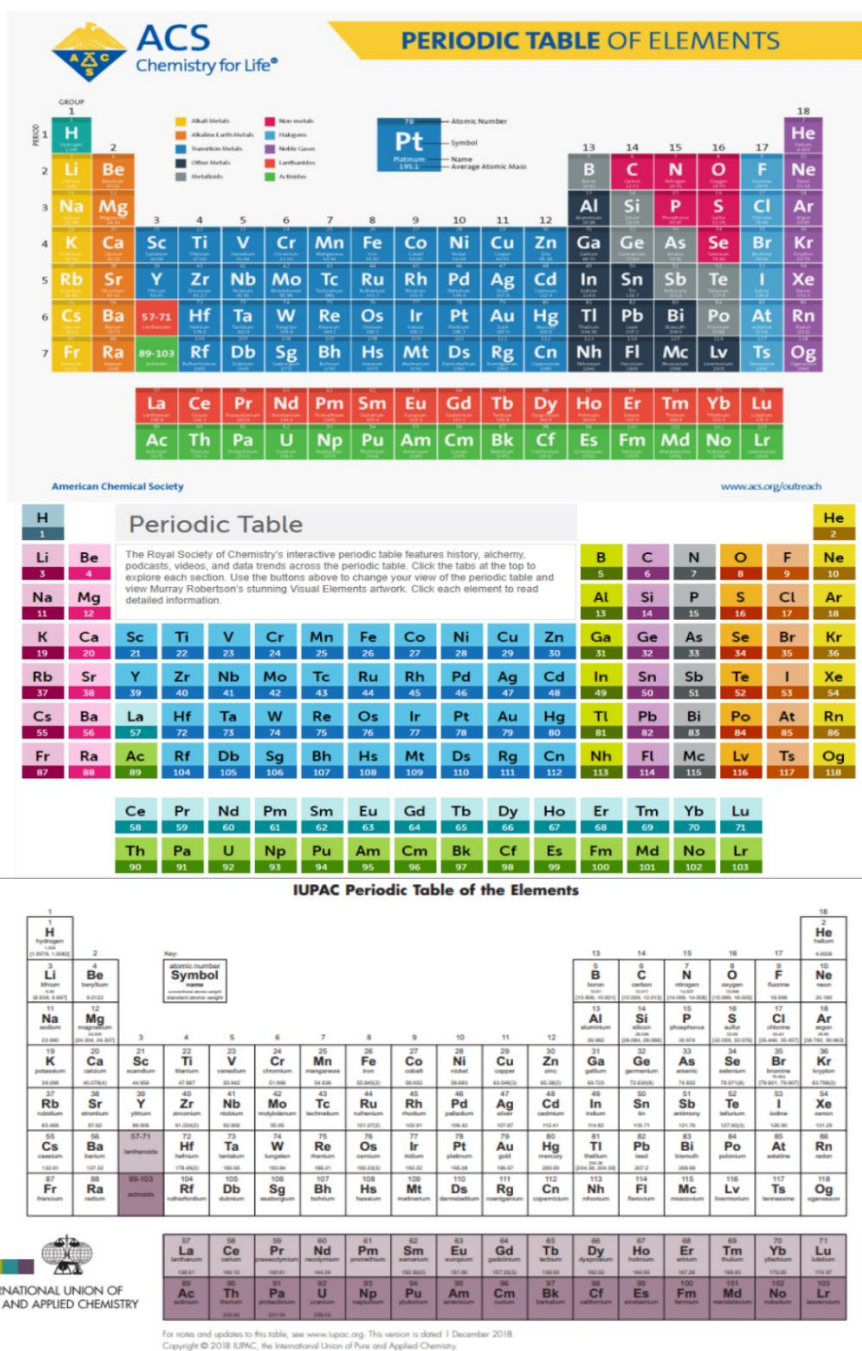
Figure 6.2. Periodic Table of the elements from ACS (top), RSC (middle) & IUPAC (bottom).

ACS: https://www.acs.org/content/acs/en/education/whatischemistry/periodictable.html

RSC: https://www.rsc.org/periodic-table

IUPAC: https://iupac.org/what-we-do/periodic-table-of-element

6.2 Computational Details

All the geometry optimisation has been performed using the Gaussian 09[65] suite of programs using the MP2 level[66] of theory. We have used Pople 6-311++G(2df,p) basis set for the optimisation for Ca-bonded complexes. Pseudopotential-based augmented correlation-consistent basis sets, aug-cc-pVDZ-PP[67] based on the small core relativistic PPs[68] were used for post-d-group 13-17 elements downloaded from the basis set exchange database[69]. For all other elements, the aug-cc-PVDZ basis has been used[70]. Although the geometry and binding energies of several of these complexes have already been reported in the literature, we computed them again to avoid method and basis set inconsistency. Frequency calculations are performed using the same level of theory for all the complexes to confirm that the obtained structures correspond to true energy minima. For each element, thirty complexes with three separate donors and ten different acceptors (mostly H_2O, NH_3, H_2S, PH_3, HCHO, C_2H_4, HCN, CO, $CH_3OH.CH_3OCH_3$) of varying nucleophilicity were studied to characterise the intermolecular bonds. Interaction energies have been calculated as the difference between complex energy and the sum of the energies of the monomers, using the supermolecule method. The interaction energies have been corrected for Basis Set Superposition Error (BSSE) using the standard counterpoise (CP)[71] method for all complexes. The AIMALL[72] software was used to conduct electron density topological investigations based on the Atoms in Molecules (AIM)[73] theory. MATLAB and the gnuplot software were used for data fitting.

6.3 Results and Discussion

6.3.1 Group 1 Metals: H, Li, and Na- Bond

In comparison to lithium and sodium bonds, hydrogen bond lengths are much shorter (See Table 6.1). This is not surprising as hydrogen has no core electrons and is the lightest element in the Periodic Table. The Li forms the strongest intermolecular bond of the three. For H, Li, and Na-bonded complexes, the D-Y⋯A (Y=H, Li, Na) angle is close to linearity. Table 6.2 illustrates the D-X stretching frequency with the

corresponding shift from its monomer. Blue shifts were found in some LiF complexes (for example, $FLi\cdots OH_2$) due to the mixing of the Li–F stretching mode with other intermolecular vibrational modes. Blue shifting lithium bonds were reported in the literature[74]. However, the H atom is light, and the HX bonds are typically covalent and strong, leading to distinct H-X stretching vibrations. The H–X stretch remains an independent local mode both in the monomer and complex. The frequency shift seen in HX stretching mode during complex formation is strongly correlated with the hydrogen bond strength. Such relationships, however, are not to be expected for X = Na and Li. In general, hydrogen bonds can exhibit red, blue, or no shift in the HX stretching mode[75]. The $(XF)_2$ (X=H, Li, Na) dimer structure demonstrates the distinction between hydrogen bonds and other metal bonds (see Figure 6.3). The optimal orientation for two dipoles is linear, with all four charges in the same line, according to classical electrostatics[76]. The $(NaF)_2$ and $(LiF)_2$ dimers are dominated by electrostatic dipole-dipole interactions, but the $(HF)_2$ structure cannot be described by simple dipole-dipole interaction. For $(LiF)_2$ and $(NaF)_2$, the linear structure is a local minimum, and the cyclic structure is the global minimum[32]. The sodium bond, as Parajuli and Arunan[32] pointed out, is not often found. Also, it is true for a complex formed by NaCl and H_2O because both have large dipole moments and favour cyclic structure. Similarly, Alkorta et al. have found an additional minimum for NaF complexes with secondary interactions[77]. However, only linear bonded geometries have been considered in this work.

The $(HF)_2$ has a nearly linear hydrogen bond ($\angle$F–H$\cdots$F 173°), while the other H is pointing away at an $\angle$HFH angle of 111°[78,79]. Buckingham and Fowler[80] showed that distributed multipole analysis (DMA) using charge, dipole, and higher-order multipoles could reproduce the experimental structure of $(HF)_2$.

Despite a plethora of research on hydrogen bonds, there is still considerable debate over the amount of covalency in a hydrogen bond. Pauling[2] believed the H-bond was purely electrostatic since it was thought hydrogen could not be covalently bond to two atoms. However, Gillette and Sherman[81] pointed out wavefunction for hydrogen bonds should include both polar and homopolar terms. Although they were unable to determine the relative importance of each, they concluded that both are important. Morokuma[82,83]

developed an energy decomposition analysis (EDA) that divides hydrogen bond energy into electrostatic, polarisation, and charge transfer components. With this EDA, electrostatics was the most important stabilising component, with relatively little stabilisations from polarisation and charge transfer. Weinhold and coworkers[84,85] reported that charge transfer states dominate H-bonds using the natural bond orbital (NBO) method. Both theories agree that covalent (charge transfer) and electrostatic aspects are both important for H-bonds. The primary disagreement is over which component is the dominant contributor and to what extent. Coulson[86] pointed out the importance of covalency in hydrogen bonding. Recently, it is shown that, the presence of valence bond structures that explicitly involve charge transfer accounts for at least 32% of the hydrogen bond energy, demonstrating the dominance of covalency[87]. Hydrogen bonding is sometimes mistaken for simple electrostatic interaction; nevertheless, a study of $(XF)_2$ geometries reveal a significant difference between hydrogen bonding and electrostatic interaction.

In an O–H⋯O hydrogen bond, Pauling[2] approximated the hydrogen bond to be around 5% covalent simply by comparing the H⋯O hydrogen bond length to the O–H covalent bond length, assuming the latter to be 100% covalent. Shahi and Arunan[35] recently found that the H⋯A hydrogen bond is about 5% covalent using natural resonance theory (NRT). In a detailed review, Grabowski[88] pointed out the covalency is the driving force of hydrogen bonds, determining their characteristics.
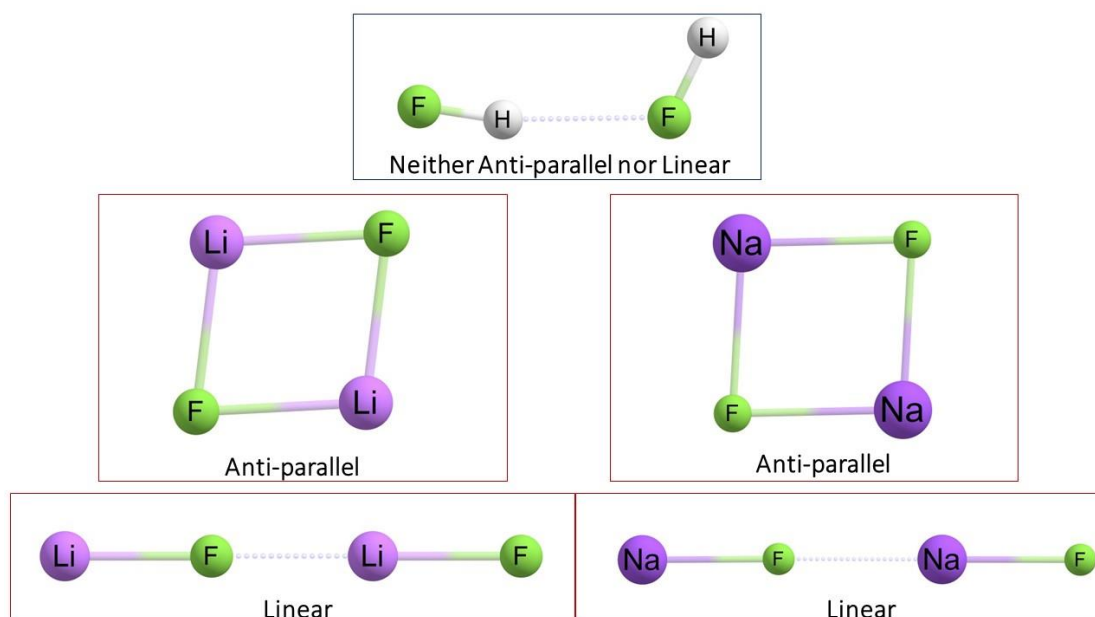
Figure 6.3. Geometries of (HF)₂, anti-parallel and linear (LiF)₂, anti-parallel and linear (NaF)₂ optimised at MP2/aug-cc-pVDZ level of theory.

Table 6.1. Binding distances of H, Li, and Na-bonded complexes Values are in Å.

Complexes	R(H•••A)(Å)	R(Li•••A)(Å)	R(Na•••A)(Å)
FX•••OH₂	1.716	1.968	2.460
FX•••SH₂	2.289	-	-
FX•••NH₃	1.690	2.097	2.505
FX•••NCH	1.851	2.087	2.480
FX•••OCH₂	1.720	1.995	2.421
FX•••C₂H₄	2.128	2.444	2.865
FX•••OHCH₃	1.662	1.925	2.338
FX•••PH₃	2.360	2.679	3.091
FX•••CO	2.067	2.324	2.742
FX•••O(CH₃)₂	1.625	1.972	2.412
FX•••NCCH₃	-	2.057	2.446

Table 6.2. Vibrational frequencies and shifts for H, Li, and Na-bonded complexes. Values are in cm^{-1}.

Complexes	X=H		X=Li		X=Na	
	Frequency	Δ	Frequency	Δ	Frequency	Δ
FX•••OH₂	3669	413	875	-12	504	20
FX•••SH₂	3798	284	-	-	-	-
FX•••NH₃	3280	802	869	-6	507	17
FX•••NCH	3792	292	866	-3	506	18
FX•••OCH₂	3644	438	787	76	468	56
FX•••C₂H₄	3842	240	859	4	514	10
FX•••OHCH₃	3543	539	813	50	479	45
FX•••PH₃	3797	285	850	13	511	13
FX•••CO	3908	174	861	2	516	8
FX•••O(CH₃)₂	3442	640	815	48	478	46
FX•••NCCH₃	-	-	858	5	502	22

6.3.2 Group 2 Metals: Be, Mg and Ca-Bond

In general, the complexes formed between group 2 donors and acceptors can be classified as a Lewis acid-base interaction. Vacant np orbitals of group 2 elements interact with the lone pair (H_2O, NH_3, H_2S, PH_3, HCHO, CH_3OH, CH_3OCH_3, and NCH), π electrons (C_2H_4) and unpaired electrons (CO) of acceptors. Binding lengths for Be-bonds are substantially shorter than those for Mg and Ca-bonds, decreasing in the sequence Be > Mg > Ca (Table 6.3). Similar to group 1 metals, the binding distances decrease as one moves down the group. The thorough examination of geometric characteristics also reveals the geometric distortion of the donor molecules. The initial geometries of the donor molecule were linear (with the exception of CaF_2, 156.4°, and $CaCl_2$, 167.8°); nevertheless, following complex formation, the D-X-D angle changes substantially. These distortions in angles are rationalised with orbital interactions[42]. In beryllium bonded complexes, distortions in donor geometries are more pronounced and correlate well with the strength of the interaction. Following complex formation, the

length of the X-F (X=Be, Mg, Ca) bond increases. Beryllium bonds can have a percentage elongation of up to 5%, depending on the nature of the donor and acceptor. In contrast, magnesium and calcium bonds have a lower percentage of elongation. Asymmetric stretching frequencies of the X-D bonds are red-shifted in all complexes (Table 6.5), whereas symmetric stretches are blue-shifted. The binding energy was estimated as the difference between the total of the monomers in their optimised states and the complexes. Because the donor molecules are considerably distorted in these complexes, the distortion energy is relatively high, but these distortion energies are not included in the interaction energies. When compared to hydrogen bonds, the interaction energies for these complexes are significantly higher. Villanueva et al.[51] demonstrated that π-beryllium bonds are approximately four times stronger than typical π-hydrogen bonds and even stronger than the strongest π-hydrogen bond previously reported. Our findings are consistent with this. Binding energies for group 1 and 2 elements are given in the next section (Table 6.6 and Table 6.7). The Be-Be bond is stronger than the Mg-Mg Bond[59] in homonuclear dimers and clusters. However, this tendency does not hold in intermolecular bonding. Mg-bonded complexes are stronger than beryllium-bonded complexes in XF_2 complexes, although, in a few complexes, the beryllium bond appears to be stronger, particularly with BeH_2 as a donor. Secondary interaction is evident in few calcium bonded compounds (Figure 6.4). The complex between CaF_2 with H_2O has two intermolecular bond critical points. The electron density at BCP for Ca-bond is 0.0312 au and for O-H$\cdots$F hydrogen bond is 0.0405 au. As a result, the binding energies of Ca-bonded complexes (with CaF_2 donor) are not a valid indicator of exclusive Ca-bond strength. Secondary (i.e., hydrogen bonding) interactions do not exist in the CaH_2 donor with the current set of acceptors.

Table 6.3. Binding distances of Be, Mg, and Ca-bonded complexes Values are in Å.

Complexes	R(Be•••A)(Å)	R(Mg•••A)(Å)	R(Ca•••A)(Å)
$F_2X•••OH_2$	1.736	2.067	2.364
$F_2X•••SH_2$	2.279	2.663	2.998
$F_2X•••NH_3$	1.790	2.188	2.524
$F_2X•••NCH$	1.836	2.208	2.541
$F_2X•••OCH_2$	1.780	2.129	2.454
$F_2X•••C_2H_4$	2.184	2.532	2.868
$F_2X•••OHCH_3$	1.703	2.051	2.379
$F_2X•••PH_3$	2.321	2.731	3.037
$F_2X•••CO$	2.014	2.430	2.781
$F_2X•••O(CH_3)_2$	1.688	2.044	2.341

Table 6.4. The F-X-F donor angle in the Be, Mg and Ca-bonded complexes. Deviation indicates the difference from its monomer state. In the monomer state, the donor molecules are linear except CaF_2 with 156°. Values are in degree.

	X=Be		X=Mg		X=Ca	
Complexes	Angle	Deviation	Angle	Deviation	Angle	Deviation
$F_2X•••OH_2$	143.2	36.8	157.1	22.9	149.3	7.1
$F_2X•••SH_2$	145.4	34.6	158.3	21.7	147.8	8.5
$F_2X•••NH_3$	138.0	42.0	151.7	28.3	149.7	6.6
$F_2X•••NCH$	141.7	38.3	152.3	27.7	144.7	11.6
$F_2X•••OCH_2$	140.9	39.1	151.9	28.1	146.4	9.9
$F_2X•••C_2H_4$	147.8	32.2	158.6	21.4	151.4	4.9
$F_2X•••OHCH_3$	141.4	38.6	155.4	24.6	150.6	5.7
$F_2X•••PH_3$	143.9	36.1	156.6	23.4	150.4	5.9
$F_2X•••CO$	148.4	31.6	162.3	17.7	153.0	3.3
$F_2X•••O(CH_3)_2$	139.3	40.7	155.2	24.8	160.3	-4.0

Table 6.5. Asymmetric stretching frequency in the X-F donor and the corresponding red-shift from the monomer state for Be, Mg and Ca-bonded complexes. Values are in cm^{-1}.

Complexes	X=Be		X=Mg		X=Ca	
	Frequency	Δ	Frequency	Δ	Frequency	Δ
$F_2X\cdots OH_2$	1315.7	200.6	808.4	53.6	530.0	47.7
$F_2X\cdots SH_2$	1335.6	180.7	815.7	46.3	575.4	2.3
$F_2X\cdots NH_3$	1269.6	246.7	795.7	66.3	510.8	66.9
$F_2X\cdots NCH$	1313.3	203.0	804.6	57.4	559.0	18.7
$F_2X\cdots OCH_2$	1306.9	209.4	796.2	65.8	556.0	21.7
$F_2X\cdots C_2H_4$	1359.1	157.2	818.5	43.5	566.0	11.7
$F_2X\cdots OHCH_3$	1285.5	230.8	796.4	65.6	554.2	23.5
$F_2X\cdots PH_3$	1319.0	197.3	811.4	50.6	561.3	16.4
$F_2X\cdots CO$	1361.6	154.7	830.0	32.0	569.0	8.7
$F_2X\cdots O(CH_3)_2$	1274.5	241.8	791.7	70.3	552.1	25.6

6.3.3 Atoms in Molecules (AIM) Analysis

The topological study of electron density enables us to gain a better understanding of the nature of intermolecular bonds. The molecular graphs of group 1 and group 2 complexes are represented in Figure 6.4. The existence of the intermolecular bond is confirmed by the bond critical point (black dot) between the two interacting atoms. The electron density (ρ), its Laplacian ($\nabla^2\rho$), and electronic energy density (H) at a bond critical point (BCP) give us information about the strength and character of the bond.
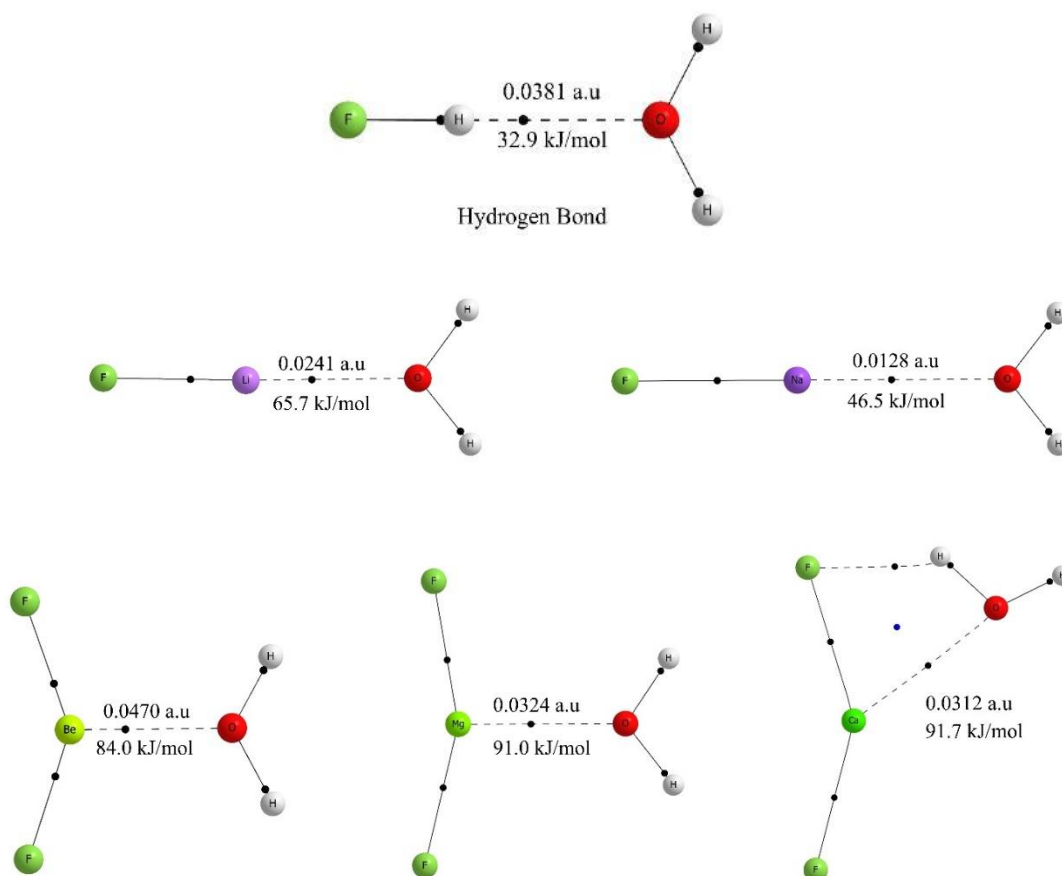
Figure 6.4. Molecular graphs of the hydrogen (H-bond) and alkalene bonded (proposed common name for Li, Na, Be, Mg, Ca Bond). Dotted lines indicate the bond paths. Black and blue dots denote BCPs and RCPs, respectively. The electron density (ρ) at BCPs (in au) and the BSSE corrected binding energies (in kJ/mol) are given along with the complex.

6.3.4 The Plot of Binding Energy versus Electron Density

6.3.4.1 Linear Correlation

The theoretical community has focused most of its attention on energy. Energy is an eigenvalue of the Schrödinger equation, and electron density may be calculated from the wavefunction, which is also an eigenfunction of the same equation. Popelier[89] questioned: "If one believes that eigenvalues and eigenfunctions are on the same level as solutions to an eigenvalue problem such as the Schrödinger equation, then why does

electron density not have the same status as energy?" We have looked at both energy (binding energy) and electron density (at the bond critical point) to understand intermolecular interaction. The topological properties of electron density at the bond critical points (BCPs) have been used to obtain information on the strength of the interaction. It is demonstrated that the electron density at the bond critical point increases almost linearly with increasing binding energy, acting as an indicator of the nature and gradual change of the strength of a vast number of test intermolecular complexes. Parthasarathi et al.[90] showed a linear relationship between the binding energy and electron density values at the H- bond BCP. There is a smooth change like interaction from van der Waals to classical H-bonding to strong H-bonding with increasing electron density at the BCPs. Amezaga et al.[91] found in both hydrogen (CC=0.93) and halogen (CC=0.97) bonds, the correlation coefficient (CC) is quite impressive. The correlation coefficient (CC) increased to 1.0 when complexes were formed by different Lewis bases and the same Lewis acid such as $H_3N\cdots ClF$, $H_2O\cdots ClF$, and $H_2S\cdots ClF$.

Similarly, Mohan and Suresh[92] pointed out that the correlation could be poor (CC = 0.64) for a heterogeneous sample of complexes consisting of neutral (A$\cdots$B), halogen-bonded (X$\cdots$B), dihydrogen-bonded (H$\cdots$H), charge-assisted hydrogen-bonded (CHB), and charge-assisted halogen-bonded (CXB) systems, but the correlation is highly satisfactory for a homogeneous sample of complexes. Their results clearly suggest that the applicability of electron density versus binding energy plot is not quite adequate to describe a large variety of complexes on a uniform scale; instead help us to classify complexes according to the nature of bonding. Further, in a recent perspective, Shahi and Arunan[35] showed that the Li-bond and H-bond slopes are significantly different, and slopes for Cl-bond are similar to H-bond. Similar results were found for H, Li, and Cl bonds with unpaired (CH_3) and σ-electron (H_2) as acceptors[93]. We attempt to broaden this work by including a significant number of intermolecular bound complexes formed by the main group elements of the Periodic Table.

Group 1: Amongst the group 1 metals, we have incorporated H, Li, and Na bonded complexes for the correlation plot. The potassium bond is still not reported in the

literature to the best of our knowledge. Due to the strong electropositivity of K, a complex between KF (donor) and H_2O (acceptor) spontaneously produces KOH and HF. When H, Li, and Na-bonded complexes are considered, the value of binding energies decreases in the sequence Li > Na > H (see Table 6.6), a somewhat different trend than the electron density (H > Li > Na). Indeed, our study of a large number of donor-acceptor complexes not only supports the linear correlation but also shows that the slopes of H-bonded complexes differ markedly from those of Li-/Na-bonded complexes.

Table 6.8 displays the correlation coefficients (CC), intercepts, and slopes for group 1 and group 2 elements. A detailed table comprising all the elements can be found in the supplementary information (Table S6.1). The overall values of the correlation coefficients (CC), intercepts, and slopes are computed in three different manners. The term "Overall (by avg.)" refers to the average value from three sets of donor-acceptor fit. The "Overall [by fit, with (0,0)]" is calculated by fitting the binding energies and electron densities of all donor-acceptor complexes with an extra (0,0) point. The origin is taken as a point because when the value of binding energy is zero, we assume that there is no electron density between the bonded atoms. Similarly, "**Overall [by fit, without (0,0)]**" was obtained without (0,0) point in the fit. Considering the error limit specified, the values produced by these three methods are equivalent in most of the elements, supporting our assumption. Linear regression without intercept (y=mx) also has been used to fit the data, but it does not improve the quality of the fit (see supplementary information, Table S6.2). We will use the values from "**Overall [by fit, without (0,0)]**" in our subsequent sections for comparison.

Hydrogen, lithium, and sodium bonding have correlation coefficients (CC) of 0.95, 0.85, and 0.91, respectively, with corresponding slopes of 901(38), 2997(239), and 4074 (238). Li and Na-bonds have considerably greater slopes due to high binding energy and low electron density at the bond critical point, typical of a closed-shell interaction. On the other hand, higher electron density and low binding energy set the H-bond slope to a lower value. This observation implies some covalency or orbital overlapping, which is the driving factor defining the properties of a hydrogen bond. Interestingly, the discrepancy may be due to the donors (HF, H_2O, H_2S) being

'covalently bound' in the H-bond and 'ionic' in the Li and Na-bonds (FD, ClD, BrD, D=Li, Na).

Table 6.6. Electron density at BCP (ρ) (au) and BSSE corrected binding energies (E_{bin}) (kJ/mol) for H, Li, and Na- bonded complexes.

Complexes	X=H		X=Li		X=Na	
	ρ	E_{bin}	ρ	E_{bin}	ρ	E_{bin}
FX•••OH₂	0.0381	32.9	0.0241	65.7	0.0128	46.5
FX•••SH₂	0.0214	19.0	-	-	-	-
FX•••NH₃	0.0506	48.7	0.0234	79.9	0.0165	58.0
FX•••NCH	0.0288	28.3	0.0203	61.3	0.0148	48.0
FX•••OCH₂	0.0395	31.1	0.0251	75.0	0.0165	66.5
FX•••C₂H₄	0.0183	17.1	0.0112	33.5	0.0082	23.5
FX•••OHCH₃	0.0452	37.4	0.0269	75.9	0.0176	61.4
FX•••PH₃	0.0202	17.6	0.0118	37.0	0.0086	26.7
FX•••CO	0.0203	13.5	0.0130	28.7	0.0093	19.6
FX•••O(CH₃)₂	0.0510	39.1	0.0275	68.8	0.0175	53.7
FX•••NCCH₃	-	-	0.0222	73.7	0.0162	58.7

Group 2: Binding energies for Be, Mg, and Ca in group 2 metals are comparable, and finding a pattern across a large number of complexes is difficult. However, the electron density at BCP follows a similar trend to that of group 1 elements, decreasing down the group ($\rho_{Be} > \rho_{Mg} > \rho_{Ca}$). Be, Mg, and Ca-bond slopes are similar, with the values being 2983(206), 3606(188), and 3081(143), respectively. A large intercept has been found for Be-bonded complexes and including origin as one of the data points in the fit, reduces the correlation coefficient (CC) from 0.88 **[Overall by fit, without (0,0)]** to 0.82 [Overall by fit, with (0,0)]. We anticipated that the binding energy might not grow at a constant pace with the electron density at low values, deviating from linearity. A power fitting in its usual form, $y=ax^r$, yields a slightly higher correlation of 0.92 than a linear fit, which yields 0.88. According to the fit, the power value (r) is 2.21(0.16). However, power fit has little effect on the quality of fit for the rest of the group 1 and

group 2 elements (see Table 6.8, a complete table in supplementary information, Table S6.3). An exponential fit gives a correlation coefficient (CC) of 0.90 (see Table S6.4) for beryllium bonded complexes.

Figure 6.5 demonstrates that the slopes of the Li, Na, Be, Mg, and Ca-bonds are equivalent, while the slopes of the hydrogen bond remain unique. As mentioned earlier, Alkorta et al.[29] called the group 1 bond (except hydrogen) and group 2 bond as '*alkali bond*' and '*alkaline Earth bond*', but their use is still not widespread. Considering the similarities between group 1 (excluding H) and group 2 metals, we suggest naming them 'alkalene bonds.'

Table 6.7. Electron density at BCP (ρ) (au) and BSSE corrected binding energies (E_{bin}) (kJ/mol) for Be- Mg, and Ca- bonded complexes.

Complexes	X=Be		X=Mg		X=Ca	
	ρ	E_{bin}	ρ	E_{bin}	ρ	E_{bin}
$F_2X\cdots OH_2$	0.0470	84.0	0.0324	91.0	0.0312	91.7
$F_2X\cdots SH_2$	0.0315	39.9	0.0200	50.9	0.0173	47.9
$F_2X\cdots NH_3$	0.0546	113.7	0.0320	107.9	0.0287	90.9
$F_2X\cdots NCH$	0.0406	59.8	0.0260	71.9	0.0244	69.1
$F_2X\cdots OCH_2$	0.0446	73.4	0.0307	84.8	0.0286	80.0
$F_2X\cdots C_2H_4$	0.0250	30.0	0.0160	43.8	0.0146	40.6
$F_2X\cdots OHCH_3$	0.0523	100.0	0.0349	103.7	0.0320	91.3
$F_2X\cdots PH_3$	0.0335	40.0	0.0188	48.5	0.0172	43.4
$F_2X\cdots CO$	0.0321	26.3	0.0177	35.5	0.0161	32.4
$F_2X\cdots O(CH_3)_2$	0.0544	107.3	0.0363	109.2	0.0358	92.9

Table 6.8. Correlation coefficients (CC), intercepts and slopes of the binding energy (kJ/mol) versus electron density (au) plot for various H, Li, Na, Be, Mg and Ca- Bonded complexes. Values in brackets denote standard deviation.

Complexes	CC	Intercept	Slope
X=H			
FX···A	0.92	0.3(3.0)	844(85)
HOX···A	0.94	-1.0(1.6)	832(73)
HSX···A	0.92	-0.0(1.0)	648(67)
Overall (by avg.)	0.93	-0.2(1.9)	775(75)
Overall (by fit, with (0,0)]	0.96	-2.2(0.9)	889(35)
Overall [by fit, without (0,0)]	**0.95**	**-2.5(1.0)**	**901(38)**
X=Li			
FX···A	0.86	1.0(8.7)	2868(408)
ClX···A	0.85	2.2(10.3)	2997(449)
BrX···A	0.85	2.7(10.5)	2995(450)
Overall (by avg.)	0.85	2.0(9.8)	2953(436)
Overall (by fit, with (0,0)]	0.89	0.7(4.4)	3011(199)
Overall [by fit, without (0,0)]	**0.85**	**1.1(5.4)**	**2997(239)**
X=Na			
FX···A	0.91	-12.7(6.9)	4274(484)
ClX···A	0.92	-9.9(6.4)	4039(423)
BrX···A	0.92	-9.7(6.6)	3978(428)
Overall (by avg.)	0.92	-10.8(6.6)	4097(445)
Overall (by fit, with (0,0)]	0.93	-7.0(3.0)	3840(202)
Overall [by fit, without (0,0)]	**0.91**	**-10.5(3.6)**	**4074(238)**
X=Be			
F_2X···A	0.96	-58.4(6.7)	3030(226)
Cl_2X···A	0.89	-76.7(18.2)	3090(380)
H_2X···A	0.92	-78.1(14.2)	3261(338)
Overall (by avg.)	0.92	-71.1(13.0)	3126(315)
Overall (by fit, with (0,0)]	0.82	-38.8(9.1)	2408(209)

Continued Table 6.8…

Overall [by fit, without (0,0)]	0.88	-64.9(9.1)	2983(206)
X=Mg			
F₂X···A	0.95	-20.6(7.6)	3596(277)
Cl₂X···A	0.93	-17.7(10.0)	3569(349)
H₂X···A	0.97	-15.3(4.2)	2960(186)
Overall (by avg.)	0.95	-17.9(7.3)	3375(271)
Overall (by fit, with (0,0)]	0.93	-16.6(4.6)	3384(176)
Overall [by fit, without (0,0)]	0.93	-22.9(5.0)	3606(188)
X=Ca			
F₂X···A	0.95	-8.9(6.7)	3137(260)
Cl₂X···A	0.94	-9.5(7.9)	3108(277)
H₂X···A	0.95	-8.0(6.0)	2931(245)
Overall (by avg.)	0.95	-8.8(6.9)	3059(261)
Overall (by fit, with (0,0)]	0.95	-6.6(3.2)	2986(125)
Overall [by fit, without (0,0)]	0.94	-9.2(3.8)	3081(143)

Figure 6.5. Linear fit of the binding energy (kJ/mol) versus electron density (au) for alkalene (Li, Na, Be, Mg, Ca) and hydrogen (H) bonded complexes. Slopes and intercepts of the best fit lines are shown along with their respective standard deviation. The quality of the fit is denoted by the R^2 value.

Table 6.9. Correlation coefficients (CC), intercepts and slopes of the binding energy (kJ/mol) versus electron density (au) plot for various H, Li, Na, Be, Mg and Ca-bonded complexes. Values in brackets denote standard deviation.

	y=mx+c	y=ax^r		
Complexes	**Linear Fit CC**	**CC**	**a**	**r**
H	0.95	0.95	1247(220)	1.13(0.05)
Li	0.85	0.85	2587(895)	0.96(0.09)
Na	0.91	0.91	8822(3409)	1.23(0.09)
*Be	0.88	0.91	61627(30220)	2.21(0.16)
Mg	0.93	0.93	11700(3612)	1.41(0.09)
Ca	0.94	0.94	4426(983)	1.13(0.06)

Plot is given in supplementary information, Figure S6.1.

Triel, Tetrel, Pnictogen, Chalcogen, and Halogen Bonds: We also calculated the slopes of the binding energy versus electron density plot for a large number of triel, tetrel, pnictogen, chalcogen, and halogen bonded complexes in order to compare them all under the same settings. In all cases, a satisfactory correlation between the aforementioned quantities was obtained. We created a Periodic Table for intermolecular bonding by incorporating slopes and correlation coefficients (CC) from binding energy versus electron density plots (Figure 6.6). Elements are classified into three regions based on the slope values. A value of more than 2000 (in blue), between 1000-2000 (in cyan), and less than 1000 (in green) are classed as high, moderate, and low slope areas, respectively. The elements in the high slope area are distinguished by the formation of an almost pure closed-shell intermolecular bond with minimal covalency. According to natural resonance theory (NRT), the Mg, and Li bonds are 2% covalent on average. Be-bonds have a somewhat greater covalency, averaging approximately 3%. NRT studies for a few Be- and Mg-bonded complexes are available in the supplemental material (see Table S6.5), while Li-bonded complexes are available in Reference 35. On the other hand, the H-bond belongs to the low slope region has a covalency of around 5%. As one moves from a high slope zone to a low slope region,

the covalency of the intermolecular bond steadily increases.

Figure 6.6. The slopes (standard deviation in the bracket) from the binding energy (kJ/mol) versus electron density (au) plot are shown for the different intermolecular bonds formed by the main group elements. The slopes below 1000 (in green), between 1000-2000 (in cyan) and above 2000 (in blue) are classified as high, intermediate, and low slope, respectively. The correlation coefficient (CC) or R^2 of the fit for each element are also indicated.

The elements of the 13th group in their numerous compounds are characterised by the occurrence of π-holes. The name of triel bonding was proposed by Grabowski[94]. Leopold et al.[95] have named these types of complexes as "partially bonded complexes" after performing a systematic investigation on the geometric features of triel bonding

complexes. The boron bond in group 13 is considerably distinct from the other members, as evidenced by the title of Grabowski's paper "Boron and other Triel Lewis Acid Centers: From Hypovalency to Hypervalency"[94], which distinguishes boron from the other triel bonds. It is noteworthy to emphasise the behaviour of triel bonds depending on their state. Due to the cooperativity effects, the triel bonding complex formed by $F_3B\cdots NCCH_3$ has a $B\cdots N$ distance of 2.01 Å in the gas phase and 1.63 Å in the solid-state[95].

The linear correlation between ρ and E_{bin} leads to a slope of 552(58) with a poor CC value of 0.76 for boron bonded complexes. The donor molecules taken for this study are BF_3, BCl_3, BF_2H. Boron hydrides and halides are examples of simple planar entities having a positive electrostatic potential that can interact with nucleophiles. The poor correlation is caused by two regimes of electron density and binding energies, one with shorter bonds and strong interactions and the other with longer bonds and weak interactions (see Table S6.6 in supplementary information). The slopes of the two regimes differ somewhat and plotting all of the complexes together yields a poor fit (see supplementary information, Figure S6.2). More intriguingly, these two regimes may coexist in a single complex. The $Cl_3B\cdots NCH$ contains two tautomeric structures, one with a $B\cdots N$ distance of 1.628 Å and the other with a distance of 2.817 Å[96]. A power fit of boron bond data results in a considerably better fit with CC 0.85 and power(r) 2.39(0.28). This kind of anomaly is absent in the rest of the group 13 congeners.

The Al-bond slope 3564(217) belongs to the high slope region and is similar to the alkalene bond. The Al-bonded complexes have reasonably high binding energies and low electron densities at the bond critical points. The binding energy $H_2FAl\cdots NH_3$ complex is 111.9 kJ/mol, and the corresponding electron density at BCP was found to be 0.0416 au. The AlF_3, when interacts with NH_3, its trigonal structure is changed to the tetrahedral structure. In general, the aluminium bonded complexes are characterised by a small electron charge shift. Still, these species exhibit the strongest interactions, and mainly, an electrostatic contribution takes place.

Mostly, as we go down a group, the electronegativity of the elements decreases. However, in going from Al to Ga, the electronegativity increases from 1.61 to 1.81. For this, the gallium complexes, the interactions possess covalent character. The electron density at BCP was found to be more than the aluminium bonded complexes. However, the binding energies are found to be less than the aluminium bonded complexes. The binding energy and electron density at BCP for $H_2FGa\cdots NH_3$ complex were 95.7 kJ/mol and 0.0597 au, respectively. The slope of Ga- bonded complexes was found to be 2048 (125), with a correlation coefficient (CC) of 0.91. Grabowski[94] also observed that gallium bonded complexes have the highest electron density value at BCP for the identical ligands.

The electronegativity falls from 1.81 to 1.78 for gallium to indium, following the typical pattern. As a result, the slope of the binding energy versus electron density plot increases from 2048 (125) in gallium to 2207(115) in indium. Thallium bonded complexes do not follow this trend, and the slope was found to be 1822(100). The slope of the Thallium bonded complexes falls in the intermediate region (cyan colour in the Periodic Table).

The tetrel family starts with the electronegative non-metal C, then continues on to the semimetals Si and Ge, and finally includes the metals Sn and Pb, making it extremely varied. In general, the ability to form the intermolecular bond requires the bridging atom's ability to develop a positively charged σ-hole. The accessibility of the σ-holes in tetrels is restricted since they are positioned in the centre of three sp^3 -hybridised bonds. In other words, the tetrel bonding differs from halogen, chalcogen, and pnictogen bonding interactions as the charge density distribution on the tetrel atom is isotropic due to the absence of lone pairs or vacant orbitals. Also, this ability depends on the element's electropositivity, which increases down the group. So, one would expect carbon to be a hesitant participant in tetrel bonds. Similarly, amongst the halogen, F is seldom engaged as an electron acceptor in halogen bonds. The same is true for the other first-row elements O and N in chalcogen and pnictogen bonds, respectively.

Furthermore, carbon (C) is frequently distinguished from the other tetrels since Si, Ge, Sn, and Pb have a significant propensity to enhance their valency due to the presence of lower energy d-orbitals. According to a recent report, carbon is selective in forming a "tetrel bond," and when it does, it may be desirable to highlight it as a "carbon bond"[97].
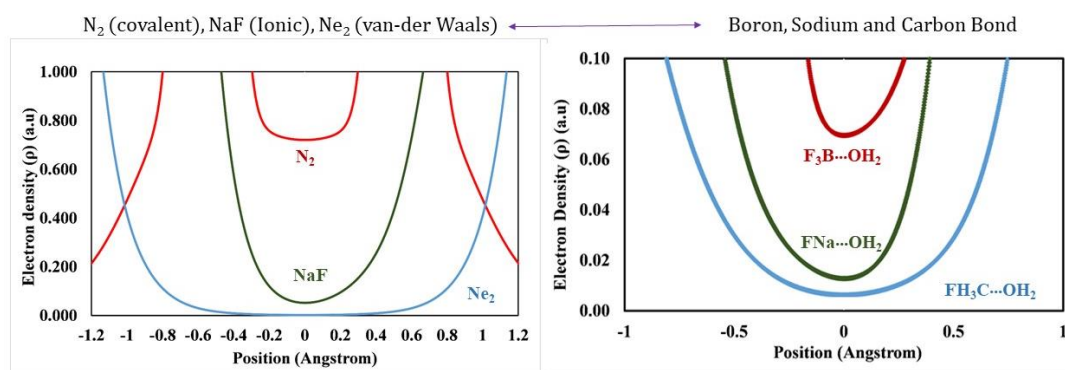
Figure 6.7. Electron density variation for a typical covalent (N_2), ionic (NaF) and van der Waals (Ne_2) molecule. Similar differences could be seen in boron ($F_3B\cdots OH_2$), sodium ($FNa\cdots OH_2$) and carbon ($FH_3C\cdots OH_2$) bonds.

Carbon bonded complexes are more weakly bound than the tetrel bonded complexes of the other members of the group. The binding energy of the $FH_3C\cdots NH_3$ complex is just 7.7 kJ/mol, whereas the binding energies for $FH_3Si\cdots NH_3$, $FH_3Ge\cdots NH_3$, $FH_3Sn\cdots NH_3$ and $FH_3Pb\cdots NH_3$ are 23.0 kJ/mol, 24.4 kJ/mol, 35.6 kJ/mol, and 31.7 kJ/mol, respectively. The electron density at BCP for $C\cdots N$, $Si\cdots N$, $Ge\cdots N$, $Sn\cdots N$ and $Pb\cdots N$ interactions are 0.0067, 0.0251, 0.0252, 0.0286 and 0.0252 au respectively. So, the electron density at the BCP for carbon bonds is much lower than the other bonds. The electron density at the BCP falls very quickly with the distance. The $C\cdots N$ distance in $FH_3C\cdots NH_3$ complex is 3.160 Å, close to the sum of the van der Waals radii for C and N, 3.25 Å.

In the correlation plot, a high slope, 1980 (145) results from weak closed-shell interactions in carbon-bonded complexes. We recently showed that Period 2 homo-nuclear diatomic molecules exhibit a rich diversity of 'bonds' that can be found in all inter- and intra-molecular interactions seen in physics, chemistry, and biology[98]. Figure 6.7 depicts (on the left) the electron density variation between two atoms in a typical covalent (N_2), ionic (NaF), and van der Waals (Ne_2) molecule. The red curve is for N_2

(covalent molecule), which has sufficient electron density between the two atoms. IUPAC gold book[99] defined covalent bond as the "A *region* of relatively high electron density between nuclei which arises at least partly from sharing of electrons and give rise to an attractive force and characteristic internuclear distance." The green curve is for the typical ionic molecule NaF. The ionic bond is defined as the "The ***bond*** between two atoms with sharply different electronegativities. In strict terms, an ionic bond refers to the electrostatic attraction experienced between the electric charges of a cation and an anion, in contrast with a purely covalent bond. In practice, it is preferable to consider the amount of ionic character of a bond rather than referring to purely ionic or covalent bonds. Ionic bonds have significantly less electron density between the two atoms. Despite the fact that the ionic bond is taught in high school, the chemical bond has become synonymous with the covalent bond, causing a lot of needless debate. The Ne_2 represents the typical van-der Waals molecule. The van der Waals forces include dipole-dipole, dipole-induced dipole and instantaneous induced dipole-induced dipole forces. The electron density in between the Ne atoms is almost close to zero. We have drawn similar analogies in intermolecular bonding as well. In Figure 6.7, the electron density variation for boron, sodium and carbon bond has been plotted (on the right). Despite the fact that the scale of the electron density (y-axis) in typical covalent and intermolecular interactions differs, we may still draw some analogies between the covalent bond in N_2 and the intermolecular boron bond. Similar comparisons are made for ionic interactions with sodium bonds and 'van der Waals interactions' with carbon bonds. As a word of caution, the term van der Waals interaction is frequently used loosely to describe some perplexing intermolecular bonds that have not been understood. For example, C-H···O connections are referred to as 'hydrogen bonds,' whereas C-H···π contacts are referred to as van der Waals interactions[100].

The van der Waals radii are frequently used as a separator between the hydrogen bond and the van der Waals interaction. However, in the most recent IUPAC hydrogen bond definition[37], this criterion has been discouraged. As a result, the above comparison should not lead us to refer to the 'carbon bonds' as 'van der Waals interactions/contacts. In fact, much of the discussion about whether all intermolecular interactions should be

referred to as 'bonded' appears to be superfluous. Most of the argument regarding the appropriateness of the term 'bond' overlooks ionic bonding.

Compared to the carbon bonds, the slope in the remainder of the group 14 bonds is relatively smaller. Semimetals Si and Ge have slopes of 823(45) and 828(47), respectively, whereas non-metals Sn and Pb have slopes of 1085(56) and 1074(74), respectively. When moving from Sn to Pb, the electronegativity increases from 1.96 to 2.33, resulting in a somewhat lower value of the slope. In general, elements with low electronegativity that are involved in intermolecular bonding have a steeper slope. Though given the diversity of intermolecular bonding examined here, this may not always be the case. Figure S6.3 and Figure S6.4 illustrate (in supplementary information) the slope from the binding energy and electron density plot with Pauling electronegativity[2] and recent thermochemical electronegativity[101] of the elements.

In pnictogen-bonded complexes, pnictogen atoms (group 15 elements) act as Lewis acid, which can accept electrons from electron donor groups. The π-Pnictogen bonds are stronger than H-bonds even when strong proton donors like water are present in the same environment[102]. Legon pointed out that tetrel, pnictogen, and chalcogen bonds were discovered in the gas phase before being named[103]. This is also highlighted in a recent book Chapter by Gnanasekar and Arunan[104]. The experimental charge density analysis confirmed the participation of a nitrogen atom acting as an electrophile in pnictogen bonding in solid[105]. For N-bonded complexes, NF_3 was taken as Lewis acid in this study. The bond energies of the complexes are within 2-6 kJ/mol. The electron-withdrawing substituent on nitrogen atom increases the ability to form a pnictogen bond. For example, the NH_3 dimer does not engage in an N$\cdots$N type bond. The NH_3 dimer has a flat potential energy surface and is hydrogen-bonded[3,106,107,108]. However, replacing one monomer with FNH_2 creates an F-N$\cdots$N pnictogen bond[109]. The N$\cdots$N pnictogen bond was also observed experimentally in the nitroethane-trimethylamine complex utilising rotational spectroscopy[110]. The binding energy correlates well with the electron density at BCP for N-bonded complexes. The N$\cdots$N bond was found for the $F_3N\cdots NH_3$ complex, having a binding energy of 3.9 kJ/mol. The strength of the N-pnictogen bond increases with the stronger electron donor. For example, the binding

energies for $F_3N\cdots OH_2$, $F_3N\cdots OHCH_3$ and $F_3N\cdots O(CH_3)_2$ were 3.7, 5.3 and 6.4 kJ/mol, respectively. The overall slope for N-bond was found to be 628(54).

The binding energy of pnictogen-bonded complexes and electron density at BCP increase as we move down the group. The binding energies of the complexes $F_3P\cdots NH_3$, $F_3As\cdots NH_3$, $F_3Sb\cdots NH_3$ and $F_3Bi\cdots NH_3$ are 18.7, 30.6, 48.9, and 55.3 kJ/mol, respectively, and the corresponding electron densities are 0.0218, 0.033, 0.0375 and 0.0348 au respectively. The slope for the binding energy and electron density increases as we move down the group. The slope for the P and As- bonds are comparable to the Si and Ge bond. The Sb and Pb bonds have slopes of 1271(54) and 1546(92).

Chalcogen bond[111] (ChB) is defined as the "*net attractive interaction between an electrophilic region associated with a chalcogen atom in a molecular entity and a nucleophilic region in another, or the same, molecular entity*". Several recent studies have shown that chalcogen bonds originate from the σ-holes localised on the electron-deficient surface of the group 16 elements[112,113,114,115]. Recently, it was demonstrated that oxygen is indeed capable of forming a chalcogen bond[116]. Oxygen difluoride (OF_2) acts as a prototype Lewis acid, σ-holes on O along F-O bond extensions in OF_2 are positive and can readily participate in chalcogen bonding with Lewis bases. The binding energy for the $F_2O\cdots NH_3$ complex is 6.4 kJ/mol, with electron density at BCP found to be 0.0111 au. The O-chalcogen bonded complex has a slope of 601 (27).

For chalcogen bond with sulphur, we have taken SF_2, SCl_2 and SO_2 as Lewis acid. The complexes involving the S-chalcogen bond are about four times stronger than the O-chalcogen bond. The S-chalcogen bond has a 785 (29) slope, which is somewhat higher than the O-bond. The bond strength of the chalcogen bond increases as we move down the group. For example, the binding energies of $F_2S\cdots NH_3$, $F_2Se\cdots NH_3$, $F_2Te\cdots NH_3$, $F_2Po\cdots NH_3$ are 29.1, 45.0, 60.8, 68.4 kJ/mol respectively. Also, the electron density at BCP increases down the group. The slopes for S, Se, Te and Po are 785(29), 866(31), 1194(74) and 1350(112), respectively.

Results and Discussion

According to the definition[117], the "*Halogen bond occurs when there is evidence of a net attractive interaction between an electrophilic region associated with a halogen atom in a molecular entity and a nucleophilic region in another, or the same, molecular entity*". Iodine, bromine, and chlorine atoms in dihalogens, interhalogens and a wide variety of organohalogen molecules frequently have positive σ-holes, which can form a halogen bond[17]. Fluorine has a positive electrostatic potential with a very strong electronegative group, allowing it to form a halogen bond. Certain experimental[118] and theoretical studies[119,120,121,122,123] have shown that fluorine atoms in F_2 and fluoroorganics can have a positive σ-hole. Here we have taken CNF, NCF and NCCCF as fluorine bond donors. The CNF acts as a better fluorine bond than NCF and NCCF. The binding energies for CNF···NH_3, NCF···NH_3 and NCCF···NH_3 complexes are 6.1, 4.4 and 4.1 kJ/mol, respectively. The corresponding electron densities are 0.0083, 0.0054 and 0.0056 au, respectively. The slope for F halogen-bond was found to be 875 (71).

The strength of the halogen bonded complexes decreases in the order of I > Br > Cl > F. The introduction of supersonic expansion methods allowed Klemperer and co-workers to study the rotational spectra of HF···ClF[124] and HF···Cl_2[125] in effective isolation by utilising molecular beam electric resonance spectroscopy. These were known as anti-hydrogen bonded complexes before being renamed the Cl-halogen bound complex. To study Cl-bond complexes, we have taken Cl_2, ClF and ClCN as the donors. The correlation coefficient (CC) in Cl-bonded complexes (0.93) is significantly higher than in F-bonded complexes. The slope for the Cl-bonded complex is 681 (36). The lower slope is due to the high electron density at the BCP.

As we proceed down the group, the binding energy increases more steeply in proportion to the electron density. The Br, I, and At bonds have slopes of 992(50), 1269(75), and 1611(114), respectively.

In the literature, there are extremely few aerogen bonded (group 18) complexes described. As a result, the aerogen bonded complexes have been excluded from this investigation. We note that this has been renamed as noble gas bond more recently[28].

The slopes of the binding energy versus electron density plots for hydrogen (H), boron (B), nitrogen (N), oxygen (O), fluorine (F), silicon (Si), phosphorus (P), sulphur (S), chlorine (Cl), germanium (Ge), arsenic (As), selenium (Se), and bromine (Br) bonds are less than 1000 and coloured green.

The bonds of lithium (Li), beryllium (Be), sodium (Na), magnesium (Mg), calcium (Ca), aluminium (Al), gallium (Ga), and indium (In) have a slope greater than 2000 and are shaded blue.

The slopes between 1000 and 2000 are indicated in cyan (a green-blue mixture), and carbon (C), thallium (Tl), tin (Sn), antimony (Sb), tellurium (Te), iodine (I), lead (Pb), bismuth (Bi), polonium (Po), and astatine (At) fall within this range.

Based on this comprehensive analysis, we propose that intermolecular bonding is divided into two types: intermolecular bonding with a covalent molecule (IMB-C) and intermolecular bonding with an ionic molecule (IMB-I). Hydrogen, halogen, chalcogen, pnictogen, tetrel (excluding carbon bond), boron bond (but not triel bond) fall under the IMB-C. IMB-I includes lithium, sodium, beryllium, and magnesium bonds (we propose a common name alkalene bond for all these) and triel bonds. Carbon bonds are somewhat different. Carbon molecules are like closed-shell ions. When they interact with an electron donor forming a carbon bond, the electron density between the two atoms is very low, and the binding energy rapidly increases with electron density. We suggest that this is a more straightforward categorisation for intermolecular bonding. It is important to point out that similarities exist between intra and intermolecular bonding, implying that our new categorisation is equivalent to the existing intramolecular bonding classification.

Alkorta[41] also recently distinguished two types of intermolecular bonding based on electrophilic sites. The first one refers to instances in which the molecular electrostatic potential has a positive area due to anisotropy of an atom's electron distribution along a covalent bond (σ-hole). This group includes hydrogen, halogen, chalcogen, pnictogen, tetrel, and aerogen bonds. The second group consists of atoms with empty orbitals in the valence shell that can accept electrons. This is true for atoms on the left side of the

Periodic Table (alkaline and alkaline-earth) and the boron group. We have realised that our classification based on two observables (i.e., binding energy and electron density) is more comprehensive.

6.3.4.2 Shared Shell versus Closed Shell Interaction: A Comparison Based on Atoms in Molecules (AIM) Methodology

Atoms in Molecules (AIM) theory provides a solid foundation for distinguishing between shared shell (covalent, polarised bonds) and closed-shell interactions/bond (ionic, intermolecular, van der Waals). It should be emphasised that a chemical bond between two atoms in a molecule cannot be wholly covalent or ionic. So, designating a bond as a 'closed-shell bond' or a 'shared-shell bond' does not imply that the bond is entirely 'ionic' or 'covalent.' Three criteria will be covered in this section.

Laplacian of Electron Density: Laplacian of electron density, $\nabla^2\rho$, is a useful quantity to differentiate between closed- and shared-shell interactions. Negative Laplacian indicates the accumulation of electron density between two atoms. Its positive value implies the depletion of charge between two atoms. For a typical covalent (e.g., N_2, $\nabla^2\rho = -3.5009$ au) or polarised bonds (e.g., H-F, $\nabla^2\rho = -3.5009$ au) Laplacian is negative at the BCP. Whereas Laplacian is positive at BCP for ionic (e.g., Li-H, $\nabla^2\rho = +0.1704$ au), hydrogen bonding (e.g., $O\cdots H$, in H_2O dimer, $\nabla^2\rho = +0.0862$ au) and van der Waals (e.g. Ne_2, $\nabla^2\rho = +0.0144$ au) interactions. Typically, a low electron density (ρ) at the BCP is associated with positive Laplacian. In most cases of hydrogen bonding, the Laplacian is positive; however, for exceptionally strong hydrogen bonds, such as those in $H_5O_2^+$ or (FHF)$^-$, the Laplacians are negative for both $O\cdots H$ and $F\cdots H$ contacts[88]. Koch and Popelier[126] suggested that the Laplacian of electron density for the H-bond should be in the range of 0.024-0.139 au. For a strong hydrogen bond $\nabla^2\rho$ is negative; hence it falls outside the proposed range. In fact, the Laplacian could be positive for some strongly bound covalent bonds like in CO[127]. For group 1, $\nabla^2\rho$ decreases in the sequence Li > H > Na. The $\nabla^2\rho$ decreases in the order Be > Mg > Ca for group 2 metals (see Table 6.10). The $\nabla^2\rho$ are comparable for H and Ca-bonded complexes. We have not proposed any range of the Laplacian for the investigated intermolecular bonded complexes. The Laplacian at the BCP is positive in our present analysis for all

complexes, indicating closed-shell interaction.

Table 6.10. Laplacian of electron density ($\nabla^2\rho$) (au) at BCP for group 1 and group 2 intermolecular bonded complexes.

Complexes	H	Li	Na	Complexes	Be	Mg	Ca
FX•••OH₂	0.154	0.187	0.086	**F₂X•••OH₂**	0.394	0.270	0.193
FX•••SH₂	0.057	-	-	**F₂X•••SH₂**	0.127	0.092	0.068
FX•••NH₃	0.139	0.149	0.091	**F₂X•••NH₃**	0.353	0.212	0.135
FX•••NCH	0.117	0.143	0.088	**F₂X•••NCH**	0.292	0.186	0.133
FX•••OCH₂	0.148	0.180	0.102	**F₂X•••OCH₂**	0.328	0.223	0.152
FX•••C₂H₄	0.048	0.053	0.034	**F₂X•••C₂H₄**	0.073	0.067	0.056
FX•••OHCH₃	0.168	0.216	0.122	**F₂X•••OHCH₃**	0.441	0.287	0.187
FX•••PH₃	0.046	0.057	0.037	**F₂X•••PH₃**	0.116	0.080	0.061
FX•••CO	0.070	0.081	0.048	**F₂X•••CO**	0.177	0.105	0.077
FX•••O(CH₃)₂	0.174	0.197	0.107	**F₂X•••O(CH₃)₂**	0.463	0.295	0.206
FX•••NCCH₃	-	0.157	0.098	**-**	-	-	-

Total Energy of the Molecule (H) and |V|/G Ratio: Cremer and Kraka[127] have proposed a criterion based on the sign of H (total energy H = V+G). It is often pointed out that the negative H at BCP is sufficient to classify interactions as closed-shell interactions (|V| > G) and positive for shared-shell interaction (G > |V|)[128]. For example, $\nabla^2\rho$ for $F_3B\cdots NH_3$ at B$\cdots$N BCP is +0.235 au whereas the H value is -0.089 au and the bond is classified as covalent one. For a large number of complexes, the value of H is close to zero, and a slight perturbation in structure can make the value positive or negative. So, this criterion is also ambiguous. Another similar criterion has been proposed by Espinoza[129] based on the ratio of the potential energy density and kinetic energy density (V/G) of electrons at the bond critical point. |V|/G < 1 indicates closed-shell interaction, and for shared-shell interaction |V|/G > 2. For values between 1 and 2, interaction is taken as the intermediate kind. Figure 6.8 summarises the average |V|/G value for each element.

The average |V|/G value of the s-block elements decreases in the following order: Be >

H> Ca > Mg > Na > Li. This ratio is more than 1 in some weakly bound beryllium bonded complexes ($F_2Be\cdots SH_2$ 1.09, $F_2Be\cdots C_2H_4$ 1.19), indicating that they are in the intermediate range. For relatively strongly bound Be-bonded complexes, this ratio is substantially lower than one ($F_2Be\cdots OH_2$ 0.86, $F_2Be\cdots NCH$ 0.89), suggesting closed-shell interaction. Interestingly, relatively weak H-bonds have a low $|V|/G$ ($FH\cdots SH_2$ 0.84, $FH\cdots C_2H_4$ 0.76) and comparatively strong bonds have a high $|V|/G$ ($FH\cdots OH_2$ 0.93, $FH\cdots NH_3$ 1.13). However, for Li, Na, Mg, and Ca bonds, this ratio does not fluctuate and significantly remains far below 1. The standard deviation of the average value of the ratio demonstrates this. The deviation remains large for Be and H, with 0.12 and 0.09, respectively, whereas it is less than 0.04 for the other s-block elements. In the binding energy versus electron density plot Li, Na, Be, Mg, and Ca-bonds belongs to a high slope region, which indicates a low $|V|/G$ ratio. Except for a few Be-bonded complexes, all of the other complexes possess a low $V|/G$ ratio.

Among the group's 13 members, the boron bond exhibits two regimes of $|V|/G$ ratio: the one with strong and short bonds has substantial covalent character with an average $|V|/G$ of 1.53(0.07), while the weak and long bonds exhibit closed-shell interaction with $|V|/G$ 0.91(0.08) (see supplementary information Table S6.7). Aluminium bonded complexes show a similar trend as Be-bond, where the weakly Al-bonded complexes possess $|V|/G$ slightly greater than 1 ($F_3Al\cdots SH_2$ 1.05, $F_3Al\cdots C_2H_4$ 1.09) whereas the stronger ones are within the closed-shell limit. All the Ga and In-bonded complexes have $|V|/G$ greater than 1.00, while the $|V|/G$ ratio of Tl bonded complexes oscillates between 0.94-1.10.

Carbon bonds have the lowest average $|V|/G$ ratio amongst all the investigated intermolecular bonds. The values are comparable to typically closed-shell interactions. However, a completely different picture was observed for the other group 14 elements. The $|V|/G$ ratios for $ClH_3X\cdots NH_3$ complexes are 1.30, 1.07, 1.08, and 1.02 for X=Si, Ge, Sn, and Pb, respectively, and 0.73 for X=C. This difference emphasises the uniqueness of carbon bonds among tetrels once again. This result is consistent with the slopes of the binding energy versus electron density curve.

For N-bonded complexes, the average value of $|V|/G$ ratio is 0.82, with almost negligible variation from the type of acceptors. For P and As bound complexes, donors

with stronger Lewis bases (H_2O, NH_3, HCN, HCHO, CH_3OH, CH_3OCH_3) have a |V|/G ratio close to 1.00. In contrast, donors with weak Lewis bases have a value closer to 0.85. However, this difference decreases with Sb and Bi bonded complexes. Group 16 and 17 follow a similar trend in the |V|/G ratio as group 15 elements.

| | | | H 0.92(0.09) | → Element |
| | | | | → Avg \|V\|/G (SD) |

1	2	13	14	15	16	17
H 0.92(0.09)						
Li 0.74(0.04)	Be 0.96(0.12)	B 1.22(0.32)	C 0.72(0.02)	N 0.82(0.03)	O 0.87(0.03)	F 0.84(0.05)
Na 0.76(0.03)	Mg 0.81(0.04)	Al 0.98(0.10)	Si 1.01(0.17)	P 0.94(0.11)	S 0.89(0.10)	Cl 0.88(0.09)
K	Ca 0.82(0.04)	Ga 1.19(0.07)	Ge 0.95(0.10)	As 1.00(0.11)	Se 0.97(0.12)	Br 0.96(0.09)
Rb	Sr	In 1.05(0.05)	Sn 0.97(0.09)	Sb 1.04(0.09)	Te 1.06(0.13)	I 1.03(0.10)
Cs	Ba	Tl 0.99(0.17)	Pb 0.95(0.07)	Bi 1.01(0.07)	Po 1.02(0.09)	At 1.03(0.07)
Fr	Ra					

<1.00(closed)   1.00-2.00(Intermediate)   >2.00 (Shared)

Figure 6.8. The ratio of the potential (|V(r)|) and kinetic (G(r)) energy densities of the electrons at BCP for the different intermolecular bonds formed by main group elements of the Periodic Table. The |V(r)|/ G(r) ratio has been used for the characterisation of bonding in three regions, namely closed-shell (<1.00) (in blue), intermediate (1.00-2.00) (in cyan), and shared-shell (>2.00) (in green) interaction.

Results and Discussion

$|\lambda_1|/\lambda_3$ Ratio: According to Sosa and co-workers[91] ratio of the first and third eigenvalue of the Hessian matrix can also be employed to identify shared-shell interactions by considering a series of hydrogen and halogen bonded complexes. $|\lambda_1|/\lambda_3$ greater than 1 has been associated with the shared-shell interaction. Among the three eigenvalues of the Laplacian, λ_1, λ_2, and λ_3, the first two are, in general, negative. The third one is positive as the electron density at BCP is maximum in the two directions orthogonal to the bond. It is a minimum along the bond path, leading to the (3, -1) bond critical points. Hence, when this ratio is more than one, the maximum (electron accumulation) is steeper than the minimum (electron depletion). In other words, this is the ratio of the perpendicular contraction to the parallel expansion along the bond path. Shahi and Arunan[35] defined a range in $|\lambda_1|/\lambda_3$ to differentiate the bonding nature into closed, intermediate, and shared. The $|\lambda_1|/\lambda_3 < 0.25$ has been identified for closed-shell interactions, $|\lambda_1|/\lambda_3 > 1$ for shared-shell interaction. Values between 0.25-1.00 indicate the interaction of the intermediate type.

H-bonded complexes possess the highest average $|\lambda_1|/\lambda_3$ values amongst the main group elements. Other s-block elements have a significantly low value of this ratio, suggesting their difference with hydrogen and the closed nature of bonding. It is consistent with the previously discussed criteria. For Be-bond, the complexes with Lewis base H_2S and PH_3 show the $|\lambda_1|/\lambda_3$ similar to hydrogen-bonded ones ($F_2Be\cdots SH_2$ 0.214, $F_2Be\cdots PH_3$ 0.233) and with other bases values are comparable to the other s-block elements.

Similar to the preceding section $|\lambda_1|/\lambda_3$ for boron bonded complexes, two regimes have been identified. The average for strong and short bonds is 0.24(0.03), slightly below the intermediate range. The average of $|\lambda_1|/\lambda_3$ ratio for weak and long bonds is 0.10 (0.02). For rest of the group 13 elements, the $|\lambda_1|/\lambda_3$ ratio follows an exactly similar trend as the $|V|/G$ ratio. Surprisingly, the average $|\lambda_1|/\lambda_3$ ratio found for Al-bonds is identical to that calculated for alkalene bound complexes. The Ga-bonds have higher $|\lambda_1|/\lambda_3$ compared to Al-bonds.

The C-bonds shows the lowest $|\lambda_1|/\lambda_3$ [0.07(0.02)] amongst all the intermolecular bonds

considered in this work. In fact, for few complexes, this value is well below 0.04 ($FH_3C\cdots FH$ 0.038). Similarly, in Si-bonded complexes, this ratio is low 0.09, well inside the closed-shell limit, while the $|V|/G$ ratio is in the intermediate range. The $|\lambda_1|/\lambda_3$ ratio for the rest of the group 14 bonds increases systematically.

Figure 6.9. The ratio of the first ($|\lambda_1|$) and third (λ_3) eigenvalues of the Hessian matrix at BCP for the different intermolecular bonds formed by the main group elements of the Periodic Table. The ($|\lambda_1|$)/λ_3 ratio has been used for the characterisation of bonding in three regions, namely closed-shell (<0.25) (in blue), intermediate (0.25-1.00) (in cyan), and shared shell interaction (>1.00) (in green).

The $|\lambda_1|/\lambda_3$ for N-bonds are pointedly lower than the rest of the congeners. Similar to the $|V|/G$ ratio, the $|\lambda_1|/\lambda_3$ ratio for P and As-bonds are larger with stronger Lewis bases H_2O, NH_3, HCN, HCHO, CH_3OH, CH_3OCH_3 and smaller with weak Lewis bases CO, PH_3, C_2H_4. On the other hand, this difference is not so evident for Sb and Bi-bonds. In group 16 elements, the average $|\lambda_1|/\lambda_3$ increases from O to Te-bonds. A slightly decreased value has been observed for Po-bond. An exactly similar trend has been observed for the group 17 elements.

6.4 **Summary**

At the MP2 level of theory, almost a thousand donor-acceptor complexes have been theoretically explored throughout the Periodic Table. The binding energy of these complexes strongly correlates with electron density at the bond critical point. As pointed out in previous literature[35], the slopes of such correlation plots are similar for H-/Cl- bonding but distinctly different for Li- bonding. Extrapolation of these fitted lines leads towards the ionic bond for Li-bonding and the covalent bond for H-bonding and Cl-bonding. We thought the slopes of these plots could be an interesting way to look at the intermolecular bonding and propose a new classification. We can summarise our findings as follows:

1. Intermolecular bonding is classified into two types: IMB with a covalent molecule (IMB-C) and IMB with an ionic molecule (IMB-I). The IMB-C includes hydrogen, halogen, chalcogen, pnictogen, tetrel (excluding carbon bonds), and boron bond (but not triel bond). IMB-I contains Lithium, sodium, beryllium, magnesium bonds and triel bonds. The binding energy versus electron density plot of the IMI-C class generally has a low slope, whereas the IMB-I class has a high slope. This difference might be explained by the donors being 'covalently bound' in the IMB-C and 'ionic' in the IMB-I. This, in turn, has an effect on the nature of the intermolecular bond.

2. Carbon bonds were expected to fall into the IMB-C category since carbon bond donors are generally covalent molecules. However, the electron density

between the two atoms is extremely low, and the binding energy rapidly increases with electron density resulting in a high value of the slope. Among all intermolecular bonds, carbon bonds have the lowest $|V|/G$ and $|\lambda_1|/\lambda_3$ ratios indicating closed-shell interactions. Boron is also significantly different from the rest of the group 13 congeners. Some boron bound compounds have two tautomeric forms and two distinct distances. The shorter ones have the characteristic of covalent bonding. Boron bonds are classified as IMB-C, whereas their 13 congeners are classified as IMB-I in our categorisation.

3. The hydrogen bond remains unique. The slopes from the binding energy versus electron density plots are similar for alkali and alkaline earth metals. Instead of having two separate names for each, we recommend referring to intermolecular bonding in alkali and alkaline earth metals as 'alkelene bond'.

6.5 **References**

1. Latimer, W. M. & Rodebush, W. H. Polarity and ionization from the standpoint of the Lewis theory of valence. *J. Am. Chem. Soc.* **42**, 1419–1433 (1920).

2. Pauling, L. *The Nature of the Chemical Bond,*. (Cornell University Press, 1960).

3. Müller-Dethlefs, K. & Hobza, P. Noncovalent Interactions: A Challenge for Experiment and Theory. *Chem. Rev.* (2000) doi:10.1021/cr9900331.

4. Mani, D. & Arunan, E. The X–C⋯Y (X = O/F, Y = O/S/F/Cl/Br/N/P) 'carbon bond' and hydrophobic interactions. *Phys. Chem. Chem. Phys.* **15**, 14377–14383 (2013).

5. Thomas, S. P., Pavan, M. S. & Guru Row, T. N. Experimental evidence for 'carbon bonding' in the solid state from charge density analysis. *Chem. Commun.* **50**, 49–51 (2014).

6. Bauzá, A., Mooibroek, T. J. & Frontera, A. Tetrel-bonding interaction: Rediscovered supramolecular force? *Angew. Chemie - Int. Ed.* **52**, 12317–12321 (2013).

7. Grabowski, S. J. Tetrel bond–σ-hole bond as a preliminary stage of the S_N2 reaction. *Phys. Chem. Chem. Phys.* **16**, 1824–1834 (2014).

References

8. Grabowski, S. J. Triel bonds, π-hole-π-electrons interactions in complexes of boron and aluminium trihalides and trihydrides with acetylene and ethylene. *Molecules* (2015) doi:10.3390/molecules200611297.

9. Murray, J. S., Lane, P. A. T. & Politzer, P. A predicted new type of directional noncovalent interaction. *Int. J. Quantum Chem.* **107**, 2286–2292 (2007).

10. Scheiner, S. A new noncovalent force: Comparison of P⋯N interaction with hydrogen and halogen bonds. *J. Chem. Phys.* **134**, 94315 (2011).

11. Del Bene, J. E., Alkorta, I., Sanchez-Sanz, G. & Elguero, J. Structures, Energies, Bonding, and NMR Properties of Pnicogen Complexes $H_2XP:NXH_2$ (X = H, CH_3, NH_2, OH, F, Cl). *J. Phys. Chem. A* **115**, 13724–13731 (2011).

12. Zahn, S., Frank, R., Hey-Hawkins, E. & Kirchner, B. Pnicogen bonds: a new molecular linker? *Chem. Eur. J.* **17**, 6034–6038 (2011).

13. Wang, W., Ji, B. & Zhang, Y. Chalcogen Bond: A Sister Noncovalent Bond to Halogen Bond. *J. Phys. Chem. A* **113**, 8132–8135 (2009).

14. Manna, D. & Mugesh, G. Regioselective Deiodination of Thyroxine by Iodothyronine Deiodinase Mimics: An Unusual Mechanistic Pathway Involving Cooperative Chalcogen and Halogen Bonding. *J. Am. Chem. Soc.* **134**, 4269–4279 (2012).

15. Bleiholder, C., Werz, D. B., Köppel, H. & Gleiter, R. Theoretical Investigations on Chalcogen−Chalcogen Interactions: What Makes These Nonbonded Interactions Bonding? *J. Am. Chem. Soc.* **128**, 2666–2674 (2006).

16. Sanz, P., Mó, O. & Yáñez, M. Characterization of intramolecular hydrogen bonds and competitive chalcogen–chalcogen interactions on the basis of the topology of the charge density. *Phys. Chem. Chem. Phys.* **5**, 2942–2947 (2003).

17. Legon, A. C. The halogen bond: an interim perspective. *Phys. Chem. Chem. Phys.* **12**, 7736–7747 (2010).

18. Metrangolo, P. & Resnati, G. Halogen Bonding: A Paradigm in Supramolecular Chemistry. *Chem. – A Eur. J.* **7**, 2511–2519 (2001).

19. Alkorta, I., Blanco, F., Solimannejad, M. & Elguero, J. Competition of Hydrogen Bonds and Halogen Bonds in Complexes of Hypohalous Acids with Nitrogenated Bases. *J. Phys. Chem. A* **112**, 10856–10863 (2008).

20. Clark, T., Hennemann, M., Murray, J. S. & Politzer, P. Halogen bonding: the σ-hole. *J. Mol. Model.* **13**, 291–296 (2007).

21. Cavallo, G. *et al.* The halogen bond. *Chem. Rev.* **116**, 2478–2601 (2016).

22. Bauzá, A. & Frontera, A. Aerogen Bonding Interaction: A New Supramolecular Force? *Angew. Chemie Int. Ed.* **54**, 7340–7343 (2015).

23. Bauzá, A. & Frontera, A. π-Hole aerogen bonding interactions. *Phys. Chem. Chem. Phys.* **17**, 24748–24753 (2015).

24. Joy, J. & Jemmis, E. D. Contrasting behavior of the Z bonds in X–Z···Y weak interactions: Z= main group elements versus the transition metals. *Inorg. Chem.* **56**, 1132–1143 (2017).

25. Joy, J. & Jemmis, E. D. Designing M-bond (XM···Y, M= transition metal): σ-hole and radial density distribution. *J. Chem. Sci.* **131**, 117 (2019).

26. Legon, A. C. & Walker, N. R. What's in a name? 'Coinage-metal'non-covalent bonds and their definition. *Phys. Chem. Chem. Phys.* **20**, 19332–19338 (2018).

27. Frontera, A. & Bauzá, A. Regium–π bonds: An unexplored link between noble metal nanoparticles and aromatic surfaces. *Chem. Eur. J.* **24**, 7228–7234 (2018).

28. Bauzá, A., Alkorta, I., Elguero, J., Mooibroek, T. J. & Frontera, A. Spodium Bonds: Noncovalent Interactions Involving Group 12 Elements. *Angew. Chemie Int. Ed.* (2020).

29. Alkorta, I., Elguero, J. & Frontera, A. Not only hydrogen bonds: Other noncovalent interactions. *Crystals* **10**, 180 (2020).

30. Kollman, P. A., Liebman, J. F. & Allen, L. C. Lithium bond. *J. Am. Chem. Soc.* **92**, 1142–1150 (1970).

31. Ault, B. S. & Pimentel, G. C. Matrix isolation infrared studies of lithium bonding. *J. Phys. Chem.* **79**, 621–626 (1975).

32. Parajuli, R. & Arunan, E. Comprehensive investigations on DNa···A (D= H/F) complexes show why 'sodium bonding'is not commonly observed. *Chem. Phys. Lett.* **568**, 63–69 (2013).

33. Esrafili, M. D. & Mohammadirad, N. Halogen bond interactions enhanced by sodium bonds—Theoretical evidence for cooperative and substitution effects in NCX··· NCNa···NCY complexes (X= F, Cl, Br, I; Y= H, F, OH). *Can. J. Chem.*

92, 653–658 (2014).

34.   Kulkarni, G. V & Rao, C. N. R. A comparative study of lithium, sodium and hydrogen bonds formed by 1: 1 interaction of electron donor molecules with lithium, sodium and hydrogen halides. *J. Mol. Struct.* **100**, 531–537 (1983).

35.   Shahi, A. & Arunan, E. Hydrogen bonding, halogen bonding and lithium bonding: an atoms in molecules and natural bond orbital perspective towards conservation of total bond order, inter- and intra-molecular bonding. *Phys. Chem. Chem. Phys.* **16**, 22935–22952 (2014).

36.   Arunan, E. *et al.* Defining the hydrogen bond: An account (IUPAC Technical Report). *Pure Appl. Chem.* **83**, 1619–1636 (2011).

37.   Arunan, E. *et al.* Definition of the hydrogen bond (IUPAC Recommendations 2011). *Pure Appl. Chem.* **83**, 1637–1641 (2011).

38.   Yáñez, M., Sanz, P., Mó, O., Alkorta, I. & Elguero, J. Beryllium bonds, do they exist? *J. Chem. Theory Comput.* **5**, 2763–2771 (2009).

39.   Albrecht, L., Boyd, R. J., Mó, O. & Yáñez, M. Cooperativity between hydrogen bonds and beryllium bonds in $(H_2O)_nBeX_2$ (n = 1–3, X = H, F) complexes. A new perspective. *Phys. Chem. Chem. Phys.* **14**, 14540–14547 (2012).

40.   Eskandari, K. Characteristics of beryllium bonds; a QTAIM study. *J. Mol. Model.* **18**, 3481–3487 (2012).

41.   Montero-Campillo, M. M., Mó, O., Yáñez, M., Alkorta, I. & Elguero, J. The beryllium bond. in *Advances in Inorganic Chemistry* vol. 73 73–121 (Academic Press, 2019).

42.   Martín-Sómer, A., Lamsabhi, A. M., Mó, O. & Yáñez, M. The importance of deformation on the strength of beryllium bonds. *Comput. Theor. Chem.* **998**, 74–79 (2012).

43.   Yang, X., Li, Q., Cheng, J. & Li, W. A new interaction mechanism of $LiNH_2$ with MgH_2: magnesium bond. *J. Mol. Model.* **19**, 247–253 (2013).

44.   Tama, R., Mó, O., Yáñez, M. & Montero-Campillo, M. M. Characterizing magnesium bonds: main features of a non-covalent interaction. *Theor. Chem. Acc.* **136**, 36 (2017).

45.   Grabowski, S. J. Magnesium Bonds: From Divalent Mg Centres to Trigonal and

Tetrahedral Coordination. *ChemistrySelect* **3**, 3147–3154 (2018).

46. Hou, M., Zhu, Y., Li, Q. & Scheiner, S. Tuning the competition between hydrogen and tetrel bonds by a magnesium bond. *ChemPhysChem* **21**, 212–219 (2020).

47. Montero-Campillo, M. M. *et al.* Alkaline-earth (Be, Mg and Ca) bonds at the origin of huge acidity enhancements. *Phys. Chem. Chem. Phys.* **20**, 2413–2420 (2018).

48. Yáñez, M., Mó, O., Alkorta, I. & Elguero, J. Can Conventional Bases and Unsaturated Hydrocarbons Be Converted into Gas-Phase Superacids That Are Stronger than Most of the Known Oxyacids? The Role of Beryllium Bonds. *Chem. Eur. J.* **19**, 11637–11643 (2013).

49. Brea, O. *et al.* Exergonic and spontaneous production of radicals through beryllium bonds. *Angew. Chemie* **128**, 8878–8881 (2016).

50. Montero-Campillo, M. M., Mó, O., Yáñez, M., Alkorta, I. & Elguero, J. Be-and Mg-Based Electron and Anion Sponges. *ChemPhysChem* **19**, 1701–1706 (2018).

51. Villanueva, E. F., Mó, O. & Yáñez, M. On the existence and characteristics of π-beryllium bonds. *Phys. Chem. Chem. Phys.* **16**, 17531–17536 (2014).

52. Li, S.-Y. *et al.* Insight into structural and π–magnesium bonding characteristics of the $X_2Mg\cdots Y$ (X = H, F; Y = C_2H_2, C_2H_4 and C_6H_6) complexes. *RSC Adv.* **6**, 102754–102761 (2016).

53. Albrecht, L., Boyd, R. J., Mó, O. & Yáñez, M. Changing weak halogen bonds into strong ones through cooperativity with beryllium bonds. *J. Phys. Chem. A* **118**, 4205–4213 (2014).

54. Alkorta, I., Elguero, J., Mó, O., Yáñez, M. & Del Bene, J. E. Using beryllium bonds to change halogen bonds from traditional to chlorine-shared to ion-pair bonds. *Phys. Chem. Chem. Phys.* **17**, 2259–2267 (2015).

55. Brea, O., Mó, O., Yáñez, M., Alkorta, I. & Elguero, J. Creating σ-Holes through the Formation of Beryllium Bonds. *Chem. Eur. J.* **21**, 12676–12682 (2015).

56. Alkorta, I., Elguero, J., Yáñez, M. & Mó, O. Cooperativity in beryllium bonds. *Phys. Chem. Chem. Phys.* **16**, 4305–4312 (2014).

57. Xu, H., Li, Q. & Scheiner, S. Effect of Magnesium Bond on the Competition

Between Hydrogen and Halogen Bonds and the Induction of Proton and Halogen Transfer. *ChemPhysChem* **19**, 1456–1464 (2018).

58. Alkorta, I. & Legon, A. C. Non-Covalent Interactions Involving Alkaline-Earth Atoms and Lewis Bases B: An ab Initio Investigation of Beryllium and Magnesium Bonds, B⋯ MR_2 (M= Be or Mg, and R= H, F or CH_3). *Inorganics* **7**, 35 (2019).

59. Heaven, M. C., Bondybey, V. E., Merritt, J. M. & Kaledin, A. L. The unique bonding characteristics of beryllium and the Group IIA metals. *Chem. Phys. Lett.* **506**, 1–14 (2011).

60. Merritt, J. M., Bondybey, V. E. & Heaven, M. C. Beryllium Dimer—Caught in the Act of Bonding. *Science (80-.).* **324**, 1548 LP – 1551 (2009).

61. Balfour, W. J. & Douglas, A. E. Absorption spectrum of the Mg2 molecule. *Can. J. Phys.* **48**, 901–914 (1970).

62. Kaplan, I. G. *Theory of Molecular Interactions*. (Elsevier, 1986).

63. Jordan, K. D. & Simons, J. Comment on the electronic structure of small beryllium and magnesium clusters and their anions. *J. Chem. Phys.* **72**, 2889–2890 (1980).

64. Arrowsmith, M. *et al.* Neutral zero-valent s-block complexes with strong multiple bonding. *Nat. Chem.* **8**, 890 (2016).

65. Frisch, M. J. *et al.* Gaussian 09 Revision D. 01, 2009. *Gaussian Inc. Wallingford CT* (2009).

66. Møller, C. & Plesset, M. S. Note on an Approximation Treatment for Many-Electron Systems. *Phys. Rev.* **46**, 618–622 (1934).

67. Peterson, K. A. Systematically convergent basis sets with relativistic pseudopotentials. I. Correlation consistent basis sets for the post-d group 13–15 elements. *J. Chem. Phys.* **119**, 11099–11112 (2003).

68. Metz, B., Stoll, H. & Dolg, M. Small-core multiconfiguration-Dirac–Hartree–Fock-adjusted pseudopotentials for post-d main group elements: Application to PbH and PbO. *J. Chem. Phys.* **113**, 2563–2569 (2000).

69. Pritchard, B. P., Altarawy, D., Didier, B., Gibson, T. D. & Windus, T. L. New basis set exchange: An open, up-to-date resource for the molecular sciences

community. *J. Chem. Inf. Model.* **59**, 4814–4820 (2019).

70.   Dunning, T. H. Gaussian basis sets for use in correlated molecular calculations. I. The atoms boron through neon and hydrogen. *J. Chem. Phys.* **90**, 1007–1023 (1989).

71.   Boys, S. F. & Bernardi, F. The calculation of small molecular interactions by the differences of separate total energies. Some procedures with reduced errors. *Mol. Phys.* **19**, 553–566 (1970).

72.   Keith, T. A. AIMAll (Version 13.05. 06). *TK Gristmill Softw. Overl. Park. KS, USA* (2013).

73.   Bader, R. F. W. Atoms in Molecules: A Quantum Theory: Oxford Univ. Press. (1990).

74.   Feng, Y., Liu, L., Wang, J.-T., Li, X.-S. & Guo, Q.-X. Blue-shifted lithium bonds. *Chem. Commun.* 88–89 (2004).

75.   Joseph, J. & Jemmis, E. D. Red-, blue-, or no-shift in hydrogen bonds: a unified explanation. *J. Am. Chem. Soc.* **129**, 4620–4632 (2007).

76.   Israelachvili, J. N. *Intermolecular and surface forces*. (Academic press, 2015).

77.   Alkorta, I., Hill, J. G. & Legon, A. C. An ab initio investigation of alkali–metal non-covalent bonds B⋯ LiR and B⋯ NaR (R= F, H or CH_3) formed with simple Lewis bases B: the relative inductive effects of F, H and CH_3 . *Phys. Chem. Chem. Phys.* **22**, 16421–16430 (2020).

78.   Dyke, T. R., Howard, B. J. & Klemperer, W. Radiofrequency and microwave spectrum of the hydrogen fluoride dimer; a nonrigid molecule. *J. Chem. Phys.* **56**, 2442–2454 (1972).

79.   Peterson, K. A. & Dunning Jr, T. H. Benchmark calculations with correlated molecular wave functions. VII. Binding energy and structure of the HF dimer. *J. Chem. Phys.* **102**, 2032–2041 (1995).

80.   Buckingham, A. D. & Fowler, P. W. A model for the geometries of van der Waals complexes. *Can. J. Chem.* **63**, 2018–2025 (1985).

81.   Gillette, R. H. & Sherman, A. The Nature of the Hydrogen Bond. I. Association in Carboxylic Acids. *J. Am. Chem. Soc.* **58**, 1135–1139 (1936).

82.   Morokuma, K. Molecular orbital studies of hydrogen bonds. III. C= O⋯ H–O

hydrogen bond in $H_2CO\cdots H_2O$ and $H_2CO\cdots 2H_2O$. *J. Chem. Phys.* **55**, 1236–1244 (1971).

83.   Morokuma, K. Why do molecules interact? The origin of electron donor-acceptor complexes, hydrogen bonding and proton affinity. *Acc. Chem. Res.* **10**, 294–300 (1977).

84.   Weinhold, F. & Landis, C. R. *Valency and bonding: a natural bond orbital donor-acceptor perspective*. (Cambridge University Press, 2005).

85.   Reed, A. E., Weinhold, F., Curtiss, L. A. & Pochatko, D. J. Natural bond orbital analysis of molecular interactions: Theoretical studies of binary complexes of HF, H_2O, NH_3, N_2, O_2, F_2, CO, and CO_2 with HF, H_2O, and NH_3. *J. Chem. Phys.* **84**, 5687–5705 (1986).

86.   Coulson, C. A. The hydrogen bond—a review of the present position. *Research* **10**, 149 (1957).

87.   Nemes, C. T., Laconsay, C. J. & Galbraith, J. M. Hydrogen bonding from a valence bond theory perspective: the role of covalency. *Phys. Chem. Chem. Phys.* **20**, 20963–20969 (2018).

88.   Grabowski, S. J. What is the covalency of hydrogen bonding? *Chem. Rev.* **111**, 2597–2625 (2011).

89.   Popelier, P. L. A., Aicken, F. M. & O'Brien, S. E. Atoms in molecules. *Chem. Model. Appl. theory* **1**, 143–198 (2000).

90.   Parthasarathi, R., Subramanian, V. & Sathyamurthy, N. Hydrogen bonding without borders: an atoms-in-molecules perspective. *J. Phys. Chem. A* **110**, 3349–3351 (2006).

91.   Amezaga, N. J. M., Pamies, S. C., Peruchena, N. M. & Sosa, G. L. Halogen bonding: a study based on the electronic charge density. *J. Phys. Chem. A* **114**, 552–562 (2009).

92.   Mohan, N. & Suresh, C. H. A molecular electrostatic potential analysis of hydrogen, halogen, and dihydrogen bonds. *J. Phys. Chem. A* **118**, 1697–1705 (2014).

93.   Raghavendra, B. & Arunan, E. Unpaired and σ bond electrons as H, Cl, and Li bond acceptors: an anomalous one-electron blue-shifting chlorine bond. *J. Phys.*

Chem. A **111**, 9699–9706 (2007).

94.   Grabowski, S. J. Boron and other triel Lewis acid centers: from hypovalency to hypervalency. *ChemPhysChem* **15**, 2985–2993 (2014).

95.   Leopold, K. R., Canagaratna, M. & Phillips, J. A. Partially bonded molecules from the solid state to the stratosphere. *Acc. Chem. Res.* **30**, 57–64 (1997).

96.   Grabowski, S. J. Two faces of triel bonds in boron trihalide complexes. *J. Comput. Chem.* **39**, 472–480 (2018).

97.   Gnanasekar, S. P. & Arunan, E. Inter/intramolecular bonds in TH_5^+ (T= C/Si/Ge): H_2 as tetrel bond acceptor and the uniqueness of carbon bonds. *J. Phys. Chem. A* **123**, 1168–1176 (2018).

98.   Das, A. & Arunan, E. Chemical bonding in Period 2 homonuclear diatomic molecules: a comprehensive relook. *J. Chem. Sci.* **131**, 1–17 (2019).

99.   McNaught, A. D. & Wilkinson, A. *Compendium of chemical terminology*. vol. 1669 (Blackwell Science Oxford, 1997).

100.   Munshi, P. & Guru Row, T. N. Exploring the Lower Limit in Hydrogen Bonds: Analysis of Weak C−H⋯O and C−H⋯π Interactions in Substituted Coumarins from Charge Density Analysis. *J. Phys. Chem. A* **109**, 659–672 (2005).

101.   Tantardini, C. & Oganov, A. R. Thermochemical electronegativities of the elements. *Nat. Commun.* **12**, 1–9 (2021).

102.   Scheiner, S. The pnicogen bond: Its relation to hydrogen, halogen, and other noncovalent bonds. *Acc. Chem. Res.* **46**, 280–288 (2013).

103.   Legon, A. C. Tetrel, pnictogen and chalcogen bonds identified in the gas phase before they had names: A systematic look at non-covalent interactions. *Phys. Chem. Chem. Phys.* **19**, 14884–14896 (2017).

104.   Gnanasekar, S. P. & Arunan, E. Molecular Beam and Spectroscopic Techniques: Towards Fundamental Understanding of Intermolecular Interactions/Bonds, Intermolecular Interactions in Crystal, Ed Novoa, J. J, The Royal Society of Chemistry (2018).

105.   Sarkar, S., Pavan, M. S. & Row, T. N. G. Experimental validation of 'pnicogen bonding'in nitrogen by charge density analysis. *Phys. Chem. Chem. Phys.* **17**,

2330–2334 (2015).

106. Nelson Jr, D. D., Fraser, G. T. & Klemperer, W. Ammonia dimer: A surprising structure. *J. Chem. Phys.* **83**, 6201–6208 (1985).

107. Nelson Jr, D. D., Klemperer, W., Fraser, G. T., Lovas, F. J. & Suenram, R. D. Ammonia dimer: Further structural studies. *J. Chem. Phys.* **87**, 6364–6372 (1987).

108. Olthof, E. H. T., Van der Avoird, A. & Wormer, P. E. S. Structure, internal mobility, and spectrum of the ammonia dimer: Calculation of the vibration–rotation-tunneling states. *J. Chem. Phys.* **101**, 8430–8442 (1994).

109. Scheiner, S. Can two trivalent N atoms engage in a direct N···N noncovalent interaction? *Chem. Phys. Lett.* **514**, 32–35 (2011).

110. Li, W. *et al.* Theory meets experiment for noncovalent complexes: The puzzling case of pnicogen interactions. *Angew. Chemie Int. Ed.* **57**, 13853–13857 (2018).

111. Aakeroy, C. B. *et al.* Definition of the chalcogen bond (IUPAC Recommendations 2019). *Pure Appl. Chem.* **91**, 1889–1892 (2019).

112. Vogel, L., Wonner, P. & Huber, S. M. Chalcogen bonding: An overview. *Angew. Chemie Int. Ed.* **58**, 1880–1891 (2019).

113. Scilabra, P., Terraneo, G. & Resnati, G. The chalcogen bond in crystalline solids: A world parallel to halogen bond. *Acc. Chem. Res.* **52**, 1313–1324 (2019).

114. Thomas, S. P., Veccham, S. P. K. P., Farrugia, L. J. & Guru Row, T. N. "Conformational simulation" of sulfamethizole by molecular complexation and insights from charge density analysis: role of intramolecular S···O chalcogen bonding. *Cryst. Growth Des.* **15**, 2110–2118 (2015).

115. Thomas, S. P., Jayatilaka, D. & Row, T. N. G. S···O chalcogen bonding in sulfa drugs: insights from multipole charge density and X-ray wavefunction of acetazolamide. *Phys. Chem. Chem. Phys.* **17**, 25411–25420 (2015).

116. Varadwaj, P. R., Varadwaj, A., Marques, H. M. & MacDougall, P. J. The chalcogen bond: can it be formed by oxygen? *Phys. Chem. Chem. Phys.* **21**, 19969–19986 (2019).

117. Definition of the halogen bond (IUPAC Recommendations 2013). *Pure and Applied Chemistry* vol. 85 1711 (2013).

118. Pavan, M. S., Prasad, K. D. & Row, T. N. G. Halogen bonding in fluorine: experimental charge density study on intermolecular F···F and F···S donor–acceptor contacts. *Chem. Commun.* **49**, 7558–7560 (2013).

119. Hathwar, V. R., Chopra, D., Panini, P. & Guru Row, T. N. Revealing the polarizability of organic fluorine in the trifluoromethyl group: implications in supramolecular chemistry. *Cryst. Growth Des.* **14**, 5366–5369 (2014).

120. Bloemink, H. I., Hinds, K., Holloway, J. H. & Legon, A. C. Characterisation of a pre-reactive intermediate in gas-phase mixtures of fluorine and ammonia: The rotational spectrum of the H_3N···F_2 complex. *Chem. Phys. Lett.* **245**, 598–604 (1995).

121. Cotti, G., Evans, C. M., Holloway, J. H. & Legon, A. C. Rotational spectroscopy of a pre-reactive mixture of H_2S and F_2 : detection and characterisation of the weakly bound complex H_2S···F_2. *Chem. Phys. Lett.* **264**, 513–521 (1997).

122. Cooke, S. A., Cotti, G., Holloway, J. H. & Legon, A. C. Detection and Characterization of a Pre-Reactive Complex in a Mixture of Water and Fluorine: Rotational Spectrum of H_2O···F_2. *Angew. Chemie Int. Ed. English* **36**, 129–130 (1997).

123. Scheiner, S. F-halogen bond: conditions for its existence. *J. Phys. Chem. A* **124**, 7290–7299 (2020).

124. Novick, S. E., Janda, K. C. & Klemperer, W. HFClF: structure and bonding. *J. Chem. Phys.* **65**, 5115–5121 (1976).

125. Baiocchi, F. A., Dixon, T. A. & Klemperer, W. The structure and hyperfine constants of HF–Cl_2. *J. Chem. Phys.* **77**, 1632–1638 (1982).

126. Koch, U. & Popelier, P. L. A. Characterization of CHO hydrogen bonds on the basis of the charge density. *J. Phys. Chem.* **99**, 9747–9754 (1995).

127. Cremer, D. & Kraka, E. Chemical Bonds without Bonding Electron Density—Does the Difference Electron-Density Analysis Suffice for a Description of the Chemical Bond? *Angew. Chemie Int. Ed. English* **23**, 627–628 (1984).

128. Cremer, D. & Kraka, E. A description of the chemical bond in terms of local properties of electron density and energy. *Croat. Chem. Acta* **57**, 1259–1281 (1984).

129. Espinosa, E., Alkorta, I., Elguero, J. & Molins, E. From weak to strong interactions: A comprehensive analysis of the topological and energetic properties of the electron density distribution involving X–H⋯ F–Y systems. *J. Chem. Phys.* **117**, 5529–5542 (2002).

6.6 **Supplementary Information**

*Table S6.1. Correlation coefficients (CC), intercepts and slopes of the binding energy (kJ/mol) versus electron density (au) plot for various intermolecular bonded complexes formed by different elements. 'Overall (by avg.)' denotes the average value of correlation coefficient (CC), intercept and slope of the three sets, 'Overall (by fit, with (0,0)]' fits all data point with the (0,0) point, '**Overall (by fit, without (0,0)]**' fits all data point without the (0,0) point. Values in the brackets denote standard deviation. The function y=mx+c has been used to fit the data.*

Complexes	CC	Intercept	Slope
X=H			
FX⋯A	0.92	0.3(3.0)	844(85)
HOX⋯A	0.94	-1.0(1.6)	832(73)
HSX⋯A	0.92	-0.0(1.0)	648(67)
Overall (by avg.)	0.93	-0.2(1.9)	775(75)
Overall (by fit, with (0,0)]	0.96	-2.2(0.9)	889(35)
Overall [by fit, without (0,0)]	**0.95**	**-2.5(1.0)**	**901(38)**
X=Li			
FX⋯A	0.86	1.0(8.7)	2868(408)
ClX⋯A	0.85	2.2(10.3)	2997(449)
BrX⋯A	0.85	2.7(10.5)	2995(450)
Overall (by avg.)	0.85	2.0(9.8)	2953(436)
Overall (by fit, with (0,0)]	0.89	0.7(4.4)	3011(199)
Overall [by fit, without (0,0)]	**0.85**	**1.1(5.4)**	**2997(239)**
X=Na			
FX⋯A	0.91	-12.7(6.9)	4274(484)
ClX⋯A	0.92	-9.9(6.4)	4039(423)
BrX⋯A	0.92	-9.7(6.6)	3978(428)
Overall (by avg.)	0.92	-10.8(6.6)	4097(445)
Overall (by fit, with (0,0)]	0.93	-7.0(3.0)	3840(202)
Overall [by fit, without (0,0)]	**0.91**	**-10.5(3.6)**	**4074(238)**
X=Be			
F_2X⋯A	0.96	-58.4(6.7)	3030(226)
Cl_2X⋯A	0.89	-76.7(18.2)	3090(380)
H_2X⋯A	0.92	-78.1(14.2)	3261(338)
Overall (by avg.)	0.92	-71.1(13.0)	3126(315)
Overall (by fit, with (0,0)]	0.82	-38.8(9.1)	2408(209)
Overall [by fit, without (0,0)]	**0.88**	**-64.9(9.1)**	**2983(206)**
X=Mg			
F_2X⋯A	0.95	-20.6(7.6)	3596(277)
Cl_2X⋯A	0.93	-17.7(10.0)	3569(349)
H_2X⋯A	0.97	-15.3(4.2)	2960(186)
Overall (by avg.)	0.95	-17.9(7.3)	3375(271)
Overall (by fit, with (0,0)]	0.93	-16.6(4.6)	3384(176)

Continued Table S6.1…

Overall [by fit, without (0,0)]	**0.93**	**-22.9(5.0)**	**3606(188)**
X=Ca			
F$_2$X···A	0.95	-8.9(6.7)	3137(260)
Cl$_2$X···A	0.94	-9.5(7.9)	3108(277)
H$_2$X···A	0.95	-8.0(6.0)	2931(245)
Overall (by avg.)	0.95	-8.8(6.9)	3059(261)
Overall (by fit, with (0,0)]	0.95	-6.6(3.2)	2986(125)
Overall [by fit, without (0,0)]	**0.94**	**-9.2(3.8)**	**3081(143)**
X=B			
BF$_3$···A	0.86	-0.4(5.9)	620(89)
BF$_2$H···A	0.87	0.5(4.1)	536(74)
BCl$_3$···A	0.66	0.9(9.0)	515(131)
Overall (by avg.)	0.80	0.3(6.3)	557(98)
Overall (by fit, with (0,0)]	0.77	0.5(3.4)	552(56)
Overall [by fit, without (0,0)]	**0.76**	**0.6(3.6)**	**552(58)**
X=Al			
F$_3$X···A	0.91	-45.9(16.5)	3814(416)
FH$_2$X···A	0.95	-36.6(8.9)	3294(265)
Cl$_3$X···A	0.91	-60.7(17.9)	3750(428)
Overall (by avg.)	0.92	-47.7(14.4)	3619(370)
Overall (by fit, with (0,0)]	0.88	-28.0(8.2)	3137(217)
Overall [by fit, without (0,0)]	**0.89**	**-44.9(9.2)**	**3564(240)**
X=Ga			
F$_2$HX···A	0.92	-38.3(11.9)	2130(229)
FH$_2$X···A	0.91	-32.2(9.9)	1964(213)
ClH$_2$X···A	0.89	-34.6(11.9)	1962(248)
Overall (by avg.)	0.91	-35.0(11.2)	2019(230)
Overall (by fit, with (0,0)]	0.88	-22.0(5.7)	1764(119)
Overall [by fit, without (0,0)]	**0.91**	**-36.3(6.1)**	**2048(125)**
X=In			
F$_2$HX···A	0.93	-27.8(9.6)	2266(220)
FH$_2$X···A	0.94	-26.6(7.2)	2175(187)
ClH$_2$X···A	0.91	-22.1(8.7)	2024(224)
Overall (by avg.)	0.93	25.5(8.5)	2155(210)
Overall (by fit, with (0,0)]	0.92	-17.0(4.4)	1959(110)
Overall [by fit, without (0,0)]	**0.93**	**-27.4(4.7)**	**2207(115)**
X=Tl			
F$_2$HX···A	0.94	**-**25.3(7.1)	1904(169)
FH$_2$X···A	0.90	-22.6(7.7)	1910(220)
ClH$_2$X···A	0.91	-17.8(6.9)	1737(198)
Overall (by avg.)	0.92	-21.9(7.2)	1850(196)
Overall (by fit, with (0,0)]	0.91	-13.1(3.5)	1625(94)
Overall [by fit, without (0,0)]	**0.92**	**-20.7(3.7)**	**1822(100)**

Continued Table S6.1…

X=C			
FH$_3$X···A	0.88	-4.1(1.3)	1777(233)
OHH$_3$X···A	0.85	-4.0(1.1)	1532(232)
ClH$_3$X···A	0.86	-4.4(1.5)	1806(257)
Overall (by avg.)	0.86	-4.2(1.3)	1705(241)
Overall (by fit, with (0,0)]	0.79	-2.6(0.7)	1429(138)
Overall [by fit, without (0,0)]	**0.87**	**-5.6(0.8)**	**1980(145)**
X=Si			
FH$_3$X···A	0.94	3.0(1.4)	822(74)
CNH$_3$X···A	0.93	2.7(1.2)	919(91)
ClH$_3$X···A	0.92	2.7(1.3)	790(83)
Overall (by avg.)	0.93	2.8(1.3)	844(83)
Overall (by fit, with (0,0)]	0.93	2.6(0.7)	844(44)
Overall [by fit, without (0,0)]	**0.92**	**3.0(0.7)**	**823(45)**
X=Ge			
FH$_3$X···A	0.93	2.3(1.4)	866(83)
CNH$_3$X···A	0.90	2.8(1.3)	866(102)
ClH$_3$X···A	0.93	2.6(1.3)	795(79)
Overall (by avg.)	0.92	2.6(1.3)	842(88)
Overall (by fit, with (0,0)]	0.93	2.3(0.7)	853(45)
Overall [by fit, without (0,0)]	**0.92**	**2.7(0.7)**	**828(47)**
X=Sn			
FH$_3$X···A	0.96	0.2(1.6)	117(81)
CNH$_3$X···A	0.96	3.2(1.0)	894(63)
ClH$_3$X···A	0.91	-0.4(2.5)	1141(130)
Overall (by avg.)	0.94	1.0(1.7)	1072(91)
Overall (by fit, with (0,0)]	0.94	1.0(0.9)	1093(52)
Overall [by fit, without (0,0)]	**0.93**	**1.0(1.0)**	**1085(56)**
X=Pb			
FH$_3$X···A	0.88	3.7(2.3)	1069(137)
CNH$_3$X···A	0.89	1.7(1.9)	1036(125)
ClH$_3$X···A	0.92	1.0(2.1)	1103(113)
Overall (by avg.)	0.90	2.1(2.1)	1069(125)
Overall (by fit, with (0,0)]	0.90	1.7(1.1)	1092(68)
Overall [by fit, without (0,0)]	**0.88**	**2.1(1.2)**	**1070(74)**
X=N			
F$_3$X···A	0.87	-0.4(0.6)	664(90)
Overall (by fit, with (0,0)]	0.93	-0.2(0.4)	628(59)
Overall (by fit, without (0,0)]	**0.87**	**-0.4(0.6)**	**664(90)**
X=P			
F$_3$X···A	0.97	0.9(0.8)	833(51)
FH$_2$X···A	0.91	0.9(1.8)	890(99)
ClH$_2$X···A	0.90	1.7(1.7)	833(100)

Continued Table S6.1…

Overall (by avg.)	0.93	1.21.4)	852(83)
Overall (by fit, with (0,0)]	0.94	0.8(0.7)	877(41)
Overall [by fit, without (0,0)]	**0.93**	**1.0(0.8)**	**865(46)**
X=As			
$F_3X\cdots A$	0.97	2.4(1.1)	868(50)
$FH_2X\cdots A$	0.89	2.6(2.3)	880(111)
$ClH_2X\cdots A$	0.91	2.0(1.8)	851(94)
Overall (by avg.)	0.92	2.3(1.7)	866(85)
Overall (by fit, with (0,0)]	0.94	1.8(0.8)	891(40)
Overall [by fit, without (0,0)]	**0.93**	**2.2(0.9)**	**872(44)**
X=Sb			
$F_3X\cdots A$	0.98	-0.8(1.6)	1274(62)
$FH_2X\cdots A$	0.92	-1.9(2.9)	1279(134)
$ClH_2X\cdots A$	0.93	-0.6(2.5)	1162(116)
Overall (by avg.)	0.94	-1.1(2.3)	1238(104)
Overall (by fit, with (0,0)]	0.96	-1.4(1.1)	1255(48)
Overall [by fit, without (0,0)]	**0.95**	**-1.7(1.2)**	**1271(54)**
X=Bi			
$F_3X\cdots A$	0.97	-2.6(2.7)	1568(102)
$FH_2X\cdots A$	0.85	-1.7(4.3)	1391(205)
$ClH_2X\cdots A$	0.87	-1.4(3.9)	1314(182)
Overall (by avg.)	0.90	-1.9(3.6)	1424(163)
Overall (by fit, with (0,0)]	0.92	-3.2(1.8)	1499(80)
Overall [by fit, without (0,0)]	**0.91**	**-4.3(2.0)**	**1546(92)**
X=O			
$OF_2\cdots A$	0.97	-0.7(0.4)	640(38)
Overall (by fit, with (0,0)]	0.98	-0.3(0.3)	601(27)
Overall [by fit, without (0,0)]	**0.97**	**-0.7(0.4)**	**640(38)**
X=S			
$F_2X\cdots A$	0.96	1.3(1.3)	779(53)
$Cl_2X\cdots A$	0.96	0.2(1.1)	810(60)
$O_2X\cdots A$	0.98	1.3(0.7)	825(45)
Overall (by avg.)	0.97	0.9(1.0)	805(53)
Overall (by fit, with (0,0)]	0.97	1.0(0.5)	795(27)
Overall [by fit, without (0,0)]	**0.96**	**1.3(0.6)**	**785(29)**
X=Se			
$F_2X\cdots A$	0.95	-1.9(2.6)	964(80)
$Cl_2X\cdots A$	0.98	2.9(1.0)	790(40)
$O_2X\cdots A$	0.97	1.9(1.0)	834(51)
Overall (by avg.)	0.97	1.0(1.5)	863(57)
Overall (by fit, with (0,0)]	0.97	1.0(0.7)	873(29)
Overall [by fit, without (0,0)]	**0.96**	**1.2(0.8)**	**866(31)**

Continued Table S6.1…

X=Te			
$F_2X \cdots A$	0.94	-15.8(5.0)	1606(146)
$Cl_2X \cdots A$	0.95	-6.7(3.1)	1294(103)
$O_2X \cdots A$	0.96	3.4(1.3)	811(55)
Overall (by avg.)	0.95	-6.4(3.1)	1237(101)
Overall (by fit, with (0,0)]	0.91	-2.7(1.9)	1172(67)
Overall [by fit, without (0,0)]	**0.90**	**-3.4(2.2)**	**1194(74)**
X=Po			
$F_2X \cdots A$	0.89	-23.2(8.5)	2089(256)
$Cl_2X \cdots A$	0.89	-15.5(7.1)	1781(222)
$O_2X \cdots A$	0.84	-1.4(4.3)	1726(268)
Overall (by avg.)	0.87	-13.4(6.6)	1865(249)
Overall (by fit, with (0,0)]	0.87	0.8(2.7)	1357(99)
Overall [by fit, without (0,0)]	**0.84**	**1.0(3.1)**	**1350(112)**
X=F			
$CNX \cdots A$	0.92	-2.6(0.8)	1007(104)
$NCX \cdots A$	0.86	-1.7(0.8)	994(142)
$NCCCX \cdots A$	0.82	-2.2(1.0)	1008(168)
Overall (by avg.)	0.87	-2.2(0.9)	1003(138)
Overall (by fit, with (0,0)]	0.86	-0.9(0.4)	792(60)
Overall [by fit, without (0,0)]	**0.84**	**-1.4(0.4)**	**875(71)**
X=Cl			
$ClX \cdots A$	0.98	1.0(0.6)	636(31)
$FX \cdots A$	0.97	1.1(1.7)	777(49)
$NCX \cdots A$	0.84	-0.3(1.9)	1050(164)
Overall (by avg.)	0.93	0.6(1.4)	821(81)
Overall (by fit, with (0,0)]	0.93	1.8(0.8)	690(35)
Overall [by fit, without (0,0)]	**0.93**	**2.0(0.9)**	**681(36)**
X=Br			
$FX \cdots A$	0.92	-8.4(4.5)	1119(120)
$ClX \cdots A$	0.97	-1.1(1.3)	836(48)
$BrX \cdots A$	0.98	-0.5(1.0)	752(41)
Overall (by avg.)	0.96	-3.3(2.3)	902(70)
Overall (by fit, with (0,0)]	0.94	-4.0(1.4)	962(46)
Overall [by fit, without (0,0)]	**0.93**	**-5.0(1.5)**	**992(50)**
X=I			
$FX \cdots A$	0.93	-8.4(4.9)	1419(138)
$ClX \cdots A$	0.95	-3.1(2.8)	1117(93)
$BrX \cdots A$	0.96	-0.8(2.1)	1001(75)
Overall (by avg.)	0.95	-4.1(3.3)	1179(102)
Overall (by fit, with (0,0)]	0.92	-4.6(2.0)	1220(67)
Overall [by fit, without (0,0)]	**0.91**	**-6.2(2.3)**	**1269(75)**
X=At			

Continued Table S6.1…

FX···A	0.91	-14.7(7.0)	1826(198)
ClX···A	0.91	-6.8(5.2)	1447(161)
BrX···A	0.91	-4.9(4.4)	1316(144)
Overall (by avg.)	0.91	-8.8(5.5)	1530(168)
Overall (by fit, with (0,0)]	0.89	-7.2(3.1)	1501(97)
Overall [by fit, without (0,0)]	**0.88**	**-10.9(3.7)**	**1611(114)**

*Table S6.2. Correlation coefficients (CC), intercepts and slopes of the binding energy (kJ/mol) versus electron density (au) plot for various intermolecular bonded complexes. 'Overall (by avg.)' denotes average value of correlation coefficient (CC), intercept and slope of the three sets, '**Overall [(by fit, without (0,0)]**' fits all data point without the (0,0) point]. Values in the brackets denote standard deviation. The function y=mx (without intercept) has been used to fit the data.*

Complexes	y=mx	
	CC	Slope
X=H		
FX···A	0.92	853(28)
HOX···A	0.94	788(24)
HSX···A	0.92	649(21)
Overall (by avg.)	0.93	763(24)
Overall [by fit, without (0,0)]	**0.94**	**813(19)**
X=Li		
FX···A	0.86	2914(107)
ClX···A	0.85	3088(114)
BrX···A	0.85	3107(114)
Overall (by avg.)	0.85	3036(112)
Overall [by fit, without (0,0)]	**0.85**	**3042(64)**
X=Na		
FX···A	0.87	3411(137)
ClX···A	0.90	3408(113)
BrX···A	0.89	3372(112)
Overall (by avg.)	0.89	3397(121)
Overall [by fit, without (0,0)]	**0.89**	**3396(67)**
X=Be		
F_2X···A	0.76	1700(119)
Cl_2X···A	0.65	1524(134)
H_2X···A	0.62	1441(139)
Overall (by avg.)	0.68	1555(131)
Overall [by fit, without (0,0)]	**0.67**	**1554(75)**
X=Mg		
F_2X···A	0.91	2875(96)
Cl_2X···A	0.90	2976(103)

Continued Table S6.2…

$H_2X \cdots A$	0.94	2316(94)
Overall (by avg.)	0.92	2722(98)
Overall [by fit, without (0,0)]	**0.88**	**2779(74)**
X=Ca		
$F_2X \cdots A$	0.94	2803(77)
$Cl_2X \cdots A$	0.93	2789(76)
$H_2X \cdots A$	0.94	2623(79)
Overall(by avg)	0.94	2738(77)
Overall [by fit, without (0,0)]	**0.93**	**2745(45)**
X=B		
$F_3X \cdots A$	0.86	614(50)
$F_2HX \cdots A$	0.87	542(44)
$Cl_3X \cdots A$	0.66	525(81)
Overall (by avg.)	0.80	560(58)
Overall [by fit, without (0,0)]	**0.76**	**559(36)**
X=Al		
$F_3X \cdots A$	0.83	2686(117)
$FH_2X \cdots A$	0.85	2228(105)
$Cl_3X \cdots A$	0.77	2328(127)
Overall (by avg.)	0.82	2414(116)
Overall [by fit, without (0,0)]	**0.79**	**2430(75)**
X=Ga		
$F_2HX \cdots A$	0.81	1410(74)
$FH_2X \cdots A$	0.80	1288(69)
$ClH_2X \cdots A$	0.77	1258(71)
Overall (by avg.)	0.79	1319(71)
Overall [by fit, without (0,0)]	**0.79**	**1324(42)**
X=In		
$F_2HX \cdots A$	0.86	1648(67)
$FH_2X \cdots A$	0.85	1500(68)
$ClH_2X \cdots A$	0.84	1467(63)
Overall (by avg.)	0.85	1538(66)
Overall [by fit, without (0,0)]	**0.84**	**1548(40)**
X=Tl		
$F_2HX \cdots A$	0.85	1318(58)
$FH_2X \cdots A$	0.80	1285(67)
$ClH_2X \cdots A$	0.83	1240(55)
Overall (by avg.)	0.83	1281(60)
Overall [by fit, without (0,0)]	**0.84**	**1286(34)**
X=C		
$FH_3X \cdots A$	0.73	1062(54)
$HOH_3X \cdots A$	0.59	704(42)
$ClH_3X \cdots A$	0.70	1039(55)

Continued Table S6.2…

Overall (by avg.)	0.67	935(50)
Overall [by fit, without (0,0)]	**0.63**	**960(40)**
X=Si		
$FH_3X{\cdots}A$	0.90	960(43)
$CNH_3X{\cdots}A$	0.88	1103(45)
$ClH_3X{\cdots}A$	0.87	946(44)
Overall (by avg.)	0.88	1003(44)
Overall [by fit, without (0,0)]	**0.87**	**988(27)**
X=Ge		
$FH_3X{\cdots}A$	0.91	988(38)
$CNH_3X{\cdots}A$	0.85	1063(46)
$ClH_3X{\cdots}A$	0.89	939(39)
Overall (by avg.)	0.88	997(41)
Overall [by fit, without (0,0)]	**0.88**	**988(24)**
X=Sn		
$FH_3X{\cdots}A$	0.96	1188(31)
$CNH_3X{\cdots}A$	0.91	1075(44)
$ClH_3X{\cdots}A$	0.91	1121(47)
Overall (by avg.)	0.93	1128(41)
Overall [by fit, without (0,0)]	**0.93**	**1135(24)**
X=Pb		
$FH_3X{\cdots}A$	0.85	1271(63)
$CNH_3X{\cdots}A$	0.88	1139(43)
$ClH_3X{\cdots}A$	0.92	1154(36)
Overall (by avg.)	0.88	1188(47)
Overall [by fit, without (0,0)]	**0.87**	**1189(29)**
X=N		
$F_3X{\cdots}A$	**0.86**	**602(24)**
X=P		
$F_3X{\cdots}A$	0.97	888(21)
$FH_2X{\cdots}A$	0.91	939(30)
$ClH_2X{\cdots}A$	0.88	928(32)
Overall (by avg.)	0.92	918(28)
Overall [by fit, without (0,0)]	**0.92**	**921(16)**
X=As		
$F_3X{\cdots}A$	0.96	964(26)
$FH_2X{\cdots}A$	0.87	1000(36)
$ClH_2X{\cdots}A$	0.90	948(31)
Overall (by avg.)	0.91	971(31)
Overall [by fit, without (0,0)]	**0.93**	**971(18)**
X=Sb		
$F_3X{\cdots}A$	0.98	1246(23)
$FH_2X{\cdots}A$	0.91	1196(36)

Continued Table S6.2…

ClH$_2$X$\cdots$A	0.93	1135(33)
overall (by avg.)	0.94	1192(31)
Overall [by fit, without (0,0)]	**0.95**	**1200(19)**
X=Bi		
F$_3$X$\cdots$A	0.96	1476(35)
FH$_2$X$\cdots$A	0.85	1313(47)
ClH$_2$X$\cdots$A	0.87	1250(45)
Overall (by avg.)	0.89	1346(42)
Overall [by fit, without (0,0)]	**0.90**	**1366(30)**
X=O		
F$_2$O$\cdots$A	**0.96**	**573(12)**
X=S		
F$_2$X$\cdots$A	0.96	828(20)
Cl$_2$X$\cdots$A	0.96	822(18)
O$_2$X$\cdots$A	0.97	900(21)
Overall (by avg.)	0.96	850(20)
Overall [by fit, without (0,0)]	**0.96**	**843(12)**
X=Se		
F$_2$X$\cdots$A	0.94	907(25)
Cl$_2$X$\cdots$A	0.96	899(20)
O$_2$X$\cdots$A	0.96	924(25)
Overall (by avg.)	0.95	910(23)
Overall [by fit, without (0,0)]	**0.96**	**908(13)**
X=Te		
F$_2$X$\cdots$A	0.86	1158(49)
Cl$_2$X$\cdots$A	0.92	1079(32)
O$_2$X$\cdots$A	0.93	940(34)
Overall (by avg.)	0.90	1059(38)
Overall [by fit, without (0,0)]	**0.89**	**1086(27)**
X=Po		
F$_2$X$\cdots$A	0.79	1399(63)
Cl$_2$X$\cdots$A	0.82	1302(52)
O$_2$X$\cdots$A	0.84	1641(75)
Overall (by avg.)	0.82	1447(63)
Overall [by fit, without (0,0)]	**0.84**	**1383(38)**
X=F		
CNX$\cdots$A	0.80	655(30)
NCX$\cdots$A	0.78	690(34)
NCCCX$\cdots$A	0.70	623(37)
Overall (by avg.)	0.76	656(34)
Overall [by fit, without (0,0)]	**0.79**	**655(19)**
X=Cl		
ClX$\cdots$A	0.98	683(12)

Continued Table S6.2…

FX···A	0.97	746(17)
NCX···A	0.84	1027(41)
Overall (by avg.)	0.93	819(23)
Overall [by fit, without (0,0)]	**0.91**	**755(19)**
X=Br		
FX···A	0.88	907(38)
ClX···A	0.97	797(16)
BrX···A	0.98	732(14)
Overall (by avg.)	0.94	812(23)
Overall [by fit, without (0,0)]	**0.91**	**840(21)**
X=I		
FX···A	0.90	1190(40)
ClX···A	0.94	1018(29)
BrX···A	0.96	973(23)
Overall (by avg.)	0.93	1060(31)
Overall [by fit, without (0,0)]	**0.89**	**1080(26)**
X=At		
FX···A	0.87	1421(52)
ClX···A	0.89	1244(42)
BrX···A	0.90	1160(39)
Overall (by avg.)	0.89	1275(44)
Overall [by fit, without (0,0)]	**0.84**	**1288(32)**

Table S6.3. Power fit ($y=ax^r$) of the binding energy (kJ/mol) versus electron density (au) data for various intermolecular bonded complexes formed by different elements. The values of the pre factor, a, and the power, r, and standard deviation from the fit, are given. Columns 1 and 2 include the correlation coefficients (CC) from the linear and power fits, which may be used to compare the fit. For Be, B, and C bonds, the power (r) is close to or greater than 2.00 (marked in red).

Elements	Linear Fit CC	Power fit CC	a	r
H	0.95	0.95	1248(220)	1.12(0.05)
Li	0.85	0.85	2585(894)	0.96(0.09)
Na	0.91	0.91	8854(3429)	1.23(0.09)
*Be	**0.88**	**0.91**	**61627(30220)**	**2.21(0.16)**
Mg	0.93	0.93	11780(3628)	1.41(0.09)
Ca	0.94	0.94	4428(982)	1.13(0.06)
*B	**0.76**	**0.85**	**15081(9686)**	**2.39(0.28)**
Al	0.89	0.90	16338(6113)	1.60(0.12)
Ga	0.91	0.93	11223(3478)	1.72(0.11)
In	0.93	0.94	38178(2178)	1.53(0.09)
Tl	0.92	0.92	5474(1524)	1.45(0.09)
*C	**0.87**	**0.85**	**165607(1.423e+05)**	**1.99(0.17)**

Continued Table S6.3…

Si	0.92	0.94	419(68)	0.78(0.04)
Ge	0.92	0.93	410(76)	0.78(0.05)
Sn	0.93	0.93	879(191)	0.93(0.06)
Pb	0.88	0.89	688(184)	0.86(0.07)
N	0.93	0.87	1083(797)	1.12(0.15)
P	0.93	0.93	683(144)	0.92(0.05)
As	0.93	0.93	610(109)	0.88(0.05)
Sb	0.95	0.95	1541(272)	1.07(0.05)
Bi	0.91	0.91	2418(631)	1.16(0.07)
O	0.98	0.83	1021(347)	1.13(0.07)
S	0.86	0.97	595(78)	0.91(0.03)
Se	0.96	0.96	779(110)	0.96(0.04)
Te	0.90	0.92	2509(769)	1.25(0.09)
Po	0.84	0.84	1456(506)	1.02(0.10)
F	0.84	0.84	3661(2129)	1.34(0.12)
Cl	0.93	0.92	542(98)	0.91(0.05)
Br	0.93	0.94	1982(415)	1.26(0.06)
I	0.91	0.92	2820(749)	1.29(0.08)
At	0.88	0.89	4831(1726)	1.40(0.11)
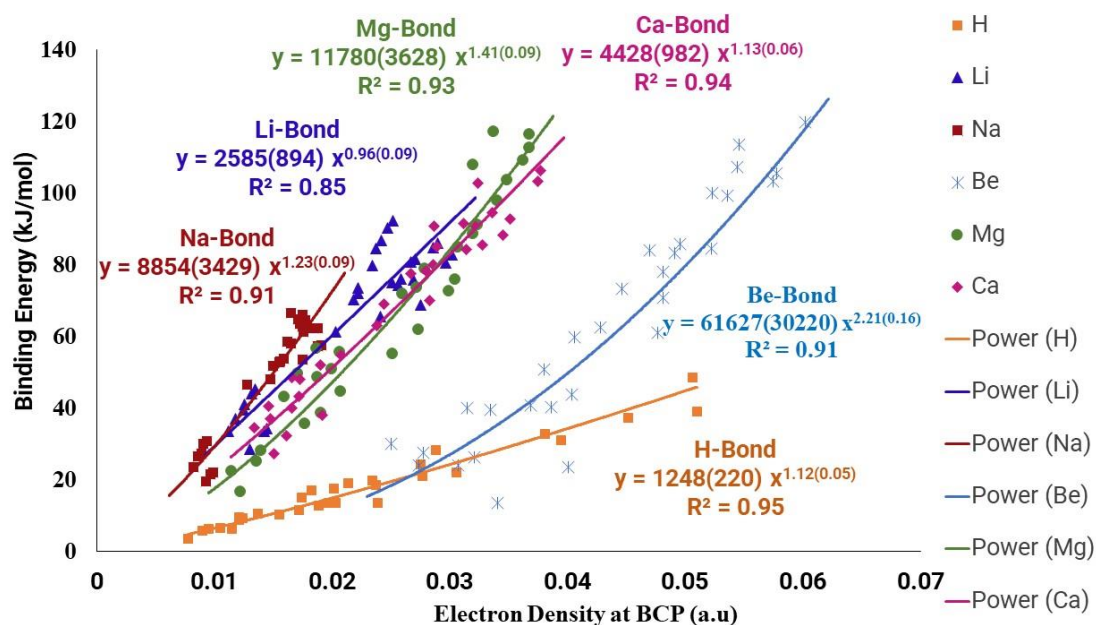
Figure S6.1. Power fit (ax^r) of the binding energy (kJ/mol) versus electron density (au) for alkalene (Li, Na, Be, Mg, Ca) and hydrogen (H) bonded complexes. Values of the prefactor (a) and power (r) of the best fit lines are shown along with their respective standard deviation. The R^2 value denotes the quality of the fit.

Table S6.4. Exponential fit [a*exp(b*x)] of the binding energy (kJ/mol) versus electron density (au) plot for Be, B, C-bonded complexes. The a, b and correlation coefficients (CC) from the fits are given. Values in the brackets denote standard deviation.

Bond	CC	a	b
Be	0.90	7.3(1.3)	47.9(3.5)
B	0.92	5.4(0.9)	23.9(1.7)
C	0.81	0.8(0.1)	341.5(31.3)

Table S6.5. Percentage covalency and ionicity calculated for X-N bond for $D_2X\cdots NH_3$ (D=F/Cl/Br, X=Be, Mg) complexes. Percentage covalency has been scaled to 100% in the last column. A Much-detailed calculation can be found in Das A (2016) Theoretical investigations on intermolecular beryllium and magnesium bonds. MS Thesis, Indian Institute of Science.

Complex	Covalent (%)	Ionic (%)	Total weightage (%)	Covalency on 100% scale
$F_2Be\cdots NH_3$	0.10	2.51	2.61	3.83
$Cl_2Be\cdots NH_3$	0.04	2.08	2.12	1.89
$Br_2Be\cdots NH_3$	0.04	2.11	2.15	1.86
$F_2Mg\cdots NH_3$	0.04	1.44	1.48	2.70
$Cl_2Mg\cdots NH_3$	0.01	0.84	0.85	1.18
$Br_2Mg\cdots NH_3$	0.02	0.83	0.85	2.35
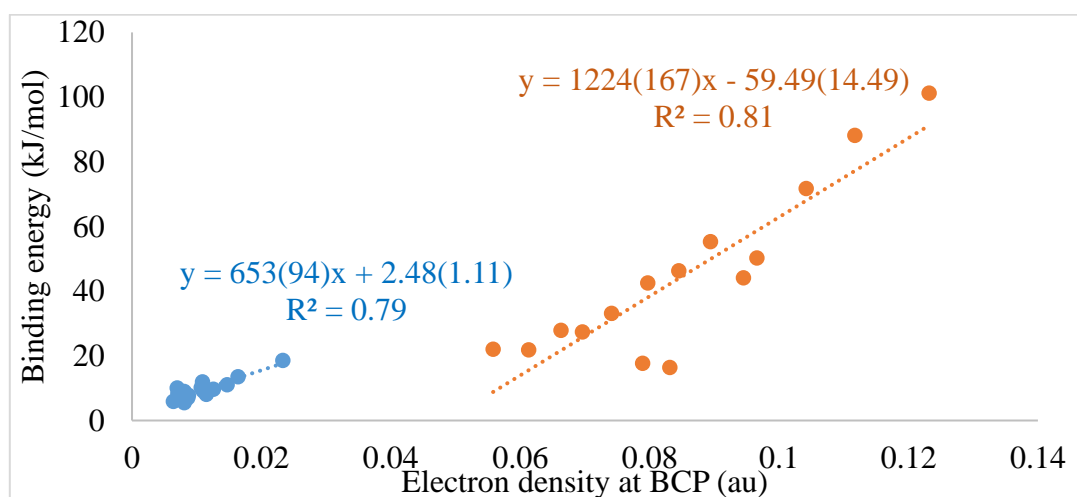
Figure S6.2. Binding energy (kJ/mol) versus electron density at BCP (au) plot for boron bonded complexes. Two different regimes have been identified as short bonds with strong interactions (in orange) and long bond with weak interactions (in blue). The slope, intercept and correlation coefficient (CC) are indicated. Values in the brackets denote standard deviation.

Table S6.6. Data set for binding energy (kJ/mol) and electron density at BCP (au) of boron bonded complexes. Two different regimes have been identified as short bonds with strong interactions (in orange) and long bond with weak interactions (in blue). For each regime, the slope, intercept, and correlation coefficient (CC) are shown individually. Values in the brackets denote standard deviation.

Complexes	Electron Density at BCP	Binding Energy (kJ/mol)
$F_3B\cdots OH_2$	0.0696	27.3
$F_3B\cdots NH_3$	0.1117	88.1
$F_3B\cdots OCH_2$	0.0663	27.8
$F_3B\cdots OHCH_3$	0.0845	46.2
$F_3B\cdots O(CH_3)_2$	0.0894	55.2
$Cl_3B\cdots OH_2$	0.0831	16.4
$Cl_3B\cdots NH_3$	0.1232	101.2
$Cl_3B\cdots OCH_2$	0.0789	17.6
$Cl_3B\cdots OHCH_3$	0.0945	44.1
$Cl_3B\cdots O(CH_3)_2$	0.0966	50.3
$HF_2B\cdots OH_2$	0.0613	21.8
$HF_2B\cdots NH_3$	0.1042	71.7
$HF_2B\cdots OCH_2O$	0.0558	22.0
$HF_2B\cdots OHCH_3$	0.0741	33.1
$HF_2B\cdots O(CH_3)_2$	0.0797	42.5
CC =0.81	Slope=1224(167)	-59.49(14.49)
$F_3B\cdots SH_2$	0.0147	11.0
$F_3B\cdots NCH$	0.0233	18.6
$F_3B\cdots CO$	0.0115	8.0
$F_3B\cdots C_2H_4$	0.0107	10.1
$F_3B\cdots PH_3$	0.0126	9.6
$Cl_3B\cdots SH_2$	0.0081	8.9
$Cl_3B\cdots NCH$	0.0109	11.9
$Cl_3B\cdots CO$	0.0064	5.9
$Cl_3B\cdots C_2H_4$	0.007	10.0
$Cl_3B\cdots PH_3$	0.0071	8.2
$HF_2B\cdots SH_2$	0.011	9.1
$HF_2B\cdots NCH$	0.0164	13.5
$HF_2B\cdots CO$	0.0081	5.5
$HF_2B\cdots C_2H_4$	0.0087	7.7
$HF_2B\cdots PH_3$	0.0086	7.0
CC =0.79	Slope=653(94)	Intercept=2.48(1.11)

Table S6.7. $|V|/G$ and $|\lambda_1|/\lambda_3$ for boron bonded complexes. Two different regimes have been identified as short bonds with strong interactions (in orange) and long bond with weak interactions (in blue). The average values from two different regimes are provided. Values in the brackets denote standard deviation.

Complexes	Electron Density at BCP	Binding Energy (kJ/mol)
$F_3B\cdots OH_2$	1.59	0.231
$F_3B\cdots NH_3$	1.52	0.269
$F_3B\cdots OCH_2$	1.67	0.246
$F_3B\cdots OHCH_3$	1.49	0.212
$F_3B\cdots O(CH_3)_2$	1.50	0.23
$Cl_3B\cdots OH_2$	1.48	0.174
$Cl_3B\cdots NH_3$	1.52	0.254
$Cl_3B\cdots OCH_2$	1.59	0.322
$Cl_3B\cdots OHCH_3$	1.45	0.234
$Cl_3B\cdots O(CH_3)_2$	1.49	0.259
$HF_2B\cdots OH_2$	1.54	0.195
$HF_2B\cdots NH_3$	1.46	0.272
$HF_2B\cdots OCH_2O$	1.67	0.23
$HF_2B\cdots OHCH_3$	1.51	0.211
$HF_2B\cdots O(CH_3)_2$	1.52	0.234
	Avg 1.53(0.07)	Avg 0.24(0.03)
$F_3B\cdots SH_2$	1.00	0.112
$F_3B\cdots NCH$	1.07	0.106
$F_3B\cdots CO$	0.86	0.077
$F_3B\cdots C_2H_4$	0.91	0.087
$F_3B\cdots PH_3$	0.96	0.11
$Cl_3B\cdots SH_2$	0.89	0.131
$Cl_3B\cdots NCH$	0.95	0.14
$Cl_3B\cdots CO$	0.79	0.098
$Cl_3B\cdots C_2H_4$	0.87	0.125
$Cl_3B\cdots PH_3$	0.83	0.112
$HF_2B\cdots SH_2$	0.94	0.087
$HF_2B\cdots NCH$	1.01	0.092
$HF_2B\cdots CO$	0.81	0.068
$HF_2B\cdots C_2H_4$	0.89	0.079
$HF_2B\cdots PH_3$	0.85	0.078
	Avg 0.91(0.08)	Avg 0.10 (0.02)
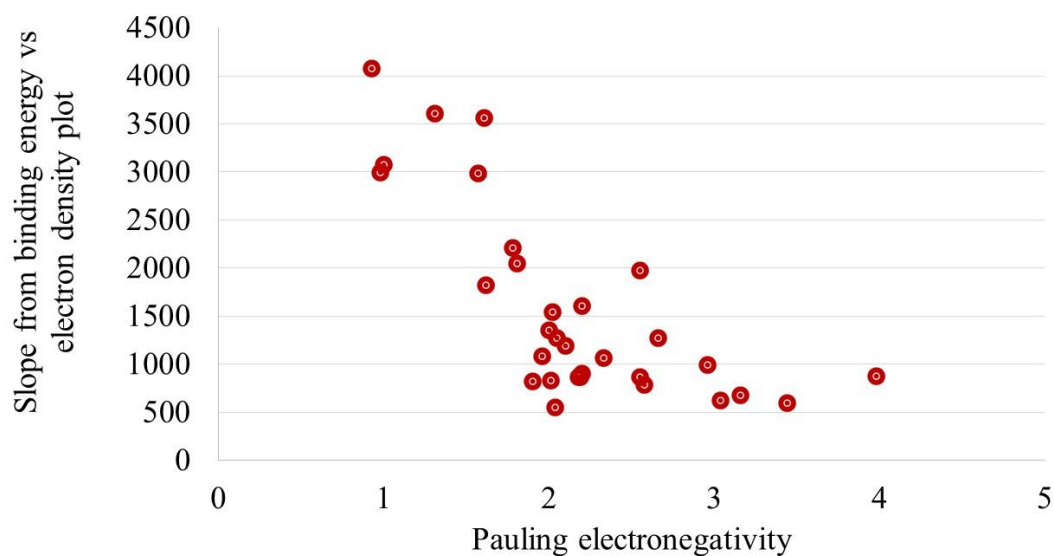
Figure S6.3. Slope (from binding energy versus electron density plot) with Pauling electronegativity.
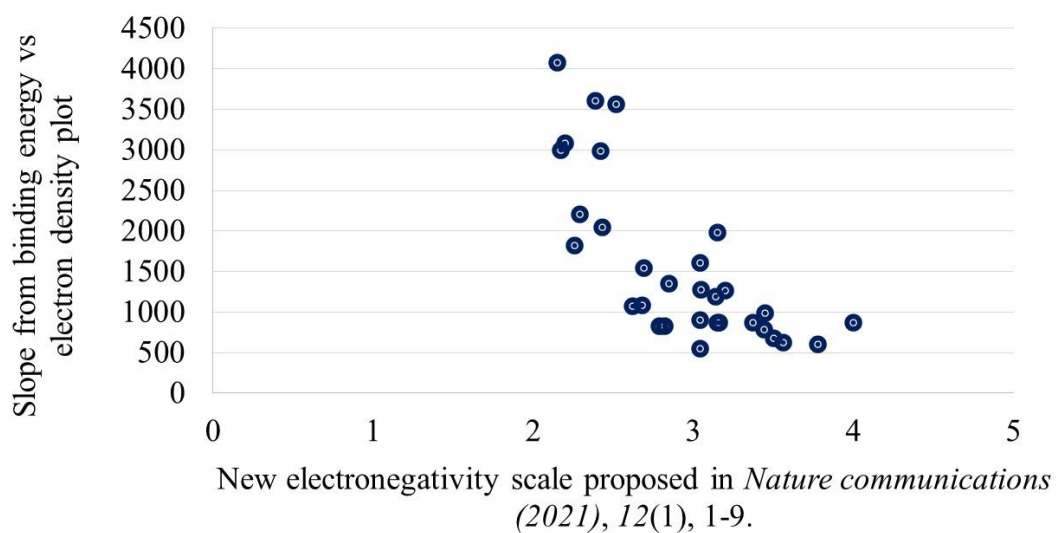
Figure S6.4. Slope (from binding energy versus electron density plot) with thermochemical electronegativity.

The following section contains all data sets. (Table D6.1 to Table D6.31).

This page intentionally left blank.

6.6.1 All Data Sets

Table D6.1. Electron density at BCP (au) and binding energy (kJ/mol) data for H-bonded complexes

Complexes	Electron Density (au)	Binding Energy (kJ/mol)
$FH\cdots OH_2$	0.0381	32.9
$FH\cdots SH_2$	0.0214	19.0
$FH\cdots NH_3$	0.0506	48.7
$FH\cdots NCH$	0.0288	28.3
$FH\cdots CO$	0.0203	13.5
$FH\cdots HCHO$	0.0395	31.1
$FH\cdots C_2H_4$	0.0183	17.1
$FH\cdots CH_3OH$	0.0452	37.4
$FH\cdots PH_3$	0.0202	17.6
$FH\cdots O(CH_3)_2$	0.051	39.1
$HOH\cdots OH_2$	0.0237	18.5
$HOH\cdots SH_2$	0.0137	10.7
$HOH\cdots NH_3$	0.0275	24.3
$HOH\cdots NCH$	0.0174	15.0
$HOH\cdots CO$	0.0115	6.4
$HOH\cdots OCH_2$	0.0234	19.8
$HOH\cdots C_2H_4$	0.0121	9.5
$HOH\cdots OHCH_3$	0.0277	21.1
$HOH\cdots PH_3$	0.0121	8.9
$HOH\cdots O(CH_3)_2$	0.0306	22.1
$HSH\cdots OH_2$	0.0155	10.4
$HSH\cdots SH_2$	0.0105	6.5
$HSH\cdots NH_3$	0.0197	13.7
$HSH\cdots NCH$	0.0124	9.4
$HSH\cdots CO$	0.0078	3.6
$HSH\cdots OCH_2$	0.0172	11.7
$HSH\cdots C_2H_4$	0.0095	6.3
$HSH\cdots OHCH_3$	0.0189	12.9
$HSH\cdots PH_3$	0.009	5.7

Figure D6.1. Binding energy (kJ/mol) versus electron density at BCP (au) plot for H-bonded complexes

Table D6.2. Electron density at BCP (au) and binding energy (kJ/mol) data for Li-bonded complexes.

Complexes	Electron Density (au)	Binding Energy (kJ/mol)
$FLi•••OH_2$	0.0241	65.7
$FLi•••NCCH_3$	0.0222	73.7
$FLi•••NH_3$	0.0234	79.9
$FLi•••NCH$	0.0203	61.3
$FLi•••OCH_2$	0.0251	75.0
$FLi •••C_2H_4$	0.0112	33.5
$FLi•••OHCH_3$	0.0269	75.9
$FLi•••PH_3$	0.0118	37.0
$FLi•••CO$	0.013	28.7
$FLi•••O(CH_3)_2$	0.0275	68.8
$ClLi•••OH_2$	0.0256	74.3
$ClLi •••NCCH_3$	0.0237	84.5
$ClLi•••NH_3$	0.0247	90.3
$ClLi•••NCH$	0.0218	70.3
$ClLi•••OCH_2$	0.0267	80.9
$ClLi•••C_2H_4$	0.0125	39.7
$ClLi•••OHCH_3$	0.0286	84.8
$ClLi•••PH_3$	0.0132	44.0
$ClLi•••CO$	0.0142	33.5
$ClLi•••O(CH_3)_2$	0.0297	80.7
$BrLi•••OH_2$	0.0259	76.2
$BrLi•••NCCH_3$	0.0242	86.8
$BrLi•••NH_3$	0.0252	92.4
$BrL•••NCH$	0.0222	72.2
$BrLi•••OCH_2$	0.0271	81.7
$BrLi •••C_2H_4$	0.0126	41.0
$BrLi•••OHCH_3$	0.029	86.3
$BrLi•••PH_3$	0.0135	45.4
$BrLi•••CO$	0.0145	34.4
$BrLi•••O(CH_3)_2$	0.0302	82.7

Figure D6.2. Binding energy (kJ/mol) versus electron density at BCP (au) plot for Li-bonded complexes.

Table D6.3. Electron density at BCP (au) and binding energy (kJ/mol) data for Na-bonded complexes.

Complexes	Electron Density (au)	Binding Energy (kJ/mol)
$FNa\bullet\bullet\bullet OH_2$	0.0128	46.5
$FNa\bullet\bullet\bullet NCCH_3$	0.0162	58.7
$FNa\bullet\bullet\bullet NH_3$	0.0165	58.0
$FNa\bullet\bullet\bullet NCH$	0.0148	48.0
$FNa\bullet\bullet\bullet OCH_2$	0.0165	66.5
$FNa\bullet\bullet\bullet C_2H_4$	0.0082	23.5
$FNa\bullet\bullet\bullet OHCH_3$	0.0176	61.4
$FNa\bullet\bullet\bullet PH_3$	0.0086	26.7
$FNa\bullet\bullet\bullet CO$	0.0093	19.6
$FNa\bullet\bullet\bullet O(CH_3)_2$	0.0175	53.7
$ClNa\bullet\bullet\bullet OH_2$	0.015	51.9
$ClNa\bullet\bullet\bullet NCCH_3$	0.0171	64.8
$ClNa\bullet\bullet\bullet NH_3$	0.0174	63.6
$ClNa\bullet\bullet\bullet NCH$	0.0156	53.0
$ClNa\bullet\bullet\bullet OCH_2$	0.0173	63.6
$ClNa\bullet\bullet\bullet C_2H_4$	0.0087	26.7
$ClNa\bullet\bullet\bullet OHCH_3$	0.0184	62.4
$ClNa\bullet\bullet\bullet PH_3$	0.0091	30.1
$ClNa\bullet\bullet\bullet CO$	0.0097	21.7
$ClNa\bullet\bullet\bullet O(CH_3)_2$	0.0188	57.4
$BrNa\bullet\bullet\bullet OH_2$	0.0155	52.9
$BrNa\bullet\bullet\bullet NCCH_3$	0.0175	66.1
$BrNa\bullet\bullet\bullet NH_3$	0.0177	64.7
$BrNa\bullet\bullet\bullet NCH$	0.0159	53.9
$BrNa\bullet\bullet\bullet OCH_2$	0.0175	62.8
$BrNa\bullet\bullet\bullet C_2H_4$	0.0089	27.3
$BrNa\bullet\bullet\bullet OHCH_3$	0.0188	62.3
$BrNa\bullet\bullet\bullet PH_3$	0.0094	30.8
$BrNa\bullet\bullet\bullet CO$	0.0099	22.1
$BrNa\bullet\bullet\bullet O(CH_3)_2$	0.0191	57.7

Figure D6.3. Binding energy (kJ/mol) versus electron density at BCP (au) plot for Na-bonded complexes.

Table D6.4. Electron density at BCP (au) and binding energy (kJ/mol) data for Be-bonded complexes.

Complexes	Electron Density (au)	Binding Energy (kJ/mol)
$F_2Be\bullet\bullet\bullet OH_2$	0.047	84.0
$F_2Be\bullet\bullet\bullet SH_2$	0.0315	40.0
$F_2Be\bullet\bullet\bullet NH_3$	0.0546	113.7
$F_2Be\bullet\bullet\bullet NCH$	0.0406	59.8
$F_2Be\bullet\bullet\bullet OCH_2$	0.0446	73.4
$F_2Be\bullet\bullet\bullet C_2H_4$	0.025	30.0
$F_2Be\bullet\bullet\bullet OHCH_3$	0.0523	100.0
$F_2Be\bullet\bullet\bullet PH_3$	0.0335	39.6
$F_2Be\bullet\bullet\bullet CO$	0.0321	26.3
$F_2Be\bullet\bullet\bullet O(CH_3)_2$	0.0544	107.3
$Cl_2Be\bullet\bullet\bullet OH_2$	0.0522	84.7
$Cl_2Be\bullet\bullet\bullet SH_2$	0.0369	40.8
$Cl_2Be\bullet\bullet\bullet NH_3$	0.0602	119.8
$Cl_2Be\bullet\bullet\bullet NCH$	0.0477	61.2
$Cl_2Be\bullet\bullet\bullet OCH_2$	0.0481	70.8
$Cl_2Be\bullet\bullet\bullet C_2H_4$	0.0278	27.6
$Cl_2Be\bullet\bullet\bullet OHCH_3$	0.0575	103.3
$Cl_2Be\bullet\bullet\bullet PH_3$	0.0404	43.8
$Cl_2Be\bullet\bullet\bullet CO$	0.0401	23.6
$Cl_2Be\bullet\bullet\bullet O(CH_3)_2$	0.0578	105.7
$H_2Be\bullet\bullet\bullet OH_2$	0.0428	62.7
$H_2Be\bullet\bullet\bullet SH_2$	0.0274	24.2
$H_2Be\bullet\bullet\bullet NH_3$	0.0496	85.9
$H_2Be\bullet\bullet\bullet NCH$	0.0386	40.3
$H_2Be\bullet\bullet\bullet OCH_2$	0.038	50.8
$H_2Be\bullet\bullet\bullet NH_2CH_3$	0.0536	99.3
$H_2Be\bullet\bullet\bullet OHCH_3$	0.0481	78.2
$H_2Be\bullet\bullet\bullet PH_3$	0.0307	24.1
$H_2Be\bullet\bullet\bullet CO$	0.0341	13.7
$H_2Be\bullet\bullet\bullet O(CH_3)_2$	0.0491	83.3

Figure D6.4. Binding energy (kJ/mol) versus electron density at BCP (au) plot for Be-bonded complexes.

Table D6.5. Electron density at BCP (au) and binding energy (kJ/mol) data for Mg-bonded complexes.

Complexes	Electron Density (au)	Binding Energy (kJ/mol)
$F_2Mg\bullet\bullet\bullet OH_2$	0.0324	91.0
$F_2Mg\bullet\bullet\bullet SH_2$	0.02	50.9
$F_2Mg\bullet\bullet\bullet NH_3$	0.032	107.9
$F_2Mg\bullet\bullet\bullet NCH$	0.026	71.9
$F_2Mg\bullet\bullet\bullet OCH_2$	0.0307	84.8
$F_2Mg\bullet\bullet\bullet C_2H_4$	0.016	43.1
$F_2Mg\bullet\bullet\bullet OHCH_3$	0.0349	103.7
$F_2Mg\bullet\bullet\bullet PH_3$	0.0188	48.5
$F_2Mg\bullet\bullet\bullet CO$	0.0177	35.5
$F_2Mg\bullet\bullet\bullet O(CH_3)_2$	0.0363	109.2
$Cl_2Mg\bullet\bullet\bullet OH_2$	0.0341	97.8
$Cl_2Mg\bullet\bullet\bullet SH_2$	0.0187	56.7
$Cl_2Mg\bullet\bullet\bullet NH_3$	0.0338	117.2
$Cl_2Mg\bullet\bullet\bullet NCH$	0.0279	78.9
$Cl_2Mg\bullet\bullet\bullet HCHO$	0.032	88.5
$Cl_2Mg\bullet\bullet\bullet C_2H_4$	0.0171	49.6
$Cl_2Mg\bullet\bullet\bullet OHCH_3$	0.0368	112.7
$Cl_2Mg\bullet\bullet\bullet PH_3$	0.0207	55.7
$Cl_2Mg\bullet\bullet\bullet CO$	0.0191	38.5
$Cl_2Mg\bullet\bullet\bullet O(CH_3)_2$	0.0368	116.4
$H_2Mg\bullet\bullet\bullet OH_2$	0.0274	61.9
$H_2Mg\bullet\bullet\bullet SH_2$	0.014	28.2
$H_2Mg\bullet\bullet\bullet NH_3$	0.0272	73.7
$H_2Mg\bullet\bullet\bullet NCH$	0.0208	44.5
$H_2Mg\bullet\bullet\bullet OCH_2$	0.0252	55.0
$H_2Mg\bullet\bullet\bullet C_2H_4$	0.0115	22.4
$H_2Mg\bullet\bullet\bullet OHCH_3$	0.03	72.6
$H_2Mg\bullet\bullet\bullet PH_3$	0.0136	25.2
$H_2Mg\bullet\bullet\bullet CO$	0.0123	16.5
$H_2Mg\bullet\bullet\bullet O(CH_3)_2$	0.0305	75.9

Figure D6.5. Binding energy (kJ/mol) versus electron density at BCP (au) plot for Mg-bonded complexes.

Table D6.6. Electron density at BCP (au) and binding energy (kJ/mol) data for Ca-bonded complexes.

Complexes	Electron Density (au)	Binding Energy (kJ/mol)
$F_2Ca\cdots OH_2$	0.0312	91.7
$F_2Ca\cdots SH_2$	0.0173	48.0
$F_2Ca\cdots NH_3$	0.0287	90.9
$F_2Ca\cdots NCH$	0.0244	69.1
$F_2Ca\cdots CO$	0.0161	32.4
$F_2Ca\cdots OCH_2$	0.0286	80.0
$F_2Ca\cdots C_2H_4$	0.0146	40.6
$F_2Ca\cdots OHCH_3$	0.032	91.3
$F_2Ca\cdots PH_3$	0.0172	43.4
$F_2Ca\cdots O(CH_3)_2$	0.0351	92.9
$Cl_2Ca\cdots OH_2$	0.0336	94.5
$Cl_2Ca\cdots SH_2$	0.0208	54.8
$Cl_2Ca\cdots NH_3$	0.0324	102.9
$Cl_2Ca\cdots NCH$	0.028	78.3
$Cl_2Ca\cdots CO$	0.0192	38.2
$Cl_2Ca\cdots OCH_2$	0.0314	84.4
$Cl_2Ca\cdots C_2H_4$	0.0166	48.6
$Cl_2Ca\cdots OHCH_3$	0.0375	103.3
$Cl_2Ca\cdots PH_3$	0.019	52.0
$Cl_2Ca\cdots O(CH_3)_2$	0.0377	106.4
$H_2Ca\cdots SH_2$	0.0166	40.0
$H_2Ca\cdots NH_3$	0.0289	85.0
$H_2Ca\cdots NCH$	0.0238	63.0
$H_2Ca\cdots CO$	0.0151	27.3
$H_2Ca\cdots OCH_2$	0.0283	70.1
$H_2Ca\cdots C_2H_4$	0.0134	34.6
$H_2Ca\cdots OHCH_3$	0.0328	85.6
$H_2Ca\cdots PH_3$	0.0148	37.1
$H_2Ca\cdots O(CH_3)_2$	0.0345	88.3
$H_2Ca\cdots CH_3CN$	0.0267	77.6

Figure D6.6. Binding energy (kJ/mol) versus electron density at BCP (au) plot for Ca-bonded complexes.

Table D6.7. Electron density at BCP (au) and binding energy (kJ/mol) data for B-bonded complexes.

Complexes	Electron Density (au)	Binding Energy (kJ/mol)
$F_3B•••OH_2$	0.0696	27.3
$F_3B•••SH_2$	0.0147	11.0
$F_3B•••NH_3$	0.1117	88.1
$F_3B•••NCH$	0.0233	18.6
$F_3B•••CO$	0.0115	8.0
$F_3B•••OCH_2$	0.0663	27.8
$F_3B•••C_2H_4$	0.0107	10.1
$F_3B•••OHCH_3$	0.0845	46.2
$F_3B•••PH_3$	0.0126	9.6
$F_3B•••O(CH_3)_2$	0.0894	55.2
$Cl_3B•••OH_2$	0.0831	16.4
$Cl_3B•••SH_2$	0.0081	8.9
$Cl_3B•••NH_3$	0.1232	101.2
$Cl_3B•••NCH$	0.0109	11.9
$Cl_3B•••CO$	0.0064	5.9
$Cl_3B•••OCH_2$	0.0789	17.6
$Cl_3B•••C_2H_4$	0.007	10.0
$Cl_3B•••OHCH_3$	0.0945	44.1
$Cl_3B•••PH_3$	0.0071	8.2
$Cl_3B•••O(CH_3)_2$	0.0966	50.2
$HF_2B•••OH_2$	0.0613	21.8
$HF_2B•••SH_2$	0.011	9.1
$HF_2B•••NH_3$	0.1042	71.7
$HF_2B•••NCH$	0.0164	13.5
$HF_2B•••CO$	0.0081	5.5
$HF_2B•••OCH_2$	0.0558	22.0
$HF_2B•••C_2H_4$	0.0087	7.7
$HF_2B•••OHCH_3$	0.0741	33.1
$HF_2B•••PH_3$	0.0086	7.0
$HF_2B•••O(CH_3)_2$	0.0797	42.5

Figure D6.7. Binding energy (kJ/mol) versus electron density at BCP (au) plot for B-bonded complexes.

Table D6.8. Electron density at BCP (au) and binding energy (kJ/mol) data for Al-bonded complexes.

Complexes	Electron Density (au)	Binding Energy (kJ/mol)
$F_3Al\cdots OH_3$	0.0436	115.7
$F_3Al\cdots SH_3$	0.0303	72.6
$F_3Al\cdots NH_3$	0.0478	159.4
$F_3Al\cdots NCH$	0.0376	97.7
$F_3Al\cdots CO$	0.0299	54.9
$F_3Al\cdots OCH_2$	0.0429	111.1
$F_3Al\cdots C_2H_4$	0.0245	59.8
$F_3Al\cdots OHCH_3$	0.0478	132.0
$F_3Al\cdots PH_3$	0.0336	78.1
$F_3Al\cdots O(CH_3)_2$	0.0501	140.2
$Cl_3Al\cdots OH_2$	0.045	102.1
$Cl_3Al\cdots SH_2$	0.0325	66.1
$Cl_3Al\cdots NH_3$	0.0506	150.5
$Cl_3Al\cdots NCH$	0.0399	87.2
$Cl_3Al\cdots CO$	0.0321	44.6
$Cl_3Al\cdots OCH_2$	0.0443	98.7
$Cl_3Al\cdots C_2H_4$	0.0257	49.9
$Cl_3Al\cdots OHCH_3$	0.05	123.0
$Cl_3Al\cdots PH_3$	0.0375	74.8
$Cl_3Al\cdots O(CH_3)_2$	0.0516	130.9
$H_2FAl\cdots OH_2$	0.0368	81.8
$H_2FAl\cdots SH_2$	0.0241	46.6
$H_2FAl\cdots NH_3$	0.0416	111.9
$H_2FAl\cdots NCH$	0.0309	64.5
$H_2FAl\cdots CO$	0.0234	31.6
$H_2FAl\cdots OCH_2$	0.0365	82.9
$H_2FAl\cdots C_2H_4$	0.0203	39.0
$H_2FAl\cdots OHCH_3$	0.041	96.1
$H_2FAl\cdots PH_3$	0.027	47.5
$H_2FAl\cdots O(CH_3)_2$	0.0427	100.2

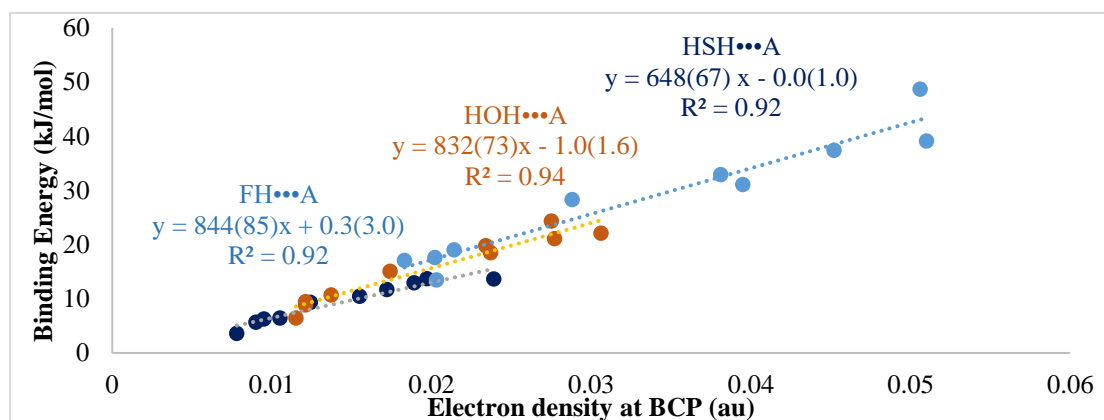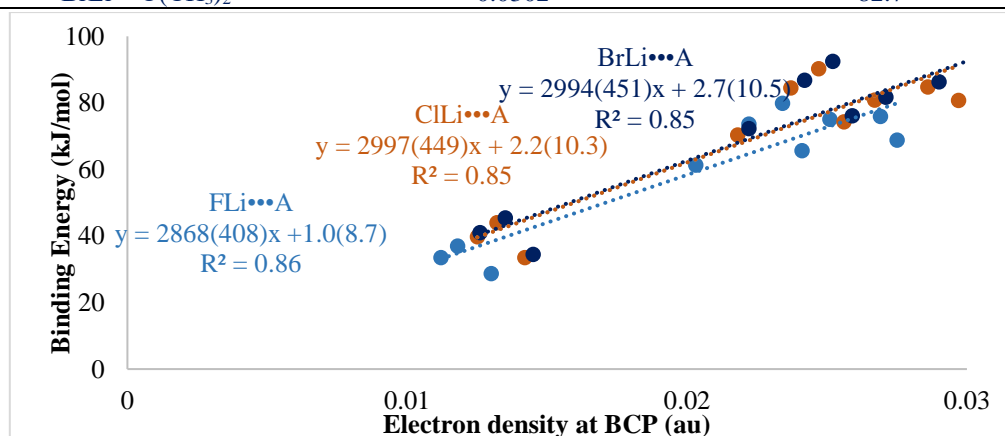*Figure D6.8. Binding energy (kJ/mol) versus electron density at BCP (au) plot for Al-bonded complexes.*

Table D6.9. Electron density at BCP (au) and binding energy (kJ/mol) data for Ga-bonded complexes.

Complexes	Electron Density (au)	Binding Energy (kJ/mol)
$HF_2Ga\cdots OH_2$	0.0577	82.7
$HF_2Ga\cdots SH_2$	0.0387	51.2
$HF_2Ga\cdots NH_3$	0.0661	116.6
$HF_2Ga\cdots NCH$	0.0485	60.6
$HF_2Ga\cdots CO$	0.0363	29.2
$HF_2Ga\cdots OCH_2$	0.0556	77.2
$HF_2Ga\cdots C_2H_4$	0.031	38.4
$HF_2Ga\cdots OHCH_3$	0.0621	94.0
$HF_2Ga\cdots PH_3$	0.0454	51.3
$HF_2Ga\cdots O(CH_3)_2$	0.064	91.7
$H_2FGa\cdots OH_2$	0.05	64.9
$H_2FGa\cdots SH_2$	0.0337	40.0
$H_2FGa\cdots NH_3$	0.0597	95.7
$H_2FGa\cdots NCH$	0.0431	48.5
$H_2FGa\cdots CO$	0.0326	23.3
$H_2FGa\cdots OCH_2$	0.0494	67.5
$H_2FGa\cdots C_2H_4$	0.029	33.7
$H_2FGa\cdots OHCH_3$	0.0558	74.6
$H_2FGa\cdots PH_3$	0.0404	40.7
$H_2FGa\cdots O(CH_3)_2$	0.0578	76.3
$H_2ClGa\cdots OH_2$	0.0505	62.8
$H_2ClGa\cdots SH_2$	0.0354	41.8
$H_2ClGa\cdots NH_3$	0.062	98.1
$H_2ClGa\cdots NCH$	0.0452	49.9
$H_2ClGa\cdots CO$	0.0356	23.3
$H_2ClGa\cdots OCH_2$	0.0497	65.0
$H_2ClGa\cdots C_2H_4$	0.0302	35.2
$H_2ClGa\cdots OHCH_3$	0.0574	76.2
$H_2ClGa\cdots PH_3$	0.0442	45.5
$H_2ClGa\cdots O(CH_3)_2$	0.0587	76.2

$H_2ClGa\cdots A$
$y = 1962(248)x - 34.6(11.9)$
$R^2 = 0.89$

$H_2FGa\cdots A$
$y = 1964(213)x - 32.2(9.9)$
$R^2 = 0.91$

$HF_2Ga\cdots A$
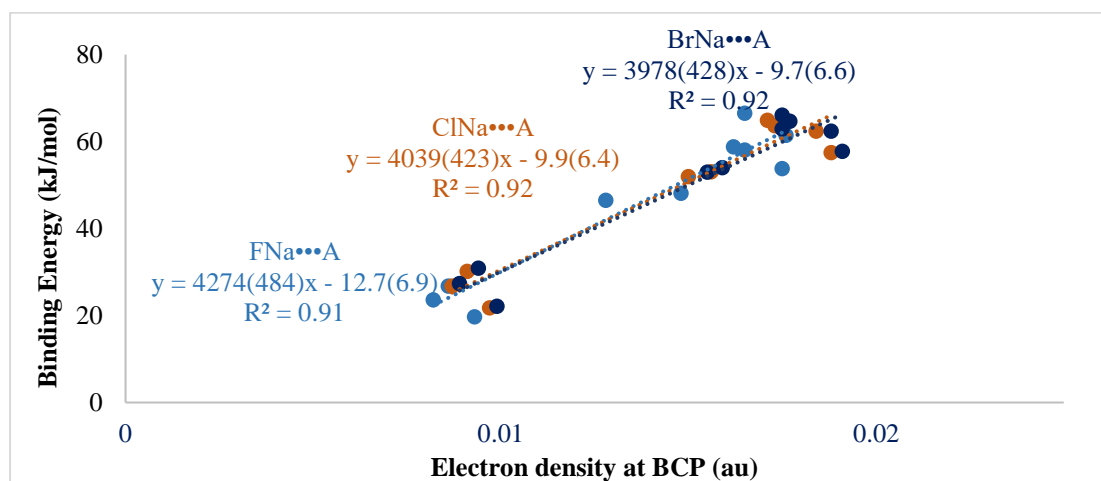$y = 2130(229)x - 38.3(11.9)$
$R^2 = 0.92$

Figure D6.9. Binding energy (kJ/mol) versus electron density at BCP (au) plot for Ga-bonded complexes.

Table D6.10. Electron density at BCP (au) and binding energy (kJ/mol) data for In-bonded complexes.

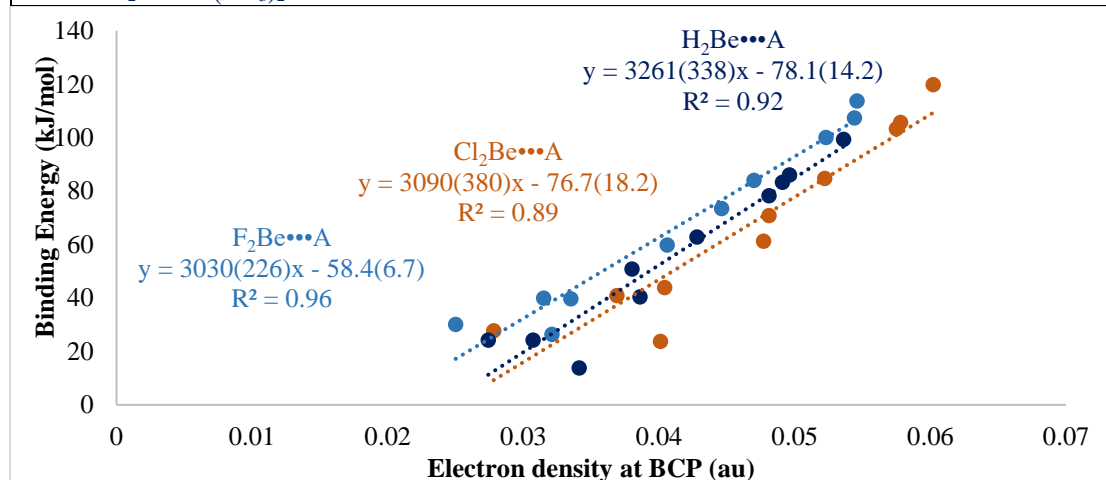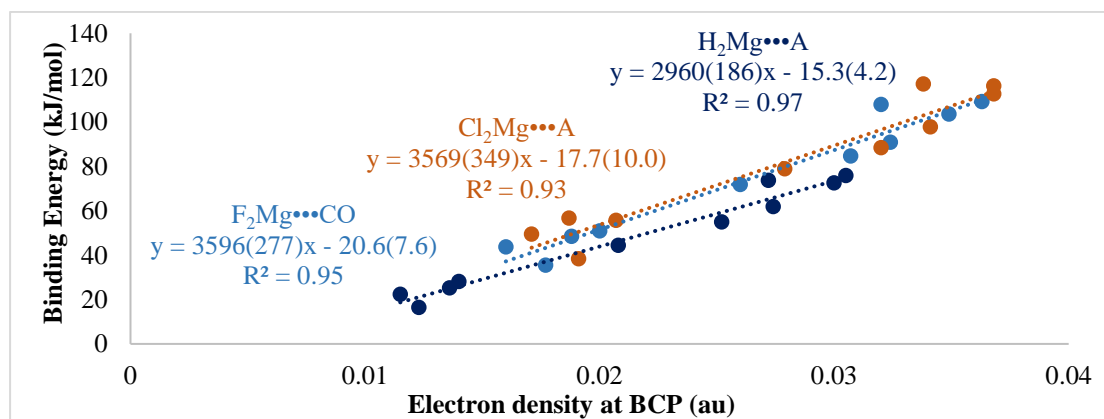| Complexes	Electron Density (au)	Binding Energy (kJ/mol)
$HF_2In\bullet\bullet\bullet OH_2$	0.0495	81.0
$HF_2In\bullet\bullet\bullet SH_2$	0.0334	55.6
$HF_2In\bullet\bullet\bullet NH_3$	0.0554	109.0
$HF_2In\bullet\bullet\bullet NCH$	0.0408	60.2
$HF_2In\bullet\bullet\bullet CO$	0.0288	29.8
$HF_2In\bullet\bullet\bullet OCH_2$	0.0469	76.0
$HF_2In\bullet\bullet\bullet C_2H_4$	0.0278	43.4
$HF_2In\bullet\bullet\bullet OHCH_3$	0.0527	90.3
$HF_2In\bullet\bullet\bullet PH_3$	0.0371	52.3
$HF_2In\bullet\bullet\bullet O(CH_3)_2$	0.0536	90.0
$H_2FIn\bullet\bullet\bullet OH_2$	0.0422	65.3
$H_2FIn\bullet\bullet\bullet SH_2$	0.0278	41.1
$H_2FIn\bullet\bullet\bullet NH_3$	0.0496	88.3
$H_2FIn\bullet\bullet\bullet NCH$	0.0358	47.03
$H_2FIn\bullet\bullet\bullet CO$	0.0251	22.7
$H_2FIn\bullet\bullet\bullet OCH_2$	0.0411	66.0
$H_2FIn\bullet\bullet\bullet C_2H_4$	0.0249	31.2
$H_2FIn\bullet\bullet\bullet OHCH_3$	0.0469	73.4
$H_2FIn\bullet\bullet\bullet PH_3$	0.0323	40.1
$H_2FIn\bullet\bullet\bullet O(CH_3)_2$	0.0467	69.2
$H_2ClIn\bullet\bullet\bullet OH_2$	0.0417	60.5
$H_2ClIn\bullet\bullet\bullet SH_2$	0.0288	42.1
$H_2ClIn\bullet\bullet\bullet NH_3$	0.0499	88.4
$H_2ClIn\bullet\bullet\bullet NCH$	0.0369	48.4
$H_2ClIn\bullet\bullet\bullet CO$	0.0258	22.9
$H_2ClIn\bullet\bullet\bullet OCH_2$	0.0409	62.6
$H_2ClIn\bullet\bullet\bullet C_2H_4$	0.0255	36.4
$H_2ClIn\bullet\bullet\bullet OHCH_3$	0.0472	70.7
$H_2ClIn\bullet\bullet\bullet PH_3$	0.0337	43.0
$H_2ClIn\bullet\bullet\bullet O(CH_3)_2$	0.0473	68.0

Figure D6.10. Binding energy (kJ/mol) versus electron density at BCP (au) plot for In-bonded complexes.

Table D6.11. Electron density at BCP (au) and binding energy (kJ/mol) data for Tl-bonded complexes.

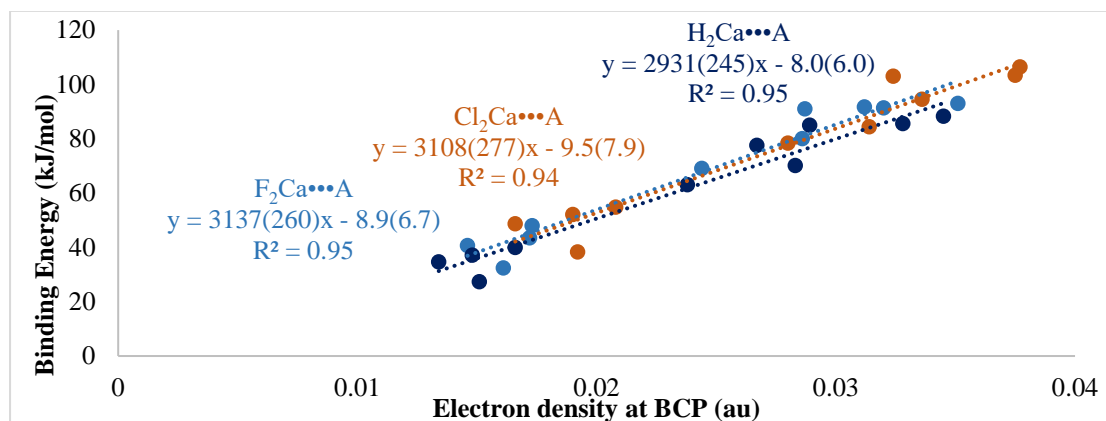| Complexes	Electron Density (au)	Binding Energy (kJ/mol)
$HF_2Tl\cdots OH_2$	0.042	54.0
$HF_2Tl\cdots SH_2$	0.0335	46.9
$HF_2Tl\cdots NH_3$	0.0569	86.0
$HF_2Tl\cdots NCH$	0.0374	42.8
$HF_2Tl\cdots CO$	0.0262	20.6
$HF_2Tl\cdots OCH_2$	0.0446	61.8
$HF_2Tl\cdots C_2H_4$	0.0283	33.3
$HF_2Tl\cdots OHCH_3$	0.0508	72.2
$HF_2Tl\cdots PH_3$	0.0385	39.9
$HF_2Tl\cdots O(CH_3)_2$	0.0508	68.4
$H_2FTl\cdots OH_2$	0.0382	55.7
$H_2FTl\cdots SH_2$	0.0271	36.5
$H_2FTl\cdots NH_3$	0.0467	66.7
$H_2FTl\cdots NCH$	0.0313	33.0
$H_2FTl\cdots CO$	0.0227	15.6
$H_2FTl\cdots OCH_2$	0.037	53.5
$H_2FTl\cdots C_2H_4$	0.0244	26.6
$H_2FTl\cdots OHCH_3$	0.0435	61.3
$H_2FTl\cdots PH_3$	0.0303	30.9
$H_2FTl\cdots O(CH_3)_2$	0.0416	49.2
$H_2ClTl\cdots OH_2$	0.0367	48.0
$H_2ClTl\cdots SH_2$	0.0264	34.5
$H_2ClTl\cdots NH_3$	0.0464	66.0
$H_2ClTl\cdots NCH$	0.0323	35.0
$H_2ClTl\cdots CO$	0.0228	16.1
$H_2ClTl\cdots OCH_2$	0.0364	50.1
$H_2ClTl\cdots C_2H_4$	0.0249	28.4
$H_2ClTl\cdots OHCH_3$	0.0428	55.7
$H_2ClTl\cdots PH_3$	0.0311	33.3
$H_2ClTl\cdots O(CH_3)_2$	0.0417	48.0

Figure D6.11. Binding energy (kJ/mol) versus electron density at BCP (au) plot for Tl bonded complexes

Table D6.12. Electron density at BCP (au) and binding energy (kJ/mol) data for C-bonded complexes.

Complexes	Electron Density (au)	Binding Energy (kJ/mol)
$FH_3C\bullet\bullet\bullet OH_2$	0.0063	7.1
$FH_3C\bullet\bullet\bullet SH_2$	0.005	4.2
$FH_3C\bullet\bullet\bullet NH_3$	0.0067	7.7
$FH_3C\bullet\bullet\bullet NCH$	0.0062	7.9
$FH_3C\bullet\bullet\bullet CO$	0.0046	3.1
$FH_3C\bullet\bullet\bullet OCH_2$	0.0061	7.4
$FH_3C\bullet\bullet\bullet C_2H_2$	0.0048	4.4
$FH_3C\bullet\bullet\bullet OHCH_3$	0.0073	7.9
$FH_3C\bullet\bullet\bullet PH_3$	0.0046	4.3
$FH_3C\bullet\bullet\bullet HF$	0.0048	4.8
$ClH_3C\bullet\bullet\bullet OH_2$	0.0061	6.7
$ClH_3C\bullet\bullet\bullet SH_2$	0.005	4.2
$ClH_3C\bullet\bullet\bullet NH_3$	0.0064	7.2
$ClH_3C\bullet\bullet\bullet NCH$	0.0061	7.7
$ClH_3C\bullet\bullet\bullet CO$	0.0044	2.8
$ClH_3C\bullet\bullet\bullet OCH_2$	0.0061	7.3
$ClH_3C\bullet\bullet\bullet OHCH_3$	0.0072	7.7
$ClH_3C\bullet\bullet\bullet C_2H_4$	0.0053	4.5
$ClH_3C\bullet\bullet\bullet PH_3$	0.0045	4.2
$ClH_3C\bullet\bullet\bullet HF$	0.0048	4.7
$HOH_3C\bullet\bullet\bullet H_2O$	0.0054	4.0
$HOH_3C\bullet\bullet\bullet H_2S$	0.0046	2.8
$HOH_3C\bullet\bullet\bullet NH_3$	0.0055	4.1
$HOH_3C\bullet\bullet\bullet NCH$	0.0054	4.7
$HOH_3C\bullet\bullet\bullet CO$	0.0042	1.9
$HOH_3C\bullet\bullet\bullet OCH_2$	0.0053	4.5
$HOH_3C\bullet\bullet\bullet HCl$	0.0042	2.1
$HOH_3C\bullet\bullet\bullet PH_3$	0.0041	2.7
$HOH_3C\bullet\bullet\bullet HF$	0.0041	2.7
$HOH_3C\bullet\bullet\bullet C_2H_2$	0.0046	3.3

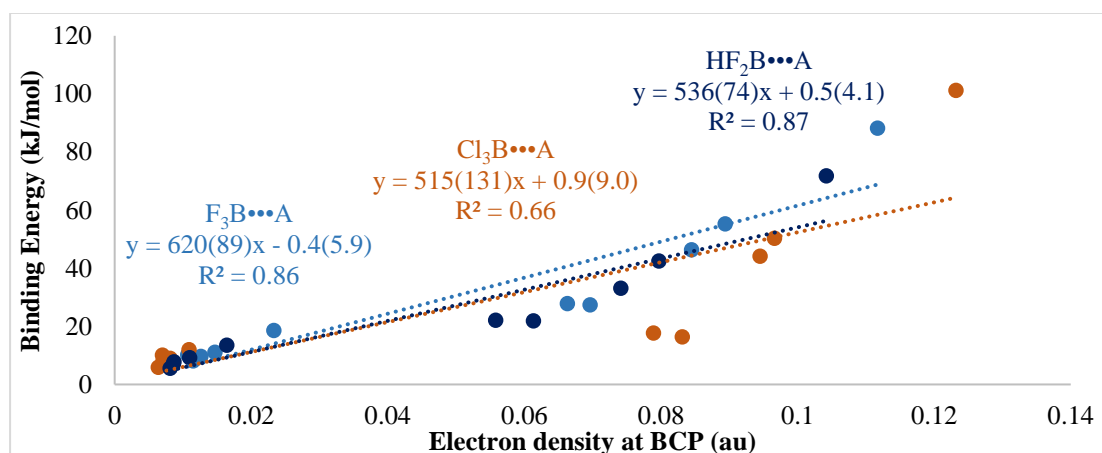*Figure D6.12. Binding energy (kJ/mol) versus electron density at BCP (au) plot for C-bonded complexes.*

Table D6.13. Electron density at BCP (au) and binding energy (kJ/mol) data for Si-bonded complexes.

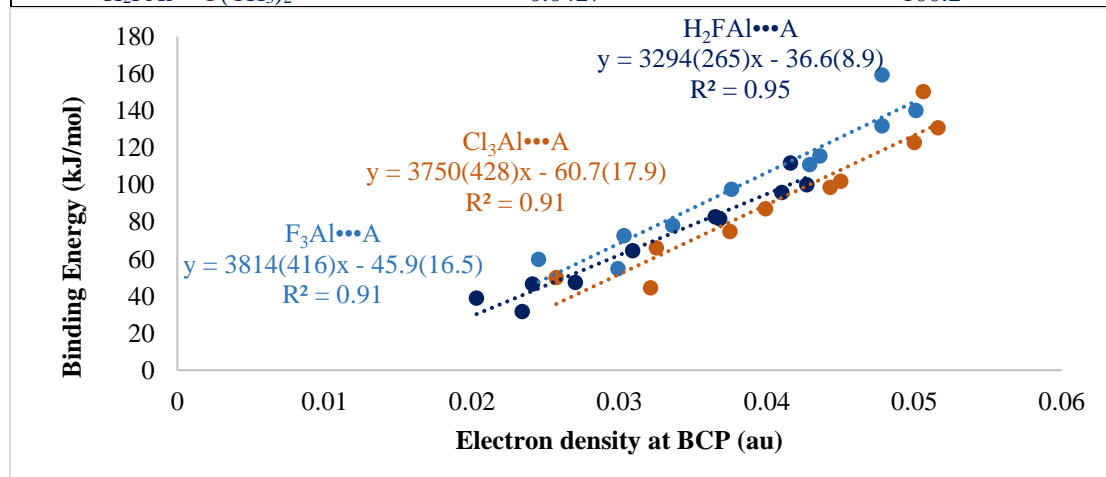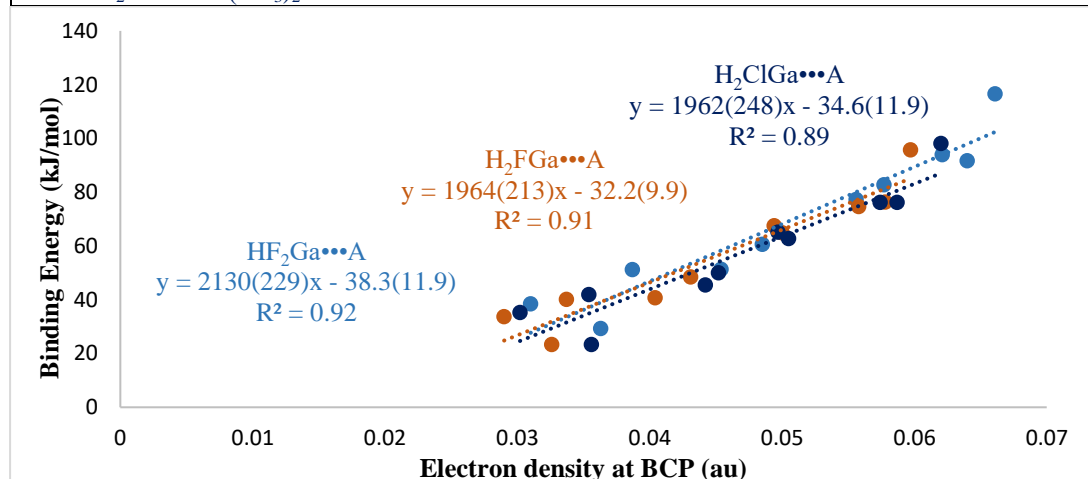| Complexes	Electron Density (au)	Binding Energy (kJ/mol)
$FH_3Si•••OH_2$	0.0128	14.4
$FH_3Si•••SH_2$	0.0081	9.3
$FH_3Si•••NH_3$	0.0251	23.0
$FH_3Si•••PH_3$	0.0079	9.2
$FH_3Si•••CO$	0.0053	3.1
$FH_3Si•••NCH$	0.0115	14.5
$FH_3Si•••OHCH_3$	0.0193	19.2
$FH_3Si•••O(CH_3)_2$	0.024	22.7
$FH_3Si•••NCCH_3$	0.0136	17.9
$FH_3Si•••NH_2CH_3$	0.0374	32.6
$ClH_3Si•••OH_2$	0.0123	13.6
$ClH_3Si•••SH_2$	0.0079	8.9
$ClH_3Si•••NH_3$	0.0259	21.3
$ClH_3Si•••PH_3$	0.0076	8.8
$ClH_3Si•••CO$	0.0052	3.0
$ClH_3Si•••NCH$	0.0112	14.0
$ClH_3Si•••OHCH_3$	0.0188	18.1
$ClH_3Si•••OCH_2$	0.0156	15.4
$ClH_3Si•••C_2H_4$	0.0075	9.4
$ClH_3Si•••O(CH_3)_2$	0.0242	21.8
$CNH_3Si•••OH_2$	0.0113	14.6
$CNH_3Si•••SH_2$	0.0072	8.8
$CNH_3Si•••NH_3$	0.0193	20.7
$CNH_3Si•••PH_3$	0.0067	8.5
$CNH_3Si•••CO$	0.0062	5.9
$CNH_3Si•••NCH$	0.0103	15.1
$CNH_3Si•••OHCH_3$	0.0168	18.3
$CNH_3Si•••OCH_2$	0.0145	15.6
$CNH_3Si•••C_2H_4$	0.0067	8.9
$CNH_3Si•••O(CH_3)_2$	0.0219	21.4

Figure D6.13. Binding energy (kJ/mol) versus electron density at BCP (au) plot for Si-bonded complexes.

Table D6.14. Electron density at BCP (au) and binding energy (kJ/mol) data for Ge-bonded complexes.

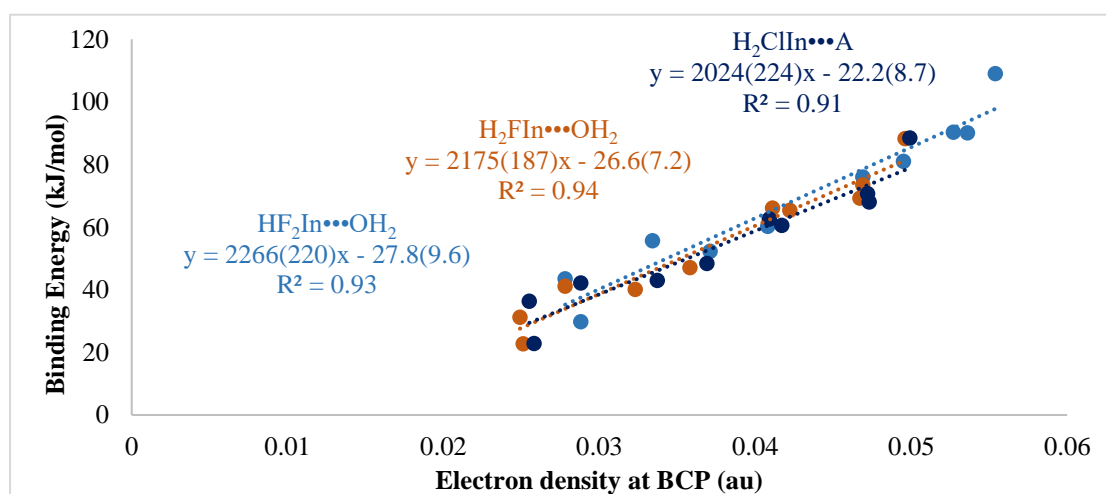| Complexes	Electron Density (au)	Binding Energy (kJ/mol)
$FH_3Ge\bullet\bullet\bullet OH_2$	0.0145	16.3
$FH_3Ge\bullet\bullet\bullet SH_2$	0.0086	10.5
$FH_3Ge\bullet\bullet\bullet NH_3$	0.0252	24.4
$FH_3Ge\bullet\bullet\bullet PH_3$	0.0083	10.2
$FH_3Ge\bullet\bullet\bullet CO$	0.0058	3.3
$FH_3Ge\bullet\bullet\bullet NCH$	0.0139	16.5
$FH_3Ge\bullet\bullet\bullet OHCH_3$	0.0216	20.6
$FH_3Ge\bullet\bullet\bullet OCH_2$	0.0186	17.7
$FH_3Ge\bullet\bullet\bullet C_2H_4$	0.0086	10.6
$FH_3Ge\bullet\bullet\bullet O(CH_3)_2$	0.0265	23.8
$ClH_3Ge\bullet\bullet\bullet OH_2$	0.0136	15.0
$ClH_3Ge\bullet\bullet\bullet SH_2$	0.0083	9.8
$ClH_3Ge\bullet\bullet\bullet NH_3$	0.0248	22.1
$ClH_3Ge\bullet\bullet\bullet PH_3$	0.008	9.5
$ClH_3Ge\bullet\bullet\bullet CO$	0.0055	3.2
$ClH_3Ge\bullet\bullet\bullet NCH$	0.0133	15.3
$ClH_3Ge\bullet\bullet\bullet OHCH_3$	0.0207	18.8
$ClH_3Ge\bullet\bullet\bullet OCH_2$	0.0176	16.30
$ClH_3Ge\bullet\bullet\bullet C_2H_4$	0.0084	10.0
$ClH_3Ge\bullet\bullet\bullet O(CH_3)_2$	0.0258	21.9
$CNH_3Ge\bullet\bullet\bullet OH_2$	0.0112	14.4
$CNH_3Ge\bullet\bullet\bullet SH_2$	0.007	8.8
$CNH_3Ge\bullet\bullet\bullet NH_3$	0.0173	19.1
$CNH_3Ge\bullet\bullet\bullet PH_3$	0.0067	8.4
$CNH_3Ge\bullet\bullet\bullet CO$	0.0064	5.9
$CNH_3Ge\bullet\bullet\bullet NCH$	0.0114	14.9
$CNH_3Ge\bullet\bullet\bullet OHCH_3$	0.0166	17.2
$CNH_3Ge\bullet\bullet\bullet OCH_2$	0.0147	14.9
$CNH_3Ge\bullet\bullet\bullet C_2H_4$	0.0072	8.7
$CNH_3Ge\bullet\bullet\bullet O(CH_3)_2$	0.0215	19.4

Figure D6.14. Binding energy (kJ/mol) versus electron density at BCP (au) plot for Ge-bonded complexes.

Table D6.15. Electron density at BCP (au) and binding energy (kJ/mol) data for Sn-bonded complexes.

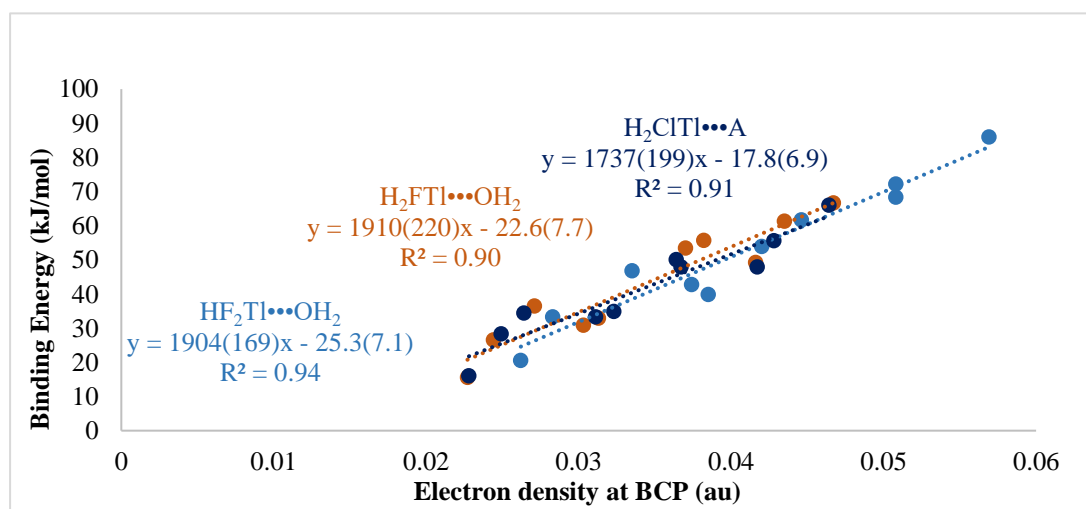| Complexes	Electron Density (au)	Binding Energy (kJ/mol)
$FH_3Sn\cdots OH_2$	0.0189	22.7
$FH_3Sn\cdots SH_2$	0.0108	13.9
$FH_3Sn\cdots NH_3$	0.0286	35.6
$FH_3Sn\cdots PH_3$	0.0104	13.6
$FH_3Sn\cdots CO$	0.0062	3.9
$FH_3Sn\cdots NCH$	0.0164	22.1
$FH_3Sn\cdots OHCH_3$	0.0254	28.9
$FH_3Sn\cdots OCH_2$	0.022	24.6
$FH_3Sn\cdots C_2H_4$	0.01	13.3
$FH_3Sn\cdots O(CH_3)_2$	0.029	32.9
$ClH_3Sn\cdots OH_2$	0.0185	21.5
$ClH_3Sn\cdots SH_2$	0.0104	13.2
$ClH_3Sn\cdots NH_3$	0.029	34.0
$ClH_3Sn\cdots PH_3$	0.0104	13.0
$ClH_3Sn\cdots CO$	0.0099	3.7
$ClH_3Sn\cdots NCH$	0.0163	21.1
$ClH_3Sn\cdots OHCH_3$	0.0254	27.5
$ClH_3Sn\cdots OCH_2$	0.0218	23.3
$ClH_3Sn\cdots C_2H_4$	0.0097	12.8
$ClH_3Sn\cdots O(CH_3)_2$	0.029	31.5
$CNH_3Sn\cdots OH_2$	0.0161	19.5
$CNH_3Sn\cdots SH_2$	0.0088	11.5
$CNH_3Sn\cdots NH_3$	0.0082	9.9
$CNH_3Sn\cdots PH_3$	0.0079	11.0
$CNH_3Sn\cdots CO$	0.008	7.3
$CNH_3Sn\cdot\cdot NCH$	0.007	10.1
$CNH_3Sn\cdots OHCH_3$	0.0225	24.3
$CNH_3Sn\cdots OCH_2$	0.0196	20.7
$CNH_3Sn\cdots C_2H_4$	0.0084	11.0
$CNH_3Sn\cdots O(CH_3)_2$	0.029	27.7

Figure D6.15. Binding energy (kJ/mol) versus electron density at BCP (au) plot for Sn-bonded complexes.

Table D6.16. Electron density at BCP (au) and binding energy (kJ/mol) data for Pb-bonded complexes.

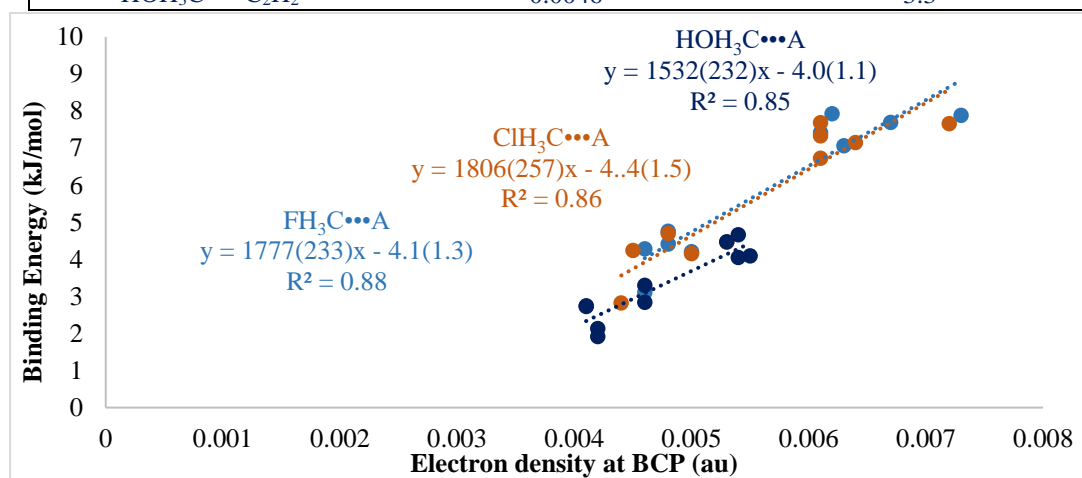| Complexes	Electron Density (au)	Binding Energy (kJ/mol)
$FH_3Pb•••OH_2$	0.0145	22.1
$FH_3Pb•••SH_2$	0.0086	14.1
$FH_3Pb•••NH_3$	0.0252	31.7
$FH_3Pb•••PH_3$	0.0083	13.9
$FH_3Pb•••CO$	0.0058	3.8
$FH_3Pb•••NCH$	0.0139	22.4
$FH_3Pb•••OHCH_3$	0.0216	26.2
$FH_3Pb•••OCH_2$	0.0186	22.8
$FH_3Pb•••C_2H_4$	0.0086	13.4
$FH_3SPb•••O(CH_3)_2$	0.0264	28.9
$ClH_3Pb•••OH_2$	0.0172	21.4
$ClH_3Pb•••SH_2$	0.011	13.8
$ClH_3Pb•••NH_3$	0.0249	31.1
$ClH_3Pb•••PH_3$	0.0103	13.5
$ClH_3Pb•••CO$	0.01	8.4
$ClH_3Pb•••NCH$	0.0167	21.8
$ClH_3Pb•••OHCH_3$	0.023	25.6
$ClH_3Pb•••OCH_2$	0.0209	22.1
$ClH_3Pb•••C_2H_4$	0.011	13.2
$ClH_3Pb•••O(CH_3)_2$	0.0269	28.5
$CNH_3Pb•••OH_2$	0.0145	18.2
$CNH_3Pb•••SH_2$	0.0088	11.1
$CNH_3Pb•••NH_3$	0.0196	24.5
$CNH_3Pb•••PH_3$	0.0079	10.8
$CNH_3Pb•••CO$	0.0082	7.0
$CNH_3Pb••NCH$	0.0139	18.7
$CNH_3Pb•••OHCH_3$	0.0192	21.1
$CNH_3Pb•••OCH_2$	0.0178	18.3
$CNH_3Pb•••C_2H_4$	0.0091	10.6
$CNH_3Pb•••O(CH_3)_2$	0.023	23.4

Figure D6.16. Binding energy (kJ/mol) versus electron density at BCP (au) plot for Pb-bonded complexes.

Table D6.17. Electron density at BCP (au) and binding energy (kJ/mol) data for N-bonded complexes.

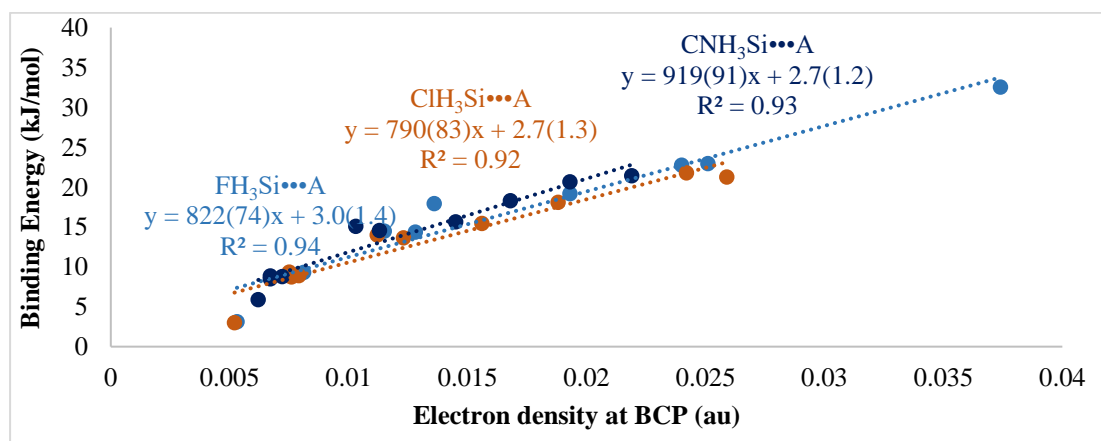| Complexes	Electron Density (au)	Binding Energy (kJ/mol)
$F_3N\cdots OH_2$	0.0065	3.7
$F_3N\cdots SH_2$	0.0036	2.7
$F_3N\cdots NH_3$	0.006	3.9
$F_3N\cdots NCH$	0.0069	3.8
$F_3N\cdots CO$	0.0047	1.9
$F_3N\cdots OCH_2$	0.0073	4.8
$F_3N\cdots C_2H_4$	0.0053	2.9
$F_3N\cdots OHCH_3$	0.0078	5.3
$F_3N\cdots O(CH_3)_2$	0.0105	6.4
$F_3N\cdots FH$	0.0056	2.9

Figure D6.17. Binding energy (kJ/mol) versus electron density at BCP (au) plot for N-bonded complexes.

:

Table D6.18. Electron density at BCP (au) and binding energy (kJ/mol) data for P-bonded complexes.

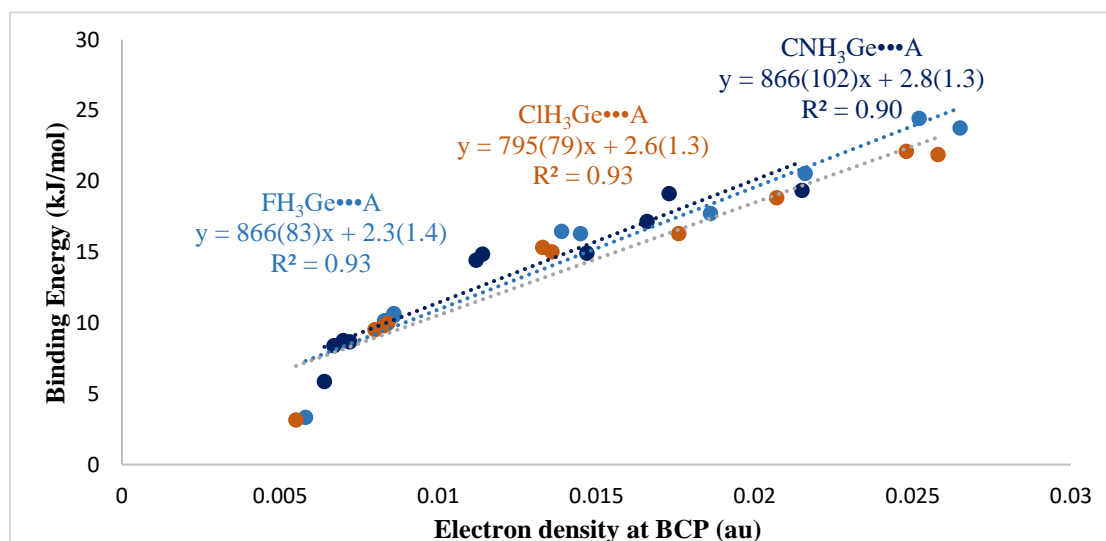| Complexes	Electron Density (au)	Binding Energy (kJ/mol)
$F_3P\cdots OH_2$	0.0158	14.2
$F_3P\cdots SH_2$	0.0084	8.5
$F_3P\cdots NH_3$	0.0218	18.7
$F_3P\cdots NCH$	0.0114	11.5
$F_3P\cdots CO$	0.0066	4.8
$F_3P\cdots OCH_2$	0.0167	16.4
$F_3P\cdots C_2H_4$	0.0079	7.4
$F_3P\cdots OHCH_3$	0.0197	17.6
$F_3P\cdots PH_3$	0.0073	6.7
$F_3P\cdots O(CH_3)_2$	0.0248	20.5
$FH_2P\cdots SH_2$	0.0131	12.9
$FH_2P\cdots NH_3$	0.0269	25.8
$FH_2P\cdots NCH$	0.0159	17.2
$FH_2P\cdots CO$	0.013	8.9
$FH_2P\cdots OCH_2$	0.0096	11.5
$FH_2P\cdots C_2H_4$	0.0154	14.5
$FH_2P\cdots OHCH_3$	0.0226	20.9
$FH_2P\cdots PH_3$	0.0161	13.5
$FH_2P\cdots C_2H_2$	0.012	12.2
$FH_2P\cdots O(CH_3)_2$	0.0263	24
$ClH_2P\cdots OH_2$	0.0146	14.8
$ClH_2P\cdots SH_2$	0.0119	11.4
$ClH_2P\cdots NH_3$	0.0241	22.3
$ClH_2P\cdots NCH$	0.0139	15.5
$ClH_2P\cdots CO$	0.0103	7.2
$ClH_2P\cdots OCH_2$	0.0098	11.8
$ClH_2P\cdots C_2H_4$	0.0135	12.7
$ClH_2P\cdots OHCH_3$	0.0203	18.3
$ClH_2P\cdots PH_3$	0.0137	11.7
$ClH_2P\cdots O(CH_3)_2$	0.0253	22

Figure D6.18. Binding energy (kJ/mol) versus electron density at BCP (au) plot for P-bonded complexes.

Table D6.19. Electron density at BCP (au) and binding energy (kJ/mol) data for As-bonded complexes.

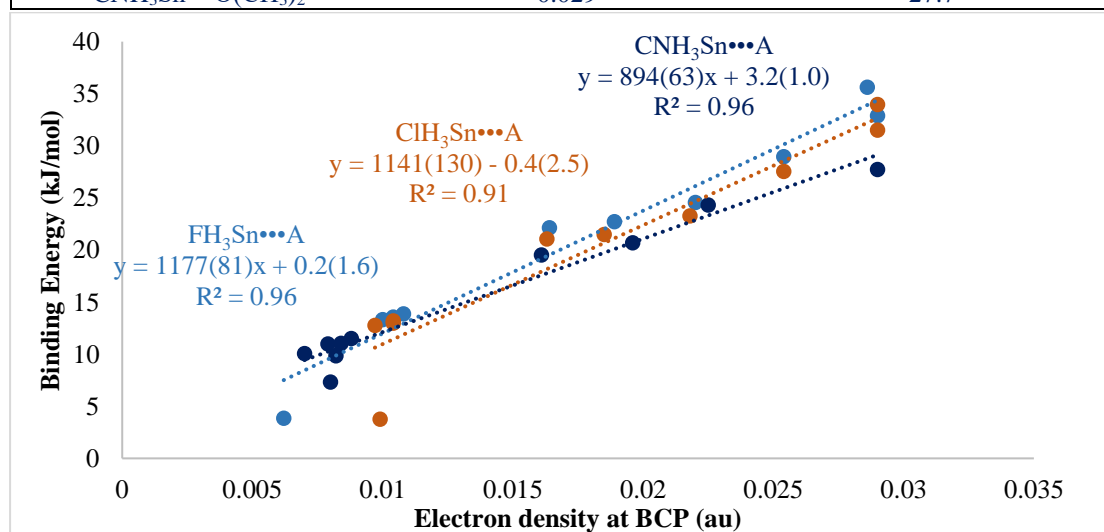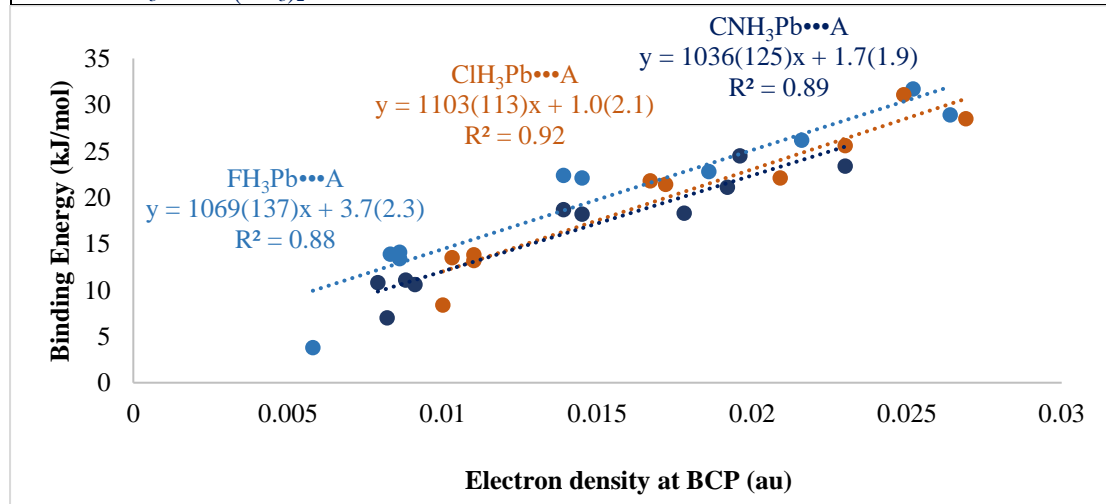| Complexes	Electron Density (au)	Binding Energy (kJ/mol)
$F_3As\bullet\bullet\bullet OH_2$	0.0239	23.3
$F_3As\bullet\bullet\bullet SH_2$	0.0113	13.7
$F_3As\bullet\bullet\bullet NH_3$	0.033	30.6
$F_3As\bullet\bullet\bullet NCH$	0.0157	17.1
$F_3As\bullet\bullet\bullet CO$	0.0085	7.2
$F_3As\bullet\bullet\bullet OCH_2$	0.0239	25.4
$F_3As\bullet\bullet\bullet C_2H_4$	0.0099	10.9
$F_3As\bullet\bullet\bullet OHCH_3$	0.0298	28.3
$F_3As\bullet\bullet\bullet PH_3$	0.0101	10.6
$F_3As\bullet\bullet\bullet O(CH_3)_2$	0.0338	30.1
$FH_2As\bullet\bullet\bullet OH_2$	0.0188	19.8
$FH_2As\bullet\bullet\bullet SH_2$	0.0146	15.2
$FH_2As\bullet\bullet\bullet NH_3$	0.0298	31.4
$FH_2As\bullet\bullet\bullet NCH$	0.0187	20.4
$FH_2As\bullet\bullet\bullet CO$	0.0141	10.4
$FH_2As\bullet\bullet OCH_2$	0.0113	14.3
$FH_2As\bullet\bullet\bullet C_2H_4$	0.0172	16.8
$FH_2As\bullet\bullet\bullet OHCH_3$	0.0253	23.8
$FH_2As\bullet\bullet\bullet PH_3$	0.0131	16.2
$FH_2As\bullet\bullet\bullet O(CH_3)_2$	0.0306	27.8
$ClH_2As\bullet\bullet\bullet OH_2$	0.017	17.5
$ClH_2As\bullet\bullet\bullet SH_2$	0.0135	13.6
$ClH_2As\bullet\bullet\bullet NH_3$	0.0287	27.9
$ClH_2As\bullet\bullet\bullet NCH$	0.0169	18.3
$ClH_2As\bullet\bullet\bullet CO$	0.0116	8.4
$ClH_2As\bullet\bullet OCH_2$	0.011	13.6
$ClH_2As\bullet\bullet\bullet C_2H_4$	0.0155	14.9
$ClH_2As\bullet\bullet\bullet OHCH_3$	0.0235	21.2
$ClH_2As\bullet\bullet\bullet PH_3$	0.0153	14.2
$ClH_2As\bullet\bullet\bullet O(CH_3)_2$	0.029	25.1

Figure D6.19. Binding energy (kJ/mol) versus electron density at BCP (au) plot for As-bonded complexes.

Table D6.20. Electron density at BCP (au) and binding energy (kJ/mol) data for Sb-bonded complexes.

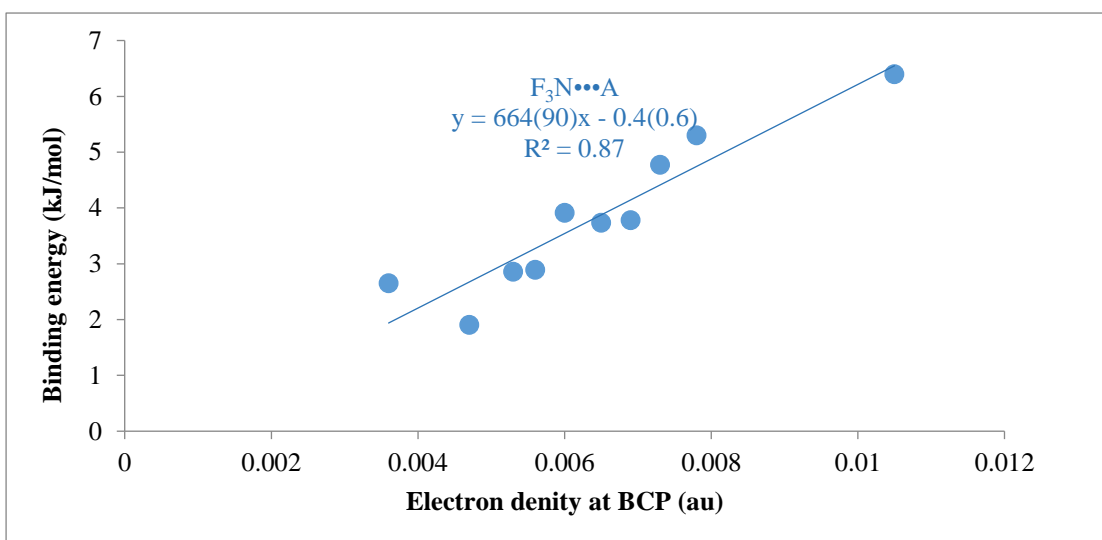| Complexes	Electron Density (au)	Binding Energy (kJ/mol)
$F_3Sb•••OH_2$	0.0312	37.1
$F_3Sb•••SH_2$	0.0148	21.3
$F_3Sb•••NH_3$	0.0375	48.9
$F_3Sb•••NCH$	0.0198	24.6
$F_3Sb•••CO$	0.0108	10.2
$F_3Sb•••OCH_2$	0.0291	37.5
$F_3Sb•••C_2H_4$	0.0123	15.6
$F_3Sb•••OHCH_3$	0.0349	43.8
$F_3Sb•••PH_3$	0.0141	16.3
$F_3Sb•••O(CH_3)_2$	0.0367	43.9
$FH_2Sb•••OH_2$	0.0207	24.7
$FH_2Sb•••SH_2$	0.015	18.6
$FH_2Sb•••NH_3$	0.0303	40.1
$FH_2Sb•••NCH$	0.02	25.1
$FH_2Sb•••CO$	0.0145	12.4
$FH_2Sb••OCH_2$	0.0149	19.7
$FH_2Sb•••C_2H_4$	0.0168	19.7
$FH_2Sb•••OHCH_3$	0.0267	32
$FH_2Sb•••PH_3$	0.0172	19.7
$FH_2Sb•••O(CH_3)_2$	0.0304	33.5
$ClH_2Sb•••OH_2$	0.0202	23
$ClH_2Sb•••SH_2$	0.0147	17.5
$ClH_2Sb•••NH_3$	0.0309	38.1
$ClH_2Sb•••NCH$	0.0196	23.5
$ClH_2Sb•••CO$	0.0131	10.6
$ClH_2Sb••OCH_2$	0.0136	18
$ClH_2Sb•••C_2H_4$	0.0164	18.3
$ClH_2Sb•••OHCH_3$	0.0268	30.1
$ClH_2Sb•••PH_3$	0.0166	18.3
$ClH_2Sb•••O(CH_3)_2$	0.0306	31.8

Figure D6.20. Binding energy (kJ/mol) versus electron density at BCP (au) plot for Sb-bonded complexes.

Table D6.21. Electron density at BCP (au) and binding energy (kJ/mol) data for Bi-bonded complexes.

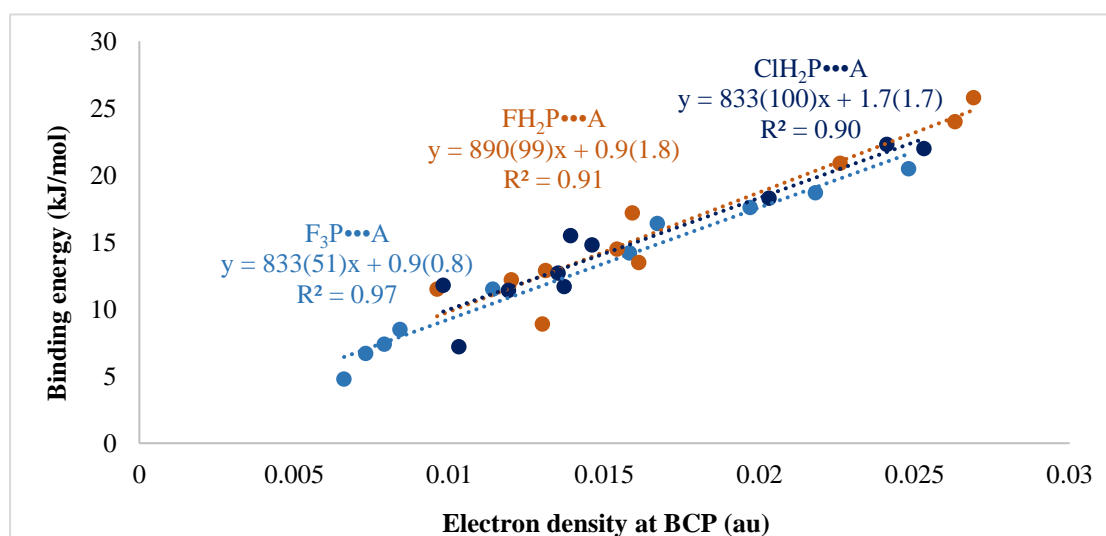| Complexes	Electron Density (au)	Binding Energy (kJ/mol)
$F_3Bi•••OH_2$	0.0322	45.5
$F_3Bi•••SH_2$	0.0163	27.7
$F_3Bi•••NH_3$	0.0348	55.3
$F_3Bi•••NCH$	0.0214	31.3
$F_3Bi•••CO$	0.0128	13.4
$F_3Bi•••OCH_2$	0.0298	45
$F_3Bi•••C_2H_4$	0.0137	19.7
$F_3Bi•••OHCH_3$	0.0344	51.8
$F_3Bi••PH_3$	0.0157	21.2
$F_3Bi•••O(CH_3)_2$	0.035	49.3
$FH_2Bi•••OH_2$	0.0208	27.7
$FH_2Bi•••SH_2$	0.0153	21.1
$FH_2Bi•••NH_3$	0.0282	41.9
$FH_2Bi•••NCH$	0.0207	28
$FH_2Bi•••CO$	0.0152	13.9
$FH_2Bi••OCH_2$	0.0157	23.1
$FH_2Bi•••C_2H_4$	0.0167	21.5
$FH_2Bi•••OHCH_3$	0.0256	34.2
$FH_2Bi•••PH_3$	0.0168	21.9
$FH_2Bi•••O(CH_3)_2$	0.0288	33.3
$ClH_2Bi•••OH_2$	0.021	26.6
$ClH_2Bi•••SH_2$	0.0156	20.5
$ClH_2Bi•••NH_3$	0.0293	41.3
$ClH_2Bi•••NCH$	0.0209	27.1
$ClH_2Bi•••CO$	0.0145	12.4
$ClH_2Bi••OCH_2$	0.0146	20.9
$ClH_2Bi•••C_2H_4$	0.0171	20.7
$ClH_2Bi•••OHCH_3$	0.0263	33.2
$ClH_2Bi•••PH_3$	0.0171	21.3
$ClH_2Bi•••O(CH_3)_2$	0.0296	32.6

Figure D6.21. Binding energy (kJ/mol) versus electron density at BCP (au) plot for Bi-bonded complexes.

Table D6.22. Electron density at BCP (au) and binding energy (kJ/mol) data for O-bonded complexes.

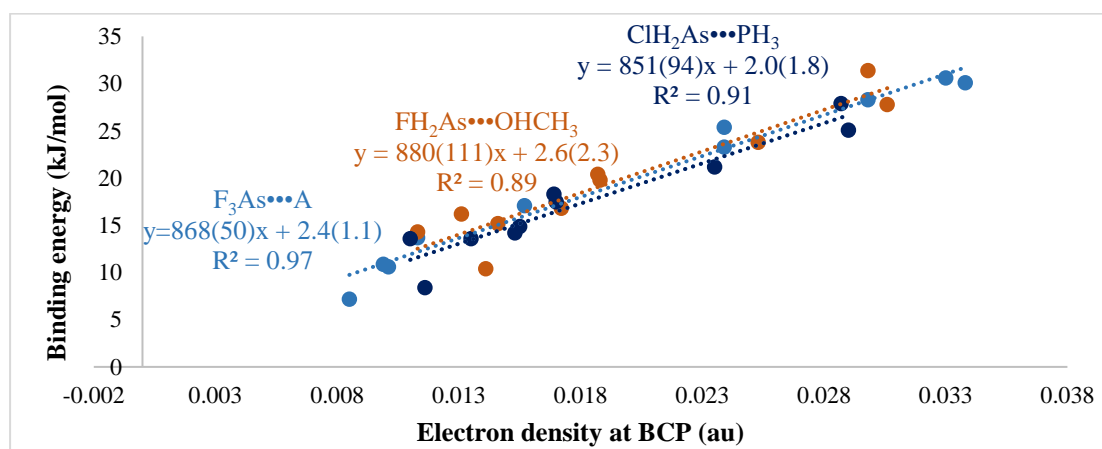| Complexes	Electron Density (au)	Binding Energy (kJ/mol)
$F_2O\cdots OH_2$	0.0100	5.4
$F_2O\cdots SH_2$	0.0067	3.8
$F_2O\cdots NH_3$	0.0111	6.4
$F_2O\cdots NCH$	0.0091	5.3
$F_2O\cdots CO$	0.0060	2.5
$F_2O\cdots OCH_2$	0.0112	6.7
$F_2O\cdots C_2H_4$	0.0076	4.4
$F_3N\cdots OHCH_3$	0.0117	6.8
$F_2O\cdots PH_3$	0.0057	3.3
$F_2O\cdots O(CH_3)_2$	0.0141	8.3

$F_2O\cdots A$
y = 639.8x - 0.6734
$R^2 = 0.97$

Figure D6.22. Binding energy (kJ/mol) versus electron density at BCP (au) plot for O-bonded complexes.

:

Table D6.23. Electron density at BCP (au) and binding energy (kJ/mol) data for S-bonded complexes.

Complexes	Electron Density (au)	Binding Energy (kJ/mol)
$F_2S\cdots OH_2$	0.0219	19
$F_2S\cdots SH_2$	0.015	13.1
$F_2S\cdots NH_3$	0.0376	29.1
$F_2S\cdots NCH$	0.0163	16.2
$F_2S\cdots CO$	0.0106	7.5
$F_2S\cdots OCH_2$	0.024	22.1
$F_2S\cdots C_2H_4$	0.0164	13.4
$F_2S\cdots OHCH_3$	0.0297	24.9
$F_2S\cdots PH_3$	0.0144	11.4
$F_2S\cdots O(CH_3)_2$	0.0363	29.1
$Cl_2S\cdots OH_2$	0.0166	13.1
$Cl_2S\cdots SH_2$	0.013	11.4
$Cl_2S\cdots NH_3$	0.0266	20.3
$Cl_2S\cdots NCH$	0.0141	12.6
$Cl_2S\cdots CO$	0.0094	6.1
$Cl_2S\cdots OCH_2$	0.0181	16.2
$Cl_2S\cdots C_2H_4$	0.0139	12.1
$Cl_2S\cdots OHCH_3$	0.0221	18
$Cl_2S\cdots PH_3$	0.0129	10.5
$Cl_2S\cdots O(CH_3)_2$	0.0271	22.8
$O_2S\cdots OH_2$	0.0158	14.4
$O_2S\cdots SH_2$	0.0097	9.9
$O_2S\cdots NH_3$	0.0203	18.9
$O_2S\cdots NCH$	0.0117	12.5
$O_2S\cdots CO$	0.0068	5.3
$O_2S\cdots OCH_2$	0.02	18.2
$O_2S\cdots C_2H_4$	0.0085	8.5
$O_2S\cdots OHCH_3$	0.0219	19.1
$O_2S\cdots PH_3$	0.0079	7.4
$O_2S\cdots O(CH_3)_2$	0.0273	22.9

Plot with:

$O_2S\cdots A$
$y = 825(45)x + 1.3(0.7)$
$R^2 = 0.98$

$Cl_2S\cdots A$
$y = 810(60)x + 0.2(1.1)$
$R^2 = 0.96$
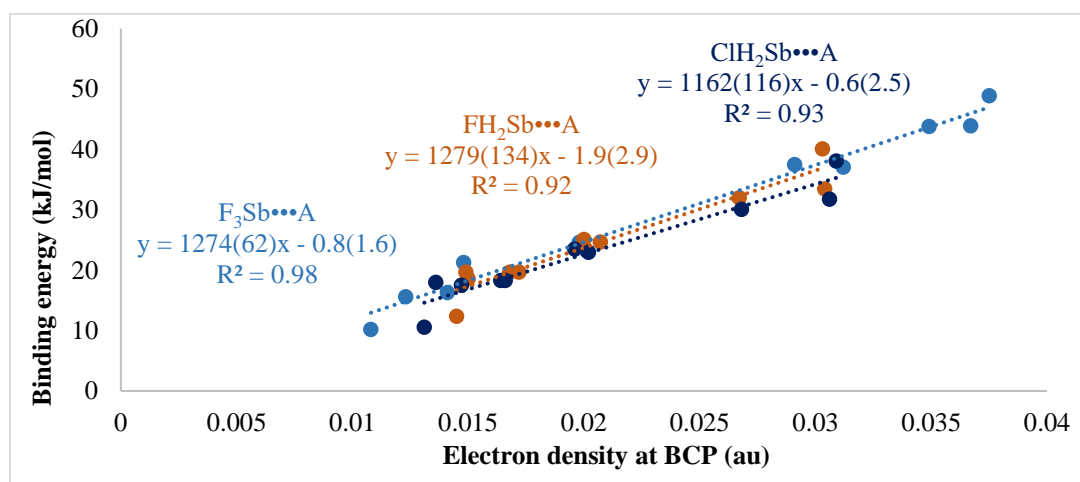
$F_2S\cdots A$
$y = 779(53)x + 1.3(1.3)$
$R^2 = 0.96$

Figure D6.23. Binding energy (kJ/mol) versus electron density at BCP (au) plot for S-bonded complexes.

Table D6.24. Electron density at BCP (au) and binding energy (kJ/mol) data for Se-bonded complexes.

Complexes	Electron Density (au)	Binding Energy (kJ/mol)
$F_2Se\cdots OH_2$	0.0297	27.9
$F_2Se\cdots SH_2$	0.0204	20.2
$F_2Se\cdots NH_3$	0.0481	45
$F_2Se\cdots NCH$	0.0231	23.1
$F_2Se\cdots CO$	0.0147	11
$F_2Se\cdots OCH_2$	0.0322	31.8
$F_2Se\cdots C_2H_4$	0.0283	20.5
$F_2Se\cdots OHCH_3$	0.0398	36.3
$F_2Se\cdots PH_3$	0.0239	18.5
$F_2Se\cdots O(CH_3)_2$	0.0459	41.4
$Cl_2Se\cdots OH_2$	0.0218	20.1
$Cl_2Se\cdots SH_2$	0.017	16.8
$Cl_2Se\cdots NH_3$	0.0381	32.6
$Cl_2Se\cdots NCH$	0.0184	18.2
$Cl_2Se\cdots CO$	0.0068	8.6
$Cl_2Se\cdots OCH_2$	0.0235	23.4
$Cl_2Se\cdots C_2H_4$	0.0198	17.1
$Cl_2Se\cdots OHCH_3$	0.0303	26.8
$Cl_2Se\cdots PH_3$	0.0188	15.9
$Cl_2Se\cdots O(CH_3)_2$	0.0367	32.2
$O_2Se\cdots OH_2$	0.0182	17.2
$O_2Se\cdots SH_2$	0.0112	12
$O_2Se\cdots NH_3$	0.0253	23.4
$O_2Se\cdots NCH$	0.0125	14.7
$O_2Se\cdots CO$	0.0072	6
$O_2Se\cdots OCH_2$	0.023	22.3
$O_2Se\cdots C_2H_4$	0.0086	9.4
$O_2Se\cdots OHCH_3$	0.0268	23.3
$O_2Se\cdots PH_3$	0.009	8.2
$O_2Se\cdots O(CH_3)_2$	0.0319	27.7

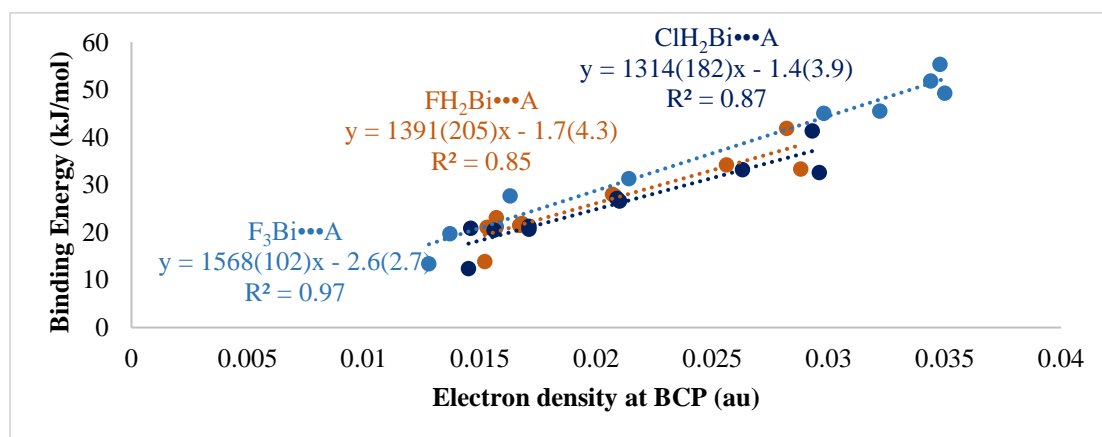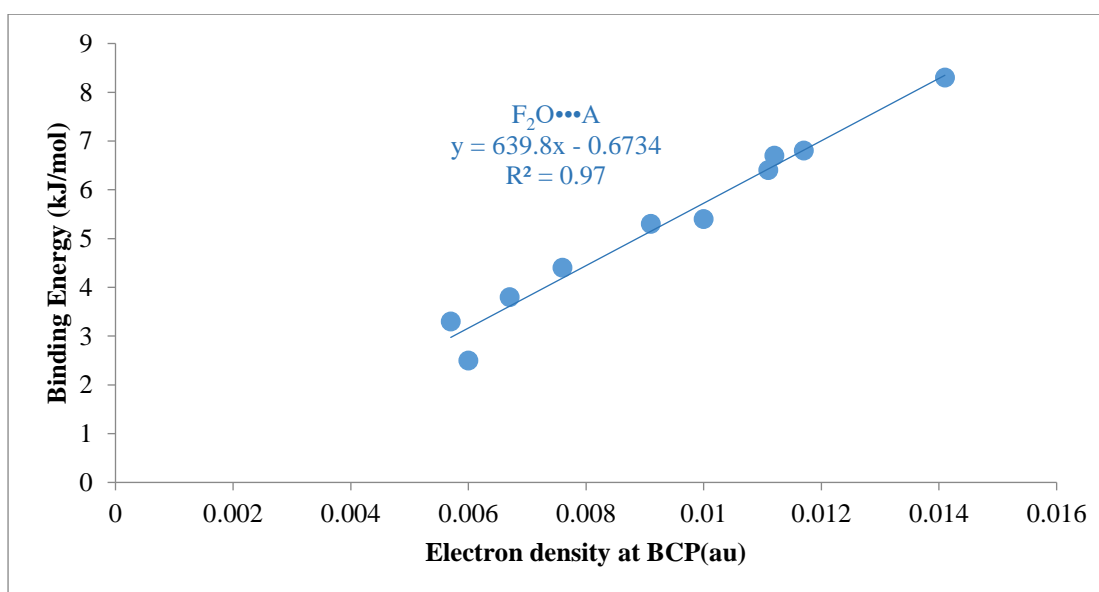*Figure D6.24. Binding energy (kJ/mol) versus electron density at BCP (au) plot for Se-bonded complexes.*

Table D6.25. Electron density at BCP (au) and binding energy (kJ/mol) data for Te-bonded complexes.

Complexes	Electron Density (au)	Binding Energy (kJ/mol)
$F_2Te•••OH_2$	0.0333	38.2
$F_2Te•••SH_2$	0.0242	29
$F_2Te•••C_2H_2$	0.0259	23.8
$F_2Te•••NH_3$	0.0459	60.8
$F_2Te•••O(CH_3)_2$	0.0446	54.3
$F_2Te•••CO$	0.0209	15.7
$F_2Te•••OCH_2$	0.0354	43.4
$F_2Te•••OHCH_3$	0.041	49
$F_2Te•••PH_3$	0.0322	29
$F_2Te•••NCH$	0.0284	31.9
$Cl_2Te•••OH_2$	0.0283	29.7
$Cl_2Te•••SH_2$	0.0206	24.5
$Cl_2Te•••NH_3$	0.0419	49.3
$Cl_2Te•••NCH$	0.0245	26
$Cl_2Te•••CO$	0.0157	12.2
$Cl_2Te••OCH_2$	0.0296	33.7
$Cl_2Te•••C_2H_4$	0.0273	24.6
$Cl_2Te•••OHCH_3$	0.0365	39.3
$Cl_2Te•••PH_3$	0.0258	24.4
$Cl_2Te•••O(CH_3)_2$	0.0407	45.5
$O_2Te•••OH_2$	0.023	20.9
$O_2Te•••SH_2$	0.0119	14.5
$O_2Te•••NH_3$	0.0346	30.2
$O_2Te•••NCH$	0.0132	17
$O_2Te•••CO$	0.007	6.7
$O_2Te••OCH_2$	0.0261	27.2
$O_2Te•••C_2H_4$	0.008	9.9
$O_2Te•••OHCH_3$	0.0335	29.3
$O_2Te•••PH_3$	0.0094	9.6
$O_2Te•••O(CH_3)_2$	0.0363	33.4

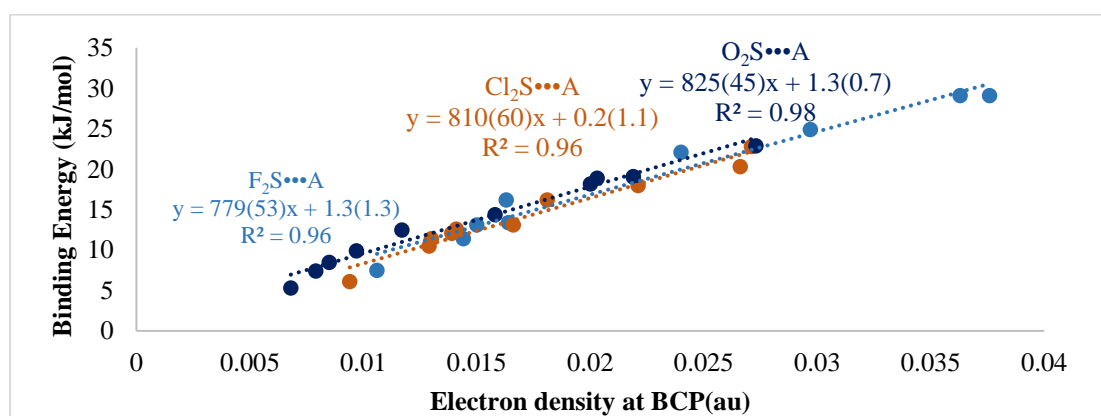*Figure D6.25. Binding energy (kJ/mol) versus electron density at BCP (au) plot for Te-bonded complexes.*

Table D6.26. Electron density at BCP (au) and binding energy (kJ/mol) data for Po-bonded complexes.

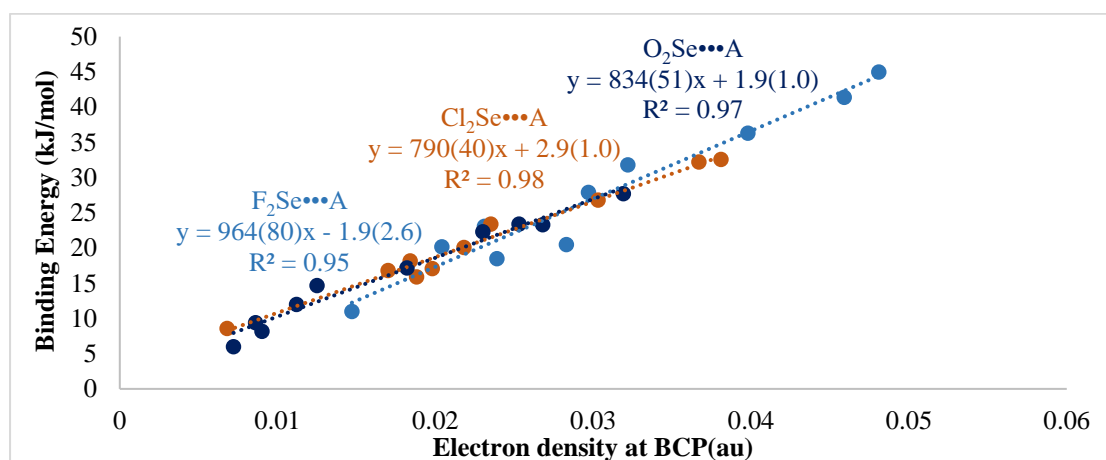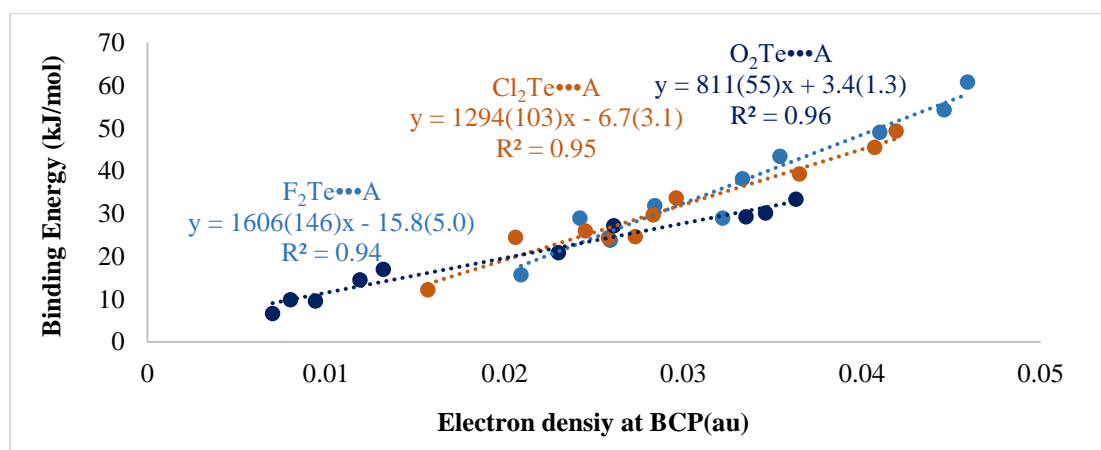| Complexes	Electron Density (au)	Binding Energy (kJ/mol)
$F_2Po•••OH_2$	0.0329	45.6
$F_2Po•••SH_2$	0.0242	35.7
$F_2Po•••NH_3$	0.041	68.4
$F_2Po•••NCH$	0.0287	39.9
$F_2Po•••OCH_2$	0.035	51.6
$F_2Po•••C_2H_2$	0.0281	31.1
$F_2Po••• OHCH_3$	0.039	56.1
$F_2Po•••PH_3$	0.0299	36
$F_2Po•••O(CH_3)_2$	0.0419	60.4
$F_2Po•••CO$	0.0242	21.4
$Cl_2Po•••OH_2$	0.0304	38.8
$Cl_2Po•••SH_2$	0.0229	32.8
$Cl_2Po•••NH_3$	0.0396	59.7
$Cl_2Po•••NCH$	0.0281	35.1
$Cl_2Po•••OCH_2$	0.032	43.2
$Cl_2Po•••C_2H_4$	0.0316	34.2
$Cl_2Po••• OHCH_3$	0.037	49.1
$Cl_2Po•••PH_3$	0.0283	34
$Cl_2Po•••O(CH_3)_2$	0.0403	54.7
$F_2Po•••CO$	0.0211	17.6
$O_2Po•••OH_2$	0.0164	32
$O_2Po•••SH_2$	0.0102	19.4
$O_2 o•••NH_3$	0.0195	33.8
$O_2Po•••NCH$	0.0141	23.1
$O_2Po•••OCH_2$	0.0191	32.2
$O_2Po•••C_2H_4$	0.0098	14.4
$O_2Po••• OHCH_3$	0.0191	35.2
$O_2Po•••PH_3$	0.0112	16.3
$O_2Po•••O(CH_3)_2$	0.023	31.4
$O_2Po•••CO$	0.0092	9.8

Figure D6.26. Binding energy (kJ/mol) versus electron density at BCP (au) plot for Po-bonded complexes

Table D6.27. Electron density at BCP (au) and binding energy (kJ/mol) data for F-bonded complexes.

Complexes	Electron Density (au)	Binding Energy(kJ/mol)
CNF•••OH$_2$	0.0081	5.6
CNF•••SH$_2$	0.0056	3.3
CNF•••NH$_3$	0.0083	6.1
CNF•••NCH	0.0083	6
CNF•••OCH$_2$	0.0065	3.8
CNF•••C$_2$H$_4$	0.0085	6.1
CNF•••OHCH$_3$	0.0064	3.5
CNF•••PH$_3$	0.0092	6.2
CNF•••CO	0.0051	3.2
CNF•••O(CH$_3$)$_2$	0.0054	2
NCF•••OH$_2$	0.0059	4.4
NCF•••SH$_2$	0.0041	2.4
NCF•••NH$_3$	0.0054	4.4
NCF•••NCH	0.0061	4.9
NCF•••FH	0.0054	3.3
NCF•••OCH$_2$	0.0065	4.8
NCF•••C$_2$H$_4$	0.0045	2.5
NCF•••OHCH$_3$	0.0069	4.7
NCF•••PH$_3$	0.0036	2.4
NCF•••CO	0.004	1.7
NCCCF•••OH$_2$	0.0061	4.2
NCCCF•••SH$_2$	0.0045	2.4
NCCCF•••NH$_3$	0.0056	4.1
NCCCF•••NCH	0.0065	4.9
NCCCF••OCH$_2$	0.0071	4.8
NCCCF•••C$_2$H$_4$	0.0049	2.4
NCCCF•••OHCH$_3$	0.0069	4.4
NCCCF•••PH$_3$	0.004	2.3
NCCCF•••CO	0.0045	1.5
NCCCF•••FH	0.006	3.2
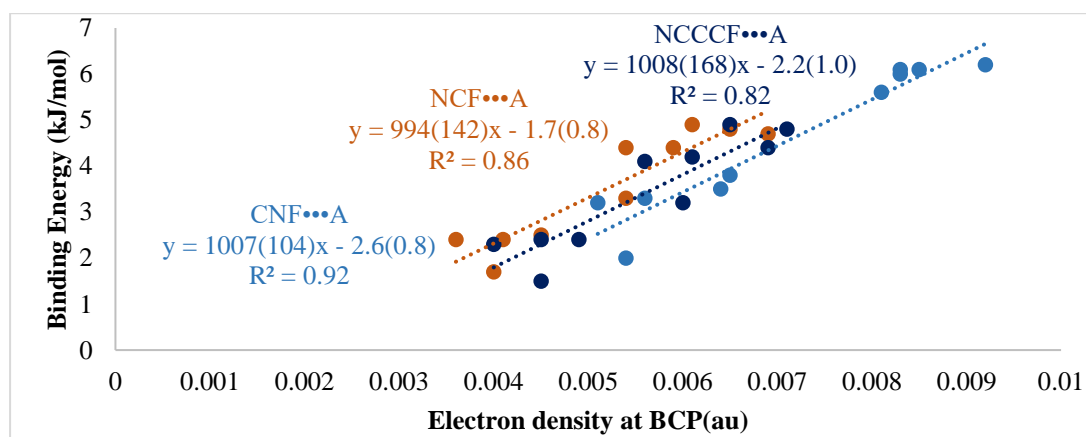
Figure D6.27. Binding energy (kJ/mol) versus electron density at BCP (au) plot for F-bonded complexes.

Table D6.28. Binding energy (kJ/mol) versus electron density at BCP (au) plot for Cl-bonded complexes.

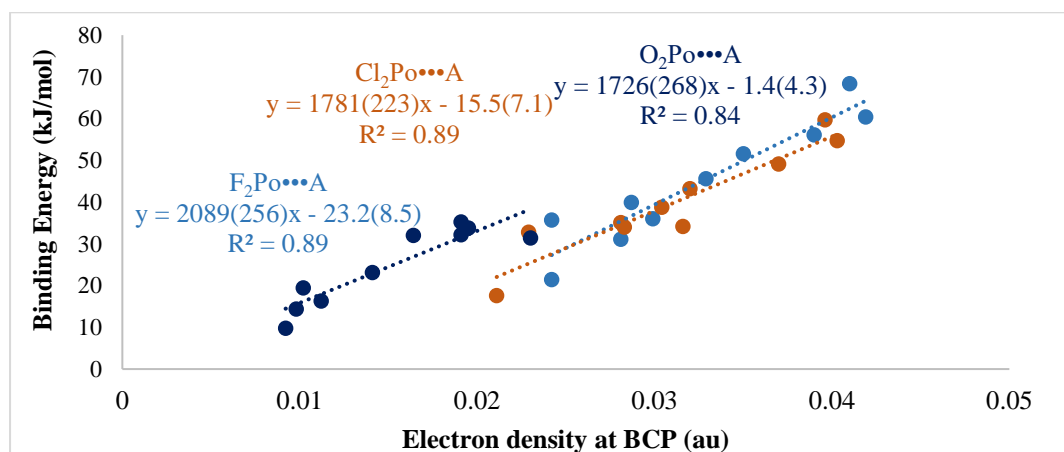| Complexes	Electron Density (au)	Binding Energy (kJ/mol)
$ClCl\cdots OH_2$	0.0167	11.8
$ClCl\cdots SH_2$	0.0158	11
$ClCl\cdots NH_3$	0.0314	20.9
$ClCl\cdots NCH$	0.0154	11.9
$ClCl\cdots CO$	0.0073	5.9
$ClCl\cdots OCH_2$	0.0202	13.5
$ClCl\cdots C_2H_4$	0.0167	12.2
$ClCl\cdots OHCH_3$	0.0225	15.4
$ClCl\cdots FH$	0.0096	5.7
$ClCl\cdots O(CH_3)_2$	0.0284	18.7
$FCl\cdots OH_2$	0.0262	20.9
$FCl\cdots SH_2$	0.0296	20.4
$FCl\cdots NH_3$	0.0566	43.4
$FCl\cdots NCH$	0.0228	20.3
$FCl\cdots CO$	0.0188	11
$FCl\cdots OCH_2$	0.0319	23.3
$FCl\cdots C_2H_4$	0.0304	22
$FCl\cdots OHCH_3$	0.0362	27.5
$FCl\cdots FH$	0.0141	9.5
$FCl\cdots O(CH_3)_2$	0.0451	32.8
$NCCl\cdots OH_2$	0.0118	13.2
$NCCl\cdots SH_2$	0.0085	8.5
$NCCl\cdots NH_3$	0.014	16.6
$NCCl\cdots NCH$	0.0112	13.8
$NCCl\cdots CO$	0.0073	5.8
$NCCl\cdots OCH_2$	0.0137	12.4
$NCCl\cdots C_2H_4$	0.0084	8.6
$NCCl\cdots OHCH_3$	0.0142	14.9
$NCCl\cdots FH$	0.0079	7.5
$NCCl\cdots O(CH_3)_2$	0.017	15.6

Figure D6.28. Binding energy (kJ/mol) versus electron density at BCP (au) plot for Cl-bonded complexes.

Table D6.29. Electron density at BCP (au) and binding energy (kJ/mol) data for Br-bonded complexes.

Complexes	Electron Density (au)	Binding Energy(kJ/mol)
$FBr\cdots OH_2$	0.0309	29
$FBr\cdots SH_2$	0.0328	29.6
$FBr\cdots NH_3$	0.0569	59.5
$FBr\cdots NCH$	0.031	28.9
$FBr\cdots OCH_2$	0.037	31.9
$FBr\cdots C_2H_4$	0.0373	32.6
$FBr\cdots OHCH_3$	0.0418	37.8
$FBr\cdots O(CH_3)_2$	0.0495	44.3
$FBr\cdots FH$	0.0159	12.5
$FBr\cdots CO$	0.0306	17
$ClBr\cdots OH_2$	0.0216	18.4
$ClBr\cdots SH_2$	0.0223	18.1
$ClBr\cdots NH_3$	0.0442	36.3
$ClBr\cdots NCH$	0.021	18.5
$ClBr\cdots OCH_2$	0.0264	20.5
$ClBr\cdots C_2H_4$	0.0246	19.5
$ClBr\cdots OHCH_3$	0.0301	24.1
$ClBr\cdots O(CH_3)_2$	0.0377	28.7
$ClBr\cdots FH$	0.0118	8.4
$ClBr\cdots CO$	0.0152	9.2
$BrBr\cdots OH_2$	0.0193	15.1
$BrBr\cdots SH_2$	0.0195	15
$BrBr\cdots NH_3$	0.0394	29.1
$BrBr\cdots NCH$	0.0191	15.2
$BrBr\cdots OCH_2$	0.0236	17.1
$BrBr\cdots C_2H_4$	0.0217	16.2
$BrBr\cdots OHCH_3$	0.0269	19.9
$BrBr\cdots O(CH_3)_2$	0.0342	24
$BrBr\cdots FH$	0.0106	6.9
$BrBr\cdots CO$	0.0131	7.4

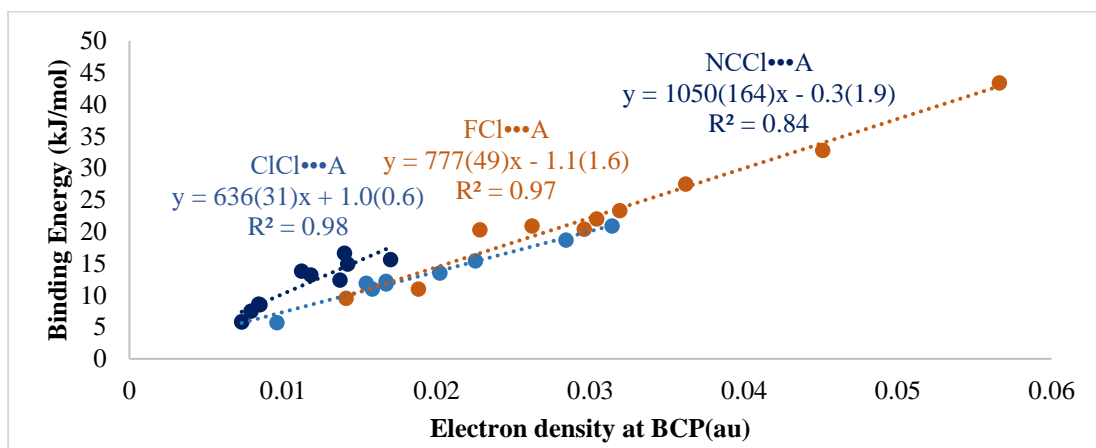Figure D6.29. Binding energy (kJ/mol) versus electron density at BCP (au) plot for Br-bonded complexes.

Table D6.30. Electron density at BCP (au) and binding energy (kJ/mol) data for I-bonded complexes.

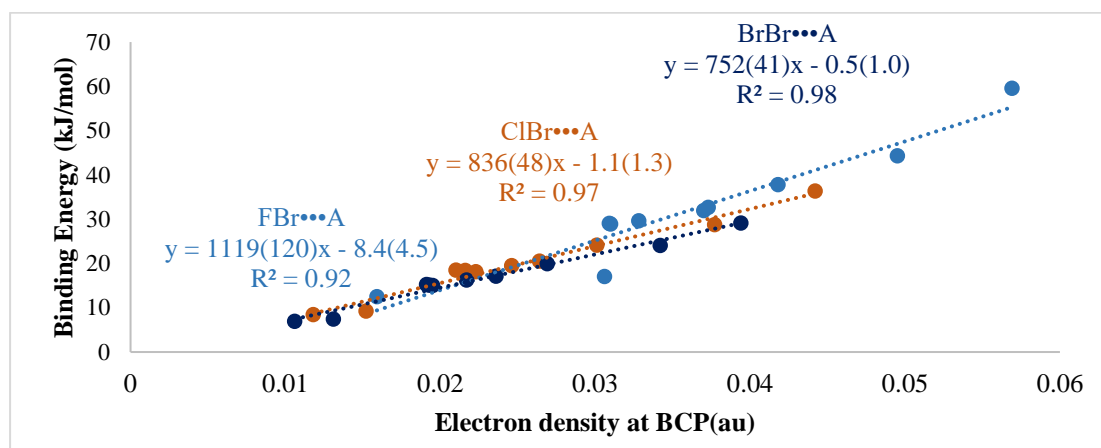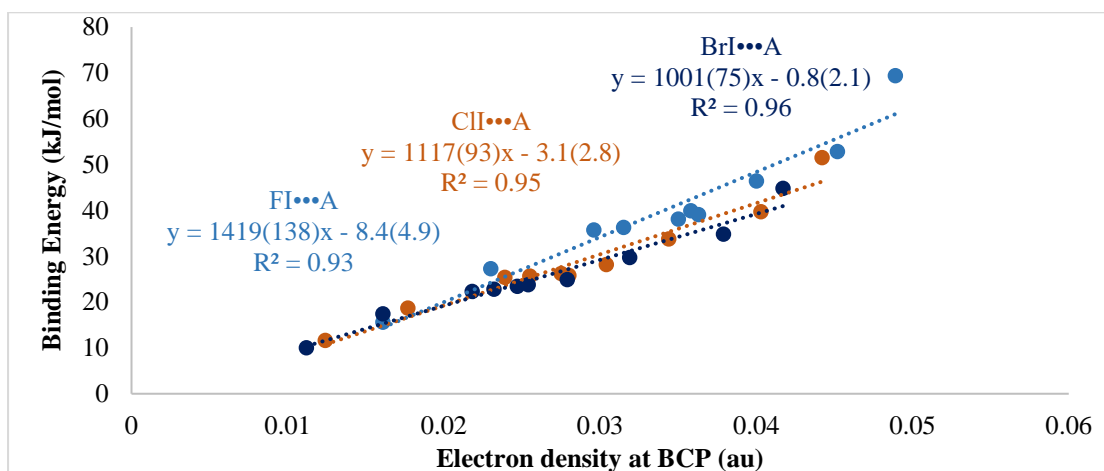| Complexes	Electron Density (au)	Binding Energy (kJ/mol)
$FI\cdots OH_2$	0.0315	36.3
$FI\cdots SH_2$	0.0296	35.7
$FI\cdots NH_3$	0.0489	69.4
$FI\cdots NCH$	0.035	38.1
$FI\cdots OCH_2$	0.0363	39.1
$FI\cdots C_2H_4$	0.0358	39.9
$FI\cdots OHCH_3$	0.04	46.4
$FI\cdots C_2H_2$	0.023	27.3
$FI\cdots O(CH_3)_2$	0.0452	52.8
$FI\cdots FH$	0.0161	15.6
$ClI\cdots OH_2$	0.0255	25.7
$ClI\cdots SH_2$	0.0239	25.4
$ClI\cdots NH_3$	0.0442	51.5
$ClI\cdots NCH$	0.0275	26.2
$ClI\cdots OCH_2$	0.0304	28.2
$ClI\cdots C_2H_4$	0.028	25.8
$ClI\cdots OHCH_3$	0.0344	33.8
$ClI\cdots FH$	0.0124	11.6
$ClI\cdots O(CH_3)_2$	0.0403	39.7
$ClI\cdots C_2H_2$	0.0177	18.7
$BrI\cdots OH_2$	0.0232	22.8
$BrI\cdots SH_2$	0.0218	22.3
$BrI\cdots NH_3$	0.0417	44.8
$BrI\cdots NCH$	0.0247	23.4
$BrI\cdots OCH_2$	0.0279	24.9
$BrI\cdots C_2H_4$	0.0254	23.8
$BrI\cdots OHCH_3$	0.0319	29.7
$BrI\cdots FH$	0.0112	10
$BrI\cdots O(CH_3)_2$	0.0379	34.8
$BrI\cdots C_2H_2$	0.0161	17.4

Figure D6.30. Binding energy (kJ/mol) versus electron density at BCP (au) plot for I-bonded complexes.

Table D6.31. Electron density at BCP (au) and binding energy (kJ/mol) data for At-bonded complexes.

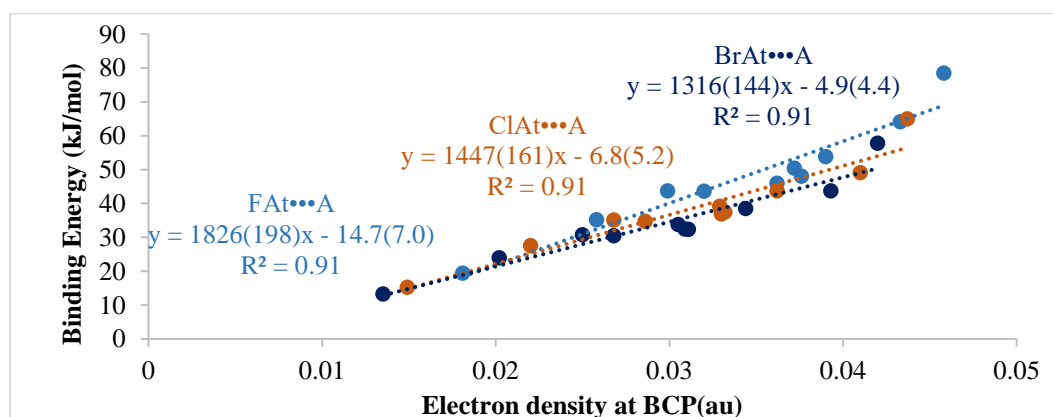| Complexes	Electron Density (au)	Binding Energy (kJ/mol)
$FAt\bullet\bullet\bullet OH_2$	0.032	43.6
$FAt\bullet\bullet\bullet SH_2$	0.0299	43.7
$FAt\bullet\bullet\bullet NH_3$	0.0458	78.5
$FAt\bullet\bullet\bullet NCH$	0.0376	48.1
$FAt\bullet\bullet\bullet OCH_2$	0.0362	46
$FAt\bullet\bullet\bullet C_2H_4$	0.0372	50.4
$FAt\bullet\bullet\bullet OHCH_3$	0.039	53.8
$FAt\bullet\bullet\bullet C_2H_2$	0.0258	35.2
$FAt\bullet\bullet\bullet O(CH_3)_2$	0.0433	64.1
$FAt\bullet\bullet\bullet FH$	0.0181	19.4
$ClAt\bullet\bullet\bullet OH_2$	0.0286	34.7
$ClAt\bullet\bullet\bullet SH_2$	0.0268	35.1
$ClAt\bullet\bullet\bullet NH_3$	0.0437	65
$ClAt\bullet\bullet\bullet NCH$	0.0332	37.5
$ClAt\bullet\bullet\bullet OCH_2$	0.033	36.9
$ClAt\bullet\bullet\bullet\bullet C_2H_4$	0.0329	39.2
$ClAt\bullet\bullet\bullet OHCH_3$	0.0362	43.7
$ClAt\bullet\bullet\bullet C_2H_2$	0.022	27.6
$ClAt\bullet\bullet\bullet O(CH_3)_2$	0.041	49.1
$ClAt\bullet\bullet\bullet FH$	0.0149	15.3
$BrAt\bullet\bullet\bullet OH_2$	0.0268	30.5
$BrAt\bullet\bullet\bullet SH_2$	0.025	30.8
$BrAt\bullet\bullet\bullet NH_3$	0.042	57.8
$BrAt\bullet\bullet\bullet NCH$	0.0309	32.5
$BrAt\bullet\bullet\bullet OCH_2$	0.0311	32.4
$BrAt\bullet\bullet\bullet C_2H_4$	0.0305	33.8
$BrAt\bullet\bullet\bullet OHCH_3$	0.0344	38.5
$BrAt\bullet\bullet\bullet C_2H_2$	0.0202	24
$BrAt\bullet\bullet\bullet O(CH_3)_2$	0.0393	43.7
$BrAt\bullet\bullet\bullet FH$	0.0135	13.3

Figure D6.31. Binding energy (kJ/mol) versus electron density at BCP (au) plot for At-bonded complexes.

This page intentionally left blank

CHAPTER 7

Summary, Conclusion and Outlook

This page intentionally left blank.

Chapter 7: Summary, Conclusion and Outlook

7.1 van der Waals Interaction, Hydrogen bonding and more…

The ideal gas law presumes that molecules have no attractive forces and take up no space. While the presence of the condensed phase conclusively disproves it, van der Waals introduced two constants, *a* and *b*, to account for intermolecular attraction and the limited volume occupied by gaseous molecules. As a result, **all** intermolecular interactions were described as van der Waals interactions. The effective volume occupied by the gases determined van der Waals radii for atoms and molecules. Keesom, Debye and London derived the expression for dipole-dipole, dipole-induced dipole and instantaneous dipole-induced dipole (dispersion) interactions, respectively. Obviously, interactions between permanent multipoles, induction, and dispersion all contribute to all intermolecular interactions. Perhaps there was a lack of chemistry in this scene. Over the last century, physicists and chemists have been captivated by chemical bonds. The notion of a covalent bond was first presented by Langmuir and Lewis. A covalent bond might explain the bond between atoms in a molecule, such as the bond between the O/S atoms and two H atoms in H_2O/H_2S. However, the issue is, does it play any role when H_2O and H_2S condense? The spectroscopy of weakly bound complexes of H_2O and H_2S is vital because it gives information on the nature of the intermolecular interactions present in them.

Water is a high boiling liquid, and H_2S is a stinking gas at ambient conditions. Ice, solid water, has only four neighbours in a loosely packed tetrahedron network. Each oxygen atom is covalently bonded to two hydrogen atoms and 'hydrogen bonded' with two hydrogen atoms from the two neighbouring molecules. On the other hand, hydrogen sulphide has 12 neighbours when it freezes, appearing to have an isotropic interaction. In the first half of the 20th century, these bulk observations led Pauling to conclude that water interacts through hydrogen bonding and H_2S interacts through van der Waals interaction. Since then, chemists/biologists have debated the fundamental physical/chemical interactions leading to hydrogen bonding and van der Waals

interactions. Chapter 3 has provided direct confirmation that $(H_2S)_2$ is hydrogen-bonded, very much like H_2O dimer. This finding enhances our understanding of intermolecular interactions. Our results also show a substantial difference between the $(H_2O)_2$ and $(H_2S)_2$ potential energy surfaces. The dynamics of $(H_2O)_2$ have been thoroughly investigated over several decades. Such detailed investigations on $(H_2S)_2$ are lacking. The present work paved the way for developing more extensive tunnelling routes and the dynamics of such complexes.

To further comprehend H_2O and H_2S complexes, a vast amount of experimental data exploring diverse areas of their potential energy surfaces is required. The obvious next choices are $(H_2O)_3$ and $(H_2S)_3$. However, rotational spectroscopy cannot detect $(H_2O)_3$ and $(H_2S)_3$ complexes due to the zero-dipole moment. The break with axial molecular symmetry allowed us to investigate $(H_2S)_2(H_2O)$ at a level of structural detail that has not yet been possible for $(H_2O)_3$ and $(H_2S)_3$ with rotational spectroscopy. Chapter 4 reports the S-H$\cdots$S, O-H$\cdots$S and S-H$\cdots$O hydrogen-bonded interactions in the complex. This geometry contains numerous characteristics that indicate the cooperative nature of the intermolecular bonding. Rotational spectroscopy has also revealed the information of their internal motion. This study contributes to our understanding of the H_2O/H_2S interactions. The ground has been prepared to search for similar/heavier species.

High-resolution spectroscopic data may be used to validate the correctness of a model intermolecular potential energy hyper-surface. In this regard, we have measured the donor-acceptor interchange tunnelling splitting in the ground vibrational state of $Ar(H_2O)_2$ in Chapter 5. Water dimer is probably the most extensively studied hydrogen bonded system. The ground vibrational state of $(H_2O)_2$ is eight-fold degenerate, and it splits into six levels (A_1, E_1, B_1, A_2, E_2, B_2). The *a*-dipole spectra could be observed for $(H_2O)_2$. The E states of $(H_2O)_2$ gives spectra of the rigid rotor type, and the A and B states give rotational tunnelling spectra. The incorporation of argon (Ar) introduces a new dipole in the system (along the trimer *a*-axis). The $(H_2O)_2$ (dimer) '*a*' axis is the '*b*' axis for the $Ar(H_2O)_2$ (trimer). In the trimer, the '*a*-dipole' transitions appear rigid rotor like for all three tunnelling states, whereas the '*b*-dipole' transitions show tunnelling splitting spectra. Due to the reduced barrier height in $Ar(D_2O)_2$, the three

states, namely A_1, E_1, B_1, could be observed previously. The splitting is measured to be only 106 MHz in $Ar(D_2O)_2$ compared to 1 GHz in $(D_2O)_2$.

On the other hand, the tunnelling splitting in $Ar(H_2O)_2$ could not be observed for several complications. Firstly, only the A_1 & E_1 states are allowed for the $Ar(H_2O)_2$ as the other B_1 state has zero statistical weight. Also, the A_1 state could appear either above or below the E_1 states depending on the K quantum number. Finally, the anticipated splitting in $Ar(H_2O)_2$ is about 4-5 GHz, which is rather large compared to the bandwidth of the Balle-Flygare Fourier transform microwave spectrometer (*BF-FTMW*), which was utilised to identify the transitions. With the help of a four-fold periodic potential, we have accurately predicted the fingerprints of donor-acceptor interchange tunnelling transitions and measured the splitting to be 4257.41(4) MHz in $Ar(H_2O)_2$. A critical structural comparison has been made with $(H_2O)_2$. The result shows the hydrogen bond in $(H_2O)_2$ remains unaffected in $Ar(H_2O)_2$. We anticipate that these findings will spur new theoretical efforts to employ precision spectroscopic data to generate precise intermolecular potentials.

In Chapter 6, we looked have beyond hydrogen bonds and studied the intermolecular bonding for all main group elements. Bader's Atoms in Molecules (AIM) theory helped us in looking at the bonds. The slopes of binding energy versus electron density have assisted in in classifying intermolecular interactions involving all elements and their molecules. This study prompted us to create a Periodic Table of intermolecular bonding. In essence, there are two types of intermolecular bonding: one in which covalent molecules (IMB-C) are engaged and another in which ionic molecules (IMB-I) are involved. The IMB-C includes hydrogen, halogen, chalcogen, pnictogen, tetrel (excluding carbon bonds), and boron bond (but not triel bond). IMB-I contains Lithium, sodium, beryllium, magnesium bonds and triel bonds. The binding energy versus electron density plot of the IMB-C class generally has a low slope, whereas the IMB-I type has a high slope. We have realised carbon is different because it has no low-lying orbital to accept or donate electrons. In simpler terms, carbon bond donors behave like ionic molecules (CH_4 acts as Cl^- K^+) in intermolecular bonding. The electron density

between the two atoms is extremely low for carbon bonds. The binding energy rapidly increases with electron density resulting in a high value of the slope. The hydrogen bond is also unique from the rest of the group members. Hydrogen bond belongs to IMB-C class while its other group members belong to IMB-I class. The slopes of the binding energy versus electron density plots for alkali and alkaline earth metals are comparable. Rather than having two distinct names for each, we propose referring to intermolecular bonding in alkali and alkaline earth metals as 'alkelene bond'.

This Thesis contributes to our fundamental understanding of intermolecular interactions. There has been a lot of confusion in the literature about the physical and chemical forces operating between molecules leading to the formation of condensed phase. We found that there was no consensus on what the terms "van der Waals interaction" and "hydrogen bonding" meant. A combination of rotational spectroscopy and theoretical methods helped us to look deeper into intermolecular bonding. Over the decade, halogen bonding, chalcogen bonding, pnictogen bonding, tetrel bonding (carbon bonding), triel bonding (boron bonding) have all been defined and investigated. We expect that the name "alkelene bond" will be recognised and attract a lot of attention in the near future.

APPENDIX

A Model Calculation with Periodic Potential

1

This page intentionally left blank

Appendix: A Model Calculation with Periodic Potential

A.1 Introduction

The century-old hydrogen bond has been gone through extensive debate about its definition, existence, and nature. IUPAC proposed the current definition as 'The hydrogen bond[1,2] is an attractive interaction between a group X–H and an atom or group of atoms Y in the same or different molecule(s), where there is evidence of bond formation'. The hydrogen bonds, typically denoted by X–H···Y, X, and Y, was initially observed to be only the most electronegative elements. However, it has been demonstrated that X may be any element with an electronegativity greater than that of H, and acceptor Y can be a lone pair, π-pair, an unpaired electron, sigma bonding electrons, and so on. There has been extensive effort to characterise hydrogen bonds in molecular entities both theoretically and experimentally. Red shift in X-H stretching frequencies, sum of the van der Waals radii of H and Y, linearity of the bond, etc., have been used widely to acknowledge the presence of hydrogen bond. Interestingly, all these criteria have well-reported anomalies and limitations[3], highlighting the uniqueness of hydrogen bonds. Theoretically, often hydrogen bonds were characterised using electron density topology studies[4]. Recently, Goswami and Arunan[5], proposed a criterion that helps us to understand the hydrogen bond formed in the weakly bound complex in the supersonic beam. According to the requirements, for a hydrogen-bonded complex, 'the zero-point energy along any large-amplitude vibrational coordinate that destroys the orientational preference for the hydrogen bond should be significantly below the barrier along that coordinate so that there is at least one bound level'. Extensive calculation on Ar_2-H_2O, Ar_2-H_2S, C_2H_4-H_2O, C_2H_4-H_2S showed that Ar_2-H_2O and Ar_2-H_2S are not hydrogen-bonded complexes but C_2H_4-H_2O, C_2H_4-H_2S complexes are. It should be emphasised that, the barrier is not related to the dissociation energy of the complexes. These large amplitude motions present in the weakly bound

molecules have periodic potentials along the vibrational coordinate that do not lead to dissociation.

In this Appendix, we have taken a model of the one-dimensional periodic potential to calculate the wavefunction and the probability density at a particular region associated with each torsional level. To find out the torsional energy levels of the molecule, we need to solve the Schrödinger wave equation. In the recent past, there have been few attempts to provide an analytic solution of a torsional Schrödinger wave equation with periodic potential[6,7]. Also, there are several numerical methods available as a solution to the problem[8]. Mathieu's tables for the internal rotation were available for understanding the spectra[9,10]. These tables were obtained from the solution of Mathieu's differential equation. Here the coupling of the angular momenta of internal and overall rotation was treated as a perturbation[11,12,13]. Laane and co-workers[14,15] have developed a computer program to solve the one-dimensional Schrödinger equation with periodic potential. This method is quite general as many potential terms could be used with different barrier heights. We used this approach to compute energy levels and wavefunctions for the periodic potential function. The probability density has been calculated "inside" and "outside" the well. An exciting result has been obtained when the probability densities are plotted with the increasing energy levels. We found a distinct preference for the wavefunction to be confined inside the well for energy levels below the barrier height. However, before complete delocalisation, the energy levels immediately above the barrier demonstrate a predilection for the edge of the well. This phenomenon is more pronounced for the large barrier and small internal rotational constant. This observation leads us to conclude that even if the energy of the molecule along any vibrational coordinate is slightly above the barrier, the molecule still felt the potential and have some finite probability of being hydrogen-bonded. Figure A.1 shows two potential wells, on the left-hand side the criteria proposed by Goswami and Arunan[5] and on the right the result from the current study. Noteworthy, localisation problem in a periodic potential (quasi-periodic potential) has been reported in literature[16,17].
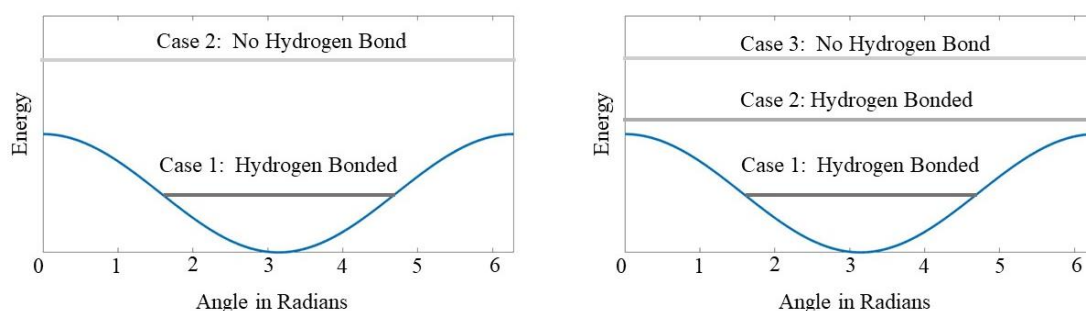
Figure A.1. Representative periodic potential showing the effect of zero-point motion on the equilibrium structure of a hydrogen-bonded complex. On the left: The criterion proposed by Goswami et al[5]. On the right: Slightly modified criterion proposed from current probability density analysis.

A.2 **Methodology and Two Test Cases**

We have obtained the torsional energy levels, wavefunction, and probability density by solving the Schrödinger equation. The wave equation for 1-D Schrödinger equation is given by,

$$-B\frac{d^2\psi}{d\varphi^2} + V\psi = E\psi \qquad (1)$$

$$\text{where,} \quad V = \frac{1}{2}V_n(1 - \cos n\varphi) \qquad (2)$$

and B is the internal rotation (or pseudorotation) constant, ϕ is the phase angle, and V_n is an n-fold barrier. In this equation, if V is large, the internal rotation will be restricted to small oscillations about the minimum, and the solutions are similar to the harmonic oscillator. On the other hand, for small V, the molecule becomes a free rotor. To solve for the energy levels and wavefunctions at the intermediate barrier height, a Hamiltonian can be set up in the representation of the free rotor.

$$\psi_m = \frac{1}{\sqrt{2\pi}} e^{im\varphi} \ldots\ldots\ldots m = 0, \pm 1, \pm 2, \ldots\ldots \tag{3}$$

The basis could be expressed using cos and sin bases to preserve even and odd symmetry.

$$\psi_n^{even} = \frac{1}{\sqrt{\pi}} \cos n\varphi \ldots\ldots\ldots n = 1, 2, \ldots\ldots$$

$$\psi_0^{even} = \frac{1}{\sqrt{2\pi}}$$

$$\psi_n^{odd} = \frac{1}{\sqrt{\pi}} \sin n\phi \ldots\ldots\ldots n = 1, 2, \ldots\ldots \tag{4}$$

The elements of the $N \times N$ Hamiltonian, N is being the number of basis functions was determined using the relation,

$$H_{kl} = \int \psi_k^* H' \psi_l d\varphi \tag{5}$$

$$\text{where } H' \psi = \lambda \psi \text{ and } \lambda = \frac{E}{B_0}. \tag{6}$$

Diagonalisation of the matrix gives both the eigenvalues and wavefunctions (eigenfunctions). The wavefunctions are provided by

$$\psi_v = \sum_i^N t_{iv} \psi_i \tag{7}$$

Where t_{iv} are the coefficients of the ψ_i

A.2.1 Matrix Elements

Laane and coworkers[14] tabulated the matrix elements. We tabulate these elements in this appendix again for convenience (Table A.1). The cosine matrix elements have been given (Table A.2). Similarly, the sine matrix elements can be calculated[15]. We have utilised MATLAB 2020A to calculate the matrix elements. The Jacobi diagonalisation with Rutishauser's modifications was used to obtain the eigenvalues and eigenfunctions.

Appendix: A Model Calculation with Periodic Potential

Table A.1. Matrix elements of the even and odd block for periodic potential.

Elements of the even (cos) block

$$<m'|H|m> = (m^2+S_T)\delta_{m,m'} - \frac{1}{2}\sum_{n=1}^{6} S_n(\delta_{m'+m,n}+\delta_{|m'-m|,n}) + \frac{1}{2}mm'\sum_{l=1}^{3} B'_l(-\delta_{m'+m,l}+\delta_{|m'-m|,l})$$

$$m' = 0,1,2,3....\ \&\ m = 0,1,2,3$$

$$\text{for } \langle 0|H|m\rangle = \langle m'|H|0\rangle = -\frac{1}{\sqrt{2}}\sum_{n=1}^{6} S_n\delta_{m'+m,n}$$

Elements of the odd (sin) block

$$<m'|H|m> = (m^2+S_T)\delta_{m,m'} + \frac{1}{2}\sum_{n=1}^{6} S_n(\delta_{m'+m,n}-\delta_{|m'-m|,n}) + \frac{1}{2}mm'\sum_{l=1}^{3} B'_l(\delta_{m'+m,l}+\delta_{|m'-m|,l})$$

$$m' = 0,1,2,3....\ \&\ m = 0,1,2,3$$

$$\text{Here } S_n = \frac{V_n}{2B_0} \quad S_T = \sum_{n=1}^{6} S_n \quad B'_n = \frac{B_n}{B_0}$$

Table A.2. Matrix elements of the even (cos) block for periodic potential.

S_T	$-\frac{S_1}{\sqrt{2}}$	$-\frac{S_2}{\sqrt{2}}$	$-\frac{S_3}{\sqrt{2}}$	$-\frac{S_4}{\sqrt{2}}$	$-\frac{S_5}{\sqrt{2}}$	$-\frac{S_6}{\sqrt{2}}$	0
$-\frac{S_1}{\sqrt{2}}$	$1^2+S_T-\frac{S_2}{2}$	$-\frac{(S_1+S_3)}{2}$	$-\frac{(S_2+S_4)}{2}$	$-\frac{(S_3+S_5)}{2}$	$-\frac{(S_4+S_6)}{2}$	$-\frac{S_5}{2}$	$-\frac{S_6}{2}$
$-\frac{S_2}{\sqrt{2}}$	$-\frac{(S_1+S_3)}{2}$	$2^2+S_T-\frac{S_4}{2}$	$-\frac{(S_1+S_5)}{2}$	$-\frac{(S_2+S_6)}{2}$	$-\frac{S_3}{2}$	$-\frac{S_4}{2}$	$-\frac{S_5}{2}$
$-\frac{S_3}{\sqrt{2}}$	$-\frac{(S_2+S_4)}{2}$	$-\frac{(S_1+S_5)}{2}$	$3^2+S_T-\frac{S_6}{2}$	$-\frac{S_1}{2}$	$-\frac{S_2}{2}$	$-\frac{S_3}{2}$	$-\frac{S_4}{2}$
$-\frac{S_4}{\sqrt{2}}$	$-\frac{(S_3+S_5)}{2}$	$-\frac{(S_2+S_6)}{2}$	$-\frac{S_1}{2}$	3^2+S_T	$-\frac{S_1}{2}$	$-\frac{S_1}{2}$	$-\frac{S_3}{2}$
$-\frac{S_5}{\sqrt{2}}$	$-\frac{(S_4+S_6)}{2}$	$-\frac{S_3}{2}$	$-\frac{S_2}{2}$	$-\frac{S_1}{2}$	4^2+S_T	$-\frac{S_1}{2}$	$-\frac{S_2}{2}$
$-\frac{S_6}{\sqrt{2}}$	$-\frac{S_5}{2}$	$-\frac{S_4}{2}$	$-\frac{S_3}{2}$	$-\frac{S_2}{2}$	$-\frac{S_1}{2}$	5^2+S_T	$-\frac{S_1}{2}$
0	$-\frac{S_6}{2}$	$-\frac{S_5}{2}$	$-\frac{S_4}{2}$	$-\frac{S_3}{2}$	$-\frac{S_2}{2}$	$-\frac{S_1}{2}$	6^2+S_T

A.2.2 Case 1: Calculation of the Energy Levels and the Wavefunctions

We begin by attempting to reproduce a test case described by Laane and coworkers[14] and then examine the overall trend of the solution. We have used similar values for V_3 =100 cm^{-1} and $\boldsymbol{B}$=1.0 cm^{-1} to reproduce the energy levels and wavefunctions with 20 basis functions (Figure A.2). The eigenvalues for the wave equations are given in Table A.3 and pictorially depicted in Figure A.2. The wavefunctions obtained from the eigenvectors are plotted in Figure A.3. The coefficients (t_{iv}) smaller than 10^{-4} are not considered for calculating wavefunction. These small values do not impose any considerable change on the result. For an infinite barrier with three-fold potential, each torsional state is three-fold degenerate. The internal rotation is restricted to small oscillations in any one of the three equivalent potential wells. Whereas, for a finite barrier (as our current model), quantum mechanical tunnelling becomes feasible, leading to the splitting of the three-fold degeneracy. These are purely quantum effects that allow the molecule to convert from one configuration to the other. From the eigenvalues in Table A.3 (also Figure A.2), it is evident that the quantum mechanical tunnelling effect leads to the splitting of triply degenerate torsional level into two levels, a nondegenerate level designated as an A level and a doubly degenerate level designated as an E level.
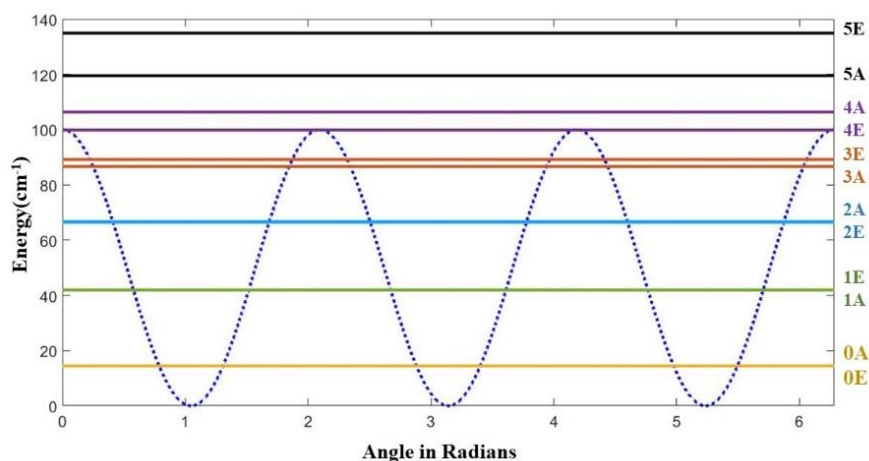

Figure A.2 Three-fold potential and energy levels (Only the first few energy levels are shown in the diagram). The energy values are given in Table A.3. Reproduced results from reference 14, figure 2.

*Table A.3. Energy level values for a three-fold potential term $V_3=100$ cm^{-1}, **B**=1.0 cm^{-1}. Values are in cm^{-1}.*

| Levels	Eigenvalues	Levels	Eigenvalues
0_A	14.4136597159937	0_E	14.4182275191760
0_E	14.4182275191760	1_E	41.9419549225863
1_E	41.9419551518163	1_A	41.9587889143474
2_A	66.4132961496408	2_E	66.7033064613649
2_E	66.7033081847880	3_E	86.6622281290002
3_E	86.6622355260075	3_A	89.1804998386363
4_A	99.8456668125753	4_E	106.368964844703
4_E	106.368968308599	5_E	119.531299635647
5_E	119.531442944688	5_A	134.907811973345
6_A	135.367587811082	6_E	153.278300163897
6_E	153.278300176604	7_E	173.674353702106
7_E	173.679428205029	7_A	196.231278049212
8_A	196.233596906804	8_E	220.891212518324
8_E	220.891212518327	9_E	247.623940757609
9_E	247.823252638209	9_A	276.578466259793
10_A	276.578469834221	10_E	307.379700730756
10_E	307.379700730756	11_E	345.518537210018
11_E	345.518537210018	11_A	380.143154964666
12_A	380.143154966502	12_E	416.807998689165
12_E	416.807998689165	13_A	455.506996892645
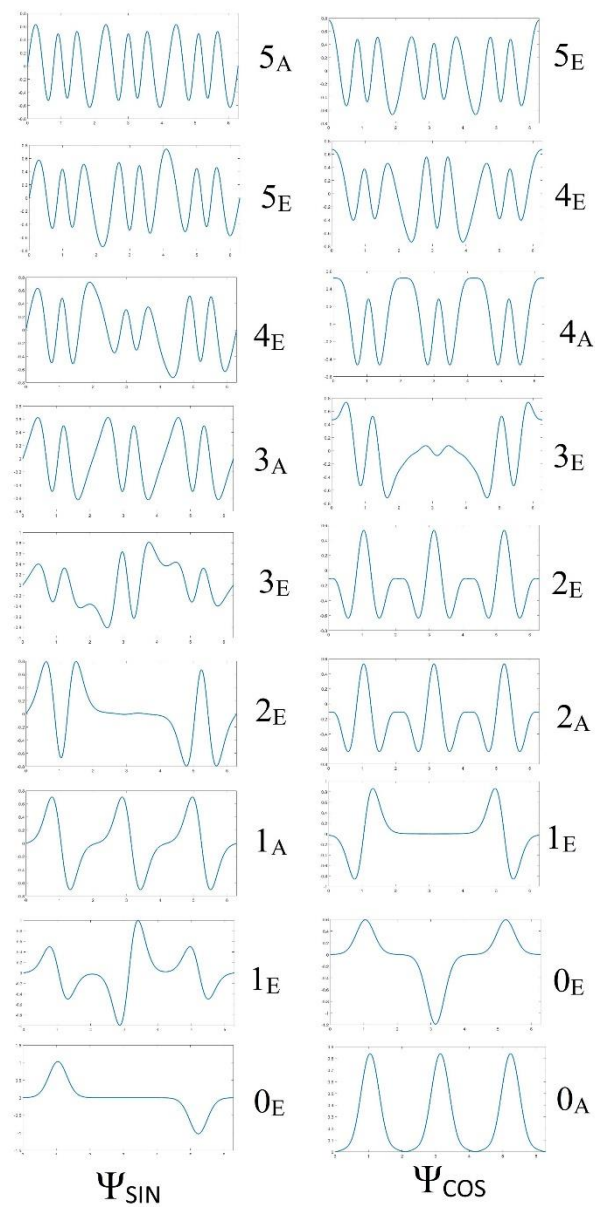
Figure A.3. Wavefunctions (even and odd block) for a three-fold potential. Reproduced results from reference 14, figure 2.

A.2.3 Case 2: $(H_2O)_2$ and $(D_2O)_2$ Donor-Acceptor Interchange Level

Another application of solving the Schrödinger equation with periodic potential is to theoretically evaluate tunnelling splitting observed in the spectra of weakly bound complexes[18,19]. As discussed in Chapter 5, donor-acceptor interchange tunnelling in $(H_2O)_2$ and $(D_2O)_2$ dimers are ~22.6 GHz[20] and ~1 GHz[21], respectively. For simulating all the torsional energy levels for $(H_2O)_2$ and $(D_2O)_2$, a four-fold potential was used[22]. It was observed that the barrier and internal rotational constant mentioned in Table A.4 reproduce the observed donor-acceptor tunnelling splitting in $(H_2O)_2$ and $(D_2O)_2$[23]. Table A.5 and Table A.6 list the torsional levels for $(H_2O)_2$ and $(D_2O)_2$.

Table A.4. Following barrier and internal rotation constants were used to reproduce the experimentally observed tunnelling splitting in $(H_2O)_2$ and $(D_2O)_2$.

	V_4 (cm^{-1})	B (cm^{-1})
$(H_2O)_2$	437	7.26
$(D_2O)_2$	402	3.635

Table A.5. Energy levels due to donor-acceptor interchange tunnelling in $(H_2O)_2$. Values are in cm^{-1}.

Even Levels	Energy Values	Odd Levels	Energy Values
1A	104.4023426	1E	104.794688
1E	104.794688	1B	105.1722059
2A	287.9819622	2E	294.4067024
2E	294.4067024	2B	302.2638695
3A	411.7927214	3E	438.3881821
3E	438.3881821	3B	487.342132
4A	522.7450285	4E	593.8155369
4E	593.8155369	4B	694.9673121
5A	699.5282408	5E	817.4238306
5E	817.4238306	5B	953.0096501
6A	953.2936696	6E	1104.033492

Continued Table A.5…

6E	1104.033492	6B	1269.83409
7A	1269.845001	7E	1450.439707
7E	1450.439707	7B	1645.753345
8A	1645.753632	8E	1855.72841
8E	1855.72841	8B	2080.328863
9A	2080.328868	9E	2319.52992
9E	2319.52992	9B	2573.313649

Table A.6. Energy levels due to donor-acceptor interchange tunnelling in $(D_2O)_2$. Values are in cm^{-1}.

Even Levels	Energy Values	Odd Levels	Energy Values
1A	72.59823	1E	72.61859
1E	72.61859	1B	72.63815
2A	208.4326	2E	209.028
2E	209.028	2B	209.6404
3A	318.4173	3E	324.1618
3E	324.1618	3B	331.5838
4A	394.1183	4E	413.6133
4E	413.6133	4B	448.3472
5A	467.7735	5E	514.7594
5E	514.7594	5B	578.1744
6A	580.8292	6E	652.9844
6E	652.9844	6B	734.4136
7A	734.612	7E	823.8222
7E	823.8222	7B	920.7446
8A	920.7545	8E	1025.196
8E	1025.196	8B	1137.096
9A	1137.096	9E	1256.405
9E	1256.405	9B	1383.092

For $(H_2O)_2$, the E states show the semi-rigid rotor spectra, whereas A and B show the rotational tunnelling spectra. The tunnelling splitting is 0.76 cm^{-1} (22.6 GHz) due to the energy difference between the 1A and 1B states. We have labelled 1A, 1E, and 1B states are as A_1^+, E_1^+, B_1^+ respectively for the consistency with water dimer energy level notation[24] in Figure A.4. Similarly, for $(D_2O)_2$, dimer tunnelling splitting was calculated as 0.39 cm^{-1} (1169 MHz).
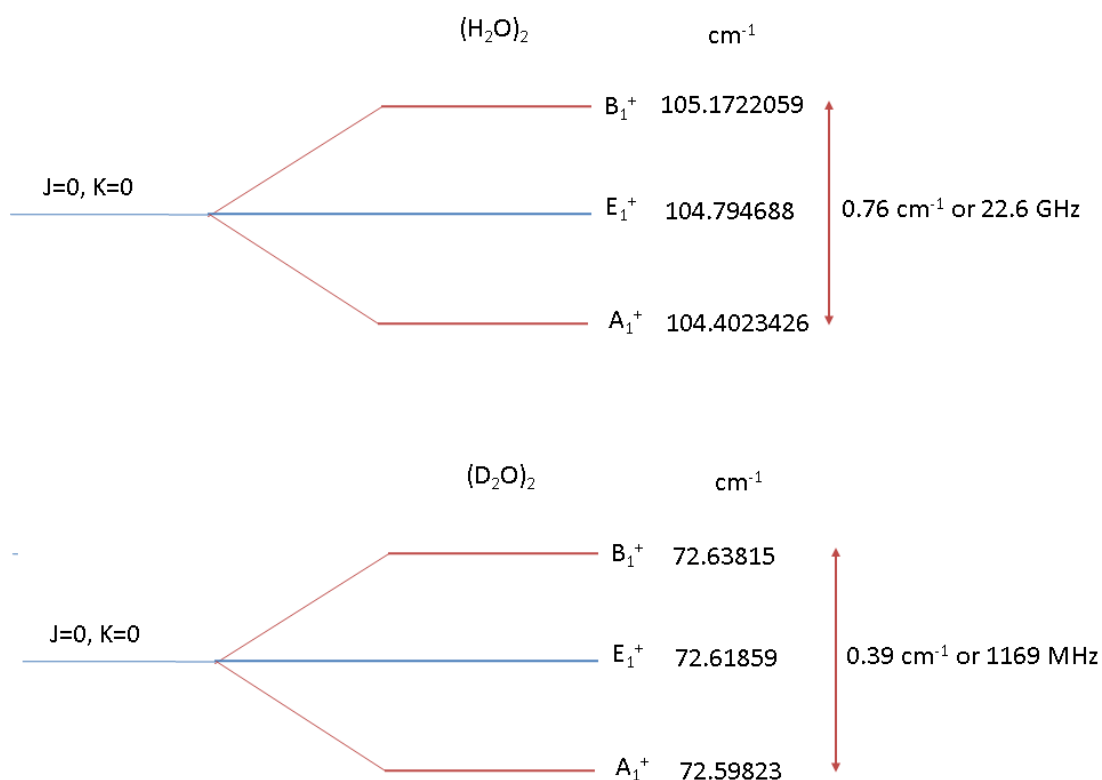

Figure A.4. Splitting due to donor-acceptor interchange tunnelling in $(H_2O)_2$ and $(D_2O)_2$. Values are in cm^{-1}.

A.2.4 Mathieu's Differential Equation

So far, we have used the methodology provided by Laane and coworkers[14] to calculate the energy levels. Similarly, energy levels corresponding to the periodic potential functions could be determined by solving Mathieu's differential equation.

$$y'' + (b - s\cos^2 x)y = 0 \qquad (8)$$

Now the parameters of the equation are related to the above equation (1) by,

$$V_n = \frac{n^2 \boldsymbol{B} s}{4}, E = \frac{n^2 \boldsymbol{B} b}{4}, 2x = n\varphi + \pi, y = \Psi. \tag{9}$$

The values of b were listed in Mathieu's table[2] for corresponding values of s. For a particular V_n, if $\boldsymbol{B}$, is known we can determine the energy levels. The values calculated from the free rotor basis and Mathieu's differential equation are identical to each other.

A.3 Results and Discussion

After reproducing some of the results from previous calculations, we have looked at these periodic potentials to understand the large amplitude motion in weakly bound complexes. We have primarily used two-fold periodic potential to calculate its energy levels and wavefunctions. The wavefunctions are further used to calculate the probability density. We have calculated probability density inside and outside the potential well for different values of potential (V_2=1000 cm^{-1}, 100 cm^{-1}, 10 cm^{-1}), reduced rotation constant ($\boldsymbol{B}$=5 cm^{-1}, 1 cm^{-1}). It is difficult to define the "inside" and "outside" of the well for these periodic potentials. We have defined well at different percentages of the potential (80%, 70 %, 60%, 50% of energy) with a bit of arbitrariness. The results are discussed in the following section.

A.3.1 Definition of Well

As mentioned earlier, it is tricky to define the inside and outside of a well for a periodic potential. Potential well defined at the different energy percentages to the total energy. A typical example has been shown in Figure A.5 with $V_2=100$ cm^{-1}. The "inside of the well" is designated by Region 2 and Region 2′, defined at 80% of the total energy. Similarly, "outside of the well" is defined by Region 1, Region 1', and Region 3.

It should be emphasised that the energy levels ranging from 80 to 100 % are a little arbitrarily referred to as "outside the well" by our definition, despite the fact that they are inside the well. These definitions are used to integrate the probability density in a given region, and the results are unaffected by them.
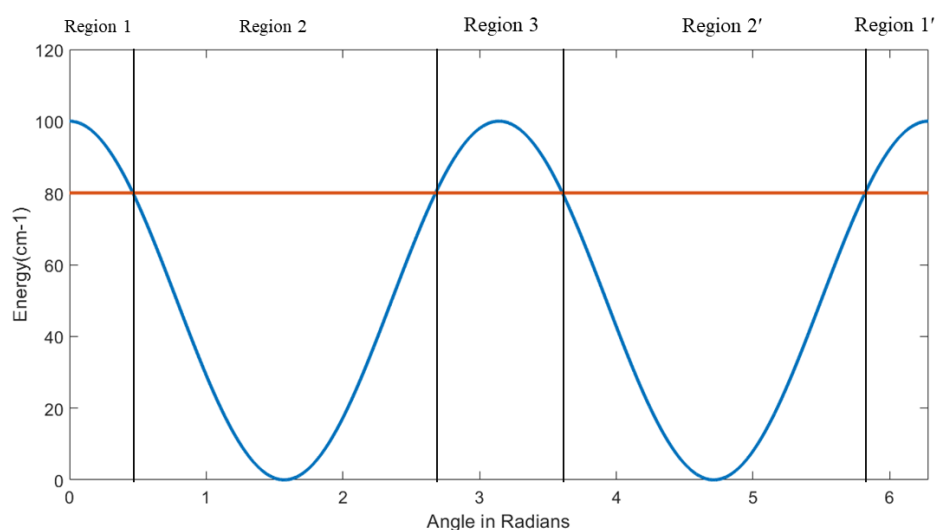

Figure A.5. Potential well defined at 80% of the energy of a two-fold potential. Region 2 and Region 2 ' have been described as the "inside the well". Region 1, Region 1', Region 3 have been defined as the "outside the well".

Similarly, Figure A.6 shows a three-fold potential. Region 2, 2' and 2" have been defined as the 'inside' and the other regions as 'outside' the well. Any energy below 100 cm^{-1} is termed 'Below the Barrier,' and above 100 cm^{-1} is termed 'Above the

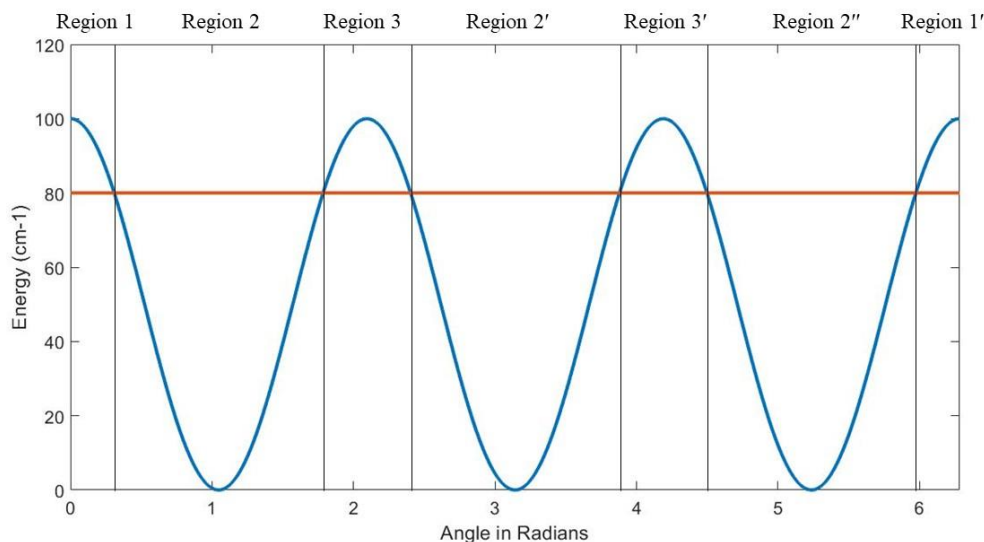Barrier.' Also, the calculations are performed by taking 70%, 60%, and 50% of the energy.

Figure A.6. Potential well defined at 80% of the energy of a three-fold potential. Region 2, Region 2', and Region 2" have been described as the "inside the well." Region 1, Region 1', Region 3, and Region 3' have been defined as the "outside the well."

A.3.2 Calculation of the Wavefunction and the Probability Density

Diagonalising the matrix (see Table A.7 and Table A.8) yields eigenvectors, which are utilised to compute the wavefunctions. Wavefunctions (ψ_v) are calculated separately for even and odd energy levels (equation 7). A typical eigenvector matrix (with five eigenvectors) for the odd and even block has been given for V_2=100 cm^{-1} and $B = 1.0$ cm^{-1} (see Table A.9 and Table A.10). The first five wavefunctions for the odd and even levels are provided in Table A.11 and Table A.12. The probability density for a particular region has been calculated by squaring the normalised wavefunction and integrating it with the appropriate range (see Table A.13 and Table A.14). The probability density for the odd and even levels are plotted with the increasing energy levels in Figure A.7 and Figure A.8. All the energy levels are

plotted in Figure A.9. The first four energy levels (0, 1, 2, 3) wavefunction are entirely localised in the two well. From the 4th energy level, probability inside the well (Region 2+Region 2') slowly decreases from 100%. At the 10th and 11th levels, which are at 90.1 and 91.8 cm^{-1} energy, probability density inside the well drops to 61.8 % and 76.6 %. At higher energy, wavefunction tends to localise at the side of the well. The way we have defined the well, a significant wavefunction remains outside the well for the energy levels above 80 cm^{-1}. The 9th energy level has the energy 78.1 cm^{-1}, and the 10th and 11th levels appear above 80 cm$^{-1,}$ which is the reason for the drastic decrease of probability density inside the well.

The 12th energy level appears just below the well (99.0 cm^{-1}), and a drastic decrease of the probability has been observed in Region 2 and Region 2'. All the energy levels from the 13th level have higher energy than the barrier and are expected to be delocalised irrespective of the integration region. The delocalisation value for a region was derived by dividing the integration limit for that region by 2π (whole region). The delocalisation values for 'inside the well' (Region 2+ Region 2') and 'outside the well' (Region 1+ Region 3+ Region 1') are calculated to be 70.6% and 29.4%, respectively. Surprisingly, the result shows that the wavefunction of energy levels above the barrier does not immediately delocalised. The wavefunction tends to localise at the side of the well, even above the barrier. This phenomenon continued for a few more energy levels before it was entirely delocalised. The consequence of this phenomenon would be necessary for hydrogen bonding in weakly bound molecules. The molecules with the energy just above the barrier are still under some influence of the potential. Hence, the complex can be hydrogen-bonded even if the zero-point energy along any large-amplitude vibrational coordinate lies just above the potential barrier. For a significantly high zero-point energy compared to the potential barrier, the molecule would not have any hydrogen bond.

Table A.7. Matrix Elements for the even levels (only 10*10 matrix is shown, for calculation we have taken a 50*50 matrix).

-50	0	35.35	0	0	0	0	0	0	0
0	-24	0	25	0	0	0	0	0	0
35.35	0	-46	0	25	0	0	0	0	0
0	25	0	-41	0	25	0	0	0	0
0	0	25	0	-34	0	25	0	0	0
0	0	0	25	0	-25	0	25	0	0
0	0	0	0	25	0	-14	0	25	0
0	0	0	0	0	25	0	-1	0	25
0	0	0	0	0	0	25	0	14	0
0	0	0	0	0	0	0	25	0	31

Table A.8. Matrix Elements for the odd levels (only 10*10 matrix is shown, for calculation we have taken a 50*50 matrix)

-74	0	25	0	0	0	0	0	0	0
0	-46	0	25	0	0	0	0	0	0
25	0	-41	0	25	0	0	0	0	0
0	25	0	-34	0	25	0	0	0	0
0	0	25	0	-25	0	25	0	0	0
0	0	0	25	0	-14	0	25	0	0
0	0	0	0	25	0	-1	0	25	0
0	0	0	0	0	25	0	14	0	25
0	0	0	0	0	0	25	0	31	0
0	0	0	0	0	0	0	25	0	50

Table A.9. Eigenvector for the even block (cos block) with $V_2=100$ cm^{-1} and $B=1.0$ cm^{-1}.

0.6077	0	-0.4680	0	-0.4724
0	-0.3913	0	-0.5186	0
-0.6920	0	0.0466	0	-0.3716
0	0.7405	0	0.2704	0
0.3656	0	0.6477	0	0.3142
0	-0.5067	0	0.5615	0
0.1306	0	-0.5524	0	0.5199
0	0.1981	0	-0.5407	0
0.0328	0	0.2256	0	-0.4847
0	-0.0506	0	0.2179	0
-0.0060	0	-0.0569	0	0.1818
0	0.0091	0	-0.0524	0
$<10^{-3}$	0	0.0098	0	-0.0404
	$<10^{-3}$	0	0.0086	0
-	-	-0.0012	0	0.0061
		$<10^{-3}$	-0.0010	0
		-	0	$<10^{-3}$
			$<10^{-3}$	
				-
			-	

Table A.10. Eigenvectors for the even block (sin block) with $V_2=100$ cm^{-1} and $B=1.0$ cm^{-1}.

0.8140	0	0.4796	0	0.3012
0	0.6574	0	0.6185	0
-0.5923	0	0.3928	0	0.6272
0	-0.6657	0	0.2223	0
0.2289	0	-0.6763	0	0.1771

Continued A.10…

0	0.3362	0	-0.6453	0
-0.0682	0	0.3787	0	-0.6055
0	-0.1051	0	0.3717	0
0.0145	0	-0.1193	0	0.3300
0	0.0224	0	-0.1132	0
-0.0023	0	0.0247	0	-0.0933
0	-0.0034	0	0.0222	0
		-0.0036	0	0.0169
			-0.0031	0
				-0.0022

Table A.11. First five wavefunctions for even (cos) energy levels.

$\psi_0^e = \frac{1}{\sqrt{2\pi}}[0.6077]\cos(0)+\frac{1}{\sqrt{\pi}}\{[-0.6920]\cos(2x)+[0.3656]\cos(4x)+[-0.1306]\cos(6x)+[0.0328]\cos(8x)\}$

$\psi_2^e = \frac{1}{\sqrt{\pi}}\{[-0.3913]\cos(x)+[0.7405]\cos(3x)+[-0.5067]\cos(5x)+[0.1981]\cos(7x)+[-0.0506]\cos(9x)+[0.0091]\cos(11x)\}$

$\psi_4^e = \frac{1}{\sqrt{2\pi}}[-0.4680]\cos(0x)]+\frac{1}{\sqrt{\pi}}\{[0.0466]\cos(2x)+[0.6477]\cos(4x)+[-0.5524]\cos(6x)+[0.2256]\cos(8x)+[-0.0569]\cos(10x)$
$+[0.0098]\cos(12x)+[-0.0012]\cos(14x)\}$

$\psi_6^e = \frac{1}{\sqrt{\pi}}\{[-0.5186]\cos(x)+[0.2704]\cos(3x)+[0.5615]\cos(5x)+[-0.5407]\cos(7x)+[0.2179]\cos(9x)+[-0.0524]\cos(11x)$
$+[0.0086]\cos(13x)+[-0.001]\cos(15x)\}$

$\psi_8^e = \frac{1}{\sqrt{2\pi}}[-0.4724]\cos(0x)+\frac{1}{\sqrt{\pi}}\{[-0.3716]\cos(2x)+[0.3142]\cos(4x)+[0.5199]\cos(6x)+[-0.4847]\cos(8x)+[0.1818]\cos(10x)$
$+[-0.0404]\cos(12x)+[0.0061]\cos(14x)]\}$

.

Table A.12. First five wavefunctions for odd (sin) energy levels.

$$\psi_1^o = \frac{1}{\sqrt{\pi}}\{[0.8140]\sin(x)+[-0.5293]\sin(3x)+[0.2289]\sin(5x)+[-0.0682]\sin(7x)+[0.0145]\sin(9x)+[-0.0023]\sin(11x)\}$$

$$\psi_3^o = \frac{1}{\sqrt{\pi}}\{[0.6574]\sin(2x)+[-0.6657]\sin(4x)+[0.3362]\sin(6x)+[-0.1051]\sin(8x)+[0.0224]\sin(10x)+[-0.0034]\sin(12x)\}$$

$$\psi_5^o = \frac{1}{\sqrt{\pi}}\{[0.4796]\sin(x)+[0.3928]\sin(3x)+[-0.6763]\sin(5x)+[0.3787]\sin(7x)+[-0.1193]\sin(9x)+[0.0247]\sin(11x)$$
$$+[-0.0036]\sin(13x)\}$$

$$\psi_7^0 = \frac{1}{\sqrt{\pi}}\{[0.6185]\sin(2x)+[0.2223]\sin(4x)+[-0.6453]\sin(6x)+[0.3717]\sin(8x)+[-0.1132]\sin(10x)+[0.0222]\sin(12x)$$
$$+[-0.0031]\sin(14x)\}$$

$$\psi_9^o = \frac{1}{\sqrt{\pi}}\{[0.3012]\sin(x)+[0.6272]\sin(3x)+[-0.1771]\sin(5x)+[-0.6055]\sin(7x)+[0.3300]\sin(9x)+[-0.0933]\sin(11x)$$
$$+[0.0169]\sin(13x)+[-0.0022]\sin(15x)\}$$

Table A.13. Probability density for even energy (cos) levels. Potential well defined at 80% of energy.

	Region				
	1	2	3	2′	1′
Energy Levels	0-0.463	0.463-2.678	2.678-3.605	3.605-5.820	5.820-6.283
0	0	50.0	0	50.0	0
2	0	50.0	0	50.0	0
4	0	49.9	0.1	49.9	0
6	0.5	49.1	0.9	49.1	0.5
8	2.6	44.7	5.3	44.7	2.6
10	9.5	30.9	19.1	30.9	9.5
12	16.7	16.6	33.4	16.6	16.7

Continued A.13…

14	15.0	20.1	29.9	20.1	15.0
16	10.1	29.9	20.1	29.9	10.1
18	9.4	31.2	18.8	31.2	9.4
20	10.0	30.0	20.0	30.0	10.0
22	9.7	30.1	19.5	30.1	9.7
24	8.7	32.7	17.3	32.7	8.7
26	7.8	34.4	15.6	34.4	7.8
28	7.7	34.7	15.4	34.7	7.7
30	8.1	33.8	16.2	33.8	8.1
32	8.5	33.0	17.0	33.0	8.5
34	8.4	33.1	16.9	33.1	8.4
36	8.0	34.1	15.9	34.1	8.0
38	7.5	35.0	15.0	35.0	7.5
40	7.4	35.3	14.7	35.3	7.4
42	7.6	34.8	15.2	34.8	7.6
44	7.9	34.1	15.9	34.1	7.9
46	8.0	33.9	16.1	33.9	8.0
48	7.9	34.3	15.7	34.3	7.9
50	7.5	35.0	15.0	35.0	7.5
52	7.3	35.4	14.6	35.4	7.3
54	7.4	35.3	14.7	35.3	7.4
56	7.6	34.8	15.2	34.8	7.6
58	7.8	34.4	15.6	34.4	7.8
60	7.8	34.4	15.6	34.4	7.8
62	7.6	34.8	15.2	34.8	7.6
64	7.4	35.3	14.7	35.3	7.4
66	7.3	35.5	14.6	35.5	7.3
68	7.4	35.2	14.8	35.2	7.4
70	7.6	34.8	15.2	34.8	7.6

Continued A.13…

72	7.7	34.6	15.5	34.6	7.7
74	7.7	34.7	15.3	34.7	7.7
76	7.5	35.1	14.9	35.1	7.5
78	7.3	35.4	14.6	35.4	7.3
80	7.3	35.4	14.6	35.4	7.3
82	7.4	35.1	14.9	35.1	7.4
84	7.6	34.8	15.2	34.8	7.6
86	7.6	34.7	15.3	34.7	7.6
88	7.6	34.9	15.1	34.9	7.6
90	7.4	35.2	14.8	35.2	7.4
92	7.3	35.5	14.6	35.5	7.3
94	7.3	35.4	14.6	35.4	7.3
96	7.5	35.2	14.7	35.2	7.5
98	7.6	34.8	15.2	34.8	7.6

Table A.14. Probability density for odd energy (sin) levels. Potential well defined at 80% of energy.

	Region				
	1	2	3	2′	1′
Energy Levels	0-0.463	0.463-2.678	2.678-3.605	3.605-5.820	5.820-6.283
1	0	50	0	50	0
3	0	50	0	50	0
5	0	49.9	0	49.9	0
7	0.4	49.2	0.8	49.2	0.4
9	2.0	46.0	4.0	46.0	2.0
11	5.8	38.3	11.7	38.3	5.8

Continued A.14…

13	10.3	29.5	20.6	29.5	10.3
15	11.8	26.3	23.7	26.3	11.8
17	10.3	29.3	20.7	29.3	10.3
19	8.5	33.0	17.0	33.0	8.5
21	8.0	33.9	16.1	33.9	8.0
23	8.5	32.9	17.1	32.9	8.5
25	9.0	32.0	18.1	32.0	9.0
27	8.8	32.3	17.7	32.3	8.8
29	8.2	33.7	16.3	33.7	8.2
31	7.6	34.9	15.1	34.9	7.6
33	7.5	35.1	15.0	35.0	7.5
35	7.8	34.4	15.6	34.4	7.8
37	8.2	33.7	16.3	33.7	8.2
39	8.2	33.6	16.4	33.6	8.2
41	7.9	34.2	15.8	34.2	7.9
43	7.8	34.6	15.6	34.6	7.8
45	7.3	35.4	14.6	35.4	7.3
47	7.5	35.1	14.9	35.1	7.5
49	7.7	34.5	15.5	34.5	7.7
51	7.9	34.2	15.9	34.2	7.9
53	7.8	34.3	15.7	34.3	7.8
55	7.6	34.9	15.1	34.9	7.6
57	7.3	35.4	14.6	35.4	7.3
59	7.3	35.4	14.6	35.4	7.3
61	7.5	35.0	15.0	35.0	7.5
63	7.7	34.6	15.4	34.6	7.7
65	7.8	34.5	15.5	34.5	7.8
67	7.6	34.7	15.3	34.7	7.6
69	7.4	35.2	14.8	35.2	7.4

Continued A.14…

71	7.3	35.5	14.6	35.5	7.3
73	7.3	35.3	14.7	35.3	7.3
75	7.5	35.0	15.0	35.0	7.5
77	7.7	34.5	15.3	34.5	7.7
79	7.7	34.7	15.3	34.7	7.7
81	7.5	35.0	15.0	35.0	7.5
83	7.3	35.3	14.7	35.3	7.3
85	7.3	35.5	14.6	35.5	7.3
87	7.4	35.3	14.7	35.3	7.4
89	7.5	35.0	15.1	35.0	7.5
91	7.6	34.8	15.3	34.8	7.6
93	7.6	34.9	15.2	34.9	7.6
95	7.4	35.1	14.9	35.1	7.4
97	7.3	35.4	14.6	35.4	7.3
99	7.3	35.4	14.6	35.4	7.3

*Figure A.7. Probability density for odd energy levels for $V_2=100$ cm^{-1} and **B**$=1.0$ cm^{-1}. The yellow line denotes the energy level below 100 cm$^{-1,}$ and the blue line indicates the energy level above 100 cm^{-1}. The top panel shows the probability density "inside the well" and the bottom one "outside the well". The black line denotes the delocalisation value.*

*Figure A.8. Probability density for even energy levels for V₂=100 cm⁻¹ and **B**=1.0 cm⁻¹. The yellow line denotes the energy level below 100 cm⁻¹, and the blue line indicates the energy level above 100 cm⁻¹. The top panel shows the probability density "inside the well" and the bottom one "outside the well". The black line denotes the delocalisation value.*

*Figure A.9. Probability density for all energy levels for V₂=100 cm⁻¹ and **B**=1.0 cm⁻¹. The yellow line denotes the energy level below 100 cm⁻¹, and the blue line indicates the energy level above 100 cm⁻¹. The top panel shows the probability density "inside the well" and the bottom one "outside the well". The black line denotes the delocalisation value.*

A.3.3   Dependence on the Definition of the Well

In the previous section integration limit is defined at 80% of the energy (provided here once again for completeness, Figure A.10). We have repeated the whole calculation with the integration limit at 70% (Figure A.11), 60% (Figure A.12), 50% (Figure A.13) of the energy. A similar pattern has been obtained in probability density with increasing energy levels. We have not normalised the probability density associated with each region. However, if we set the integration limit to 50%, we obtain normalised probabilities. The delocalisation limit for the "inside" and "outside" the well is the same. Hence, it is easy to compare the probability density in these two regions. The results for the barrier at 50% of the energy have been discussed in detail here.

The 0th and 1st energy levels have a 100% probability inside the well and start decreasing from the 2nd energy level. The probability density kept on decreasing inside the well with oscillations. As the integration limit is kept at 50% of the total energy, a sharp decrease in probability 'inside the well' has been observed above 50 cm^{-1}. The 5th energy level has an energy of 46.5 cm^{-1} and has 92 % probability inside the well, and it suddenly decreases to 72.2 % for the 6th energy level, which has an energy of 63.0 cm^{1}. The probability density kept on decreasing in an oscillatory manner up to the 12th energy level as the wavefunction tend to localise at the side of the well.

On the other hand, the energy level above 100 cm^{-1} (i.e., from the 13th energy level) probability density inside the well-kept increasing in an oscillatory manner before complete delocalisation. Precisely, an opposite trend has been observed for the probability density outside the well. The essential point here, as in the preceding section, is that *"the wavefunction does not appear to be immediately delocalised above the well"*.
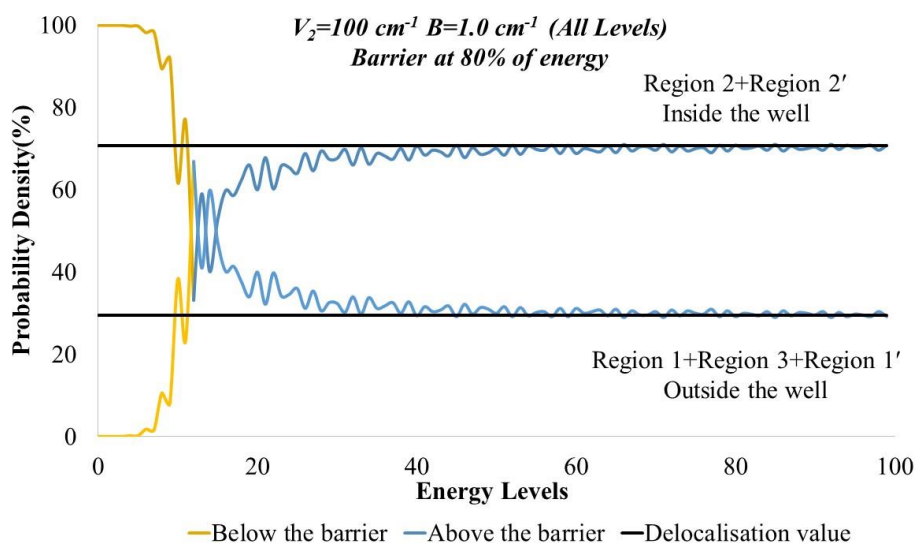
*Figure A.10. Probability density for all energy levels for V₂=100 cm⁻¹ and **B**=1.0 cm⁻¹. The yellow line denotes the energy level below 100 cm⁻¹, and the blue line indicates the energy level above 100 cm⁻¹. The top panel shows the probability density "inside the well" and the bottom one "outside the well". The black line denotes the delocalisation value. The integrating region is kept at 80% of total energy. This diagram is similar to Figure A.9 and provided once again for completeness.*
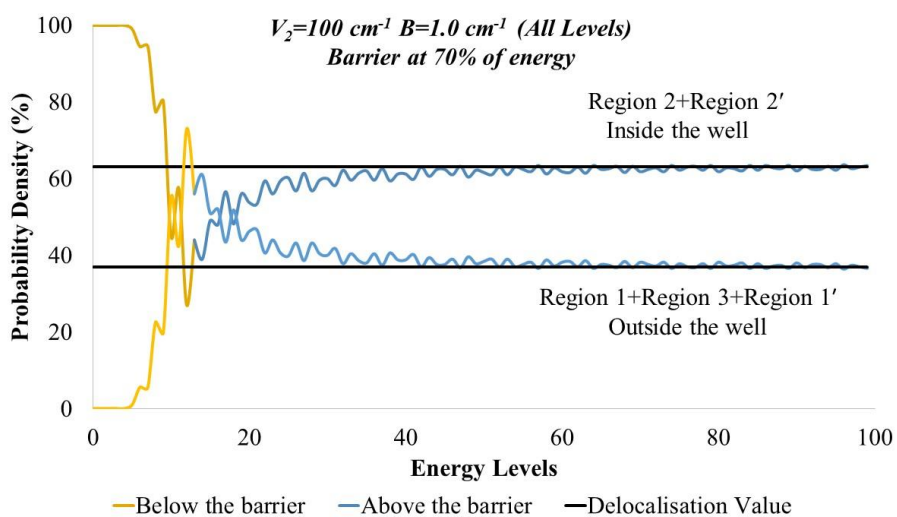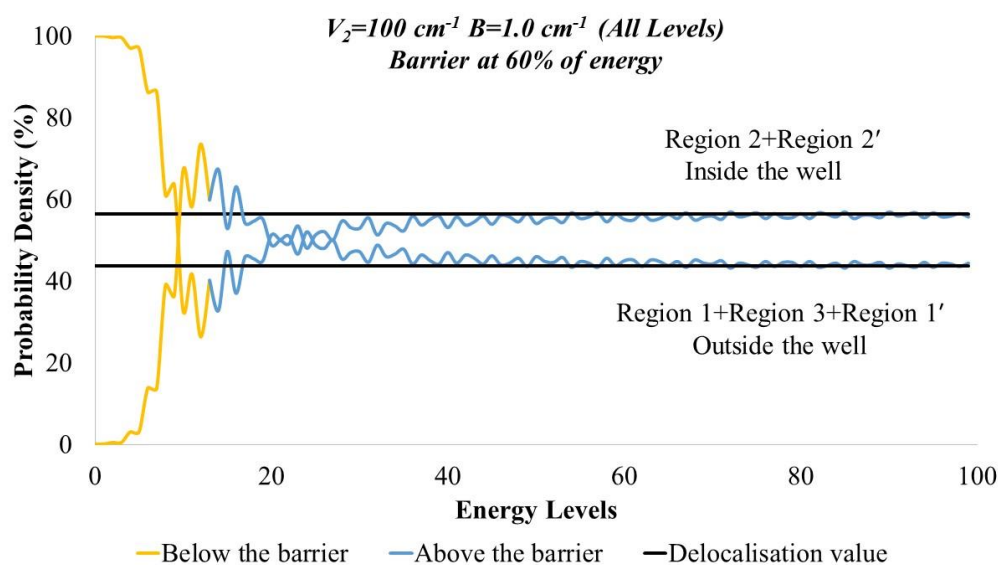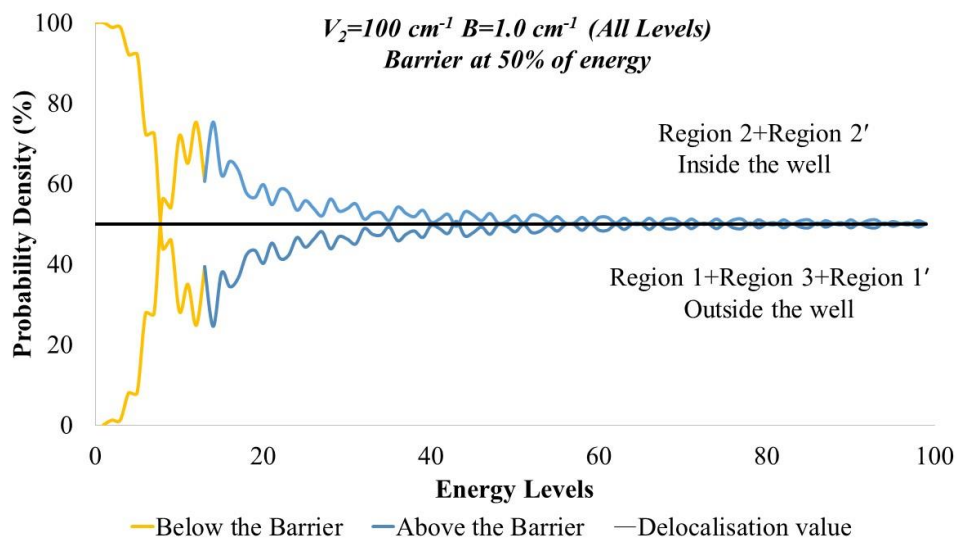

*Figure A.11. Probability density for all energy levels for V₂=100 cm⁻¹ and **B**=1.0 cm⁻¹. The yellow line denotes the energy level below 100 cm⁻¹, and the blue line indicates the energy level above 100 cm⁻¹. The top panel shows the probability density "inside the well" and the bottom one "outside the well". The black line denotes the delocalisation value.*

Figure A.12. Probability density for all energy levels for $V_2=100\ cm^{-1}$ and $\boldsymbol{B}=1.0\ cm^{-1}$. The yellow line denotes the energy level below $100\ cm^{-1}$, and the blue line indicates the energy level above $100\ cm^{-1}$. The top panel shows the probability density '"inside the well" and the bottom one "outside the well". The black line denotes the delocalisation value.

Figure A.13. Probability density for all energy levels for $V_2=100\ cm^{-1}$ and $\boldsymbol{B}=1.0\ cm^{-1}$. The yellow line denotes the energy level below $100\ cm^{-1}$, and the blue line indicates the energy level above $100\ cm^{-1}$. The top panel shows the probability density "inside the well" and the bottom one "outside the well". The black line denotes the delocalisation value.

A.3.4 Dependence on the Barrier Height

In the previous section, a barrier height of V_2=100 cm^{-1} has been considered to calculate the energy level, wavefunctions, and probability density. In this section, two different barrier heights V_2=10 cm^{-1} (odd levels, Figure A.14; even levels, Figure A.15; all levels, Figure A.16) and V_2=1000 cm^{-1} (odd levels, Figure A.17; Figure A.18 even levels,; all levels, Figure A.19) are used to check the dependence of the result on barrier height. The internal rotational constant $\boldsymbol{B}$=1.0 cm^{-1} has been used with the barrier at 80% of the energy. For the small barrier V_2=10 cm^{-1}, only four energy levels are below the barrier (0th, 1st, 2nd, 3rd), and the 4th energy level appears above 10 cm^{-1} at 10.6 cm^{-1}. As the integration limit is specified at 80% of the energy (i.e., at 8 cm^{-1}), a significant change in the probability density for the third energy level at 8.5 cm^{-1} has been observed. A similar pattern has been observed for a 10 cm^{-1} barrier as well. The wavefunction delocalises through the oscillation. These oscillations have been observed for very few energy levels owing to the small barrier height.

For a two-fold potential with a 1000 cm^{-1} barrier, a total of 40 energy levels appears below the barrier. Up to the 23rd energy level, we have observed that the wavefunctions have a 100% probability of staying inside the well. The boundaries for the integration have been kept at the 80% of the energy (i.e., at 800 cm^{-1}). Hence, the probability inside decreases effectively from the 30th energy level (at 836.9 cm^{-1}). The energy levels above 1000 cm^{-1} do not delocalise immediately. Before the wavefunction is entirely delocalised, oscillations can be detected for several energy levels. According to this study, the larger the barrier, the more oscillation the wavefunction undergoes before total delocalisation.
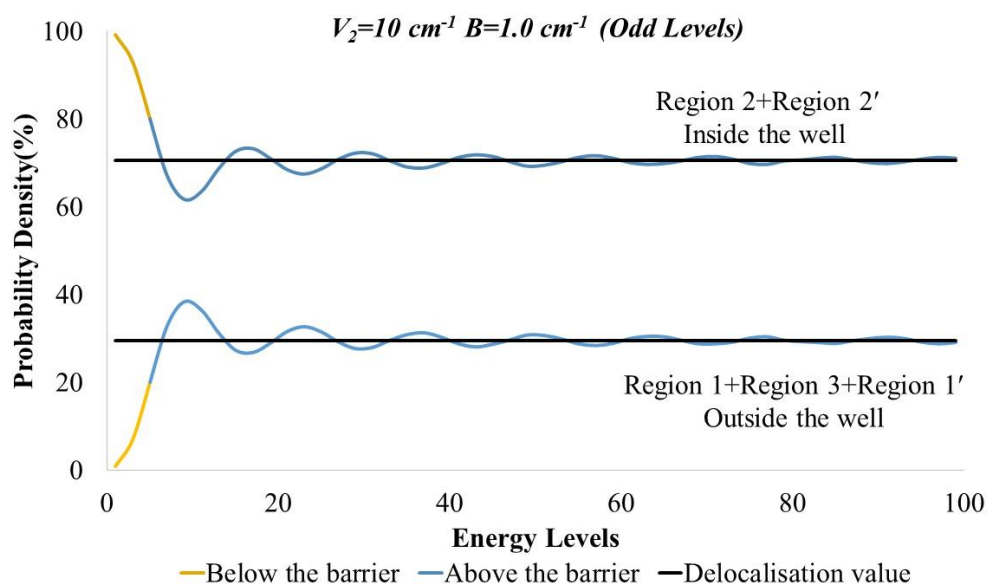
*Figure A.14. Probability density for odd energy levels for $V_2=10$ cm^{-1} and **B**$=1.0$ cm^{-1}. The yellow line denotes the energy level below 10 cm^{-1}, and the blue line denotes the energy level above 10 cm^{-1}. The top panel shows the probability density "inside the well" and the bottom one "outside the well". The black line denotes the delocalisation value.*
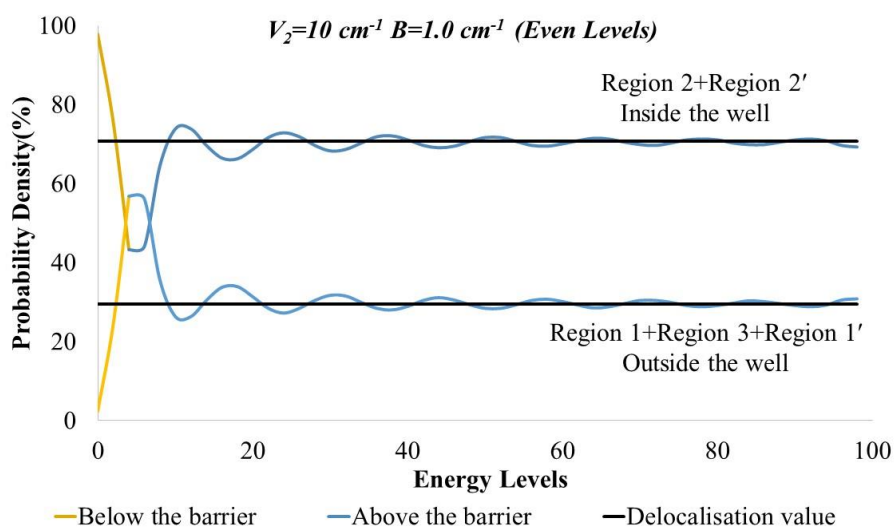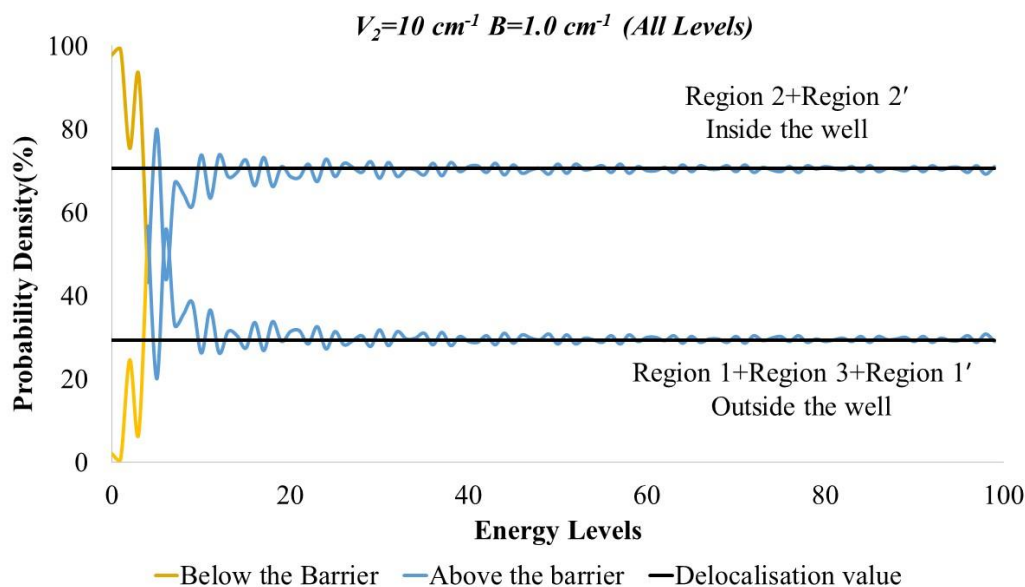

*Figure A.15. Probability density for even energy levels for $V_2=10$ cm^{-1} and **B**$=1.0$ cm^{-1}. The yellow line denotes the energy level below 10 cm^{-1}, and the blue line denotes the energy level above 10 cm^{-1}. The top panel shows the probability density "inside the well" and the bottom one "outside the well". The black line denotes the delocalisation value.*
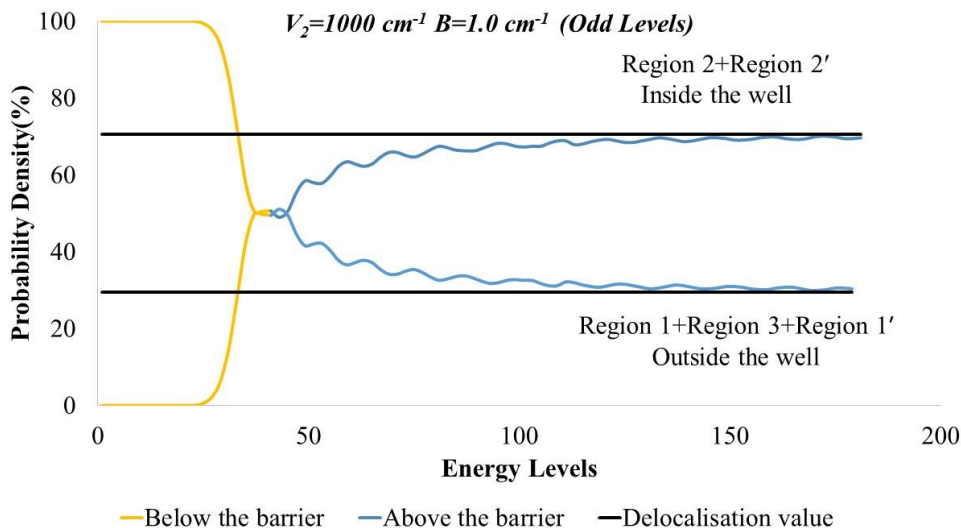
*Figure A.16. Probability density for all energy levels for $V_2=10$ cm^{-1} and **B**$=1.0$ cm^{-1}. The yellow line denotes the energy level below 10 cm$^{-1,}$ and the blue line indicates the energy level above 10 cm^{-1}. The top panel shows the probability density "inside the well" and the bottom one "outside the well". The black line denotes the delocalisation value.*
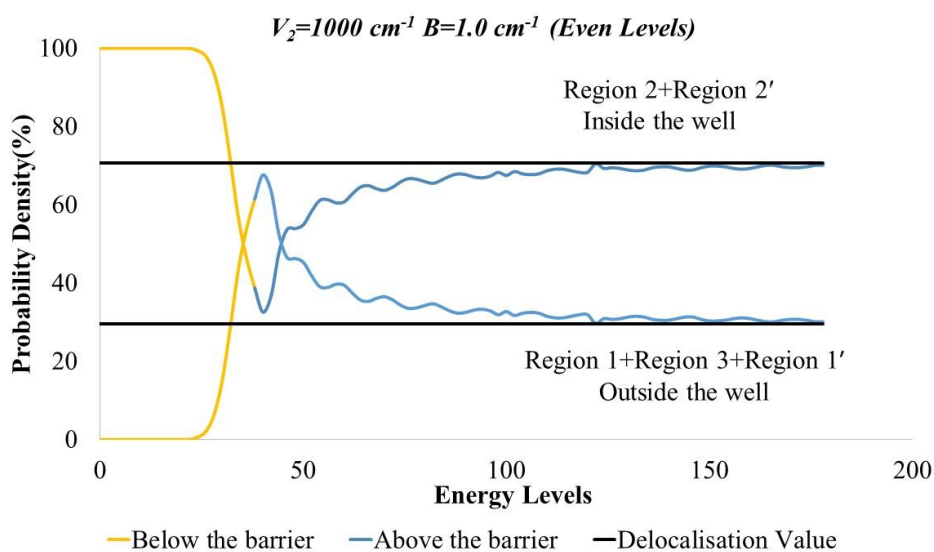

*Figure A.17. Probability density for odd energy levels for $V_2=1000$ cm^{-1} and **B**$=1.0$ cm^{-1}. The yellow line denotes the energy level below 1000 cm-1, and the blue line denotes the energy level above 1000 cm^{-1}. The top panel shows the probability density "inside the well" and the bottom one "outside the well". The black line denotes the delocalisation value.*

.

Figure A.18. Probability density for even energy levels for V_2=10 cm^{-1} and $\boldsymbol{B}$=1.0 cm^{-1}. The yellow line denotes the energy level below 1000 $cm^{-1,}$ and the blue line denotes the energy level above 1000 cm^{-1}. The top panel shows the probability density "inside the well" and the bottom one "outside the well". The black line denotes the delocalisation value.
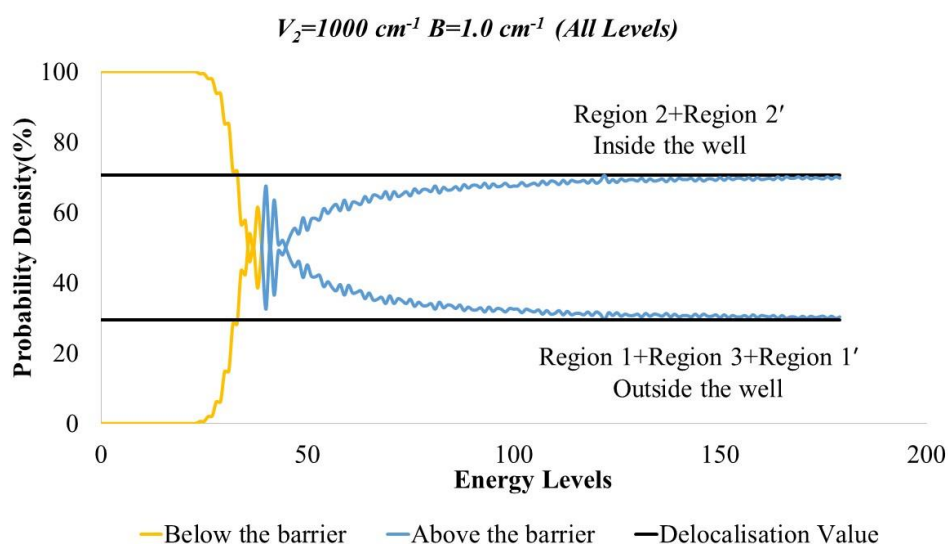

Figure A.19. Probability density for all energy levels for V_2=1000 cm^{-1} and $\boldsymbol{B}$=1.0 cm^{-1}. The yellow line denotes the energy level below 1000 $cm^{-1,}$ and the blue line indicates the energy level above 1000 cm^{-1}. The top panel shows the probability "inside the well" and the bottom one "outside the well". The black line indicates the delocalisation value.

A.3.5 Dependence on the Internal Rotational Constant

Internal rotational constant (B) is an essential parameter in the Hamiltonian. In general, B is a function of coordinates, and we could expand B in a series like the following:

$$B = B_0 + \sum B_n \cos n\phi \tag{10}$$

In the current problem, we have not used a variable B with ϕ. In all the previous calculations, the internal rotation constant has been kept at 1.0 cm^{-1}. Here we have used $B=10.0$ cm^{-1} for a two-fold potential with $V_2=100$ cm^{-1} to calculate the energy levels, wavefunction, and probability density (see Figure A.20). As we increase the value of B, the effective barrier height decreases. In equation (11), S_n is defined as follows.

$$S_n = \frac{V_n}{2B_0} \tag{11}$$

A two-fold potential with $V_2=100$ cm^{-1}, $B=10.0$ cm^{-1} and $V_2=10$ cm^{-1}, $B=1.0$ cm^{-1} have same energy levels, wavefunction. The result for $V_2=100$ cm^{-1} with $B=10.0$ cm^{-1} are presented in Figure A.20 which is exactly equivalent to Figure A.16.

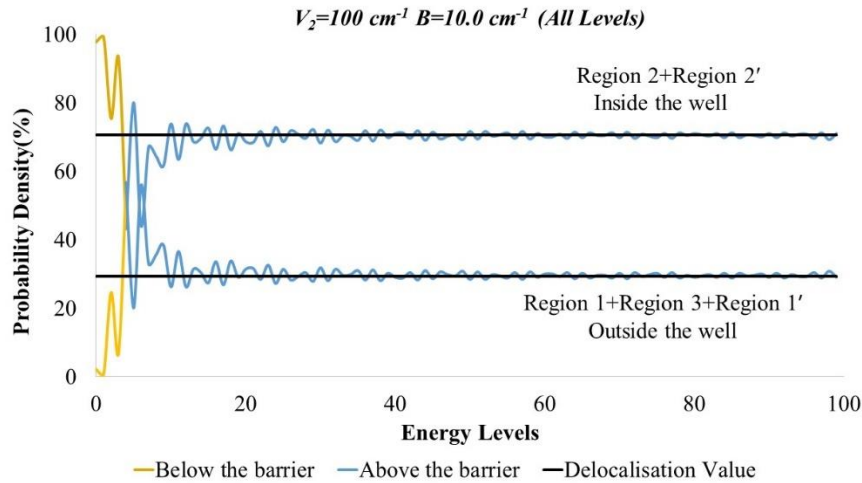*Figure A.20. Probability density for all energy levels for $V_2=100$ cm^{-1} and $B=10.0$ cm^{-1}. The yellow line denotes the energy level below 100 cm^{-1}, and the blue line indicates the energy level above 100 cm^{-1}. The top panel shows the probability density "inside the well" and the bottom one "outside the well". The black line denotes the delocalisation value.*

A.3.6 **Dependence on the Fold of the Potential**

So far in the discussion, we have used two-fold potentials to calculate its energy levels and probability density. To check the validity of the result, we have considered the three-fold potential here with V_3 =100 cm^{-1} and $\boldsymbol{B}$ =1.0 cm^{-1}. Similar parameters have been used in the first test case in section A.2.2 to evaluate the energy levels and wavefunction. Here, from the previously calculated wavefunctions and with integration range at 80 % of the total energy, we have calculated the probability density in the designated regions as described in Figure A.6. Figure A.21 shows the probability density with increasing energy levels and a similar pattern observed as previous.
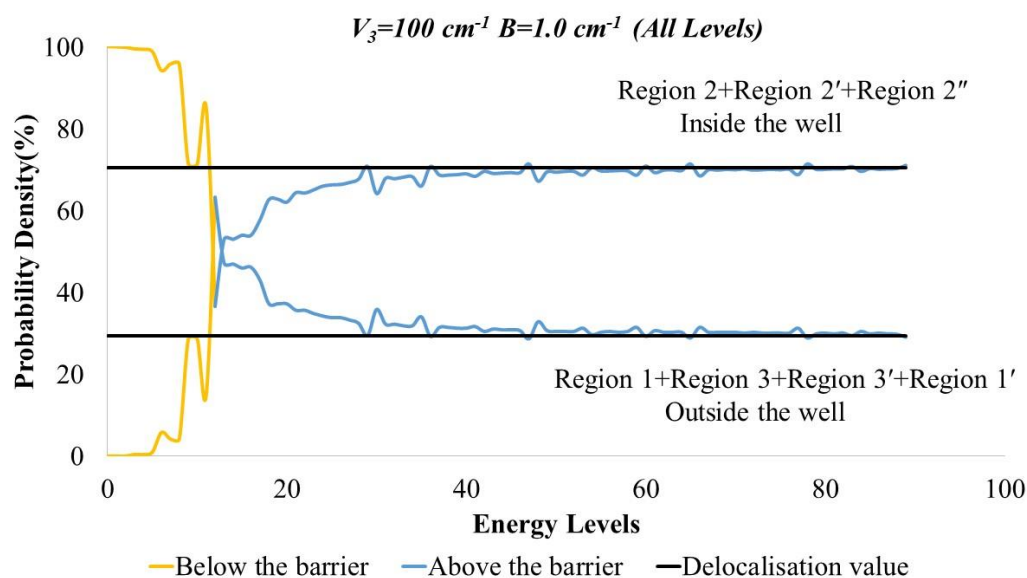

Figure A.21. Probability density for all energy levels for V_3=100 cm^{-1} and $\boldsymbol{B}$=1.0 cm^{-1}. The yellow line denotes the energy level below 100 cm^{-1}, and the blue line denotes the energy level above 100 cm^{-1}. The top panel shows the probability density "inside the well" and the bottom one "outside the well". The black line denotes the delocalisation value.

A.4 **Summary**

To summarise, we have calculated the probability density associated with each well in a periodic potential. Our results suggest that the wavefunction for the lower energies than the barrier height is localised inside the well. The wavefunctions just above the barrier remain localised to some extent. Since these periodic potentials govern large amplitude motion in weakly bound molecules along a vibrational coordinate, the localisation of the wavefunction above the barrier height suggests the likelihood of a hydrogen bond above the barrier. The current study modifies the criteria given by Goswami and Arunan[5] for hydrogen bonding in supersonic beams for weakly bound complexes.

A.5 **References**

1. Arunan, E. *et al.* Definition of the hydrogen bond (IUPAC Recommendations 2011). *Pure Appl. Chem.* **83**, 1637–1641 (2011).

2. Arunan, E. *et al.* Defining the hydrogen bond: An account (IUPAC Technical Report). *Pure Appl. Chem.* **83**, 1619–1636 (2011).

3. Joseph, J. & Jemmis, E. D. Red-, blue-, or no-shift in hydrogen bonds: a unified explanation. *J. Am. Chem. Soc.* **129**, 4620–4632 (2007).

4. Koch, U. & Popelier, P. L. A. Characterization of CHO hydrogen bonds on the basis of the charge density. *J. Phys. Chem.* **99**, 9747–9754 (1995).

5. Goswami, M. & Arunan, E. The hydrogen bond: a molecular beam microwave spectroscopist's view with a universal appeal. *Phys. Chem. Chem. Phys.* **11**, 8974–8983 (2009).

6. Turovtsev, V. V, Orlov, M. Y. & Orlov, Y. D. Solution of a torsional Schrödinger equation with a periodic potential of general form. The probability amplitude and probability density. *Opt. Spectrosc.* **123**, 217–224 (2017).

7.   Turovtsev, V. V, Belotserkovskii, A. V & Orlov, Y. D. Solution of a one-dimensional torsion Schrödinger equation with a general periodic potential. *Opt. Spectrosc.* **117**, 710–712 (2014).

8.   Ercolani, G. Numerical evaluation of energy levels and wave functions for hindered internal rotation. *J. Chem. Educ.* **77**, 1495 (2000).

9.   Laboratory, U. S. N. B. of S. C. *Tables Relating to Mathieu Functions: Characteristic Values, Coefficients, and Joining Factors*. vol. 59 (US Department of Commerce, National Bureau of Standards, 1967).

10.   Herschbach, D. R. Tables of Mathieu integrals for the internal rotation problem. *J. Chem. Phys.* **27**, 975 (1957).

11.   Wilson Jr, E. B., Lin, C. C. & Lide Jr, D. R. Calculation of Energy Levels for Internal Torsion and Over-All Rotation. I. CH_3BF_2 Type Molecules. *J. Chem. Phys.* **23**, 136–142 (1955).

12.   Kilb, R. W., Lin, C. C. & Wilson Jr, E. B. Calculation of Energy Levels for Internal Torsion and Over-All Rotation. II. CH_3CHO Type Molecules; Acetaldehyde Spectra. *J. Chem. Phys.* **26**, 1695–1703 (1957).

13.   Herschbach, D. R. Calculation of Energy Levels for Internal Torsion and Over-All Rotation. III. *J. Chem. Phys.* **31**, 91–108 (1959).

14.   Lewis, J. D., Malloy Jr, T. B., Chao, T. H. & Laane, J. Periodic potential functions for pseudorotation and internal rotation. *J. Mol. Struct.* **12**, 427–449 (1972).

15.   Lewis, J. D. & Laane, J. Periodic potential energy functions with sine and cosine terms. *J. Mol. Spectrosc.* **65**, 147–154 (1977).

16.   Kohmoto, M., Kadanoff, L. P. & Tang, C. Localization problem in one dimension: Mapping and escape. *Phys. Rev. Lett.* **50**, 1870 (1983).

17.   Ostlund, S., Pandit, R., Rand, D., Schellnhuber, H. J. & Siggia, E. D. One-dimensional Schrödinger equation with an almost periodic potential. *Phys. Rev.*

References

Lett. **50**, 1873 (1983).

18. Pine, A. S., Lafferty, W. J. & Howard, B. J. Vibrational predissociation, tunneling, and rotational saturation in the HF and DF dimers. *J. Chem. Phys.* **81**, 2939–2950 (1984).

19. Fraser, G. T. *et al.* Infrared and microwave investigations of interconversion tunneling in the acetylene dimer. *J. Chem. Phys.* **89**, 6028–6045 (1988).

20. Fraser, G. T., Suenram, R. D. & Coudert, L. H. Microwave electric-resonance optothermal spectroscopy of $(H_2O)_2$. *J. Chem. Phys.* **90**, 6077–6085 (1989).

21. Suenram, R. D., Fraser, G. T. & Lovas, F. J. Microwave spectrum of $(D_2O)_2$. *J. Mol. Spectrosc.* **138**, 440–449 (1989).

22. Karyakin, E. N., Fraser, G. T. & Suenram, R. D. Microwave spectrum of the K a= 1← 0 rotation-tunnelling band of $(D_2O)_2$. *Mol. Phys.* **78**, 1179–1189 (1993).

23. Karyakin, E. N., Fraser, G. T., Lovas, F. J., Suenram, R. D. & Fujitake, M. Donor–acceptor interchange tunneling in HDO–DOH and the higher energy HDO–HOD isotopomer. *J. Chem. Phys.* **102**, 1114–1121 (1995).

24. Fraser, G. T. $(H_2O)_2$: spectroscopy, structure and dynamics. *Int. Rev. Phys. Chem.* **10**, 189–206 (1991).

List of Publications

(1) Das, A., Mandal, P. K., Lovas, F. J., Medcraft, C., Walker, N. R., & Arunan, E. The H_2S Dimer is Hydrogen-Bonded: Direct Confirmation from Microwave Spectroscopy. *Angew. Chemie Int. Ed.* **57**, 15199–15203 (2018).

(2) Das, A. & Arunan, E. Chemical bonding in Period 2 homonuclear diatomic molecules: a comprehensive relook. *J. Chem. Sci.* **131**, 1–17 (2019).

(3) Das, A., Gougoula, E., Medcraft, C., Walker, N. R., & Arunan, E. Rotational spectra, structure and dynamics of $(H_2S)_2(H_2O)$ (*Manuscript under preparation*).

(4) Das, A., Arunan, E. Donor-acceptor interchange tunnelling in $Ar(H_2O)_2$ and a relook at its structure and bonding (*Manuscript under preparation*).

(5) Das, A., Periodic Table of intermolecular bonding *(Manuscript to be submitted).*